

Copyright

by

Melissa Travis Jerkins

2010

The Dissertation Committee for Melissa Travis Jerkins
certifies that this is the approved version of the following dissertation:

**From Atoms to Astronomy: New Approaches
in Neutrino Physics**

Committee:

Mark G. Raizen, Supervisor

Joshua Klein

Eiichiro Komatsu

Karol Lang

John Keto

**From Atoms to Astronomy: New Approaches
in Neutrino Physics**

by

Melissa Travis Jerkins, B.S.

Dissertation

Presented to the Faculty of the Graduate School of

The University of Texas at Austin

in Partial Fulfillment

of the Requirements

for the Degree of

Doctor of Philosophy

The University of Texas at Austin

August 2010

To Nathan

Acknowledgments

When I told my friends I was going to have two graduate research advisers, most of them responded with a consolatory, “I’m so sorry,” assuming that I would end up with twice the normal amount of work and only half the mentoring; I owe a tremendous debt of gratitude to Mark Raizen and Josh Klein for proving them wrong. I want to thank both of them for the countless conversations they have taken the time to have with me. Their love of physics is contagious, and their optimism and creativity is unmatched. They were always ready to ask the hard questions, listen when I was stuck, and offer timely encouragement. They treat their students as peers, and working with them for the past few years has been both a joy and a privilege.

I also owe a special thanks to Aubra Anthony, whose work on SNO’s low-multiplicity burst search laid the foundation for much of my research. Thanks to Aubra, as well as to Stan Seibert and Gabriel Orebi Gann, for patiently answering all of my questions. I am indebted to the entire SNO Collaboration, and particularly to Joseph Formaggio, Jeffery Secrest, James Loach, Nikolai Tolich, Feng Zhang, Helen O’Keeffe, Art MacDonald, Gersende Prior, and the entire exotics group. I believe I was the last member to join the SNO Collaboration, but they welcomed me as if I had always been part of

the family.

I want to thank everyone in the Raizen Laboratory for giving me a place to belong when I was undertaking the strange task of studying atoms and neutrinos at the same time. I am especially grateful for my office-mates, Rob Clark, Adam Libson, Tom Mazur, and Isaac Chavez, who always made coming to work enjoyable. Whether we were discussing physics, sports, movies, or geopolitics, the conversations were both entertaining and thought-provoking.

For my friends and family, I am extremely thankful. My friends here in Austin have encouraged and supported me through my entire graduate school experience (and they have even feigned a keen interest in the details of neutrino physics when they could tell I needed to talk about it). Especially to everyone at Immanuel Austin, thanks for your constant reminders of what matters most in my life. Although no one else in my immediate family pursued a career in science, my parents could not have been more supportive of my decision to study physics. Thanks to both of them for their trust and faith in teaching me how to ask interesting questions and search for satisfying answers.

Most of all I want to thank my husband, Nathan. I am forever grateful to him for making sacrifices in order to help me pursue this path; for constantly encouraging me and making me laugh when I most needed to; for loving me just as much on the days I failed as on the days I succeeded. The last day of writing this dissertation is one of the good days, and it would not have been possible without him.

MELISSA TRAVIS JERKINS

The University of Texas at Austin
August 2010

From Atoms to Astronomy: New Approaches in Neutrino Physics

Publication No. _____

Melissa Travis Jerkins, Ph.D.

The University of Texas at Austin, 2010

Supervisor: Mark G. Raizen

In this thesis I present research in neutrino physics utilizing tools from both atomic physics and astrophysics. Recent advances in atomic physics enable a new type of β decay experiment to measure the absolute mass scale of the neutrino using a sample of ultracold atomic tritium. These initial conditions enable the detection of the helium ion in coincidence with the β . I construct a two-dimensional fit incorporating both the shape of the β spectrum and the direct reconstruction of the neutrino mass peak. I present simulation results of the feasible limits on the neutrino mass achievable in this new type of tritium

β decay experiment.

The same advances in atomic physics that enable the creation of an atomic source for tritium β decay also suggest a new method of achieving large-scale isotope separation. Multiple experiments that are investigating the absolute mass scale of the neutrino through neutrinoless double β decay could benefit from this new technique, which applies generally to many elements, including the double β emitter ^{150}Nd that is particularly difficult to separate in large quantities. The method is based on an irreversible change of the mass-to-magnetic moment ratio of a particular isotope in a supersonic atomic beam, followed by a magnetic multipole whose gradients deflect and guide the atoms. I present numerical simulations of isotope separation for a range of examples and demonstrate that large-scale isotope separation should be possible using ordinary inexpensive magnets and the existing technologies of supersonic beams and lasers.

Additionally I report results from a search for low-multiplicity neutrino bursts in the Sudbury Neutrino Observatory (SNO). Such bursts could indicate detection of a nearby core-collapse supernova explosion. The data were taken from November 1999 to May 2001 when the detector was filled with heavy water (Phase I), as well as data from July 2001 to August 2003 when NaCl was added to the detector (Phase II). The search was a blind analysis in which the potential backgrounds were estimated and analysis cuts were developed to eliminate such backgrounds with 90% confidence before the data were examined. The search maintained a greater than 50% detection probability for standard supernovae occurring at a distance of up to 60 kpc for Phase I and up to 70 kpc for Phase II. No low-multiplicity bursts were observed during the data-taking period.

Contents

Acknowledgments	v
Abstract	viii
Contents	x
List of Tables	xvii
List of Figures	xix
Chapter 1 Introduction	1
Chapter 2 Neutrino Physics Past and Present	5
2.1 Background	5
2.1.1 Neutrino Discovery	5
2.1.2 Neutrinos in the Standard Model	7
2.1.3 Neutrino Oscillations	8
2.1.4 MSW Effect	13
2.2 Neutrino Applications	16
2.2.1 Supernova Detection and the DSNB	17
2.2.2 Astrophysics and the Relic Neutrino Background	18

2.2.3	Geoneutrinos	19
2.2.4	Quantum Gravity Investigations	19
2.3	Open Questions	20
2.3.1	Absolute Mass Scale and Hierarchy	20
2.3.2	Majorana or Dirac	21
2.3.3	Electromagnetic Moments	23
2.3.4	θ_{13}	23
2.3.5	Role in Astrophysics and Cosmology	24
2.4	Measuring Neutrino Mass	26
2.4.1	Previous Beta Decay Experiments	26
2.4.2	KATRIN	35
2.4.3	MARE	37
2.4.4	Neutrinoless Double Beta Decay	38
2.4.5	Cosmological Limits	43
Chapter 3 Recent Advances in Atomic Control		48
3.1	General Method of Atomic Slowing: Atomic Coilgun	49
3.1.1	Supersonic Beam	49
3.1.2	The Coilgun	50
3.1.3	Trapping	55
3.2	General Method of Atomic Cooling: Single Photon Cooling . .	55
3.2.1	Methods of Cooling	55
3.2.2	Single Photon Cooling	57
3.2.3	Maxwell's Demon	58
3.3	Isotopes of Hydrogen	60

Chapter 4	Using Cold Atoms to Measure Neutrino Mass	62
4.1	Introduction	63
4.1.1	Beta Decay Spectrum	64
4.2	Kinematic Reconstruction	67
4.2.1	Overview	67
4.2.2	ROOT Simulation	69
4.3	Atomic Tritium Source	71
4.3.1	Final State Effects	72
4.4	Helium Ion Detection	73
4.4.1	Microchannel Plate	73
4.4.2	Background Rate	76
4.5	Beta Energy Measurement	80
4.6	Beta Momentum Measurement	83
4.6.1	Rydberg Atoms	83
4.6.2	Rydberg Atom Detector Design	85
4.7	Simulation Results	87
4.7.1	Simulation Parameters and Detector Resolutions	87
4.7.2	Two-Dimensional Fit for Neutrino Mass	91
4.7.3	Maximum Likelihood Fits	100
4.7.4	Fit Results and Number of Decays	104
4.7.5	Tests of the 2D Fit	110
4.8	Future Prospects	114
Chapter 5	Separating Isotopes to Measure Neutrino Mass	116
5.1	Neutrinoless Double Beta Decay	117
5.2	SNO+	119

5.2.1	Neodymium-Loaded Liquid Scintillator	122
5.2.2	Expected Sensitivity	123
5.3	Established Methods of Isotope Separation	125
5.4	Introduction to Single Photon Atomic Sorting	130
5.4.1	Single Gradient Simulation Results	134
5.4.2	Double Gradient Simulation Results	141
5.4.3	Optical Pumping	146
5.5	Single Photon Atomic Sorting With Magnetic Guiding	147
5.5.1	Experimental Setup	147
5.5.2	Theoretical Field Equations	151
5.5.3	Simulation Results for Lithium	154
5.5.4	Additional Simulation Details	160
5.5.5	Simulation Results for Other Elements	163
5.6	Neodymium Estimate and Entrainment Capabilities	172
Chapter 6 Searching for Supernova Neutrino Bursts in SNO		185
6.1	Sudbury Neutrino Observatory	186
6.1.1	Introduction	186
6.1.2	The Detector	187
6.1.3	Data Acquisition Electronics	189
6.1.4	Neutrino Reactions	192
6.1.5	Standard SNO Backgrounds	195
6.1.6	Calibrations	197
6.1.7	Detector Simulation	199
6.1.8	Event Reconstruction	200
6.2	Supernova Neutrino Bursts	201

6.2.1	Introduction	201
6.2.2	Gravitational Core Collapse	202
6.2.3	Neutrino Energy and Time Distributions	206
6.2.4	Supernova Models	209
6.3	SNO's Supernova Detection Potential	210
6.4	Super-Kamiokande Triggerless Burst Search	212
6.5	SNO Triggerless Burst Search	213
6.5.1	Data Set	214
6.5.2	Confidence Interval	214
6.5.3	Search Windows	215
6.6	Backgrounds	218
6.6.1	Accidentals	218
6.6.2	Physics Backgrounds	220
6.7	Analysis Cuts	226
6.7.1	Standard Cuts	226
6.7.2	High NHIT Cut	228
6.7.3	Non-Electron Follower Cut	233
6.7.4	Δr Cut	235
6.7.5	$\Delta r \Delta t$ Cut	241
6.7.6	Bursts Found in the Antibox	250
6.8	Results	255
6.8.1	Bursts Found in the Box	255
6.9	Sensitivity Study	258

Chapter 7 Conclusions

265

Appendix A Beta Spectrum Derivation	268
A.0.1 Fermi’s Golden Rule	268
A.0.2 Final State Effects	276
Appendix B Boundstate Tritium Beta Decay	280
B.1 Boundstate Decay	280
B.2 Experimental Design	281
B.3 Simulation Results	283
Appendix C Mössbauer Neutrinos	286
C.1 Ordinary Mössbauer Effect	287
C.1.1 Ordinary Resonance Fluorescence	287
C.1.2 Mössbauer’s Discovery	290
C.2 Mössbauer Effect for Neutrinos	293
C.2.1 Boundstate Decay	293
C.2.2 Physics Potential	294
C.2.3 Recoilless Fraction	295
C.2.4 Previous Proposals	296
C.3 Calculations	297
C.3.1 cross section	297
C.3.2 Linewidth and Broadening	299
C.3.3 Second Order Doppler Shift	300
C.3.4 Isomer Shift	301
C.4 Experimental Design	302
C.5 Simulation Results	305
C.6 Lattice Expansion and Contraction	308

Bibliography	310
Vita	329

List of Tables

2.1	Previous tritium β decay experiments	34
4.1	Fit results comparing two interpolation techniques	97
4.2	Fit results for simulated data with various neutrino masses . .	106
4.3	Fit results when fit was limited to slices in the β spectrum . .	111
4.4	Fit results limited to slices in m_ν^2	112
4.5	Fit results for various m_ν starting values	113
4.6	Fit results for various allowed m_ν ranges	113
4.7	Fit results with various dataset binnings	114
5.1	High energy double β decay emitters	118
5.2	Single photon atomic sorting simulation results	139
5.3	Simulation results with magnetic guiding	167
6.1	Evolution of a 15-solar mass star	205
6.2	Summary of search windows and energy thresholds	216
6.3	Expected physics backgrounds	225
6.4	Standard SNO cuts	227
6.5	Summary of $\Delta r \Delta t$ cut	249
6.6	Bursts expected and observed in the antibox	250

6.7	Antibox bursts expected and observed, no NEF or NHIT cuts	251
6.8	Multiplicities in Phase II antibox, no NEF or NHIT cuts . . .	252
6.9	Multiplicities in Phase I antibox, no NEF or NHIT cuts	252
6.10	Results of low-multiplicity burst search	255

List of Figures

2.1	MSW effect	16
2.2	Neutrino mass hierarchy	22
2.3	Previous tritium β decay experiments	29
2.4	MAC-E-Filter Spectrometer	30
2.5	Beta spectrum fit from the Troitsk experiment	32
2.6	Beta spectrum fit from the Mainz experiment	33
2.7	KATRIN experimental overview	36
2.8	Simulation results for KATRIN	37
2.9	Feynman diagram of neutrinoless double beta decay	40
2.10	Double β decay energy spectrum	42
2.11	Effect of neutrino mass on CMB	47
3.1	Atomic coilgun slowing results for metastable neon	52
3.2	Conceptual illustration of the atomic coilgun	53
3.3	Atomic coilgun schematic	54
3.4	Conceptual illustration of single photon cooling	58
3.5	Illustration of single photon cooling of hydrogen	61
4.1	Beta energy spectrum	65

4.2	Kurie plot	66
4.3	Experimental setup of detectors for proposed m_ν experiment .	69
4.4	BURLE's 2-micron pore MCP	74
4.5	Simulation results of MCP hit pattern	75
4.6	Simulated velocity of ^3He ion	76
4.7	Simulated TOF of ^3He ion to MCP	77
4.8	Error introduced by MCP background hits	79
4.9	Effect of detector resolutions on m_ν fit errors	81
4.10	Diagram of hemispherical analyzer	83
4.11	m_ν^2 vs. the β -ion opening angle	90
4.12	m_ν^2 vs. initial tritium momentum	91
4.13	2D probability distribution function	93
4.14	Delaunay triangulation	95
4.15	Voronoi diagram	96
4.16	$m\nu^2$ peak broadenings caused by detector resolutions	99
4.17	Negative log-likelihood space for $m_\nu=0.4$ eV case	103
4.18	Negative log-likelihood space for $m_\nu=5.0$ eV case	104
4.19	Pull distribution of fit results	107
4.20	m_ν fit results for simulated data runs with different statistics .	108
4.21	PDF fit to simulated $m_\nu=0.2$ eV data projected in m_ν^2	109
4.22	PDF fit to simulated $m_\nu=0.2$ eV data projected in β energy .	110
5.1	Predicted solar neutrino flux vs. energy	121
5.2	SNO+ simulation of one year of data taking	123
5.3	SNO+ simulation of light output as a function of Nd-loading .	125
5.4	Periodic table showing isotope separation methods	128

5.5	Three level atom illustrating single photon atomic sorting . . .	131
5.6	Schematic of single photon atomic sorting (constant gradients)	132
5.7	Simulation results for ^{44}Ca using a constant gradient	136
5.8	Simulation results for ^{137}Ba using a constant gradient	137
5.9	Simulation results for ^{71}Ga using a constant gradient	138
5.10	Simulation results for ^{50}Ti using a constant gradient	140
5.11	Schematic for isotope separation using two constant gradients	141
5.12	Simulation results for ^{50}Ti using two constant gradients	143
5.13	Simulation results for ^{150}Nd using two constant gradients . . .	145
5.14	Schematic for isotope separation using magnetic guiding . . .	148
5.15	COMSOL simulation of magnetic hexapole	150
5.16	COMSOL simulation of magnetic quadrupole	151
5.17	Simulation results of where ^6Li hits the wall of the tube	153
5.18	Simulation results of where ^7Li hits the wall of the tube	154
5.19	Simulation results of ^6Li enrichment using magnetic guiding .	156
5.20	Simulation results of where ^7Li hits the tube wall	158
5.21	Probability of ^6Li traversing the tube vs. initial position . . .	159
5.22	Probability of ^7Li traversing the tube vs. initial position . . .	160
5.23	Schematic of isotope separation using a bent tube	164
5.24	Simulation results of ^{44}Ca enrichment using magnetic guiding	166
5.25	Unwanted Ca isotopes hitting the tube wall	167
5.26	Unwanted Nd isotopes hitting the tube wall	169
5.27	Simulation results of ^{150}Nd enrichment with magnetic guiding	170
5.28	Probability of ^{150}Nd traversing the tube vs. initial position . .	171
5.29	Probability of $^{142-148}\text{Nd}$ traversing the tube vs. initial position	172
5.30	Simulation results of lithium entrainment	176

5.31	Simulation results of neon beam percentage in entrainment . . .	177
5.32	Mean free path of lithium during entrainment	178
5.33	Number density of atoms during entrainment	179
5.34	Simulation results of entrainment speed map	180
5.35	Simulation results of entrainment temperature map	181
5.36	Simulation results of entrainment pressure map	182
6.1	Diagram of the SNO detector	189
6.2	Muon flux for various underground laboratories	196
6.3	Expected distribution of energies for supernova neutrinos . . .	207
6.4	Neutrino luminosity vs. time relative to core collapse	208
6.5	Neutrino energy and luminosity vs time on a log scale	209
6.6	Illustration of the burst search windows	217
6.7	Phase I accidental background for various energy thresholds .	219
6.8	Phase II accidental background for various energy thresholds .	220
6.9	Background burst multiplicity expected from ^{238}U fission . . .	223
6.10	Number of PMTs hit vs. energy for Phase I	229
6.11	Number of PMTs hit vs. energy for Phase II	230
6.12	Sample events tagged by the High NHIT cut	231
6.13	Burst eliminated by the High NHIT cut's 200 ms dead window	232
6.14	Unusual event eliminated by NEF cut	234
6.15	Δr cut	236
6.16	Δr cut in log scale	237
6.17	Phase I atm. simulation compared to Cf calibration source . .	238
6.18	Phase I atm. simulation compared to Cf calibration source . .	239
6.19	Phase II atm. simulation compared to Cf calibration source .	240

6.20	Phase II atm. simulation compared to Cf calibration source	241
6.21	$\Delta r \Delta t$ cut for Phase II 1 s window	243
6.22	$\Delta r \Delta t$ cut for Phase II 50 ms window	244
6.23	$\Delta r \Delta t$ cut for Phase II 10 s window	245
6.24	$\Delta r \Delta t$ cut for Phase I 200 ms window	246
6.25	$\Delta r \Delta t$ cut for Phase I 50 ms window	247
6.26	$\Delta r \Delta t$ cut for Phase I 10 s window	248
6.27	Comparison of antibox and atm. bursts Δr distributions	253
6.28	Δr for bursts failing the Muon Follower Short cut	254
6.29	Comparison of Δr distributions	257
6.30	Comparison of Δt distributions	258
6.31	Probability of detecting a standard supernova for Phase I	263
6.32	Probability of detecting a standard supernova for Phase II	264
A.1	Beta energy spectrum	269
A.2	Feynman diagram for beta decay of the neutron	270
A.3	Effect of final state corrections on Kurie plot	279
B.1	Grotrian diagram for ${}^3\text{He}$	282
B.2	Experimental setup for tritium boundstate β decay	283
B.3	Simulated data assuming a 20 eV neutrino mass	284
B.4	m_ν limits vs. statistics	285
C.1	Illustration of ordinary resonance fluorescence	289
C.2	Illustration of the Mössbauer effect for neutrinos	294
C.3	Proposed experimental setup	304
C.4	Debye temperature vs. pressure for solid ${}^3\text{He}$	305

C.5 Simulation results of event rate	307
--	-----

Chapter 1

Introduction

Neutrinos play a key role in several fields of physics including elementary particle physics, unified field theories, cosmology, and astrophysics. They are excellent probes of environments that are concealed from other observational methods, but the difficulty in detecting them has left many important questions surrounding them unanswered. For the past few years I have focused on utilizing recent advances in atomic physics to investigate neutrinos, as well as on combining methods from particle physics to examine neutrino questions in cosmology and astrophysics. By working in a cross-discipline environment, I have been able to explore neutrino physics from a unique perspective that incorporates tools ranging from atoms to astronomy.

Chapter 2 begins with a brief history of neutrino physics. I discuss some of the potential applications of neutrinos and highlight a few of the most important outstanding questions in neutrino physics. One of those open questions is the absolute mass scale of the neutrino, and the chapter concludes by summarizing the current approaches to measuring the neutrino mass.

Although atomic physics is traditionally disconnected from elementary

particle research, recent advances in slowing and cooling of atoms may have important applications in neutrino studies. Chapter 3 summarizes the general methods of slowing and cooling that have been developed in the past few years. These methods make possible the creation of the first atomic tritium source ever utilized in a tritium beta decay study of the neutrino.

Chapter 4 discusses the details of a proposed experiment to measure the neutrino mass using an atomic tritium source. This source would allow not only the β but also the helium ion to escape without scattering. I discuss the detectors that would be necessary to measure the kinematic properties of the ion and the β , particularly a new detection technique utilizing the properties of Rydberg atoms. This new technique offers a novel way of measuring multiple components of the β 's momentum without significantly disturbing its energy. I discuss the details of the simulation of this proposed experiment, and I explore its sensitivity to the neutrino mass. While traditional tritium β decay experiments have attempted to measure the neutrino mass using only the energy spectrum of the β , this experiment measures both the β energy spectrum and the kinematically reconstructed neutrino mass squared peak. In order to utilize all of the available information in fitting for the neutrino mass, I create two-dimensional probability density functions that I use in fitting for the neutrino mass. I conclude this chapter by presenting the simulation fit results and discussing the prospects for scalability to obtain competitive sensitivity to the mass of the neutrino.

While the experiment discussed in Chapter 4 would be able to measure the neutrino mass whether the neutrino is a Dirac or Majorana particle, a large number of collaborations are currently investigating the neutrino mass through neutrinoless double β decay, a process which can only occur if neutrinos are

Majorana. The potential sensitivity of these methods is very promising, however, and Chapter 5 begins with a discussion of neutrinoless double β decay before proceeding to highlight one proposed double β decay experiment called SNO+. I describe the SNO+ detector, which the collaboration intends to fill with tens of kilograms of ^{150}Nd , a double β emitting isotope. SNO+ is currently exploring a variety of options for isotope enrichment to obtain the ^{150}Nd that they require, and the bulk of Chapter 5 introduces a new technique for isotope separation called single-photon atomic sorting. I compare this method with other techniques for isotope separation, and I discuss the potential application of this technique to ^{150}Nd . I outline three different experimental implementations of the single-photon atomic sorting technique, and I describe simulation results for these various schemes. I conclude by discussing ongoing efforts to build an experiment demonstrating this technique for ^6Li .

In addition to aiding SNO+ by attempting to separate ^{150}Nd , I also joined the Sudbury Neutrino Observatory (SNO) collaboration to perform a low-multiplicity burst search of their data. SNO was an underground observatory that detected neutrino interactions with a large tank of heavy water. Chapter 6 introduces the SNO detector and describes how neutrinos were detected. I discuss two phases of the SNO experiment, one in which only heavy water was used, and one in which salt was added to increase the neutron capture efficiency. The primary physics motivation for searching for low-multiplicity bursts is supernovae since stars emit large numbers of neutrinos as they undergo core collapse. I give an overview of the physics of supernovae before discussing the parameters of the low-multiplicity burst search. I performed a triggerless burst search, meaning that I estimated all of the potential coincidence backgrounds, designed cuts to eliminate those backgrounds with

90% confidence, and then performed the search. I outline all of the sources of background that I considered and explain the analysis cuts that were necessary to account for those backgrounds. Some parameters like the search window length and energy threshold had to be optimized for maximum potential supernova detection, and I describe the simulations used to model a standard supernova explosion. When I performed the low-multiplicity burst search, no candidate supernova bursts were observed. I conclude by discussing the results of the search and presenting a sensitivity study showing the supernova detection probabilities at various distances for this low-multiplicity burst search.

Chapter 7 gives an overview of these attempts to investigate neutrinos using the non-traditional techniques detailed earlier. I summarize the physics implications for neutrino studies and speculate on the next steps in these efforts.

In Appendix A I derive the equation for the tritium β spectrum, emphasizing its dependence on the neutrino mass. I also discuss some of the final state effects that distort the spectrum.

Appendices B and C are related to boundstate beta decay, which occurs a remarkable 0.7% of the time for tritium. Appendix B outlines how one could use boundstate decays to measure the mass of the neutrino, although the final sensitivity is not competitive with other techniques. Appendix C explores whether boundstate beta decay could be utilized to observe the Mössbauer effect for neutrinos. Both appendices include discussions of the proposed experimental design and simulations of the expected results.

Chapter 2

Neutrino Physics Past and Present

Neutrino physics has a long and rich history spanning more than 80 years. This chapter begins with a brief overview of the discovery of neutrinos and their integration into the Standard Model of particle physics. I discuss their potential applications and highlight some of the most significant outstanding questions concerning them. One of those unresolved questions is the absolute mass scale of the neutrino, and I conclude the chapter by discussing previous experiments and proposals for measuring the neutrino mass.

2.1 Background

2.1.1 Neutrino Discovery

Wolfgang Pauli first proposed the existence of the neutrino in 1930 in a desperate attempt to preserve such sacred principles as the conservation of en-

ergy, conservation of momentum, and conservation of angular momentum. Although the neutron had not yet been discovered, experiments observed that some atomic nuclei decayed into a proton and an electron, a process we now understand to be β decay of the neutron:

$$n \rightarrow p + e^{-} + \bar{\nu} \tag{2.1}$$

If this decay were a simple two-body decay, the electron ought to always emerge with the same energy, but experiments confirmed that the β energy spectrum was quite broad. Pauli hypothesized that an undetected particle was carrying away the observed difference between the initial and final state energies. Although he originally named this particle a neutron, that name ultimately fell to the much heavier neutral particle discovered by James Chadwick in 1932. Enrico Fermi, who later developed the theory of β decay more fully, named the new elusive particle a neutrino.

The process of β decay suggests the possibility of detecting neutrinos by observing β capture. In 1956 the Cowan-Reines experiment [1] detected neutrinos created in a nuclear reactor by observing the neutrons and positrons from inverse β decay, for which they received the 1995 Nobel Prize in physics. In 1962 Leon M. Lederman, Melvin Schwartz, and Jack Steinberger demonstrated that more than one neutrino flavor exists by detecting interactions of the muon neutrino [2], which earned them the 1988 Nobel Prize in physics. The first direct detection of tau neutrino interactions was seen by the DONUT collaboration at Fermilab in 2000 [3], making ν_{τ} the latest particle of the Standard Model to have been directly observed.

2.1.2 Neutrinos in the Standard Model

The Standard Model of particle physics is a theory of three of the four fundamental interactions (electromagnetic force, weak force, and strong force), as well as the elementary particles that take part in those interactions. One of the first major cornerstones of the Standard Model was the 1967 paper by Steven Weinberg and Abdus Salam, which incorporated the Higgs mechanism into electroweak theory and outlined the currently accepted incorporation of leptons into the Standard Model. Because no chirally right-handed neutrinos had been observed¹, the Standard Model developed with the assumption that only left-handed neutrinos exist in nature. Under this assumption the Dirac mass term in the Standard Model Lagrangian must be zero since the neutrino mass component of the general Lagrangian is of the form

$$\mathcal{L}_\nu = m(\overline{\psi}_R\psi_L + \overline{\psi}_L\psi_R) \tag{2.2}$$

where ψ_L and ψ_R are SU(2) doublets:

$$\psi_L = \begin{pmatrix} \nu_L \\ e_L \end{pmatrix} \quad \text{and} \quad \psi_R = \begin{pmatrix} \nu_R \\ e_R \end{pmatrix}$$

The Lagrangian term indicates that if neutrinos have mass, both right and left-handed neutrinos should exist. The right-handed neutrino has never been experimentally observed. The weak interaction, however, only couples to

¹Particles are considered to have left-handed helicity if the directions of spin and velocity are opposite, while particles with right-handed helicity have their spin and velocity vectors aligned. Chirality is defined more abstractly by whether a particle transforms in a right-handed or left-handed representation of the Poincaré group, and it can be thought of as being somewhat like “apparent helicity.”

chirally left-handed particles, which means that detecting right-handed neutrinos would be even more difficult than detecting left-handed ones. An interaction between a right-handed neutrino and the Higgs boson has been predicted but never observed. The Majorana picture of neutrinos differs in its treatment of ν_L and ν_R since it views them as two different versions of the same particle, but it still requires the existence of right-handed neutrinos if the neutrino mass is nonzero. The Standard Model, therefore, certainly did not predict that neutrinos had mass, but its original formulation did not exclude the possibility.

2.1.3 Neutrino Oscillations

The first experimental sign that the neutrino mass could be nonzero came from the sun. The Standard Solar Model (SSM) predicts that a significant number of electron neutrinos are produced in solar core reactions, while other neutrino flavors would not be expected. In 1968 Ray Davis began an experiment to measure the flux of electron neutrinos from the sun, and much to everyone's surprise, he found a large deficit of electron neutrinos compared to the SSM predictions [4]. Subsequent experiments such as SAGE [5, 6] and GALLEX [7, 8] confirmed Davis's result, and this discrepancy became known as the solar neutrino problem. Although many people believed that the SSM was incorrectly modeling the interior temperature or pressure of the sun, an alternative explanation was that neutrinos could be changing flavor as they traveled to terrestrial detectors, which would require neutrinos to be massive.

The physics community became more convinced of massive neutrinos after Super-Kamiokande released their 1998 results. Super-Kamiokande is a 50 kiloton water Cherenkov detector located under 2700 meter-water-equivalent

of rock in Kamioka, Japan. Over 11,000 photomultiplier tubes (PMTs) monitored the water and detected Cherenkov radiation from charged particles moving inside the detector. Their primary sensitivity was to elastic scattering reactions (i.e. $\nu + e^- \rightarrow \nu + e^-$), in which the ν_e flavor participates approximately six times more than the other flavors since it can scatter via the W or Z channel. The collaboration observed fewer muon neutrinos coming through the earth than coming directly above the detector, and their results were consistent with the hypothesis that muon neutrinos were oscillating as they traveled through the earth.

The first direct evidence of solar neutrino oscillations came in 2001 from the Sudbury Neutrino Observatory (SNO), which will be discussed more fully in Chapter 6. Unlike Super-Kamiokande, they could detect neutral current neutrino interactions, in which all neutrino flavors participate equally. The neutral current interactions yielded a measurement of the total solar neutrino flux, and the charged current neutrino interactions measured the fraction of that flux coming from ν_e . While the total number of solar neutrinos agreed quite well with the SSM, only about 35% of those neutrinos were electron-flavored, implying that neutrino flavor oscillations were occurring.

Neutrino oscillations occur because neutrinos are created in flavor eigenstates, but they propagate in the mass basis. A similar phenomenon had already been studied in the quark sector, where the eigenstates of the free particle Hamiltonian differ from the flavor eigenstates because the free particle Hamiltonian and the weak interaction Hamiltonian do not commute. The analogue to the CKM matrix for quarks is the unitary Pontecorvo-Maki-Nakagawa-

Sakata (PMNS) matrix:

$$\begin{pmatrix} \nu_e \\ \nu_\mu \\ \nu_\tau \end{pmatrix} = \begin{pmatrix} U_{e1} & U_{e2} & U_{e3} \\ U_{\mu1} & U_{\mu2} & U_{\mu3} \\ U_{\tau1} & U_{\tau2} & U_{\tau3} \end{pmatrix} \begin{pmatrix} \nu_1 \\ \nu_2 \\ \nu_3 \end{pmatrix}$$

If neutrino flavor conservation held, then this matrix would have to be diagonal. Neutrino oscillation data indicates, however, that non-zero off-diagonal elements exist for the PMNS matrix, and that matrix can be written in a more expanded form:

$$U = \begin{pmatrix} 1 & 0 & 0 \\ 0 & c_{23} & s_{23} \\ 0 & -s_{23} & c_{23} \end{pmatrix} \times \begin{pmatrix} c_{13} & 0 & s_{13}e^{i\delta} \\ 0 & 1 & 0 \\ -s_{13}e^{-i\delta} & 0 & c_{13} \end{pmatrix} \times \begin{pmatrix} c_{12} & s_{12} & 0 \\ -s_{12} & c_{12} & 0 \\ 0 & 0 & 1 \end{pmatrix}$$

where $c_{ij} = \cos\theta_{ij}$, $s_{ij} = \sin\theta_{ij}$, θ_{ij} is the mixing angle, and δ is the CP violating phase. Although there are three known lepton generations, neutrino mixing can be treated in a simpler way as mixing between two groups, either (ν_e, ν_μ) or (ν_μ, ν_τ) . This simplification is appropriate because θ_{13} is small and $\Delta m_{23}^2 \gg \Delta m_{12}^2$.

Exploring the two-neutrino mixing picture, the neutrino can be represented by two different flavors traveling at different speeds. These two propagating wave packets create an interference pattern with each other. We can write the flavor eigenstates in terms of the mass eigenstates:

$$\begin{pmatrix} \nu_e \\ \nu_\mu \end{pmatrix} = \begin{pmatrix} \cos\theta & -\sin\theta \\ \sin\theta & \cos\theta \end{pmatrix} \begin{pmatrix} \nu_1 \\ \nu_2 \end{pmatrix}$$

From the time-dependent Schrödinger equation, the time evolution of the mass states is:

$$\begin{pmatrix} \nu_1(\vec{x}, t) \\ \nu_2(\vec{x}, t) \end{pmatrix} = \begin{pmatrix} e^{iE_1 t} |\nu_1(0)\rangle \\ e^{iE_2 t} |\nu_2(0)\rangle \end{pmatrix}$$

which can be written in matrix form:

$$\begin{pmatrix} \nu_1(\vec{x}, t) \\ \nu_2(\vec{x}, t) \end{pmatrix} = \begin{pmatrix} e^{-iE_2 t} & 0 \\ 0 & e^{-iE_2 t} \end{pmatrix} \begin{pmatrix} \nu_1(0) \\ \nu_2(0) \end{pmatrix}$$

By combining the expressions for the flavor eigenstates as a function of mass and the mass eigenstates as function of time, one can determine the time-evolution of the flavor eigenstates, assuming that they are free-particles:

$$\begin{pmatrix} \nu_e(\vec{x}, t) \\ \nu_\mu(\vec{x}, t) \end{pmatrix} = \mathbf{U} \begin{pmatrix} e^{-iE_1 t} & 0 \\ 0 & e^{-iE_2 t} \end{pmatrix} \mathbf{U}^\dagger \begin{pmatrix} \nu_e(0) \\ \nu_\mu(0) \end{pmatrix}$$

If we take the mass of the neutrino m_1 to be much less than its momentum, we can expand E_1 :

$$E_1 = \sqrt{p^2 + m_1^2} \approx p + m_1^2/2p \approx p + m_1^2/2E \quad (2.3)$$

which implies that:

$$\begin{pmatrix} \nu_e(\vec{x}, t) \\ \nu_\mu(\vec{x}, t) \end{pmatrix} \approx e^{-ipt} \mathbf{U} \begin{pmatrix} e^{-im_1^2 t/2E} & 0 \\ 0 & e^{-im_2^2 t/2E} \end{pmatrix} \mathbf{U}^\dagger \begin{pmatrix} \nu_e(0) \\ \nu_\mu(0) \end{pmatrix}$$

By expanding the exponential one obtains:

$$\begin{pmatrix} \nu_e(\vec{x}, t) \\ \nu_\mu(\vec{x}, t) \end{pmatrix} \approx e^{-ipt} \mathbf{U} \begin{pmatrix} 1 - im_1^2 t/2E & 0 \\ 0 & 1 - im_2^2 t/2E \end{pmatrix} \mathbf{U}^\dagger \begin{pmatrix} \nu_e(0) \\ \nu_\mu(0) \end{pmatrix}$$

The unitarity of \mathbf{U} implies that:

$$|\nu_\alpha(\vec{x}, t)\rangle \approx e^{-ipt} \left(e_{\alpha\beta}^{-im^\dagger m t/2E} \right) |\nu_\beta\rangle \quad (2.4)$$

A solution to the Schrödinger equation is now

$$i \frac{d}{dt} |\nu_\alpha(\vec{x}, t)\rangle \approx (m^\dagger m/2E) |\nu_\alpha\rangle \quad (2.5)$$

where the phase factor e^{-ipt} has been omitted. In order to determine the survival propagation probabilities for any initial flavor state, one can write:

$$|\nu_\alpha(\vec{x}, t)\rangle = \begin{pmatrix} \cos(\frac{\Delta m^2}{4E})t - i\sin(\frac{\Delta m^2}{4E})t\cos 2\theta & -i\sin(\frac{\Delta m^2}{4E})t\sin 2\theta \\ -i\sin(\frac{\Delta m^2}{4E})t\sin 2\theta & \cos(\frac{\Delta m^2}{4E})t + i\sin(\frac{\Delta m^2}{4E})t\cos 2\theta \end{pmatrix} |\nu_\beta\rangle$$

If a neutrino traveling through vacuum is initially an electron neutrino, then at time $t = 0$, $|\nu_e(0)\rangle = (1, 0)^T$, and the transition rate is:

$$\langle \nu_e(x, t) | \nu_e \rangle = \cos(\Delta m^2/4E)t - i\sin(\Delta m^2/4E)t\cos 2\theta \quad (2.6)$$

The probability for the ν_e to be measured in the same flavor eigenstate after a time t has passed is:

$$P_{\nu_e \rightarrow \nu_e} = |\langle \nu_e(x, t) | \nu_e(x, 0) \rangle|^2 = 1 - \sin^2 2\theta \sin^2(\Delta m^2/4E)t \quad (2.7)$$

This equation helpfully describes neutrino oscillations in terms of a mixing angle, θ , which indicates the degree to which mixing occurs between different flavors. Since neutrinos propagate very near the speed of light, t is on the order of L , the distance between the source of the neutrinos and the detector, indicating that the probability of transition depends upon $\sin^2(\Delta m^2/4E)L$. That dependence highlights the importance of the distance between a neutrino source and a detector for neutrino oscillation experiments.

2.1.4 MSW Effect

When neutrinos are traveling through matter instead of through vacuum, Equation 2.7 that describes the survival probability must be modified. This matter effect is named the MSW effect after the three men who developed the theory describing it, Mikheev, Smirnov, and Wolfenstein. At solar neutrino energies the muon and tau neutrinos are limited to only neutral current interactions in matter, while electron neutrinos can also undergo charged current interactions. The electrons in matter enhance the oscillation probability of electron neutrinos due to the fact that they can interact via the exchange of both W and Z bosons. The possibility of undergoing a charged current interaction for the ν_e adds an effective potential $V_{eff} = \sqrt{2}G_F N_e$, where G_F is the Fermi constant and N_e is the electron number density. The Hamiltonian can then be written:

$$H = \Delta m^2/4E \begin{pmatrix} -\cos 2\theta + V_{eff} & \sin 2\theta \\ \sin 2\theta & \cos 2\theta \end{pmatrix} \quad (2.8)$$

This Hamiltonian must be re-diagonalized to find the propagating states.

For the simple case in which the matter density is uniform, the survival probability is similar in form to Equation 2.7, except that the vacuum mixing angle term $\sin^2 2\theta$ must be replaced by $\sin^2 2\theta_m$ [9]:

$$\sin^2 2\theta_m = \frac{\sin^2 2\theta}{(\omega - \cos 2\theta)^2 + \sin^2 2\theta} \quad (2.9)$$

where ω is given by

$$\omega = -\frac{\sqrt{2}G_F N_e E_\nu}{\Delta m^2} \quad (2.10)$$

The MSW resonance occurs at a critical electron density:

$$N_e = \frac{1}{2\sqrt{2}G_F} \frac{\Delta m^2}{E} \cos 2\theta \quad (2.11)$$

With a large mixing angle the MSW effect predicts a transition from the matter-dominated regime (Equation 2.9) to the vacuum-dominated regime (Equation 2.7) as a function of neutrino energy [10]. In the matter-dominated regime the survival probability is:

$$P_{\nu_e \rightarrow \nu_e} = \sin^2 \theta_{12} \quad (2.12)$$

which does not depend on the neutrino's energy. In the vacuum-dominated regime neutrinos produced in the sun are all at different phases in their oscillation when they reach earth, and the survival probability can be written as the average of Equation 2.7:

$$P_{\nu_e \rightarrow \nu_e} = 1 - \frac{1}{2} \sin^2 2\theta_{12} \quad (2.13)$$

which is also independent of the neutrino energy. In between these two limits

the survival probability does depend on energy.

Figure 2.1 illustrates three various density regions in which solar neutrinos can begin in the sun (so the initial state is a ν_e). The flavor conversion depends on how far from the resonance layer (in the density scale) the neutrino is produced, and in the figure the resonance is marked by a yellow line. In the first case, the production is far above the resonance; the initial mixing is strongly suppressed, and the flavor transformations follow the matter-dominated probability of $\sin^2\theta$. In the second case, the production is above the resonance, but the initial mixing is not suppressed, and the survival probability is a more complicated expression. In the third case, the production is below resonance, and the MSW effect gives only small corrections to the vacuum oscillation survival probability. The resonance density is inversely proportional to the neutrino energy, so for the same density profile the first case is realized for high energies, the second case for intermediate energies, and the third case for low energies.

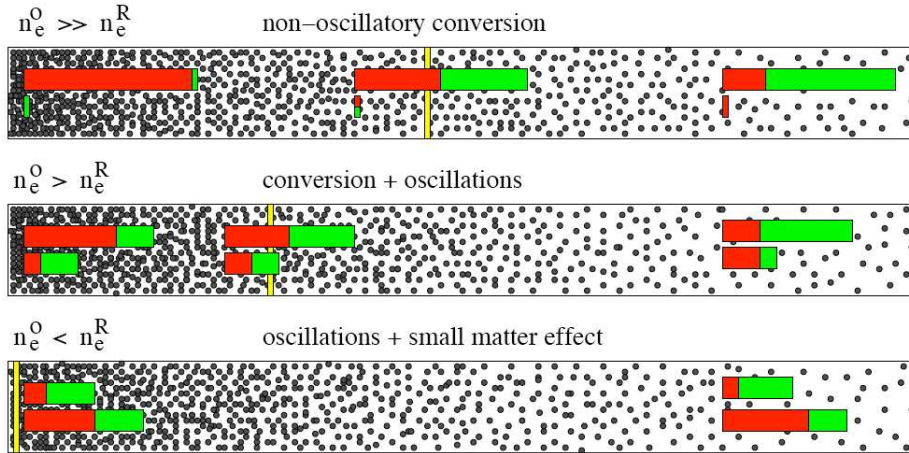


Figure 2.1: Evolution of ν_e state for three different initial conditions as the propagation medium decreases in density. The yellow vertical line indicates the position of resonance. The colors represent the flavors, which follow the density change. Figure taken from [11].

2.2 Neutrino Applications

As we learn more about neutrinos and how to detect them, new ideas continue to emerge for how to utilize these elusive particles. While they began as the objects under investigation for their own sake, they are becoming the tools through which we can explore other processes and phenomena. The following section highlights just a few of the developing ideas that utilize neutrinos as investigative aids.

2.2.1 Supernova Detection and the DSNB

SN 1987A was a supernova in the Large Magellanic Cloud, approximately 51.4 kiloparsecs (kpc) from earth. It was so close that it could actually be seen with the naked eye, and it was the closest observed supernova since 1604, when a star went supernova within the Milky Way itself. Approximately three hours before the visible light reached earth on February 23, 1987, three separate neutrino observatories detected a burst of neutrinos. Kamiokande-II detected 11 antineutrinos [12], IMB detected 8 [13], and Baksan detected 5 [14]. These 24 events marked the first time supernova neutrinos had been detected, and even though the statistics were not high, the observations were consistent with theoretical supernova models in which 99% of the energy of the collapse is radiated in neutrinos.

Another nearby core collapse supernova during the runtime of an underground water Cherenkov experiment could provide a wealth of information to both neutrino physics and astrophysics. A high statistics observation would reveal details about the core collapse process, possibly allowing various supernova models to be distinguished. Additionally, the matter-enhanced oscillations in a core-collapse supernova are sensitive to small variations in the mixing angle θ_{13} as discussed in Section 2.3.4, and the neutrino spectra might reveal information about that angle. Supernova neutrinos may also contain information about the neutrino mass hierarchy. Although some difficulties could arise in separating questions concerning supernova models from questions concerning neutrino properties, no one doubts that a statistically significant supernova neutrino detection would contain a wealth of information.

Future underground neutrino experiments also have the potential to de-

tect the Diffuse Supernova Neutrino Background (DSNB), which is the weak glow of MeV neutrinos from distant core-collapse supernovae. The DSNB is made up of all the past supernovae in the universe. The current upper limit on the $\bar{\nu}_e$ flux from Super-Kamiokande is close to theoretical predictions for the DSNB. If Super-Kamiokande were modified with dissolved gadolinium to reduce detector backgrounds and increase the analysis energy range, then theorists predict it could detect the DSNB at a rate of a few events per year [15]. This rate could establish a new probe of supernova neutrino emission and the cosmic core-collapse rate.

2.2.2 Astrophysics and the Relic Neutrino Background

The cosmic neutrino background is analogous to the cosmic microwave background (CMB), but while photons decoupled from matter when the universe was $\sim 380,000$ years old, neutrinos decoupled when the universe was less than 1 s old. The relic neutrino background is estimated to have a temperature of approximately 1.95 K, which is actually colder than the CMB temperature of 2.725 K. Neutrinos and photons were certainly in thermal equilibrium when the neutrinos decoupled at around 2×10^{10} K, but until the universe cooled to 1.2×10^{10} K photons were still being created through $e^+ + e^- \rightarrow \gamma + \gamma$, which explains the CMB's slightly higher temperature today. Although these low energy relic neutrinos would be extremely difficult to detect, they contain potentially enormous amounts of information about the formation of the universe from its earliest moments. Although many people have discussed using nuclei that could undergo neutrino capture to detect the cosmic neutrino background, no experimentally viable approach has yet been found.

2.2.3 Geoneutrinos

Geoneutrinos are electron antineutrinos produced by natural radioactivity in the earth, such as β decays of the nuclei in the decay chains of ^{238}U and ^{232}Th . KamLAND detected the first geoneutrinos in 2005 and published an upper limit on the radiogenic power of U and Th in the earth based on geoneutrino detection [16]. Geoneutrino detection offers a new avenue through which to explore the inner workings of the earth and to distinguish between geophysical models.

2.2.4 Quantum Gravity Investigations

Quantum gravity investigations are limited by the inability to probe Planck-scale energies. Many quantum gravity theories suggest that Lorentz invariance may be violated or spontaneously broken. For example, if neutrinos have a limiting velocity other than the speed of light, VLI-induced neutrino oscillations could occur, producing experimental signatures in high energy atmospheric neutrino searches. Theorists predict that violation of Lorentz invariance, the equivalence principle, or the superposition principle would leave distinctive energy-dependent signatures on the transition probability of neutrino flavor oscillations. Some signatures of violations may be suppressed by many orders of Planck energy, but even those might be observable for ultra-high energy neutrinos that have originated from cosmological distances. As experiments like Amanda and IceCube attempt to detect these high energy atmospheric neutrinos, any deviations from the expected flavor ratios could point to physics beyond the Standard Model.

2.3 Open Questions

Neutrinos are the least understood particles in the Standard Model, even though they are the second most abundant in the universe. Our universe contains approximately three million neutrinos per cubic meter, but because they are difficult to detect, many fundamental questions about their nature remain unanswered. The following section highlights a few of the most significant open questions in neutrino physics.

2.3.1 Absolute Mass Scale and Hierarchy

The discovery that neutrinos have mass was the first hint of new physics beyond the Standard Model. While neutrino mass was not terribly difficult to include in the Standard Model, it was unexpected. The neutrino mass is now known to be at least 100,000 times lighter than the electron mass, which means that probing the neutrino mass is probing a new mass regime, in which new physics may become evident.

As accurate as neutrino oscillation experiments have become, they cannot convey any information about the absolute mass scale. If the neutrino masses are degenerate, then the absolute mass scale is large compared to the mass splittings, which may put it within the reach of several experiments currently under development. If the neutrino masses are hierarchical, then the neutrino mass splittings are large compared to the absolute mass scale. Theories, such as various seesaw models, try to explain the smallness of the neutrino mass relative to the much larger charged fermions. Precise determination of the absolute mass scale of the neutrino may allow one to distinguish between these various models. The best current experimental measurements of the

neutrino mass splittings are [17]:

$$\left| \Delta m_{32}^2 \right| = (2.43 \pm 0.13) \times 10^{-3} \text{eV}^2 \quad (2.14)$$

$$\Delta m_{21}^2 = (7.59 \pm 0.20) \times 10^{-5} \text{eV}^2 \quad (2.15)$$

These measurements provide a lower limit on the sum of the neutrino masses of 0.056 eV.

Neutrino mass also features prominently in cosmology. In the early universe neutrinos acted as hot dark matter, which disrupted structure formation. Although neutrinos have been ruled out as the dominant source of dark matter, their masses still need to be included in cosmological data fits, as discussed in more detail in Section 2.4.5.

In addition to the absolute mass scale, the sign of Δm_{32} is unknown, meaning that the neutrino masses could be ordered two different ways. Both hierarchies are shown in Figure 2.2, and future experiments hope to distinguish which ordering is correct.

2.3.2 Majorana or Dirac

One of the most important outstanding questions in neutrino physics is whether neutrinos are Majorana (meaning that they are their own antiparticles) or Dirac particles. If neutrinos were massless and traveled at the speed of light, then the difference between the two types of particles would not be an experimental question because a Lorentz transformation to a faster moving frame would not be possible. If neutrinos are Majorana, then the differences we observe between neutrinos and antineutrinos are actually due to the two dif-

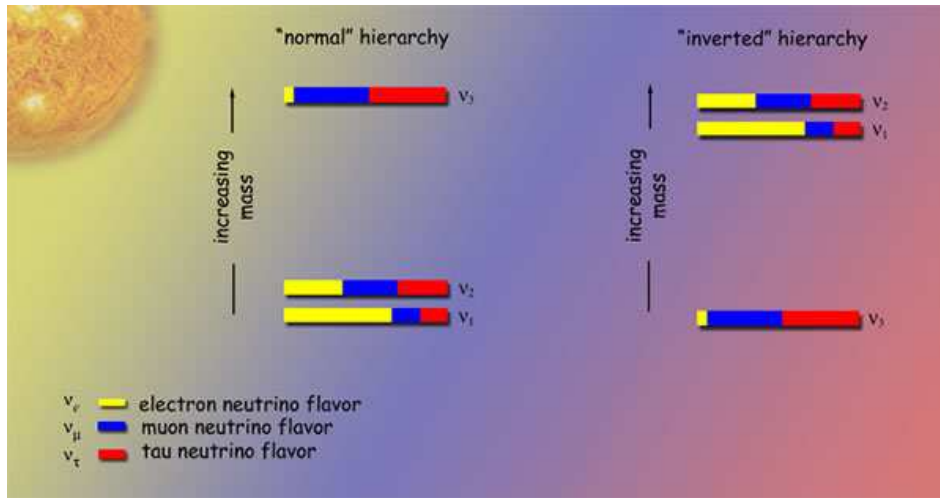


Figure 2.2: The neutrino mass hierarchy could be normal or inverted, and the absolute scale of the neutrino mass could lead to degenerate or hierarchical neutrino masses. Figure taken from the Lawrence-Berkeley National Laboratory.

ferent helicity states of a single particle. Direct observations of the Dirac or Majorana nature of neutrinos are difficult because the effects are suppressed by the small neutrino mass, but some processes, such as neutrinoless double β decay, may allow for an experimental determination of the question.

Majorana neutrinos carry no conserved quantum number that could distinguish particles from antiparticles, where Dirac neutrinos maintain conservation of lepton number. Majorana neutrinos lead to a violation of lepton number conservation, which could open the door for an explanation of the puzzling matter/antimatter asymmetry that had to exist shortly after the Big Bang in order to produce the current observable universe. Since the current Standard Model does not require lepton number conservation, many theorists favor the idea that neutrinos are Majorana. Majorana neutrinos also allow

for a natural explanation of the smallness of neutrino masses through a see-saw mechanism in which the right handed partners of neutrinos are extremely massive. The theoretical attractiveness of Majorana neutrinos is, however, currently without experimental confirmation; neutrinos have often proven surprising in the past, and no experiment has yet detected a conclusive Majorana neutrino signature.

2.3.3 Electromagnetic Moments

If neutrinos are Majorana particles, they cannot contain any internal electromagnetic structure; their electromagnetic moments must be zero, or they would lead to reversals under CP conjugation that would distinguish neutrinos from antineutrinos. If neutrinos are Dirac, however, they could possess nonzero electromagnetic moments.

2.3.4 θ_{13}

The neutrino mixing angle θ_{13} is one of the most important unknown parameters of the Standard Model. This angle is the key parameter regulating three-neutrino oscillations, and it regulates at first order the ability of oscillation experiments to measure the sign of Δm_{23}^2 and δ_{CP} . By combining data from SNO and KamLAND, one can set the experimental limit $\sin^2\theta_{13} < 0.057$ C.L. = 95% [18].

Supernova neutrinos are sensitive to extremely small values of θ_{13} and could possibly determine the neutrino mass hierarchy at θ_{13} as low as 10^{-10} [19] by studying MSW resonances inside the star. Supernova neutrinos must pass through two resonance layers, the H-resonance layer at $\rho_H \sim 10^3$ g/cc and

the L-resonance layer at $\rho_L \sim 10$ g/cc. The dynamics of conversions is determined by an adiabaticity parameter γ , which depends on the mixing angle and the mass-squared difference between the involved flavors: θ_{13} and Δm_{13}^2 at H-resonance, and θ_{12} and Δm_{12}^2 at L-resonance. When $\gamma \gg 1$ the resonance is called adiabatic, and the fluxes of the two involved mass eigenstates are completely exchanged. When $\gamma \ll 1$ the resonance is nonadiabatic, and the conversion does not occur. The H-resonance also carries information about the mass hierarchy since it will appear in the neutrino channel for a normal hierarchy and the antineutrino channel for an inverted hierarchy. Other distinctive signals particular to certain mixing and hierarchy schemes could be seen through earth matter effects if a signal were observed by two detectors, only one of which is shadowed by the earth. If the ν_e signal from a supernova neutronization burst were observed to be suppressed, that would indicate a normal mass hierarchy and a value of $\theta_{13} > 10^{-3}$ [19]. Various shock wave effects that results in sharp changes in the characteristics of the observed spectra for a short time while the shock wave is passing the H-resonance may also convey information about neutrino properties. If a nearby supernova were to occur while a neutrino detector were operating, allowing high statistics measurements of neutrino spectra, significant questions like the value of θ_{13} and the neutrino mass hierarchy could be resolved.

2.3.5 Role in Astrophysics and Cosmology

Many open questions in astrophysics and cosmology are being explored through neutrinos. For example, ultra high energy (UHE) cosmic rays can have energies up to and even exceeding 10^{20} eV, and as they interact with the CMB,

they produce UHE neutrinos. UHE neutrinos could also come from other interesting phenomena like the decay of exotic massive particles or the warped space near black holes. Detection of these UHE neutrinos could yield important information about the underlying physics behind their astrophysical sources.

In addition to supernovae, which I have already mentioned, other high energy astrophysical objects include active galactic nuclei (AGN), gamma-ray bursts (GRB), and black holes. Neutrinos, unlike cosmic rays, point back at their source of origin, and they carry information about some of the most dense and energetic regions of high energy sources. Astrophysicists hope to utilize neutrinos coming from these types of objects as probes of energy and gravitational regimes far exceeding anything we could hope to produce in a terrestrial laboratory.

Big bang nucleosynthesis (BBN) is the cosmological theory of the origin of the light element isotopes such as D, ^3He , ^4He , and ^7Li . The number of light neutrinos, N_ν , would directly influence the ratio of neutrons to protons, which in turn affects the ^4He abundance. Through measurements of ^4He , therefore, astrophysics can set limits on N_ν ; actually the BBN bound is not solely restricted to neutrinos but applies to any relativistic particle species present at the time of BBN, which implies that $N_\nu > 3$ could point to a new particle species.

The CMB also conveys interesting information regarding neutrinos. Changing N_ν changes the expansion rate of the universe, which leads to a change in the sound horizon and damping length of the photon-baryon fluid, ultimately resulting in a shift in the position of the peaks and troughs in the anisotropy spectrum, as well as some amplitude changes. Additionally in the

presence of radiation the gravitational potential changes with time, and the photons traversing these potential wells pick up a net red-shift or blue-shift which enhances the amplitude of the anisotropy spectrum. (These effects are similar to those caused by neutrino mass, which are discussed further in Section 2.4.5, though the changes from m_ν are not degenerate with those caused by N_ν [20].)

2.4 Measuring Neutrino Mass

The unknown absolute mass scale of the neutrino can be investigated through multiple means. This section describes several of the previous and on-going experiments that attempted to measure the neutrino mass. Against this backdrop, I will later propose a new idea for measuring the neutrino mass in Chapter 4.

2.4.1 Previous Beta Decay Experiments

Tritium β decay offers a unique opportunity to probe the absolute mass scale of the neutrino. By studying the highest region of the β energy spectrum, one hopes to detect small distortions due to the energy required to create a massive neutrino. The shape of the β spectrum with nonzero neutrino mass is:

$$\frac{dN}{dE} = C \times F(Z, E) p E (E_o - E) [(E_o - E)^2 - m_\nu^2]^{\frac{1}{2}} \Theta(E_o - E - m_\nu) \quad (2.16)$$

where E is the electron energy, p is the electron momentum, E_o is the total decay energy (18.6 keV for tritium), $F(Z, E)$ is the Fermi function, $\Theta(E_o -$

$E - m_\nu$) ensures energy conservation, and C is a constant. In Appendix A I discuss this equation in greater detail, but its relevance to the neutrino mass is clear. The effect of nonzero neutrino mass emerges as a cut-off of the spectrum at $E_o - E = m_\nu^2 c^4$. To observe this cut-off would be a clear signature of this effect, but the paucity of statistics in the significant region of the β spectrum makes detection of an obvious signature unlikely. For example, only 2×10^{-13} of all tritium decays produce β energies in the last 1 eV of the spectrum, and that fraction only gets worse for other β decaying atoms with higher endpoint energies. Typical experimental energy resolutions exceed the absolute mass scale of the neutrino, and background events also contribute to washing out the measured result. To extract the neutrino mass from an experimental measurement of the β spectrum, therefore, requires doing a fit of the spectrum with several free parameters, one of which is m_ν^2 . Generally, any factor causing an additional concave bend of the experimental spectrum produces a more negative value of m_ν^2 , and any additional convex bend results in a more positive value of m_ν^2 .

For more than 50 years physicists have been searching for a nonzero neutrino mass signal in tritium beta decay. In 1980, the ITEP group from Moscow reported observing a neutrino mass effect corresponding to a rest mass of $30 \text{ eV}/c^2$ [21]. This result stimulated a large number of experimental proposals to check the claim, and after several years, experimental groups from Zurich [22], Tokyo University [23], Los Alamos [24], and Livermor [25] produced results refuting the ITEP claim. These experiments also highlighted many difficulties in extracting m_ν^2 from the tritium β spectrum. For example, all four of those experiments obtained an obviously nonphysical negative fit value of m_ν^2 .

Two collaborations in the early 1990s, the Troitsk group at the Institute for Nuclear Research and the Mainz group at the Institute for Physics, independently developed a new spectrometer technology that significantly advanced the study of tritium β decay. These spectrometers, known as MAC-E-Filters (Magnetic Adiabatic Collimation combined with an Electrostatic Filter), combine the attractive features of high luminosity, low backgrounds, and high energy resolution. Figure 2.4 illustrates the main principle of the MAC-E-Filter. Two superconducting solenoids produce a magnetic guiding field. The electrons, which start from the tritium source in the left solenoid, are guided magnetically on a cyclotron motion around the magnetic field lines into the spectrometer, thus allowing for an extremely large solid angle acceptance. On their way into the center of the spectrometer, the magnetic field drops by many orders of magnitude; therefore, the magnetic gradient force transforms most of the cyclotron energy E_{\perp} into longitudinal motion. This process is illustrated in Figure 2.4 by the momentum vector shown below the schematic. Due to the slowly varying magnetic field, the momentum transforms adiabatically, keeping the magnetic moment μ approximately constant. The practical result of this transformation is that the electrons, which are isotropically emitted at the source, are transformed into a broad beam flying almost parallel to the magnetic field lines. This parallel beam of electrons encounters an electrostatic potential formed by a system of cylindrical electrodes. All electrons with enough energy to pass the electrostatic barrier are reaccelerated and collimated onto a detector, and the other electrons are reflected by the barrier. The spectrometer, therefore, acts primarily as an integrating high-energy pass filter. Figure 2.3 shows how dramatically the MAC-E-Filter technology improved the size of the error bars on the neutrino mass compared to previous

tritium β decay experiments.

ITEP	m_ν
T_2 in complex molecule magn. spectrometer (Tret'yakov)	17-40 eV
Los Alamos	
gaseous T_2 - source magn. spectrometer (Tret'yakov)	< 9.3 eV
Tokio	
T - source magn. spectrometer (Tret'yakov)	< 13.1 eV
Livermore	
gaseous T_2 - source magn. spectrometer (Tret'yakov)	< 7.0 eV
Zürich	
T_2 - source impl. on carrier magn. spectrometer (Tret'yakov)	< 11.7 eV
Troitsk (1994-today)	
gaseous T_2 - source electrostat. spectrometer	< 2.5 eV
Mainz (1994-today)	
frozen T_2 - source electrostat. spectrometer	< 2.2 eV

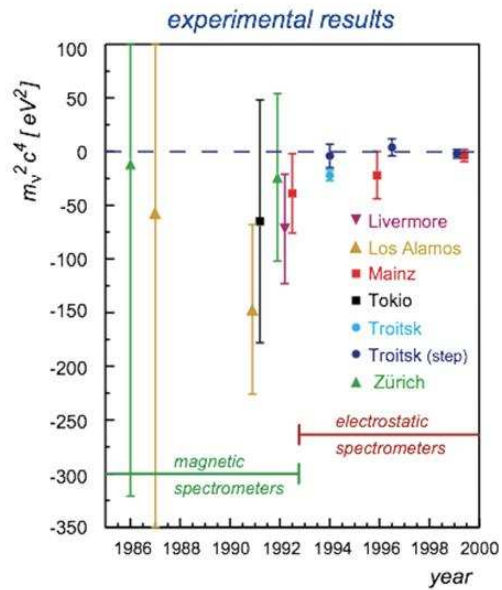


Figure 2.3: History of neutrino mass measurements performed using tritium β decay. Figure from the KATRIN Collaboration.

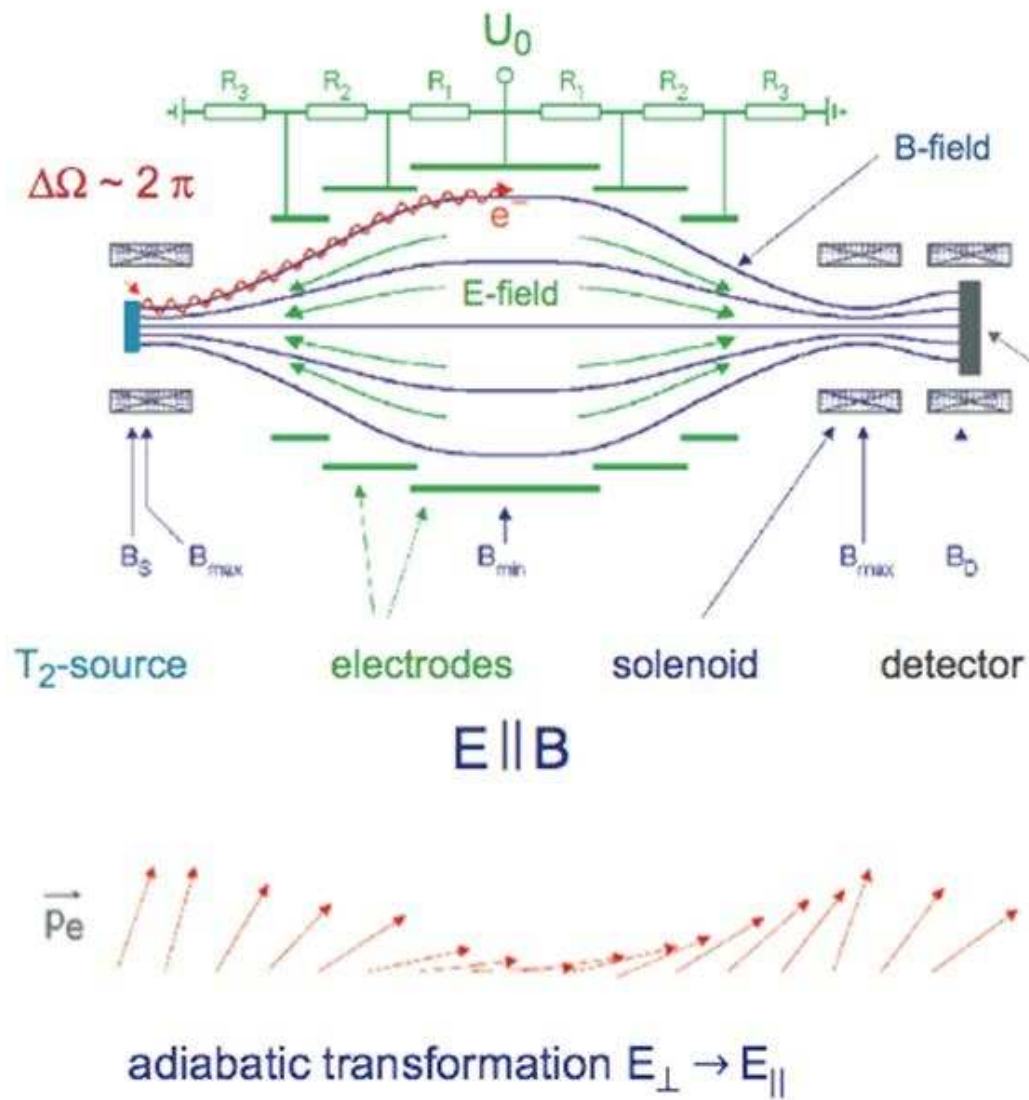


Figure 2.4: Summary of the MAC-E-Filter, utilized by Mainz, Troitsk, and KATRIN. The electrons are guided by the field lines until their momentum vectors are perpendicular to an electrostatic barrier, meaning the spectrometer operates much like an integrating high-pass filter. Figure from the KATRIN Collaboration.

The major difference between the Mainz and Troitsk experiments was their tritium source. The Troitsk experiment used a windowless gaseous tritium source (WGTS), which is based on the adiabatic transport of electrons in a strong magnetic field and circulation of tritium gas at low pressure by means of a differential pumping system. While this technology was first developed by the Los Alamos experiment, Troitsk made the critical addition of strong magnetic fields for electron transport, which allowed for smooth coupling to the MAC-E-Filter spectrometer. Mainz used a film of molecular tritium quenched onto a substrate of pyrolytic graphite. Once these two experiments were optimized, their count rates, backgrounds, and energy resolutions were comparable.

The Troitsk experiment observed a small anomaly in the β energy spectrum located a few eV below the endpoint. The distortion resembled a sharp step in the count rate, and the position of the distortion seemed to oscillate. The cause of this anomaly was unknown, and the Troitsk group corrected for it phenomenologically in their fit by adding free parameters to describe the amplitude and position of the distortion. Figure 2.5 shows the β spectrum fit for the Troitsk experiment, as well as the anomaly.

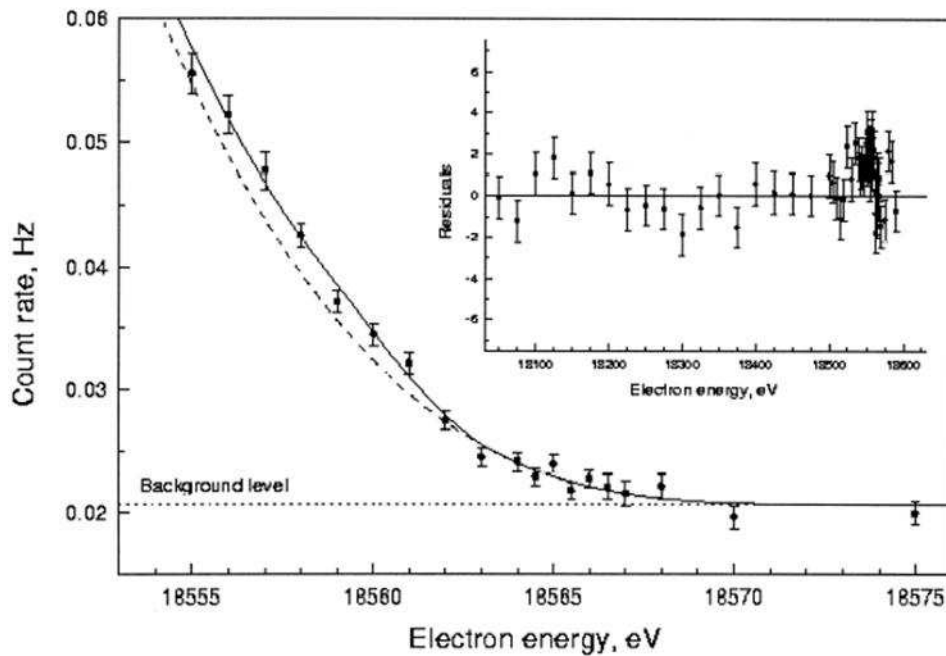


Figure 2.5: β spectrum data from the Troitsk experiment, along with their best-fit to the data. The inset shows the unexplained “Troitsk anomaly” that had to be parametrized in the fit in order to obtain sensible results. Figure taken from [26].

The Mainz experiment experienced many difficulties related to their quench-condensed source such as the scattering of the β particles within the tritium film, the excitation of neighbor molecules due to the β decay, and the self-charging of the tritium film by its radioactivity. Figure 2.6 shows the initial (obviously incorrect) β spectrum obtained from their early quench-condensed source, as well as the much-improved spectrum they obtained years later when they had solved some of their source difficulties. The Mainz experiment set a

limit of

$$m(\nu_e) \leq 2.2 \text{ eV} \quad (95\% \text{ C.L.}) \quad (2.17)$$

This limit is the best direct experimental limit on the neutrino mass.

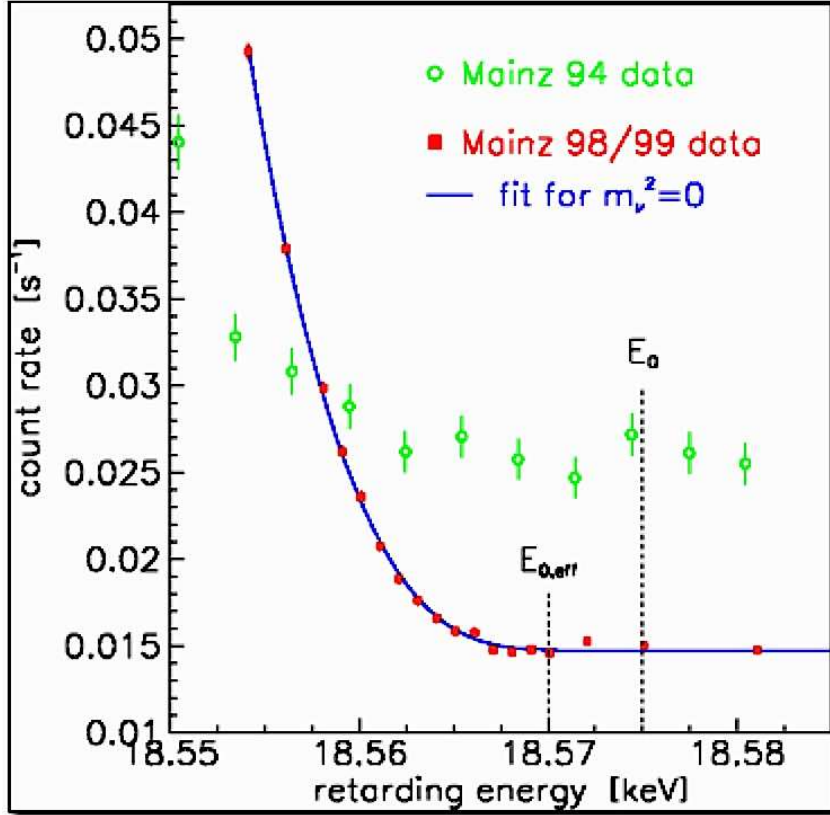


Figure 2.6: β spectrum data from the Mainz experiment, along with their best-fit to the data. The 1994 data is clearly unreasonable due to problems with their tritium source; by 1999 the improved source allowed better data to be taken. Figure from [27].

Table 2.1 summarizes the most significant of the tritium β decay experiments that have already occurred.

Table 2.1: Summary of previous tritium β decay experiments .

Experiment	Source	Resolution (eV)	$E - E_o$ in Analysis (eV)	m_ν^2 (eV²)	Upper limit m_ν (eV), 95% C.L.
LANL	T ₂ gas solenoidal trans- port	23 FWHM	2030	$-148 \pm 68 \pm 41$ (stat., syst.)	< 9.3
Zurich	R-CH ₂ T T-impl. in carbon	17 FWHM	925	$-24 \pm 48 \pm 61$	< 11
Tokyo INS	R-CH ₂ T monomol.	16 FWHM	625	$-65 \pm 85 \pm 65$	< 13
Livermor	T ₂ gas solenoidal transp.	18 FWHM	160	$-72 \pm 41 \pm 30$	< 8
Mainz	T ₂ frozen on graphite	6 FW	70	$-1.6 \pm 2.5 \pm 2.1$	< 2.2
Troitsk	T ₂ gas magnetic transp.	3.7 FW	170	$-1.0 \pm 3.0 \pm 2.5$	< 2.5

2.4.2 KATRIN

The Karlsruhe Tritium Neutrino (KATRIN) experiment will be the first direct experimental measurement of the neutrino mass in the sub-eV range, and it hopes to set a limit of

$$m(\nu_e) < 0.2 \text{ eV} \quad (90\% \text{C.L.}) \quad (2.18)$$

Figure 2.7 shows an experimental overview of KATRIN. KATRIN utilizes a WGTS and a MAC-E-Filter spectrometer, but its scale is significantly larger than the Troitsk experiment. The WGTS is 10 m long with a 9 cm diameter and a column density of 5×10^{17} molecules/cm², corresponding to 9.5×10^{10} decays/s. Its energy resolution is a $\Delta E = 1$ eV, a factor of 4 improvement on Mainz and Troitsk, which it achieves with a spectrometer that is 23.23 m long and 9.8 m in diameter. In addition to improved energy resolution, KATRIN is also increasing the isotopic purity of their source to 95% and optimizing the distribution of electron energy thresholds, as well as the time spent collecting data at each threshold. They have studied their systematics extensively and estimate that their background count rate will be no more than 10^{-2} counts/s near the endpoint region. KATRIN also utilizes a pre-spectrometer located between the source and the main spectrometer, which acts as a pre-filter to eliminate the β particles that are more than 100 eV away from the endpoint. The pre-spectrometer reduces the number of electrons entering the main spectrometer by 7 orders of magnitude, helping to eliminate residual tritium in the spectrometer that could decay and lead to errors.

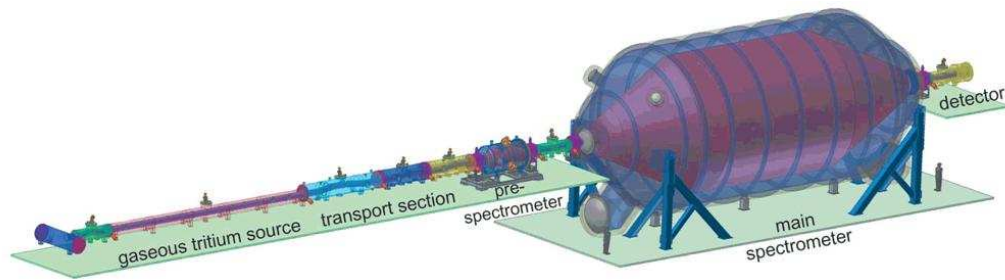


Figure 2.7: Overview of the KATRIN experiment. Figure from the KATRIN Collaboration.

KATRIN has not yet begun taking data, and it will need 3-5 years of data to make a significant statement regarding neutrino mass. Figure 2.8 shows how similar the β spectrum curves measured by KATRIN would look for a neutrino of 0.5 eV compared to 0 eV, and the similarity in the curves highlights the importance of obtaining sufficient statistics and eliminating systematic errors.

KATRIN's enormous spectrometer was delivered in 2006, and they have performed their first commissioning tests. They expect to be able to start taking their first measurements in 2012.

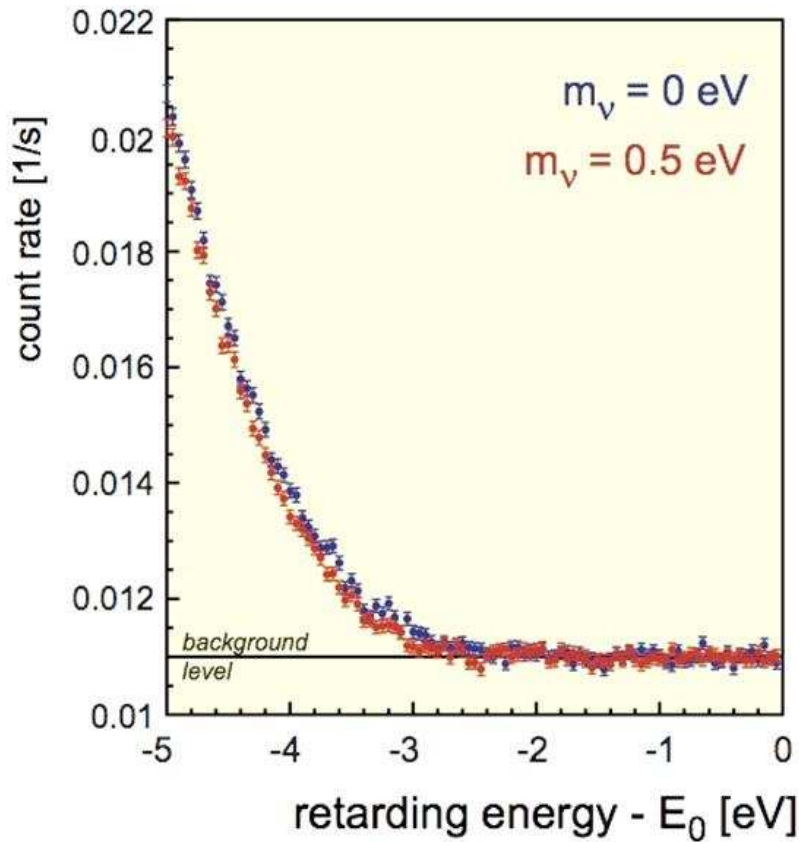


Figure 2.8: Simulation results of the β spectrum KATRIN anticipates measuring after three years of running for a neutrino mass of either 0 or 0.5 eV. Figure from the KATRIN Collaboration.

2.4.3 MARE

The Microcalorimeter Arrays for a Rhenium Experiment (MARE) will consist of arrays of low temperature calorimeters measuring the β decay of ^{187}Re , which has an endpoint energy of 2.47 keV, the lowest known in nature. The low endpoint energy means that the fraction of β decays occurring in the in-

interesting region below 1 eV will be 350 times larger than for tritium. MARE would have completely different systematics than KATRIN, and its modular design could allow for extensive scalability. A quantum calorimeter detects the energy of individual quanta as a thermal signal at low temperatures, typically less than 0.1 K. It consists of a photon or particle absorber and a sensor to determine the temperature rise due to the energy deposited. In a neutrino mass experiment, the absorber would be the element that contains the isotope that is decaying, which in the case of MARE would mean rhenium crystals. Each crystal has a typical mass of a few hundred micrograms, and it is cooled below 100 mK, which allows a semiconductor thermistor to detect the energy deposited in a β decay. Since the source and detector are the same device, one does not have to worry about β energy loss in traveling from the source to the detector. The main intrinsic limitation of a microcalorimeter experiment is the effect of unresolved pileup near the endpoint energy, which affects the spectral shape. ^{187}Re has an extremely long half-life of 4.4×10^{10} years, which explains why experiments have traditionally chosen to work with tritium, which has a half-life of 12.3 y. MARE phase I is planned to include 300 detectors and reach a sensitivity of 2-3 eV. MARE phase II, which could reach a sensitivity of 0.2 eV, is planned to include 10000-50000 detectors and would require significant research and development to achieve such large scalability.

2.4.4 Neutrinoless Double Beta Decay

In ordinary double β decay two neutrons within a nucleus decay into protons, emitting two β particles and two neutrinos (or antineutrinos). If neutrinos are Majorana, meaning they are their own antiparticles, then the first emitted

neutrino can be absorbed by the second neutron, meaning that no neutrinos are emitted from the nucleus. Obviously this process cannot occur if neutrinos are Dirac particles instead of Majorana ones. Neutrinoless double β decay can be observed in a few isotopes for which all other decay channels are forbidden for energetic reasons. This process would violate lepton number conservation by two units, and its observation would definitively establish the Majorana or Dirac nature of neutrinos. Figure 2.9 shows the Feynman diagram for neutrinoless double beta decay.

When neutrinoless double β decay is mediated by the exchange of a light virtual neutrino, the $\beta\beta(0\nu)$ rate is expressed as

$$[T_{1/2}^{0\nu}]^{-1} = G^{0\nu} |M^{0\nu}|^2 |\langle m_\nu \rangle|^2 \quad (2.19)$$

where $G^{0\nu}$ is the calculable phase space integral, $|M^{0\nu}|^2$ is the nuclear matrix element, and $\langle m_\nu \rangle$ is a linear combination of the neutrino masses:

$$\langle m_\nu \rangle = \sum_{k=1}^3 |U_{ek}^L|^2 m_k e^{i\phi_k} \quad (2.20)$$

which, for small masses becomes

$$\langle m_\nu \rangle = c_{12}^2 c_{13}^2 m_1 + s_{12}^2 c_{13}^2 e^{i\alpha_1} m_2 + s_{13}^2 e^{i\alpha_2} m_3 \quad (2.21)$$

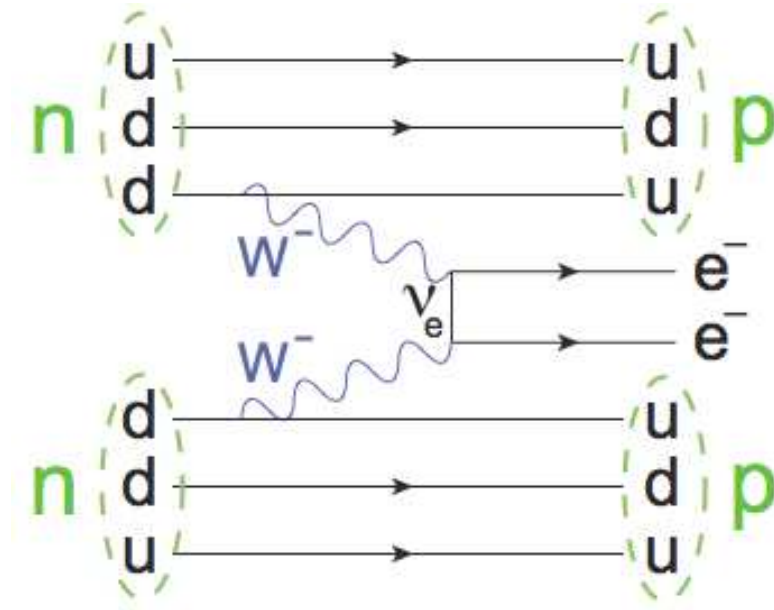


Figure 2.9: Feynman diagram of neutrinoless double beta decay. The two W bosons exchange a massive Majorana neutrino, resulting in no emitted neutrinos in the final state.

Unfortunately the Majorana phases α_k in the neutrino mass expression imply that cancellations are possible. A Dirac neutrino would be equivalent to two degenerate Majorana neutrinos with opposite CP phases, which would lead to complete cancellations, further illustrating why neutrinoless double β decay can only occur if neutrinos are Majorana particles.

Extracting the neutrino mass from neutrinoless double beta decay also requires accurate determination of the nuclear matrix element for the decay. Many evaluations are available in the literature, but they often conflict. The two main calculation methods are the Shell Model and the Quasiparticle Ran-

dom Phase Approximation (QRPA). QRPA calculations include many single-particle levels outside a small inert core, but they do not include complicated correlations. The Shell Model includes arbitrarily complicated correlations, but it can only include a few single-particle orbitals outside the inert core. Although these methods ought to be complementary, their calculated nuclear matrix elements disagree by a factor of about two. Current investigations are underway to carefully check both models for missing physics and to better understand their basic assumptions.

Most neutrinoless double β decay experiments are designed to measure the energy of the two β particles, and the signal will be a sharp line at the transition energy for $\beta\beta(0\nu)$, compared to a continuous distribution from ordinary double β decay, as shown in Figure 2.10 . The daughter nucleus can carry almost no energy due to the kinematic effects of its large mass, and without neutrinos to carry away energy, the measured energy of the β will be a peak at the endpoint energy, smeared by the detector resolution. The major considerations in building an experiment are, therefore: a detector with good energy resolution, a stable detector technology that can run for a long time, large isotopic abundance of the isotope under investigation, and an effective background suppression strategy.

Many neutrinoless double β decay experiments are currently being developed, and since they focus on different isotopes with different nuclear matrix elements, their results may ultimately be complementary. MAJORANA [28] and GERDA [29] are both large scale extensions of past successful experiments using ^{76}Ge . CUORE [30] uses ^{130}Te , which has a large natural abundance and can be investigated through the use of many TeO_2 bolometric arrays. EXO [31] plans to use isotopically enriched ^{136}Xe , which does not allow for as high of

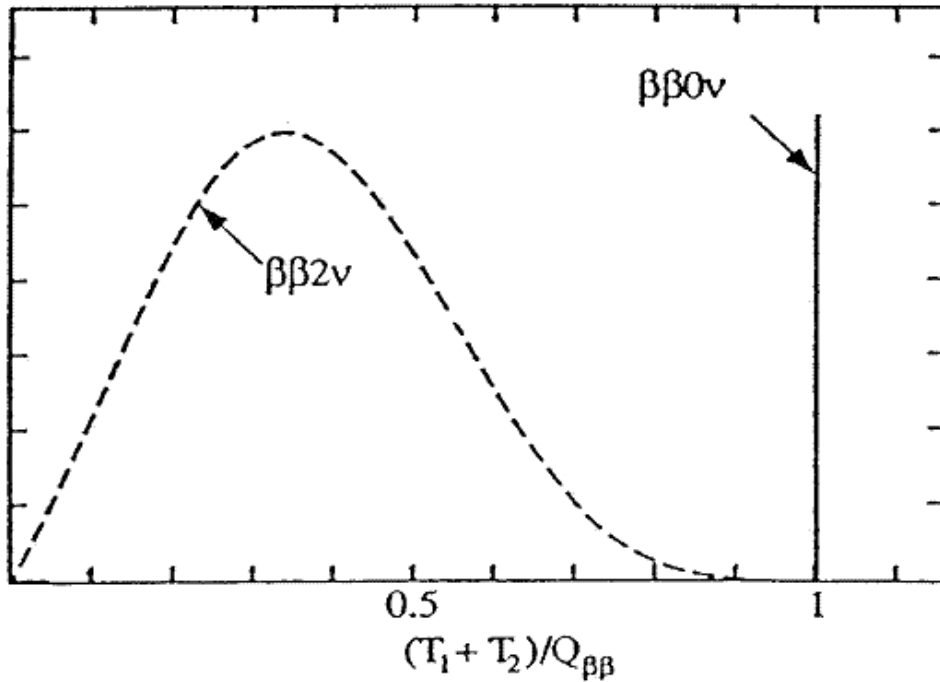


Figure 2.10: Idealized double β decay energy spectrum. In an actual experiment the neutrinoless double β decay peak would be smeared by the detector resolution. Figure from the SuperNEMO Collaboration.

an energy resolution, but it does enable excellent background suppression if the resulting $^{136}\text{Ba}^{++}$ can be tagged. SuperNEMO [32] has the advantage of working with multiple isotopes simultaneously, where each source consists of approximately 5 kg of a double β decaying isotope as a thin foil, surrounded by a tracking chamber with drift cells in Geiger mode and colorimetric walls with plastic scintillators and photomultipliers (PMTs). SNO+ [33] is pursuing the goal of studying ^{150}Nd by adding anywhere from 50 to 500 kg of enriched neodymium to liquid scintillator in the acrylic vessel previously utilized by SNO, and I will discuss SNO+ in greater detail in Chapter 5. The primary goal of all of these experiments is the determination of the Dirac or Majorana

nature of neutrinos, but by measuring the observed rate of neutrinoless double β decays, they also obtain some (model-dependent) sensitivity to neutrino mass.

A collaboration led by H. V. Klapdor-Kleingrothaus has recently published a series of papers claiming to see a neutrinoless double β decay signal that would place the neutrino mass in the 0.15-0.5 eV range, depending on the nuclear matrix element [34]. This claim has not yet been verified, and it has been highly criticized within the neutrino physics community [35]. Those skeptical of the claim believe that the group's peak finding procedure may return spurious peaks; many are not convinced that the candidate neutrinoless double β decay peak is anything other than a spurious peak or a real but unidentified background peak. This on-going debate within the neutrino community only highlights the need for more sensitive neutrinoless double β decay experiments, preferably utilizing a variety of different isotopes, since the Klapdor-Kleingrothaus claim may be related to properties unique to ^{76}Ge .

2.4.5 Cosmological Limits

Neutrino mass is also an important target in cosmology, and cosmology is becoming an increasingly useful tool in probing neutrino properties. All standard Big Bang models predict that an enormous number of neutrinos and antineutrinos were generated shortly after the birth of the universe. The present contribution to the matter density of the universe from massive neutrinos is estimated to be [36]:

$$\Omega_\nu h^2 = \frac{\sum m_\nu}{92.5 \text{ eV}} \quad (2.22)$$

where h is the Hubble constant. This equation shows that even a sub-eV neutrino mass gives a significant neutrino contribution to the energy density, meaning it affects structure formation.

Neutrinos are called hot dark matter because they were extremely relativistic around the time of matter-radiation equality. Their high velocities interfered with their clustering gravitationally, meaning matter in a universe with massive neutrinos is more clustered than if neutrinos were massless. Since neutrinos cannot cluster due to gravitational instabilities on scales shorter than their free-streaming distance, a characteristic length scale is introduced into the problem. The free-streaming distance decreased with time as the neutrinos slowed down, and the effect of neutrino free-streaming is more significant on the scale of galaxies than on the scale of clusters of galaxies. On larger scales neutrinos can participate in gravitational collapse (when the free streaming scale becomes smaller than the length scale in question), which means the suppression of clustering is less noticeable. Analyzing galaxy surveys, such as the Sloan Digital Sky Survey, can provide a useful power spectrum of matter distribution, but because the galaxy distribution does not necessarily accurately trace the mass distribution, bias is difficult to remove from these calculations. Varying other cosmological parameters can also produce similar effects on the power spectrum of matter distribution, meaning that degeneracies are hard to remove.

The neutrino mass limit can be further tightened by using observational data on the Lyman- α forest because they go deeper into the range of scales affected by the neutrino mean free path. Spectra of distant quasars show absorption at wavelengths corresponding to the Lyman- α transition. The clustering of lines in the spectra encodes information about the clustering of the neutral

hydrogen, and by extension the entire matter distribution. Strong systematic effects continue to be of concern with the Lyman- α data, however, meaning that the reliability of constraints obtained from it is difficult to determine [37].

Gravitational lensing also has the potential to convey important information about structure formation. As light from distant galaxies passes through the fluctuating gravitational potentials along the line of sight, it is deflected. The advantage to this approach is that there is no bias; the technique depends on one of the simplest principles of general relativity, as opposed to using galaxies or absorption lines as mass tracers. In order to take full advantage of the information contained in structure formation data, however, one must understand how massive neutrinos affect nonlinear growth. Most of the past work with this data has concentrated on how massive neutrinos affect linear growth, while ignoring nonlinear effects. A consistent treatment of massive neutrinos in nonlinear structure formation using cosmological perturbation theory and numerical simulations is in its infancy and may eventually lead to conclusive constraints [38].

The anisotropy of the CMB temperature has provided a wealth of cosmological information over the past decade, and it also contains some sensitivity to the neutrino mass. Figure 2.11 shows how the CMB power spectrum is affected by various neutrino masses, assuming all other fit parameters are held constant. The neutrino mass causes a shift in the first peak due to the fact that a larger m_ν implies that the distance to the last scattering surface is shorter. This shift, however, is easily compensated for by the uncertainty in the Hubble constant, meaning that the position of the first peak cannot place a particularly strong constraint on the neutrino mass. The first peak is also visibly suppressed if the neutrino mass is greater than ~ 0.6 eV because that

implies neutrinos became non-relativistic prior to the epoch of recombination; in this case the neutrinos cause a shift in the time of matter-radiation equality, which leads to observable modifications in the CMB temperature power spectrum. If the largest neutrino mass is below ~ 0.6 eV, then neutrinos are not expected to affect the CMB power spectra very dramatically.

Neutrino mass can therefore be investigated through both the CMB anisotropy and large-scale structure data. Multiple data sets can be combined to obtain constraints on the sum of the neutrino mass species. The most generally accepted fit includes WMAP's CMB data as well as baryon acoustic oscillation (BAO) data and type Ia supernovae (SN) data, and it limits the sum of the neutrino masses to be $\sum m_\nu < 0.67$ eV [39]. The BAO and SN datasets aid the CMB constraint primarily by reducing fit degeneracies related to the Hubble constant. Tighter constraints have been published making use of structure formation data, but those constraints are more questionable due to systematic effects, bias, and nonlinearities.

Astrophysics and particle physics are developing an ever-closer collaboration as their interests in certain questions like neutrino mass converge, and their investigative tools are complementary. Experiments currently underway like the Planck Surveyor CMB satellite could conceivably provide the first hints of a positive neutrino mass signal, but cosmological constraints on the neutrino mass are necessarily based on a particular cosmological model, making them indirect and inherently model-dependent constraints. While they are currently better constraints than any terrestrial-based particle physics experiment has provided, the ideal neutrino mass measurement would be direct and devoid of model dependencies. Such a direct measurement would enable cosmologists to input the neutrino mass as a known value rather than having to include it in

their multi-parameter fits of astrophysical data.

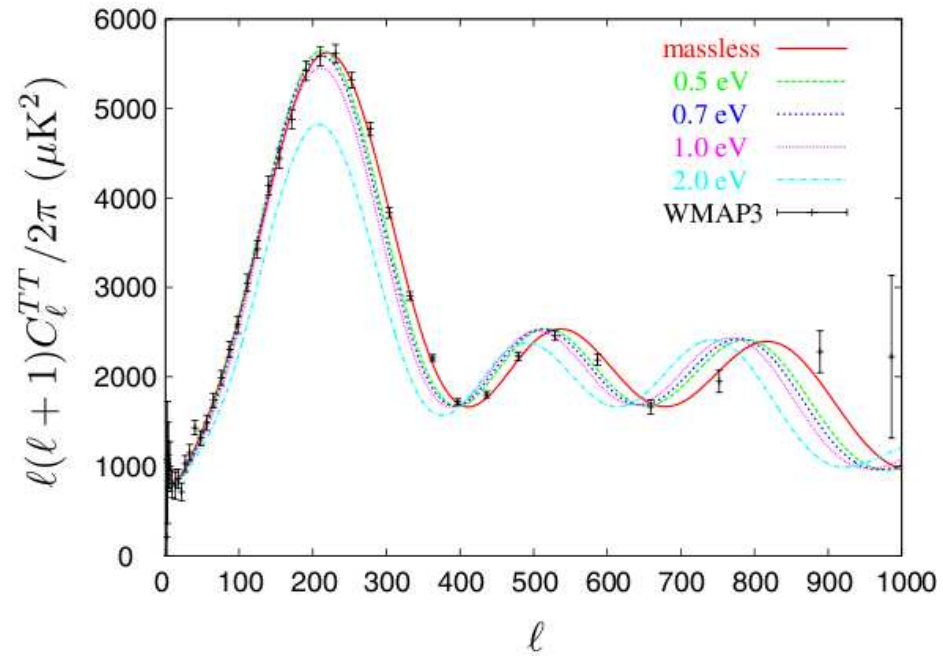


Figure 2.11: Effects of massive neutrinos on the CMB temperature power spectrum. All other fit parameters are held constant. Figure from [40].

Chapter 3

Recent Advances in Atomic Control

The mass of the neutrino is an important but elusive measurement, and few model-independent avenues exist through which to pursue it. As particle physics searches for new ideas through which to investigate neutrinos, one under-utilized approach is collaboration with seemingly unrelated fields of physics. Because tritium atoms have long been the favorite medium for neutrino mass investigations, studying progress in controlling and manipulating atoms could lead to better sources for tritium β decay experiments. This chapter provides a brief overview of developments in atomic physics that could enable the slowing, trapping, and cooling of atomic tritium for the purpose of a new type of tritium β decay measurement proposed in Chapter 4. These techniques are general in their applicability to almost the entire periodic table, and they also lay the groundwork for the general methods of isotope separation proposed in Chapter 5.

3.1 General Method of Atomic Slowing: Atomic Coilgun

Recent advances in trapping and cooling atoms open the door to new possible experiments and have applications even in the realm of neutrino physics. Nearly all atoms have an unpaired electron in the outer orbital, leading to paramagnetic effects that can be harnessed for atomic control. Those atoms that do not exhibit paramagnetic behavior in the ground state often exhibit it in a metastable state, meaning that techniques designed to manipulate atoms through magnetism can possess almost completely general applicability to the entire periodic table. Atoms in a laboratory are typically at room temperature and often in solid phase, and any general technique must accept these starting conditions before proceeding to trap and cool the atoms.

3.1.1 Supersonic Beam

The starting point for these new methods of slowing and cooling is a supersonic beam [41]. The basic working principle of a supersonic beam is that an inert gas under high pressure expands through a small aperture into vacuum, undergoing adiabatic cooling in the process since the mean free path of the particles is much smaller than the size of the aperture. The resulting beam of atoms is moving very fast in the laboratory frame (hundreds of meters per second), but in the co-moving frame the atoms are very cold, with temperatures of a few tens of millikelvin. Supersonic beams often operate in a pulsed mode, and the elements used are typically noble gases due to their stability under high pressures. The beam of noble gas atoms, however, can become a carrier gas

into which atoms of almost any other element can be entrained. As atoms of the two elements collide, they quickly come into thermal equilibrium, and the newly entrained atoms are swept along at the same high laboratory velocity but low co-moving frame velocity. In order to trap the atoms, however, one must slow them down in the laboratory frame.

The Raizen Laboratory, which developed this slowing method, produces a supersonic beam using an Even-Lavie supersonic nozzle that is cooled with liquid nitrogen so that the atoms' laboratory velocity is as low as possible from the outset. The Even-Lavie supersonic nozzle is capable of creating pulses as short as 10 μ s FWHM. The flux intensity is very bright, 4×10^{23} atoms/s/sr, which makes supersonic beams the brightest source of atoms currently available [42, 43].

3.1.2 The Coilgun

Military coilguns utilize electromagnetic coils to launch projectiles at high velocities, and by applying that principle in reverse, one can create an “atomic coilgun” that slows atoms by a series of pulsed electromagnetic coils [42]. Depending on the orientation of the atoms' magnetic moments, they can be classified as either low-field seekers or high-field seekers. Low-field seekers minimize their potential energy by going to a lower magnetic field, and these atoms can be conveniently trapped in a magnetic trap. As a low-field seeking atom enters the first coil in the atomic coilgun, the atom sees a potential hill that it must climb as it moves into the center of the coil. As it climbs the hill, it loses kinetic energy equal to the energy shift induced by the magnetic field:

$$\Delta E = \mu_B g_j m_j H \tag{3.1}$$

where μ_B is the Bohr magneton, g_j is the Landé factor, m_j is the projection of the total angular momentum on the quantization axis, and H is the peak magnetic field. If the atom were allowed to continue through the coil normally, it would simply roll down the hill and regain its lost kinetic energy. As shown in Figure 3.2, however, just as the atom reaches the center of the coil, the magnetic field is turned off. The atom has no choice but to continue to the next coil, having lost some of its original kinetic energy. Through a series of 64 coils, the atoms can be brought to rest over the space of just a meter in the laboratory. The slowing coils consist of 30 copper wire windings (0.5 mm diameter) with a bore diameter of 3 mm. The coil is encased in a magnetic steel shell with Permendur discs that confine the field and minimize inductance between adjacent coils. The peak magnetic field density is ~ 5 T. The timing of the coils is optimized using the principles of phase stability similar to those originally developed for synchrotrons. A low phase angle corresponds to turning off the coils before the atoms reach the peak magnetic field, which enhances the stability of the process. More stages of slowing allow one to slow a larger flux of atoms. When the atoms leave the coils, their co-moving temperature is still cold, but their laboratory velocity has been reduced dramatically. This cooling technique relies on the Zeeman effect in much the same way that a Stark decelerator relies on the Stark effect.

The Raizen Laboratory has demonstrated this technique by slowing both metastable neon and molecular oxygen. Figure 3.1 shows results of the slowing of metastable neon from an initial velocity of 447 m/s to 56 m/s. Their experimental setup is illustrated in Figure 3.3 part a) which gives a general overview of the design, and in part b) which shows a more detailed schematic. The skimmer has a diameter of 5 mm and is placed 15 cm from the

nozzle in order to ensure a well-behaved beam. The microchannel plate (MCP) placed after the coils detects the metastable neon after it has been slowed. (In this particular setup some final velocity is necessary so that the atoms can reach the detector). Parallel work has also been done by another group who independently developed a similar coilgun and demonstrated slowing of atomic hydrogen [44].

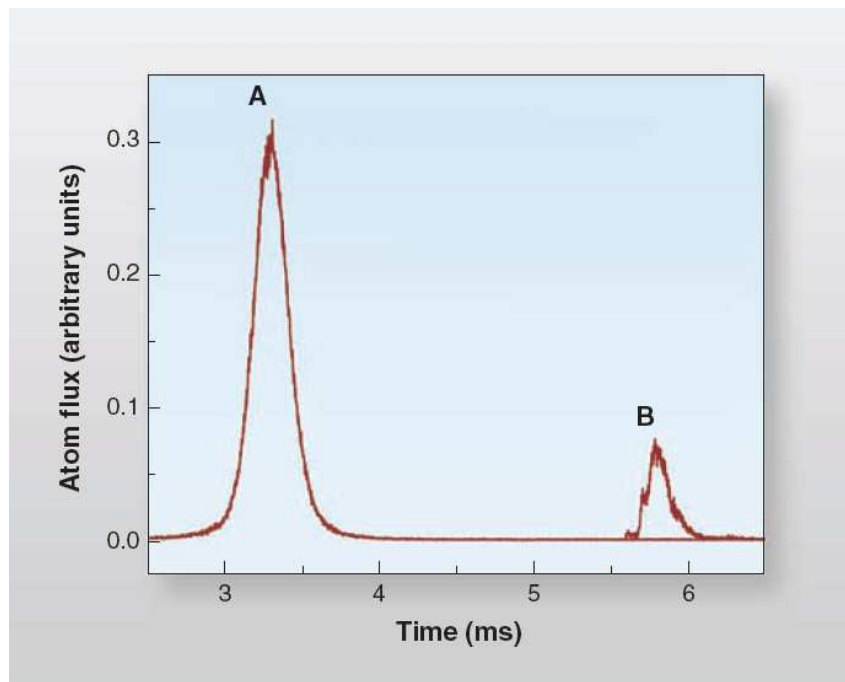


Figure 3.1: Atomic coilgun slowing results for metastable neon. The atoms' time-of-flight is shown, indicating a reduction in velocity from 447 m/s to 56 m/s. Figure from [43]

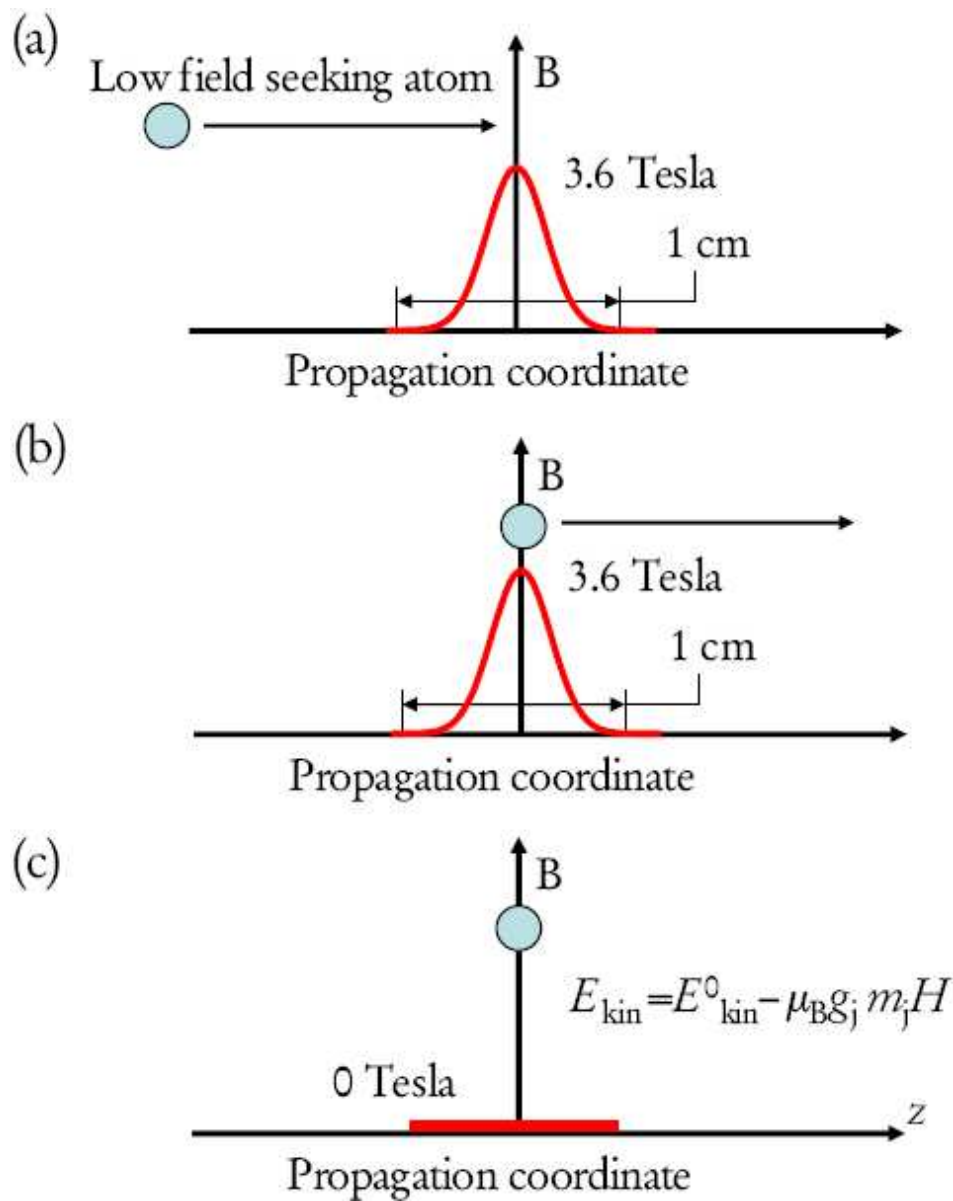


Figure 3.2: The slowing process for the atomic coilgun (taken from [42]). a) Low-field seeking atom enters coil and climbs magnetic hill b) Atom reaches center of coil where it has lost the maximum amount of kinetic energy c) Coil is turned off, and atom travels to the next coil with reduced kinetic energy

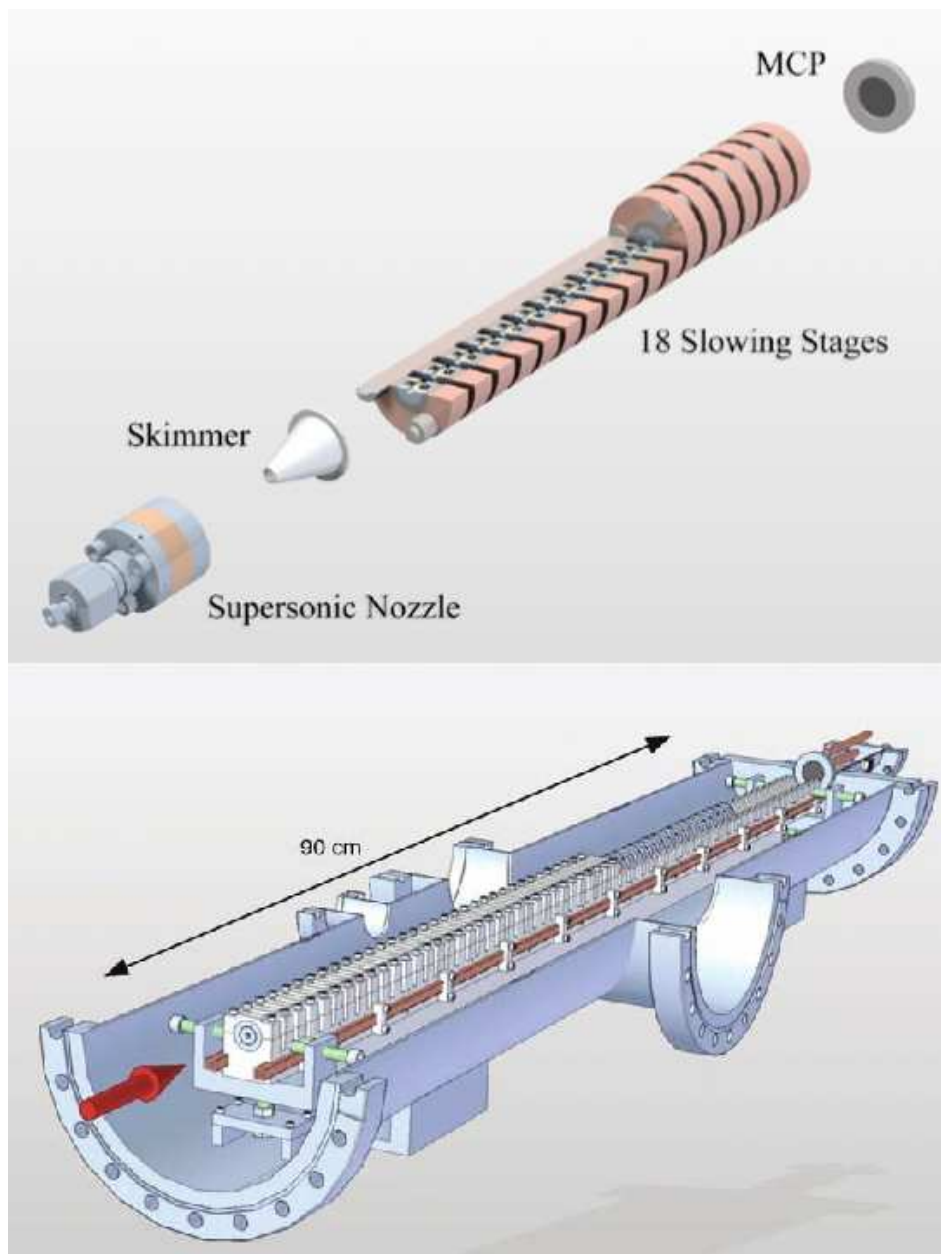


Figure 3.3: The top figure shows a conceptual drawing of the atomic coilgun (not to scale) that highlights the most important elements [43]. The bottom figure shows a schematic drawing of the 64-stage slower constructed in the Raizen Laboratory. Figure from [45].

3.1.3 Trapping

After the atoms have been slowed to a velocity near zero, they can be trapped in static magnetic fields that create a field minimum. The simplest way to produce these static fields is through an anti-Helmholtz pair of coils, in which the current in the coils flows in opposite directions. Anti-Helmholtz coils produce magnetic gradients of approximately 10 gauss/cm over a trap size of ~ 1 cm. The trap potential is on the order of 10 mK deep, and the quadrupole magnetic field has a zero at the center of the trap.

Once the atoms are trapped at temperatures of ~ 10 mK, they need to be further cooled to enable applications such as precision spectroscopy. The ideas discussed in Chapter 4 for measuring neutrino mass depend on having an extremely cold source of atomic tritium; the initial temperature of the tritium is, in fact, the biggest source of uncertainty in that chapter's proposed experiment. The following discussion of cooling the atoms further once they have been trapped is essential groundwork for any further investigations, including neutrino studies.

3.2 General Method of Atomic Cooling: Single Photon Cooling

3.2.1 Methods of Cooling

For more than 30 years trapping and cooling has been a primary research focus in atomic physics. Trapping and cooling atoms enables precision research in the study of spectroscopy and fundamental symmetries. The standard method

for cooling atoms has been laser cooling, which requires an available cycling transition so that the atoms can scatter many photons.

One implementation of laser cooling relies on the Doppler effect and utilizes a laser whose frequency is tuned slightly below a transition, which means that atoms will absorb more photons if they move towards the light source. The atom receives a momentum kick when it absorbs the photon, and it receives a second kick when it emits a photon in a random direction, meaning that the net effect of the momentum kicks acts to slow the atoms. Other laser cooling implementations include optical molasses, Sisyphus cooling, lattice cooling, VSCPT, and Raman cooling [46], but all of these still rely on the momentum transfer from photons to atoms. If an atom does not have a cycling transition that can be reached with a tunable laser, laser cooling will be ineffective since the momentum transfer from a single photon absorption is very small. A surprisingly small fraction of the periodic table is actually amenable to laser cooling, and molecules are also excluded. Even hydrogen, the simplest atom in the periodic table, cannot be laser cooled because of the lack of far-ultraviolet lasers that can access 121 nm. Laser cooling has enabled a tremendous amount of work, particularly in alkali atoms, but new methods with more general applicability could stimulate investigations of other atoms and ultimately lead to new discoveries.

Once atoms have been slowed by the atomic coilgun and trapped in a magnetic trap, their temperature is tens of millikelvin, but further cooling is required in order to probe interesting physics. Evaporative cooling allows the most energetic atoms to leave the magnetic trap, thereby lowering the kinetic energy of the entire ensemble as the remaining atoms re-equilibrate through collisions. In addition to the obvious problem of reducing the number

of trapped atoms, evaporative cooling can be difficult to achieve within the lifetime of the trap since the trap density is not high and re-equilibration times are often long.

3.2.2 Single Photon Cooling

Single photon atomic cooling begins with the idea of creating a one-way barrier for atoms [47]. In this method cooling is not based on the momentum of the scattered photon; scattering a photon is merely an irreversible step through which atoms cross a one-way barrier. If atoms can be made to cross this barrier at a time when their kinetic energy is low, they can be cooled. This method relies not on photon momentum but on the compression of phase space. The essential components of single photon cooling are a conservative potential and an irreversible step. The conservative potential can be created using magnetic fields, as discussed with anti-Helmholtz coils, or using light, as is done with optical tweezers.

The principle of single photon atomic cooling is best illustrated in one dimension. Figure 3.4 shows atoms trapped in a conservative potential, with a one-way wall in the wings of the main trap. The one-way wall is slowly swept through the main trap, and atoms encounter the wall when they have converted most of their kinetic energy to potential energy and are at their classical turning points. The one-way barrier is essentially a laser that causes the atom to scatter a single photon, putting it in a different internal state than it occupied previously. A three-level atom is the simplest case in which single-photon cooling can be applied. In a two-level atom, which is ideal for laser cooling, single photon cooling would not work because a one-way barrier

could not be created.

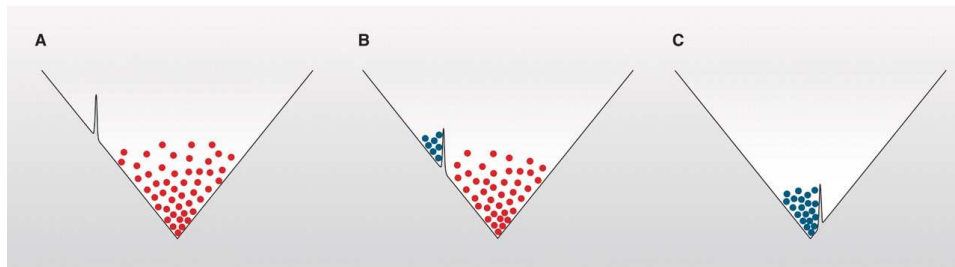


Figure 3.4: One dimensional illustration of single photon cooling in which atoms begin in a magnetic trap. As the one way wall is swept through the trap, atoms that were in an initial (red) state are converted to a different final state (blue) by scattering a single photon. A) The one way barrier begins in the wings of the trap. B) It sweeps slowly through the trap, catching atoms at their classical turning points. C) All atoms are eventually caught. Figure taken from [45].

Currently single photon cooling has been demonstrated in ^{87}Rb atoms, and the phase space was compressed by a factor of 350 [48, 49]. Since ^{87}Rb can also be laser cooled, the next important step will be demonstrating the technique on an atom like hydrogen that cannot be cooled via traditional laser cooling methods. While traditional cooling methods depend on photon momentum transfer, single photon cooling relies on phase space compression and is made possible by the concept of informational entropy. As discussed in the next section, single photon cooling is a kind of realization of Maxwell’s demon paradox.

3.2.3 Maxwell’s Demon

James Clerk Maxwell envisioned a “very observant and neat-fingered being,” who later became known as Maxwell’s demon, who was able to open or close

a hole between two partitions. In this thought experiment the two partitions are full of a gas, and the demon can open and close the hole so as to allow the faster atoms to accumulate on one side of the partition and the slower atoms to accumulate on the other side. The paradox of the thought experiment is that this demon could lower the entropy of the gas apparently without doing any work, thus violating the second law of thermodynamics. Maxwell was attempting to demonstrate that the second law was only statistical and could be violated under certain circumstances. In 1929 Leo Szilard proposed an interesting solution to Maxwell's demon by suggesting that the demon collects information about the atoms before deciding whether or not to open the door, and that information could carry entropy [50]. This "exorcism" of Maxwell's demon foreshadowed Shannon's later work in developing information theory, which establishes an analytical link between information and the entropy it carries [51].

In single photon atomic cooling, the one-way wall plays the role of Maxwell's demon. When the atom scatters its photon, a detection of that photon would provide experimental information about the turning point and kinetic energy of the atom. One can calculate the entropy increase due to the scattered photon, and computationally it exactly balances the entropy decrease for the cooled atoms [52, 53]. One does not actually have to measure all of the scattered photons; the fact that the information is available and could be collected is enough to save the second law of thermodynamics.

3.3 Isotopes of Hydrogen

Single photon atomic cooling is capable of cooling hydrogen and its isotopes, which cannot currently be cooled via laser cooling. Figure 3.5 shows the transitions in atomic hydrogen that could be utilized in single photon cooling. The 1S ground state of hydrogen is split into two hyperfine states, $F = 1$ and $F = 0$, separated by 1.42 GHz. The $F = 1$ state is further split into three states by the magnetic field, $m = -1, m = 0, m = 1$. Using a 243 nm laser, one can drive a two photon transition from the ground state to the 2S state. The 2S state couples to the 2P state, which decays by emitting a Lyman alpha photon near 121 nm. Atoms in the $F = 0, m = 0$ state can be optically trapped in a standing wave of light inside a build-up cavity.

The slowing and cooling methods described here are well suited to hydrogen and its isotopes, including tritium. Beginning with a supersonic beam of metastable neon, one could entrain tritium atoms in the carrier gas. An atomic coilgun could slow the tritium until it could be trapped, and single photon cooling could reduce its temperature even further. The applications of such a source of atomic tritium will be discussed in the following chapter.

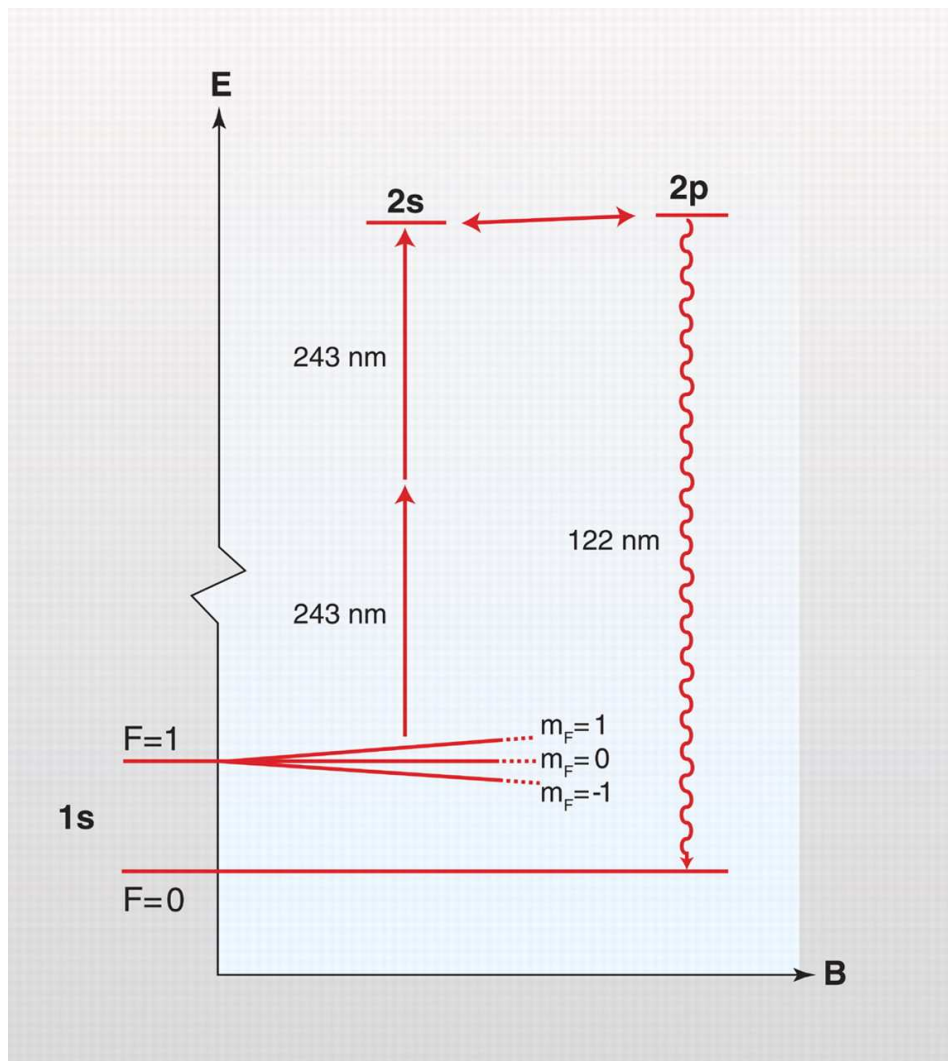


Figure 3.5: Illustration of the transitions in atomic hydrogen that could be utilized for single photon cooling. Figure taken from [45].

Chapter 4

Using Cold Atoms to Measure Neutrino Mass

The atomic coilgun and single-photon atomic cooling are tools that simply did not exist a decade ago. These techniques may enable a wide variety of interesting experiments, and this chapter explores one potential application of these tools in neutrino physics. If we could create an ultracold source of atomic tritium, then both the β and the helium ion could leave the source without scattering and be detected, which implies that the neutrino mass squared peak could be directly reconstructed from basic kinematics. This chapter begins by describing a potential experiment to perform such a kinematic reconstruction of m_ν . I outline the necessary detectors and the resolutions required in order to achieve an interesting measurement. The chapter describes the simulation I created of this experiment, and it presents results of a two-dimensional fitting technique that simultaneously utilizes both the β spectrum and neutrino mass squared peak information. I conclude by discussing the future prospects for

this type of experiment.

4.1 Introduction

The past decade has transformed our understanding of the neutrino; nevertheless, the absolute scale of the neutrino mass remains unknown. The best neutrino mass limits from direct measurements come from the tritium endpoint experiments Mainz and Troitsk [27, 26] discussed in Chapter 2, both of which place $m_\nu < 2.2$ eV. Measurements of the cosmic microwave background, coupled with cosmological models, have led to somewhat better (but model-dependent) constraints of $\Sigma m_\nu < 0.67$ eV [39].

The next generation of tritium endpoint measurement is now being pursued by the KATRIN experiment [54]. They expect to push the limit on the neutrino mass as low as $m_\nu < 0.2$ eV. An independent avenue of research is neutrinoless double β -decay, which could test the Majorana nature of the neutrino and possibly determine its mass, though uncertainties in the nuclear matrix elements make extracting the neutrino mass from neutrinoless double β decay quite difficult [55].

Of the established avenues for exploring the absolute mass scale of the neutrino, KATRIN is the only one that does not suffer from significant model dependencies. It has the best chance of observing an unambiguous measurement of m_ν . Unfortunately KATRIN struggles to control a large number of systematics, and an independent means of verifying any potential signal they might observe is desirable. KATRIN also represents the largest possible implementation of a tritium β decay experiment utilizing a windowless gaseous tritium source and MAC-E-Filter spectrometer; it cannot be scaled up an or-

der of magnitude in sensitivity. Ideas are scarce for future experiments with more potential scalability than KATRIN, and as cosmologists continue to extend their limits closer to the edge of KATRIN's potential sensitivity, now is an appropriate time to brainstorm unconventional approaches to the question of the neutrino mass scale.

The recent developments in trapping and cooling atoms discussed in Chapter 3 raise the possibility of a fundamentally new type of tritium β decay experiment. A small source of ultracold atomic tritium would allow not only the β but also the ion to exit the source without scattering and be detected. This approach combines the direct kinematic reconstruction of the neutrino mass squared peak with the information from the β energy spectrum itself, providing two handles on determining the neutrino mass. Before discussing how the kinematic construction could be implemented, I will first discuss in greater detail how the neutrino mass affects the β spectrum and why additional information from the kinematic reconstruction could prove significantly helpful.

4.1.1 Beta Decay Spectrum

In ordinary β decay experiments like the ones discussed in Chapter 2, the only experimental observable is the energy of the electron from the decay. The neutrino mass appears directly in the equation for the shape of the β spectrum curve:

$$\frac{dN}{dE} = C \times F(Z, E) p E (E_o - E) [(E_o - E)^2 - m_\nu^2]^{\frac{1}{2}} \Theta(E_o - E - m_\nu) \quad (4.1)$$

where E is the electron energy, p is the electron momentum, E_o is the total decay energy (18.6 keV for tritium), $F(Z, E)$ is the Fermi function, $\Theta(E_o - E - m_\nu)$ ensures energy conservation, and C is a constant. Appendix A includes a derivation of this equation, as well as a detailed discussion of the final state effects that are accounted for in the Fermi function. Figure 4.1 emphasizes the troubling fact that only 2×10^{-13} of the decays produce betas in the last 1 eV of the spectrum that is most sensitive to the neutrino mass.

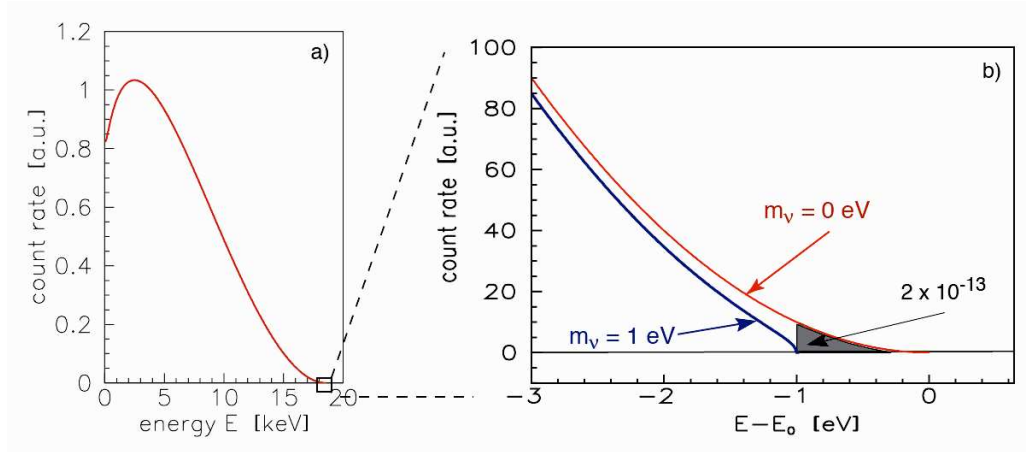


Figure 4.1: Beta energy spectrum from tritium beta decay, highlighting the fact that only 2×10^{-13} of the events occur in the critical last 1 eV. Figure taken from [54].

The β spectrum is often represented in the form of a Kurie plot [56], where it is linearized and written as:

$$K(E) \equiv \left(\frac{dN/dE}{pEF(Z, E)} \right)^{\frac{1}{2}} \sim \left[(E_o - E) \left((E_o - E)^2 - m_\nu^2 \right)^{\frac{1}{2}} \right]^{\frac{1}{2}} \quad (4.2)$$

Figure 4.2 shows the shape of a Kurie plot, which visually accentuates the

distortion due to the mass of the neutrino.

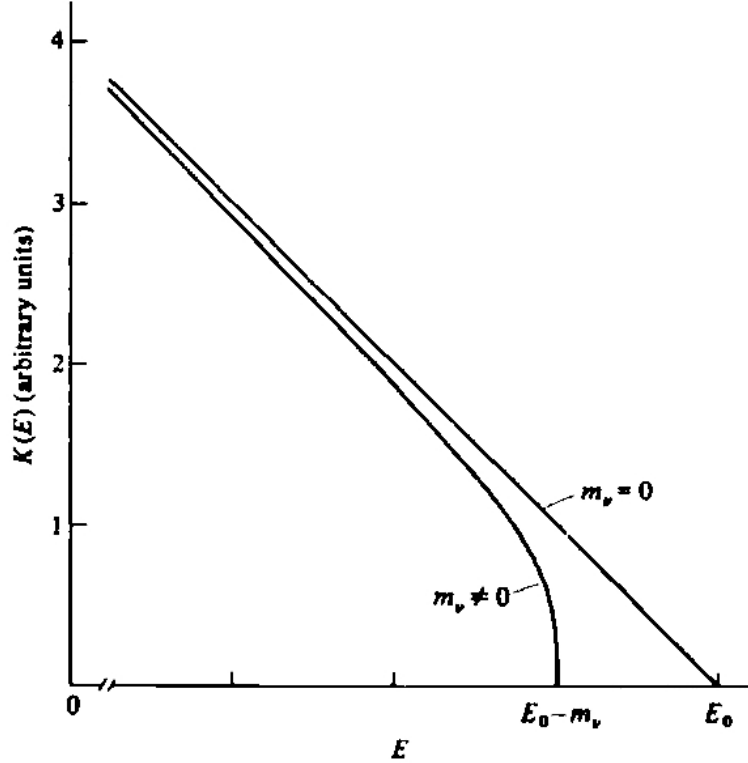


Figure 4.2: Linearized beta spectrum near the endpoint, known as a Kurie plot. Figure taken from reference [56]

Although the β spectrum is obviously sensitive to the mass of the neutrino, its greatest sensitivity lies in the part of the spectrum near the endpoint where the statistics are small. If a large enough number of β decay events could be measured, Figure 4.2 indicates that the neutrino mass could simply be read off of the spectrum by looking at the intersection point on the Kurie plot. Unfortunately even large experiments such as KATRIN cannot hope to obtain sufficient statistics to see clearly where their Kurie plots intersect the

x-axis, meaning that multi-parameter fits must be performed on the measured β spectrum. Rather than merely looking for the precise endpoint, data analysts must attempt to extract the neutrino mass from the overall distortion of the spectrum, using free parameters for m_ν^2 , the endpoint energy, background, and overall normalization. Additionally the smaller the neutrino mass is, the smaller the spectrum distortions it causes and the more problematic systematic errors in the experiment become. As the Chapter 2 discussion of the Mainz and Troitsk experiments makes clear, tritium β decay experiments have historically proven to be difficult and plagued by systematics. The kinematic reconstruction of the neutrino mass itself could allow a neutrino mass measurement to be made utilizing more than just the events that happen to fall within last few eV of the β spectrum.

4.2 Kinematic Reconstruction

4.2.1 Overview

The idea of directly reconstructing the neutrino mass is an approach fundamentally different from both KATRIN and neutrinoless double β -decay. This section will give an overview of an experiment to observe the β decay of ultra-cold atomic tritium. The decay produces an outgoing ${}^3\text{He}^+$ ion and a β , both of which can be detected. We need a spectrometer to measure the energy of the β , along with a non-invasive technique for measuring two components of its momentum. By utilizing the coincidence between the β and the ${}^3\text{He}^+$ ion, we can determine the ion's three momentum components from its time-of-flight. Measurement of the four-momenta of the ion (\tilde{p}_{He}) and the β (\tilde{p}_β) yields the

neutrino mass squared:

$$m_\nu^2 = \tilde{p}_\nu \cdot \tilde{p}_\nu = (\tilde{p}^{3H} - \tilde{p}^{He^3} - \tilde{p}^\beta) \cdot (\tilde{p}^{3H} - \tilde{p}^{He^3} - \tilde{p}^\beta) \quad (4.3)$$

The advantages of this approach include: an extremely thin source that results in low scattering; an atomic tritium source with simple final state effects; a coincidence measurement with the β to reduce background; a direct neutrino mass peak reconstruction; and the utilization of at least 500 eV of the β energy spectrum. Nevertheless, this approach faces several experimental challenges, particularly regarding the measurement of the β momentum to sufficient precision, and trapping enough tritium atoms to obtain sufficient statistics.

We address these challenges with an experimental setup that would consist of three detectors shown in Figure 4.3: a microchannel plate (MCP) to detect the helium ion, a spectrometer to measure the β 's energy, and an optical lattice of rubidium Rydberg atoms capable of measuring two of the β 's three momentum components.

We can place the β -spectrometer close to the source, with the MCP for the ${}^3\text{He}^+$ ion detection several meters away from the source. Using the β event detected by the spectrometer as the initial time, we can determine the time-of-flight of the ion to the MCP. Combining the time-of-flight with the MCP hit position yields the three momentum components of the helium ion. For example:

$$p_x = \gamma m v \sin\theta \cos\phi \quad (4.4)$$

where $v = z/(TOF)\cos\theta$ and θ and ϕ are reconstructed from the MCP hit position assuming the tritium decay came from the center of the source. Here

z is the distance from the MCP to the source.

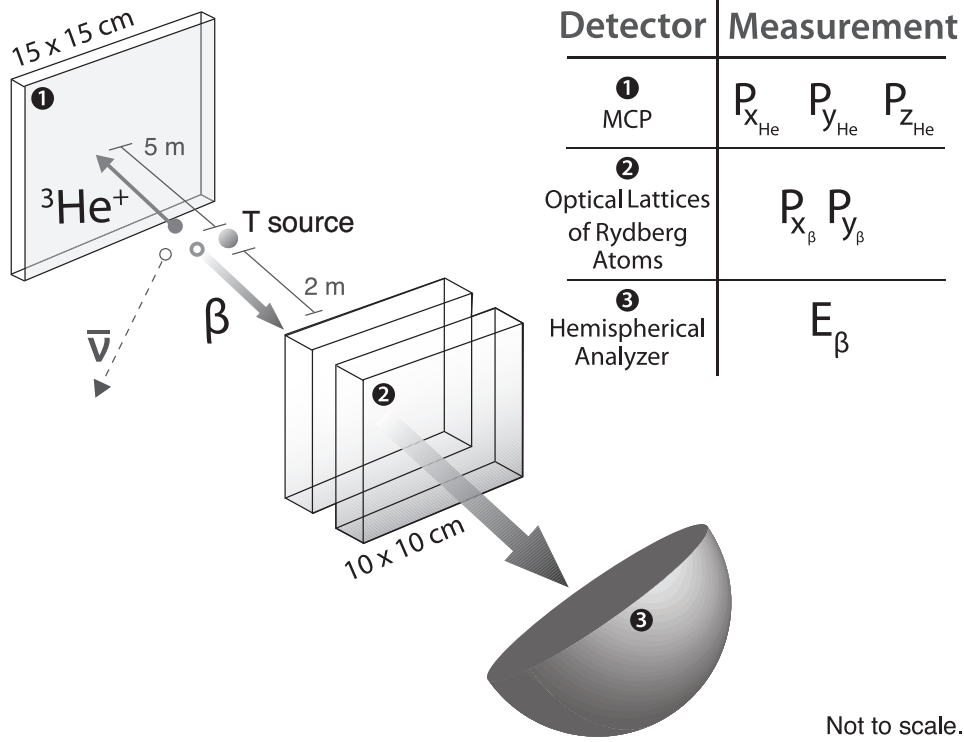


Figure 4.3: Experimental setup of the three detectors proposed for kinematic reconstruction of the neutrino mass: a microchannel plate (MCP), optical lattices of rubidium Rydberg atoms, and a spectrometer.

4.2.2 ROOT Simulation

Unlike most particle physics simulations, a simulation of this experiment does not depend sensitively on energy loss or propagation of particles through matter. While most experiments require the tracking of individual particles through various detectors, this experiment is governed primarily by the phase space available to the decay products, which can be determined analytically.

Consequently I developed a simulation of this experiment that did not involve individual particle tracking, which allowed me to simulate large numbers of events without expending outrageous computing resources.

I wrote my simulation in ROOT, which is an object-oriented program and library developed and maintained by CERN. ROOT includes many useful packages such as implementations of histogramming, graphing, curve fitting, minimization, data analysis, matrix algebra, and four-vector computations. One of the basic building blocks of ROOT is a data container called a *tree*, which has substructures known as *branches* and *leaves*. A tree is like a sliding window to the stored raw data, and data from the next entry in the file can be retrieved by advancing the index in the tree. Trees extend the concept of ntuples to all complex objects and data structures found in the raw data. ROOT is used for data analysis primarily in high energy physics, meaning many of its packages are tailored to the needs of particle physics.

For example ROOT includes packages that greatly simplify the simulation of tritium β decays. The phase space calculations are performed using ROOT's TGenPhaseSpace class, which is an adaptation of the widely used FORTRAN program GENBOD [57]. In order to account for information about the weak interaction that TGenPhaseSpace does not include, the interaction weight calculated by ROOT must be multiplied by $(E_\nu)(E_\beta)$. Because the phase space calculation is computationally intensive, I store all of the kinematic information of the resulting decays in a large ntuple that can be easily read as input to the main simulation that models the detectors.

For each decay, the simulation reads from the ntuple the four-vectors of the three resulting particles. Those particles then propagate until they encounter the various detectors shown in Figure 4.3. Rather than model the

particles in a step-by-step way as they move through the detectors, I model most of the detectors as Gaussian smearings that represents those detectors' resolutions. In the following sections I discuss each of the detectors and their resolutions in greater detail, and I also discuss the atomic tritium source, which is the starting point for the simulation of this experiment.

In choosing the detector specifications, I attempted to select state-of-the-art devices that represent the best that is currently available. In exploring the potential of this reconstruction technique, I made optimistic but feasible assumptions about the devices under consideration. Thus this simulation deliberately approaches the limits of what is currently possible in detector technology, and simultaneously it delineates the detector resolutions that would be required in order to make such an experiment worthwhile.

4.3 Atomic Tritium Source

The recently developed atomic coilgun and single-photon cooling technique enable the creation of an atomic tritium source. As discussed in Chapter 3, the tritium would be entrained into a supersonic beam, slowed with a series of magnetic coils, and trapped in a magnetic trap. The temperature of the tritium in the magnetic trap would be a few tens of millikelvin. In order to enable adequate kinematic reconstruction, the tritium would have to be further cooled. Laser cooling is not possible on hydrogen or any of its isotopes, and evaporative cooling has the disadvantage of sacrificing statistics. Single photon atomic cooling occurs as the tritium is transferred into an optical trap, and estimates indicate that the final tritium temperature could be as low as $1 \mu\text{K}$, which is the temperature assumed in the simulation. Although the optical

trap would probably not be spherical, the simulation assumes a spherical trap with a 100 μm diameter.

The simulation assumes a Maxwell-Boltzmann temperature distribution where the average kinetic energy of the atoms is defined as $\frac{3}{2}kT$ and the average momentum of the atoms is $(pc)^2 = E_{kin}^2 + 2E_{kin}mc^2$. Each component of an individual atom's initial momentum is then defined by a Gaussian whose mean is zero and whose variance is mkT . Since the source is assumed to be a sphere, the atom's initial decay position is chosen with a random radius inside the sphere and a random θ and ϕ .

We would like our tritium β decay source to be strong, but we also need to minimize scattering within the source. The density of this atomic source must be small enough that both the β and the ion have a high probability of escaping with any multiple scattering. The source cannot exceed 10^{15} atoms/cm³ without introducing non-negligible scattering. Fortunately if either particle does multiple scatter, the β and ion are very unlikely to emerge at the near-180° opening angle necessary for them to both be detected. What little multiple scattering does occur, therefore, is almost certainly simply a statistical loss and not a source of error in the neutrino mass reconstruction. Consequently the simulation does not directly include multiple scattering effects because we assume our source density will remain below 10^{15} atoms/cm³.

4.3.1 Final State Effects

In tritium β -decay, the helium ion is formed in the ground state in 70% of the decays, and our simulation simplifies the true spectrum of final states by assuming that the helium ion goes into the first excited state for the remaining

30% of the decays. For more than 99.9% of the events, the magnitude of the reconstructed neutrino mass is larger when the wrong state is assumed for the helium ion, which provides us with a simple method of determining the true state of the helium ion. This method does not bias the neutrino mass fit in any significant way.

4.4 Helium Ion Detection

4.4.1 Microchannel Plate

Detection of the helium ion as it leaves the source can be accomplished with a microchannel plate (MCP). The MCP is capable of measuring the ion's time of flight, as well as its hit position. We assume that our MCP has a high spatial resolution of $2\ \mu\text{m}$, which is in keeping with the capabilities of devices currently being manufactured by BURLE Electro-Optics, Inc. While BURLE currently manufactures the only $2\ \mu\text{m}$ MCP available for commercial sale, $5\text{-}10\ \mu\text{m}$ devices are fairly standard. BURLE's device, shown in Figure 4.4, shows holes $2\ \mu\text{m}$ wide with $3\ \mu\text{m}$ center-to-center spacing. Using a $5\ \mu\text{m}$ MCP with holes spaced $6\ \mu\text{m}$ center-to-center actually allows for larger geometrical acceptance and therefore does not represent a significantly worse option. We would require a large MCP, $15\ \text{cm} \times 15\ \text{cm}$, which would be a significant engineering challenge both to construct and to read out, though not prohibitively complex. In the simulation I assume that the acceptance of the device is equal to its geometrical acceptance as determined by the sizes and spacings of the MCP holes.

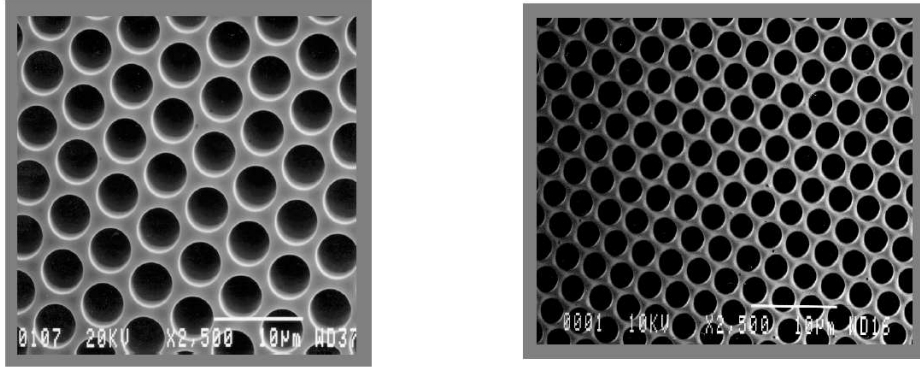


Figure 4.4: Comparison of 5 micron pore and 2 micron pore MCP's (same magnification) BURLE's 2-micron pore MCP is currently offered in an 18 mm diameter.

Each microchannel acts like an electron multiplier. The helium ion enters the channel, collides with the walls of the channel, and begins a cascade of electrons that propagate through the channel to amplify the signal. This process yields both the spatial hit position of the ion and its time-of-flight, assuming that the β 's hit in the spectrometer is used to define $t=0$. Since we do not know exactly where inside the tritium source the decay occurred, our momentum reconstruction improves as the distance between the source and the MCP is increased, but our geometrical acceptance of events decreases. Simulations indicate that the optimal distance for the MCP is 5 m from the source, and Figure 4.5 shows simulated results of the hit pattern observed on the MCP positioned at that distance. The MCP's necessary size is determined by the size and position of the Rydberg atom detectors for the β , which will be discussed in Section 4.6. We have chosen 15 cm \times 15 cm because that

is large enough to accept all of the ions whose β particles pass through the Rydberg detectors. The simulation assumes a timing resolution of 20 ps, which is achievable by the best devices on the market [58].

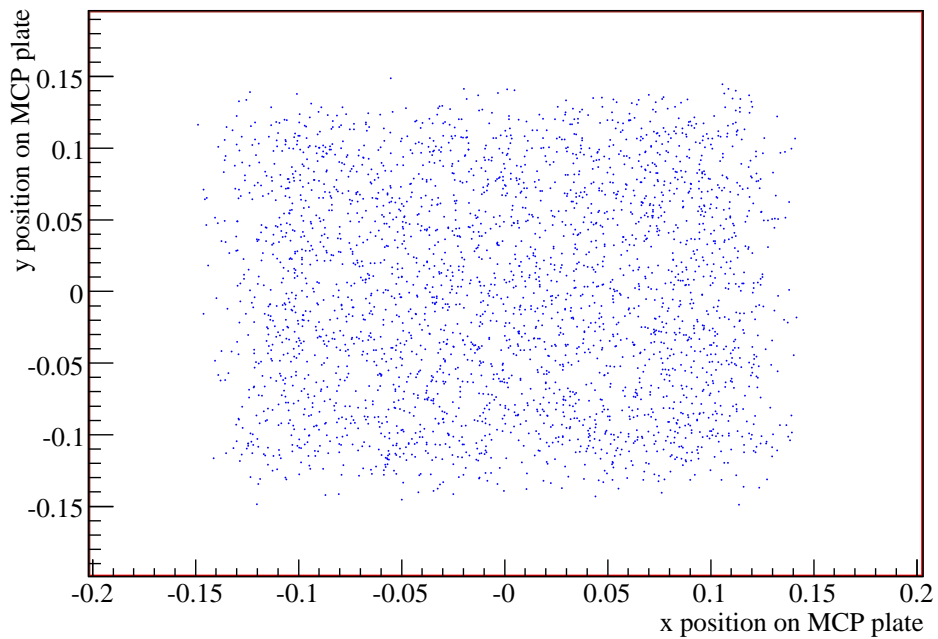


Figure 4.5: Simulation results of the hit pattern on MCP.

While most particle physics experiments can safely ignore gravity in their simulations, this experiment does require the inclusion of gravitational effects on the ion, which travels approximately 5 m at a v/c of approximately 4.9×10^{-5} , as can be seen in Figure 4.6.

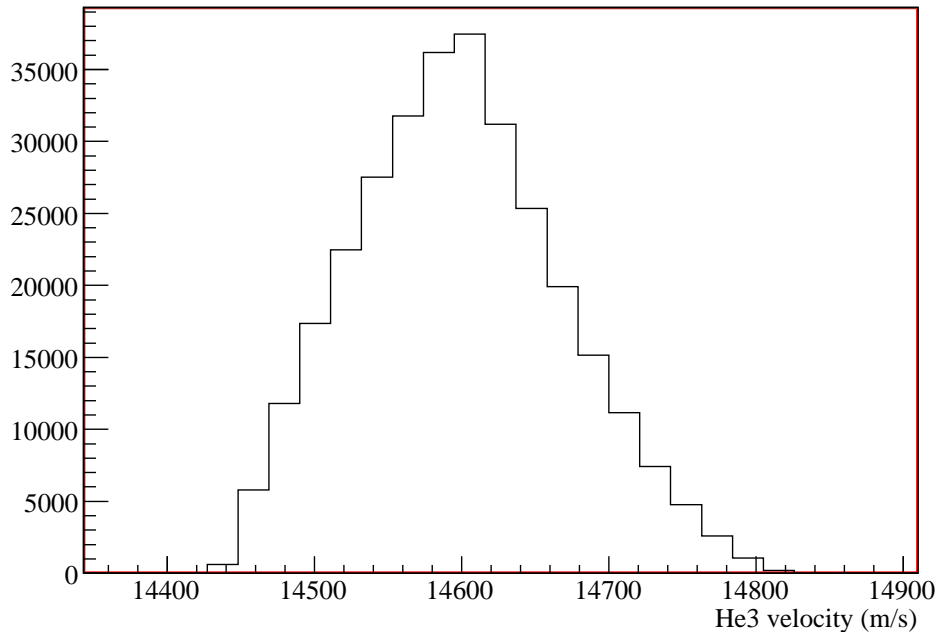


Figure 4.6: Simulation results of velocity of ${}^3\text{He}$ ion

4.4.2 Background Rate

The background event rate from the MCP would be < 1 event/cm²/s [59], where cosmic ray events are eliminated either by deploying the detector in an underground laboratory or by implementing an efficient veto. Although the coincidence in the β -spectrometer would be helpful, for any given β event of the correct energy there will be a 7% chance of seeing a background MCP hit, given that the coincidence time between the β and the ion will be on the order of 0.3 ms, as is shown in Figure 4.7.

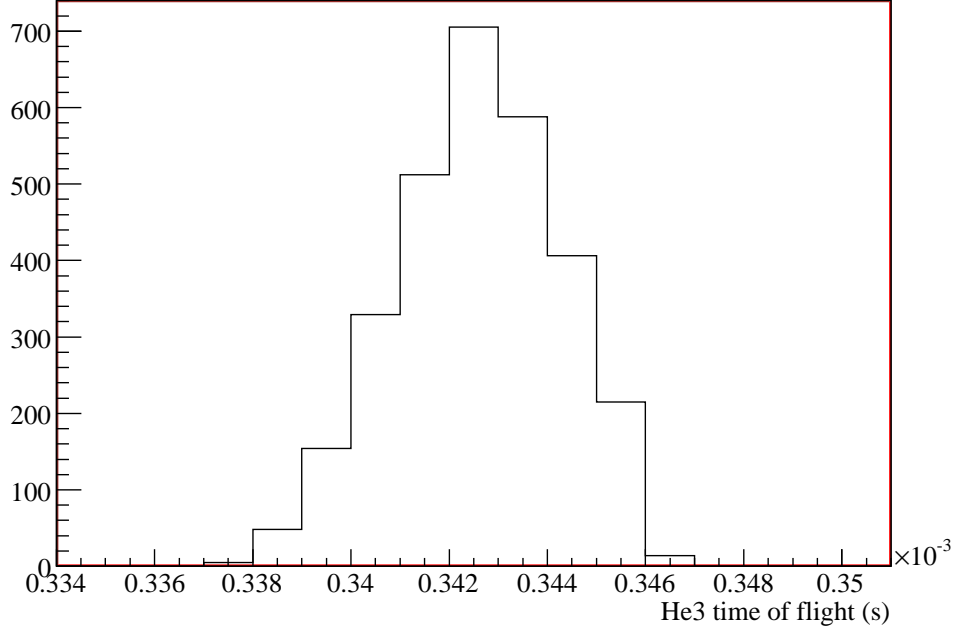


Figure 4.7: Simulation results of the TOF of the ^3He ion to the MCP

In order to evaluate our ability to discriminate true events from backgrounds, we simulated data in which the MCP hit position was randomized, and we studied how our reconstruction algorithm evaluated the neutrino mass for such random events. Such events typically reconstruct to be more negative than -10^6 eV^2 and would be clearly separated from true helium ion hits. Our simulations indicate it is possible to reduce backgrounds to 1.0×10^{-5} , not including the rejection due to the coincidence requirement, simply by cutting any events that reconstruct the neutrino mass squared to be more negative than -5000 eV^2 . This cut introduces negligible bias into the neutrino mass squared peak. Figure 4.8 shows the reconstructed neutrino mass values for

background MCP hits where the time-of-flight to the MCP was left unchanged but the MCP hit position was randomly chosen, and the neutrino masses reconstruct extremely negative. The negative reconstruction is due to the fact that most of the energy of the ion comes from its rest mass, so changing the momentum of the ion by selecting a false MCP hit position does not alter the total energy of the system by a large amount. The neutrino, however, must acquire a large amount of momentum in order to enforce conservation of momentum, leading to a very negative neutrino mass in the reconstruction.

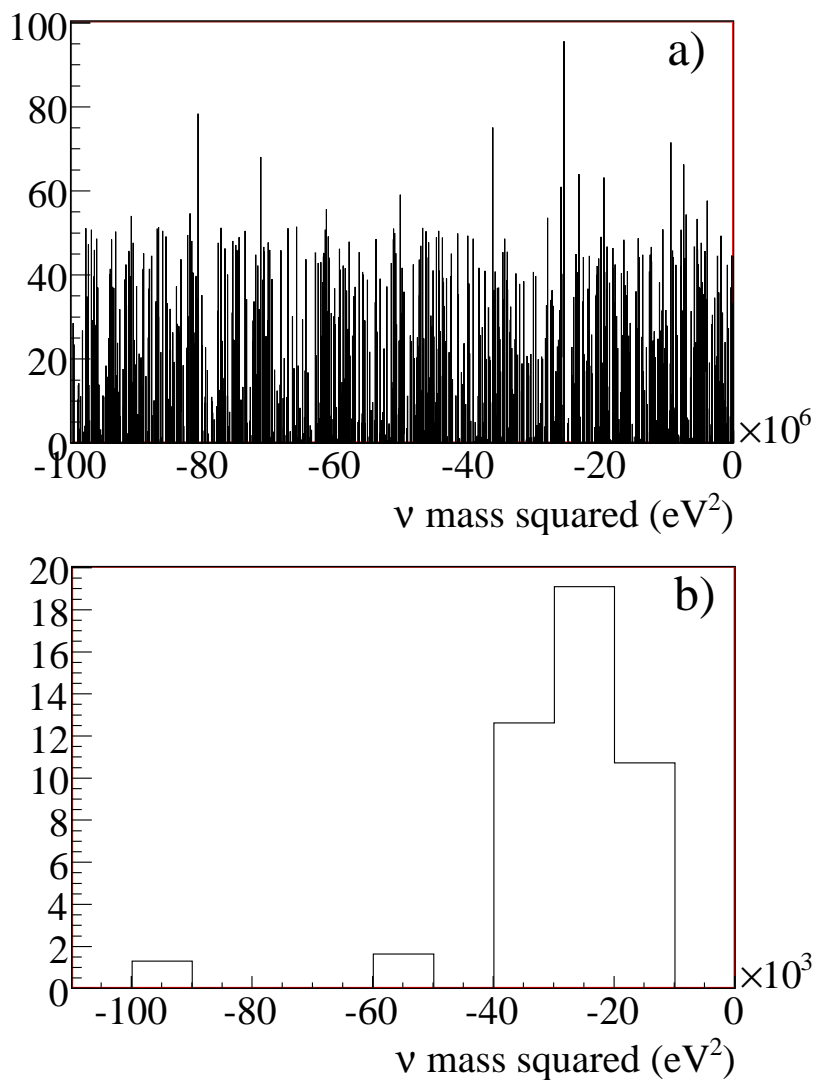


Figure 4.8: The neutrino mass squared in tests in which the MCP hit position has been randomized to simulate MCP background hits. a) The neutrino mass reconstructs extremely negative for these simulated background events. b) A zoomed in view of the above plot, showing the most positive of the neutrino mass squared reconstructions coming from the background events.

4.5 Beta Energy Measurement

We cannot use the same detection technique for the β that we used for the ion because we need to know its energy quite well in order to reconstruct the β energy spectrum that we use in our two-dimensional fits.

The detailed inner workings of the energy detector were not included in the simulations since one of the simulation's goals was to determine what energy resolution would be necessary to make such an experiment possible. The β energy detector was modeled as a simple Gaussian energy smearing whose width corresponded to the energy resolution of the detector. Figure 4.9 illustrates that the necessary energy resolution is between 5-50 meV, and the best tool for achieving energy resolutions in the meV range is probably a hemispherical analyzer.

2D Fit Dependence on Experimental Resolutions for $m_\nu = 0.2\text{eV}$

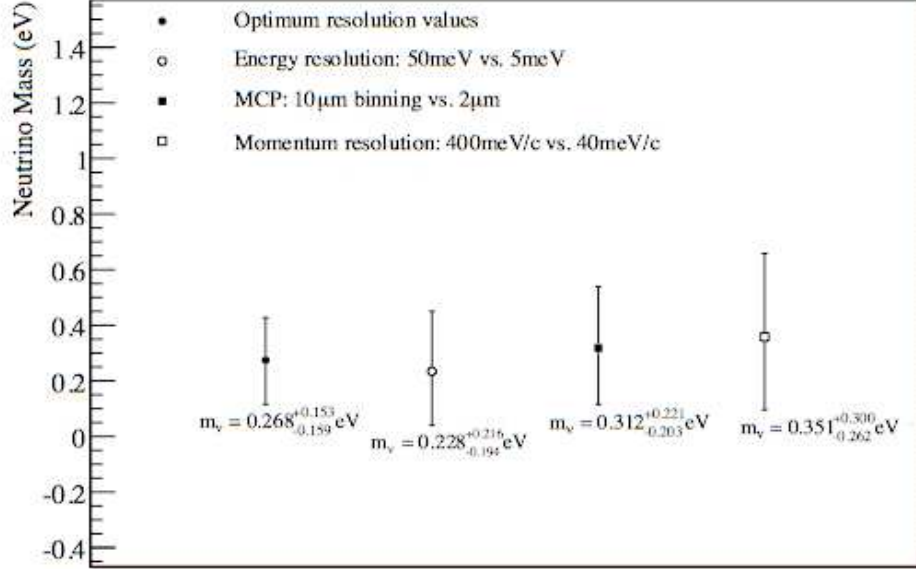


Figure 4.9: Illustration of the effect of various detector resolutions on the quality of the two-dimensional fit for the neutrino mass.

A hemispherical analyzer consists of two concentric hemispheres of radii R_1 and R_2 . A potential ΔV is placed across the hemispheres such that the outer hemisphere is negative and the inner hemisphere is positive with respect to the potential at the center line, $R_o = (R_1 + R_2)/2$. The center line potential is known as the pass energy, and most analyzers operate with a constant pass energy, which corresponds to a constant ΔE resolution. The pass energy can be written as:

$$E_{\text{pass}} = \frac{eV}{\frac{R_o}{R_i} - \frac{R_i}{R_o}} \quad (4.5)$$

Figure 4.10 gives a basic overview of the operation of a standard hemi-

spherical analyzer. The electrons are counted after they have passed through the energy analyzer. The electrons arrive at the analyzer exit with a variety of different energies based on their curvature through the device, and they are typically detected using a multichannel array to count the electrons arriving at the various energies.

As shown in Figure 4.10, one can arrange the array to be two-dimensional to provide information concerning not only the electron's energy but also one component of its momentum. For the purposes of this experiment the momentum measurement is not necessary and would be used only as a confirmation check on the momentum measurements described in the next section.

SPECS PHOIBOS analyzers are among the best currently available for commercial sale. In discussions with engineers from that company, they have drawn up a quote for a hemispherical analyzer that would be suitable for this experiment.

We do not intend to rely on the hemispherical analyzer for a momentum measurement because it could provide only one component of the β momentum, and we need to measure two components to adequately reconstruct the neutrino mass. The most difficult experimental challenge in a reconstruction experiment like this one would be finding a way to measure two components of the β 's momentum without significantly disturbing its energy. In order to accomplish such a non-invasive measurement, we can use the effect of a passing electron on a Rydberg atom.

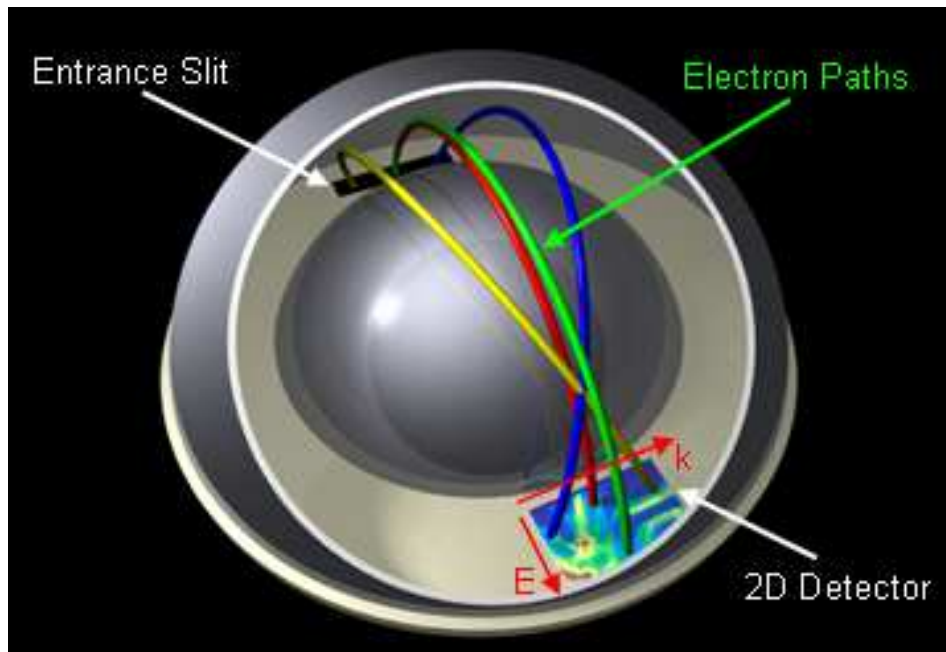


Figure 4.10: Conceptual diagram of hemispherical analyzer, taken from the Shen Group at Stanford University (http://arpes.stanford.edu/facilities_ssrl.html)

4.6 Beta Momentum Measurement

4.6.1 Rydberg Atoms

Rydberg atoms have at least one electron with a very high principle quantum number. These atoms have a number of interesting properties, including being easily perturbed or ionized by collisions or external fields. The core electrons shield the outer electron from the nucleus, making the potential similar to that seen by electrons in hydrogen atoms.

Despite the limitations of Bohr's atomic model, it is quite useful in explaining the peculiar properties of these atoms. Classically the orbit of an electron about a proton can be described by:

$$\frac{ke^2}{r^2} = \frac{mv^2}{r} \quad (4.6)$$

Orbital momentum is quantized in units of \hbar , where $mvr = n\hbar$. By combining those expression, one obtains:

$$r = \frac{n^2\hbar^2}{ke^2m} \quad (4.7)$$

The radius and dipole moment increase like n^2 , while the geometrical cross section increases like n^4 . Because the binding energy of a Rydberg atom's electron is proportional to $1/r$, it falls off like $1/n^2$, and the energy level spacing falls off like $1/n^3$, leading to ever more closely spaced levels converging on the first ionization energy. When one takes into account quantum mechanical effects, the energy levels can be written as:

$$\frac{-1}{2(n - \delta_l)^2} \quad (4.8)$$

where δ_l is a quantum defect term that corrects for the core electrons, n is the principle quantum number, and l is the orbital angular momentum of the electron. The lifetimes of these Rydberg states scale like n^3 , meaning that rubidium $n = 50, l = 1$ has a lifetime of $238 \mu\text{s}$, compared to just $0.026 \mu\text{s}$ for the $5p$ state. For more than a decade now rubidium Rydberg atoms have been trapped in optical lattices so that their unique properties could be studied [60], and the ability to hold Rydberg atoms in such a lattice creates the opportunity

for a new kind of particle detector.

4.6.2 Rydberg Atom Detector Design

In order to measure the momentum of the β without significantly altering its energy, we can use the effect of a passing electron on Rydberg atoms [61]. No other detection technique currently exists that can measure the momentum of an electron as accurately without noticeably disrupting its energy. While this technique would require significant research and development to implement, it represents a fundamentally new detection scheme that may have applications beyond those described here.

In the β 's flight path before it reaches the spectrometer, we create an optical lattice filled with rubidium atoms in the ground state [62, 60]. Using laser excitation, we can excite the atoms to a high Rydberg state [63, 64]. When the β passes one of these atoms, it can excite the atom from a 53s state to a 53p state, and the atom will remain trapped in its optical lattice position. The electrons would have to be slowed with a controlled voltage soon after they leave the source so that by the time they reach the optical lattice, they have a maximum energy of 900 eV, which increases their cross section for exciting a Rydberg atom to $0.36 \times 10^{-9} \text{ cm}^2$.

We calculated this transition cross section using the first order Born approximation, which is applicable because the electron energy is more than 10^7 times larger than the transition energy, and the transition is dipole allowed. The radial part of the transition matrix element is found numerically using a Numerov algorithm that computes the radial orbits on a square root mesh in r . Using 4th order integration, the product of the radial orbits and the

Bessel function, $j_1(qr)$, was numerically integrated. To obtain the total cross section, we numerically integrated over the momentum transfer q from $q_{min} = k - \sqrt{k^2 - 2\Delta E}$ to a $q_{max} = 0.25/n$ using equally spaced points in q with a $\Delta q = 0.01/n^2$.

When a β signal is detected downstream in the spectrometer, the 53s atoms are optically de-excited using STIRAP (stimulated Raman adiabatic passage) [64], and an electric field of 100 V/cm is ramped within ~ 130 ns to ionize any Rydberg atoms in a 53p state. Once the atoms are ionized, they will be detected by an MCP. Based on realistic density limits, the β will excite several Rydberg atoms as it passes through the optical lattice, so we will be able to obtain the projection of a track from the passing β .

In order to obtain the two β momentum components necessary for reconstruction, we need to have a second optical lattice to project the momentum component in a direction orthogonal to the first. By combining the track projections from these two MCPs with the energy measurement from the spectrometer, we can reconstruct the momentum of the β that traversed the optical lattices using equation 4.4 and the reconstructed velocity:

$$v = c(1 - 1/(T/m + 1)^2)^{1/2} \quad (4.9)$$

where T is the kinetic energy of the β as measured in the spectrometer and θ and ϕ are obtained from the β tracks in the optical lattices. Using Rydberg atoms with a principle quantum number $n=53$ would result in a negligible change in the β 's four-momentum as it passes. We estimate that we can obtain a density of 10^{11} atoms/cm³ in the optical lattice [46], and we expect the passing β to excite an atom within $5 \mu\text{m}$, leading to a high spatial resolution.

The two major sources of backgrounds that must be eliminated for this Rydberg technique are collisions and black body excitations. Holding the Rydberg atoms in an optical lattice eliminates collisions that could cause spurious transitions to the 53p state [62]. By surrounding the optical lattice with a wire mesh, we can eliminate most of the black body radiation that could excite atoms from the 53s to the 53p state. The spacing of the mesh would be small compared to the microwave wavelength, suppressing blackbody emission of the mesh itself. Additionally, the rubidium atoms can be periodically cycled back to the ground state and then up to the Rydberg 53s state [63, 64], which will prevent background 53p events from accumulating, while still allowing the atoms to spend most of their time in the 53s state. This non-invasive method may find other applications in the detection of low-energy electrons.

4.7 Simulation Results

4.7.1 Simulation Parameters and Detector Resolutions

Our current experimental simulation makes several assumptions about detector precision in order to determine the required equipment, and the most important parameters are summarized here. We assume an MCP of 15 cm x 15 cm with a timing resolution of 20 ps and a high spatial resolution of 2 μm [65, 66, 67]. It is placed 5 m from the tritium source and has a 44% acceptance for detecting an ion when it is hit. The tritium source is modeled as a 100 μm sphere at a temperature of 1 μK . Given that the density of the source cannot exceed 10^{15} atoms/cm³ and that the radius of the source is 50 μm , the column density of the source is less than 10^{13} atoms/cm². We therefore esti-

mate multiple scattering within the source to be small and do not include it in the simulation. The β -spectrometer is a hemispherical analyzer with an energy resolution of 5 meV, which is reasonable given current devices [68]. Simulations indicate that the Rydberg atom method of measuring the β momentum results in a resolution that varies from 40 meV/c to 2.8 eV/c depending on the β 's four-momentum. We assume a large Rydberg atom optical lattice with dimensions 10 cm x 10 cm x 1 cm placed 2 m from the source, which optimizes the detector's resolution and solid-angle acceptance.

The reconstruction of the neutrino mass requires large statistics to obtain accurate results, as can be seen in a simple error propagation. The neutrino mass squared is simple:

$$p_\nu \cdot p_\nu = m_\nu^2 \quad (4.10)$$

where p_ν is the four-vector momentum of the neutrino. Conservation laws dictate:

$$p_\nu + p_{\text{ion}} + p_\beta = p_{\text{tritium}} \quad (4.11)$$

The neutrino mass squared is, therefore:

$$m_\nu^2 = p_\nu \cdot p_\nu = (p_{\text{tritium}} - p_{\text{ion}} - p_\beta) \cdot (p_{\text{tritium}} - p_{\text{ion}} - p_\beta) \quad (4.12)$$

Writing the initial tritium energy as W ,

$$m_\nu^2 = W^2 - 2WE_{\text{ion}} - 2WE_\beta + m_{\text{ion}}^2 + m_\beta^2 + 2|\mathbf{p}_{\text{ion}}||\mathbf{p}_\beta|\cos\theta \quad (4.13)$$

where θ is the opening angle between the β and the ion. This formula raises a

disturbing question because when you look at the uncertainty in the neutrino mass squared due the uncertainty in θ ,

$$\delta\theta \frac{\partial m_\nu^2}{\partial\theta} = -2\delta\theta |\mathbf{p}_{\text{ion}}| |\mathbf{p}_\beta| \sin\theta \quad (4.14)$$

Plugging in some typical values for the ion and β momentum leads to the unfortunate conclusion that

$$\delta\theta \frac{\partial m_\nu^2}{\partial\theta} \sim \delta\theta \sin(\theta) 10^{10} \text{ (eV/c)}^2 \quad (4.15)$$

This calculation implies that the uncertainty in any one reconstructed tritium decay is going to be very large, but there are two mitigating factors that prevent disaster. The first factor is that we are primarily interested in events near the end of the beta spectrum, and these events have an opening angle that is almost 180° . As shown in Figure 4.11, the uncertainty in a particular given event increases dramatically as the opening angle increases, which is what our error propagation estimate would lead us to expect. Given a large enough number of tritium decays, however, one can measure a neutrino mass squared peak. Even if that peak is very broad, the uncertainty in the mean of the peak will go like $1/\sqrt{N}$, which means that given enough statistics, the neutrino mass could be determined accurately. An actual estimate of the width of the neutrino mass peak and the error bars on the neutrino mass squared fit value is unhelpful because the fit is two-dimensional and utilizes β spectrum information as well. This calculation does highlight, however, that while event-by-event smearings can be tolerated by increased measurement statistics, any systematic shifts in the detector measurements would introduce problems for

such a reconstruction experiment.

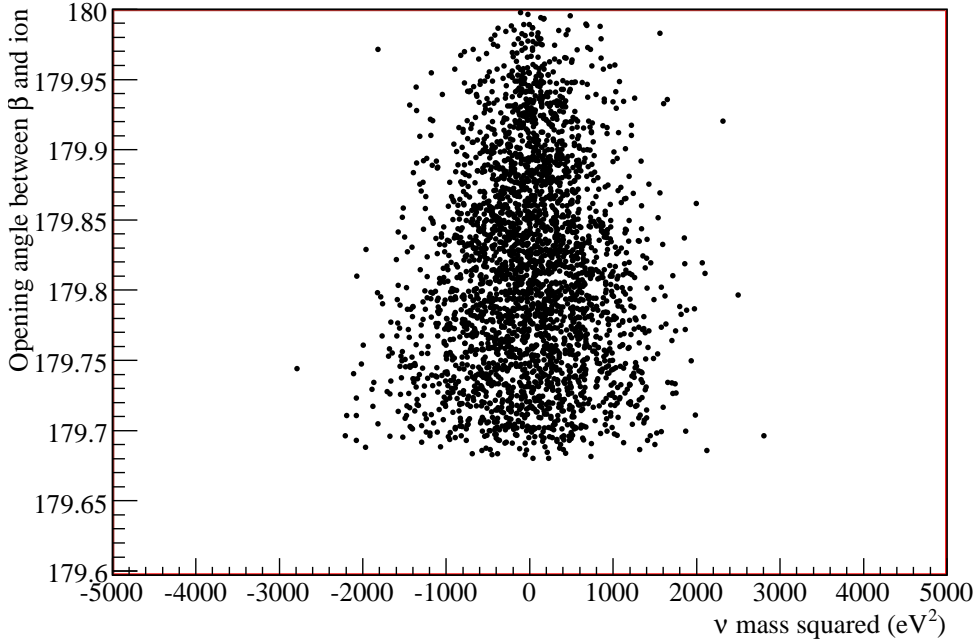


Figure 4.11: As the opening angle between the β and the ion increases, the uncertainty in the reconstructed neutrino mass increases dramatically.

Figure 4.12 illustrates one of the worst smearings in the neutrino mass reconstruction, and that is the initial tritium momentum. The colder the tritium can be initially, the better the neutrino mass can be reconstructed. Currently the simulation assumes a starting temperature of $1 \mu\text{K}$, but the possibility of creating a BEC of tritium at a temperature closer to a few nK might dramatically improve the prospects for this kind of experiment. While single-photon cooling might be capable of creating a tritium BEC, creating such a sample with sufficient statistics would be quite challenging.

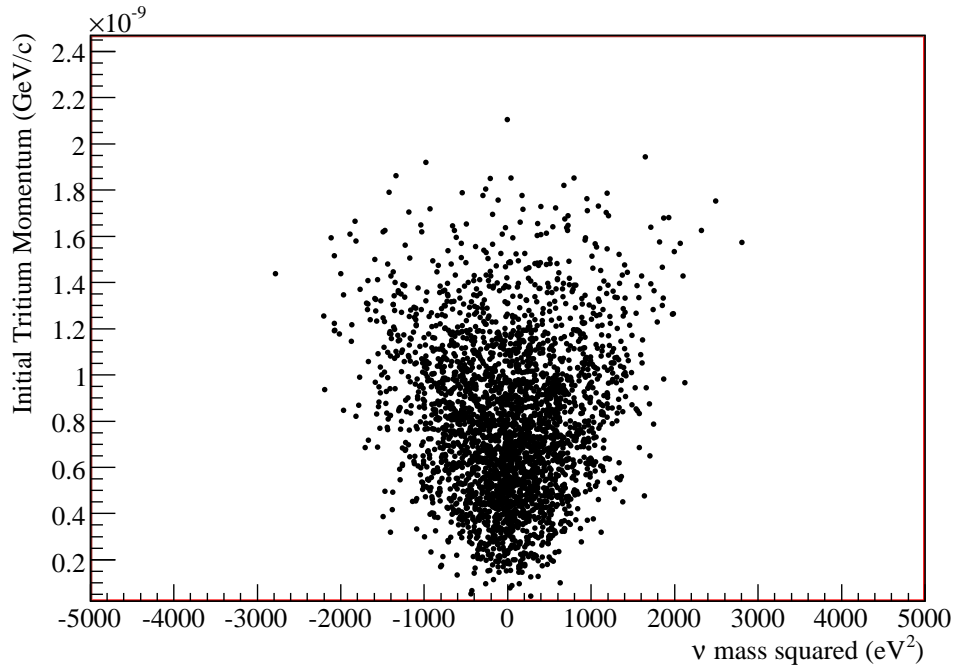


Figure 4.12: As the initial momentum of the tritium atom increases, the uncertainty in the reconstructed neutrino mass rapidly increases.

4.7.2 Two-Dimensional Fit for Neutrino Mass

Both the neutrino's reconstructed mass peak and the shape of its β -spectrum contain information about its mass. The β spectrum information obtained in this type of experiment is insufficient to set an interesting constraint on the neutrino mass, and fitting the neutrino mass squared peaks alone also falls far short of the power available in a fit that tries to fit both spectra simultaneously. In order to utilize all of the available information, I perform a maximum-likelihood fit using two-dimensional probability density functions (pdfs). These pdfs cannot be analytic since we have no way of knowing the expected shape of

the neutrino mass squared peak except through the simulation itself. I create a series of 2D pdfs using an order of magnitude more statistics than we use for our simulated data. Each of the six pdfs I create has a different assumed neutrino mass, and the assumed mass values are 4.0 eV apart. Figure 4.13 shows the 2D pdf for the case of zero neutrino mass. By interpolating between the pdfs, I find the most likely value for the neutrino mass for a particular data set. Since I do not have an analytical expression that depends on the neutrino mass, the only way to vary m_ν in performing the fit is to create separate pdfs that correspond to different values of m_ν , and the pdfs must be separated by a sufficient distance in m_ν to allow meaningful interpolation between them.

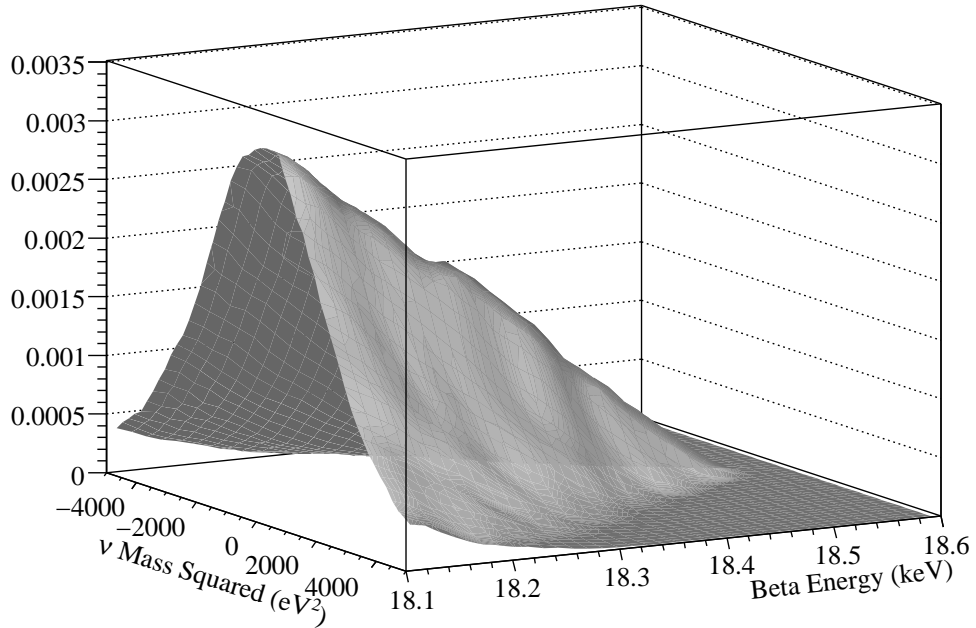


Figure 4.13: One of the six 2D probability distribution functions used in the fitting process. This sheet corresponds to a neutrino mass of 0.0 eV, and the data set was fit by interpolating between pdfs of different assumed neutrino mass.

To interpolate between the pdfs I simply utilized a spline fit. What was more difficult was interpolating on the two-dimensional pdf itself in order to evaluate the pdf for a given β energy and neutrino mass squared. To interpolate on the two-dimensional surface I used two different interpolation techniques, and I required the results of the neutrino mass fits from the two interpolation techniques to agree within the fit error. The first technique employed Delaunay triangulation, which is illustrated in Figure 4.14. Delaunay

triangulation for a set of \mathbf{P} points inside the plane is a triangulation such that no point in \mathbf{P} is inside the circumcircle of any triangle. Delaunay triangulation maximizes the minimum angle of all the angles in the triangles, so it tends to avoid skinny triangles. The Voronoi diagram, illustrated in Figure 4.15, is the partitioning of the plane into n convex polygons such that each polygon contains exactly one point, and every point in a given polygon is closer to its central point than to any other. Delaunay interpolation then uses a “nearest neighbor” calculation such as

$$G(x, y) = \sigma_{i=1}^n w_i f(x_i, y_i) \quad (4.16)$$

where $G(x, y)$ is the estimation at the point (x, y) , n is the number of nearest neighbors used for the interpolation, $f(x_i, y_i)$ is the observed value at (x_i, y_i) , and w_i is the weight associated with $f(x_i, y_i)$. Two points are considered neighbors if they lie on the same circumcircle, as shown in Figure 4.14. The weights are determined by the areas of the voronoi polygons, as opposed to the distance between points, which is utilized in the inverse distance weighting method.

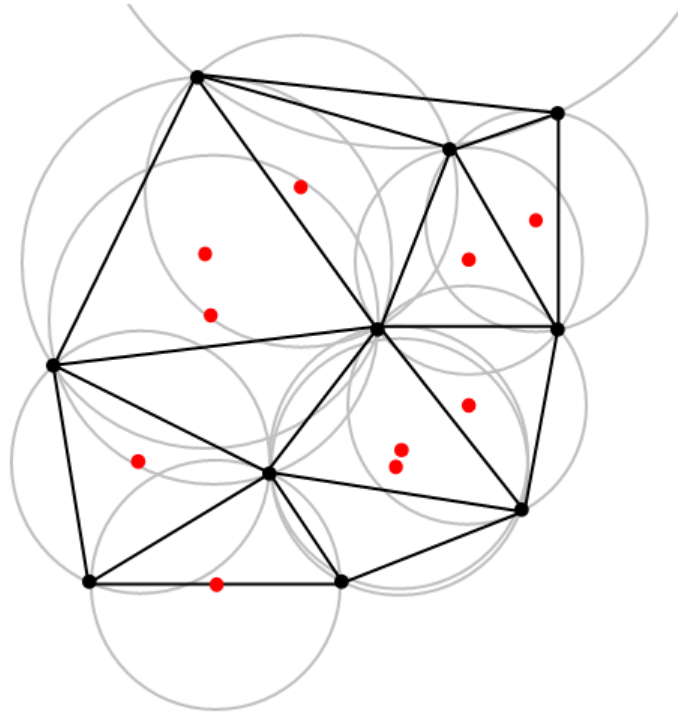


Figure 4.14: Delaunay triangulation for a set of \mathbf{P} points inside the plane is a triangulation such that no point in \mathbf{P} is inside the circumcircle of any triangle. Delaunay triangulation maximizes the minimum angle of all the angles in the triangles. Figure taken from http://en.wikipedia.org/wiki/Delaunay_triangulation

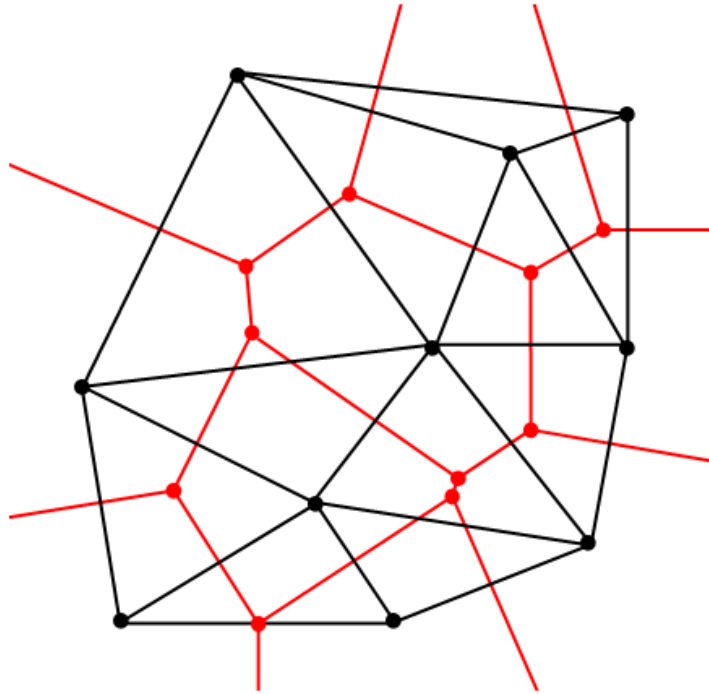


Figure 4.15: The Voronoi diagram is the partitioning of the plane shown in Figure 4.14 into n convex polygons such that each polygon contains exactly one point, and every point in a given polygon is closer to its central point than to any other. Figure taken from http://en.wikipedia.org/wiki/Delaunay_triangulation

This method would have become too computationally intensive if I had tried to apply Delaunay triangulation to each entire two-dimensional pdf every time I had to evaluate its value at a particular point, so I defined a small surface consisting of 11 bins in the x direction and 11 bins in the y direction over which I could apply Delaunay interpolation. The point whose value I was attempting to estimate was chosen to be in the center of this 121-point surface.

I still found that obtaining a good fit using Delaunay interpolation required a lot of time, so I began to rely on a faster interpolation technique. The method first applies a boundary-safe interpolation of the weights in one dimension at a particular value, followed by a second interpolation of the resulting array. The results of the fits from this technique agreed well with the results of the fits from the more complicated Delaunay triangulation, as shown in Table 4.1.

Assumed m_ν (eV)	Slow interpolation result (eV)	Fast interpolation result (eV)
0.2	0.268 $^{+0.153}_{-0.159}$	0.235 $^{+0.174}_{-0.141}$
0.4	0.506 $^{+0.188}_{-0.165}$	0.494 $^{+0.176}_{-0.163}$
1.0	0.781 $^{+0.271}_{-0.214}$	0.767 $^{+0.260}_{-0.202}$

Table 4.1: Fit results comparing Delaunay triangulation, which is computationally time-intensive, with a faster spline interpolation technique. Note that these results are not the final fit results discussed in section 4.7.4 because they were performed with an earlier version of the simulation, but they serve to illustrate the generally good agreement between the two interpolation techniques.

Because the pdfs needed to be high-statistics, I developed a method of creating higher statistics pdfs without increasing the required runtime significantly. For both the simulated data and the simulated pdfs I created ntuples with the decay information from TGenPhaseSpace, meaning that changing the detector specifications did not require recalculating the phase space and kinematic parameters for the decays. Since we ignore all events below 18 keV, most of the β spectrum events are below our region of interest and are not recorded.

Consequently I created high-statistics pdfs using the following procedure. I simulated an “unweighted” β spectrum for which the β is equally likely to emerge at any energy, and I created my ntuple of events using this spectrum. I also simulated a “true” β spectrum that accurately represented the likelihood of an electron emerging with an energy above 18 keV. For runs intended to simulate real data, the probability of my using any particular event from the ntuple was simply the ratio of the true spectrum to the unweighted spectrum. For runs intended to simulate pdfs I wanted the statistics to be higher, so the probability of my keeping an event from those ntuples was the spectrum ratios multiplied by a factor of 10. This procedure allowed me to create pdfs that had 10 times the statistics of my simulated data runs without unnecessarily wasting computational resources. I tested the procedure to ensure that the probability of an event being used was never greater than 1.

Unlike previous tritium β -decay experiments that utilize information only a few eV away from the endpoint, our fit extends back to 18.1 keV, a full 500 eV from the endpoint. The statistics gained by moving away from the endpoint substantially improve the precision on the neutrino mass even as the spread in reconstructed mass gets broader. Figure 4.16 shows how individual detector and reconstruction uncertainties contribute to broadening the reconstructed neutrino mass squared peak, especially the β momentum measurement and the initial ${}^3\text{H}$ temperature. These smearings create large uncertainties for each reconstructed event, but the uncertainty in the mean of the peak decreases with added statistics. Combining this neutrino mass peak information with the information from the beta spectrum fit allows for a sub-eV determination of the neutrino mass. Clearly, systematic shifts in the mean of the reconstructed mass spectrum would have to be controlled at a very high

level, but calibrations of the spectrometer using the conversion electron from ^{83m}Kr as well as information from the energy spectrum itself should allow us to mitigate these effects.

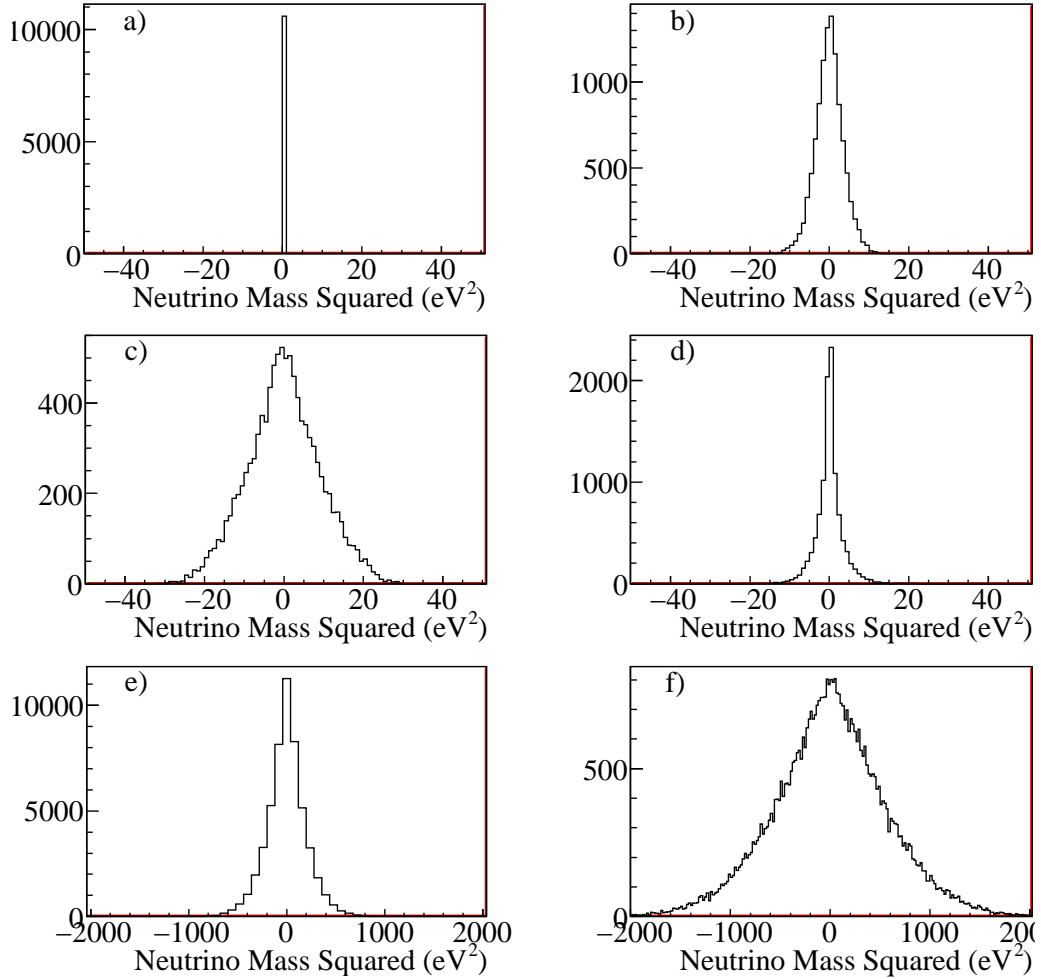


Figure 4.16: Reconstructed neutrino mass squared peak broadenings caused by various uncertainties and detector resolutions. a) All smearings turned off. b) β energy resolution. c) ^3He ion's MCP binning resolution. d) ^3He ion's MCP timing resolution. e) β momentum resolution. f) ^3H $1\mu\text{K}$ initial temperature.

4.7.3 Maximum Likelihood Fits

In fitting the simulated data to the probability density functions, I utilized the technique of maximum likelihood estimation (MLE). MLE tunes model parameters in order to make the observed data more likely than they would be with any other parameter values.

Suppose that there is a sample of n independent data observations, x_1, x_2, \dots, x_n , coming from an unknown distribution that depends on the model parameter θ . MLE attempts to find $\hat{\theta}$, an estimation of θ that is as close to the true value as possible. The joint density function for all of the observations can be written

$$f(x_1, x_2, \dots, x_n|\theta) = f(x_1|\theta) \cdot f(x_2|\theta) \cdots f(x_n|\theta) \quad (4.17)$$

If we assume that the observations x_1, x_2, \dots, x_n are fixed parameters of this function and we allow θ to vary freely, then we can write what is called the likelihood:

$$\mathcal{L}(\theta|x_1, x_2, \dots, x_n) = f(x_1, x_2, \dots, x_n|\theta) = \prod_{i=1}^n f(x_i|\theta) \quad (4.18)$$

Taking the log of the likelihood yields:

$$\Lambda = \ln \mathcal{L}(\theta|x_1, x_2, \dots, x_n) = \sum_{i=1}^n \ln f(x_i|\theta) \quad (4.19)$$

The average log-likelihood estimates the expected log-likelihood of a single

observation in the model, and it is written as:

$$\hat{l} = \frac{1}{n} \ln \mathcal{L} \quad (4.20)$$

The MLE method estimates the true value of θ by finding the value of θ that maximizes $\hat{l}(\theta|x)$. Obviously the estimated value of θ will be the same regardless of whether one maximizes the likelihood or the log-likelihood. As the sample size increases, the MLE method tends to a Gaussian distribution with a mean θ . Under fairly basic conditions the MLE method is consistent, meaning that as the sample size increases to a sufficiently large number n , the estimate of θ can become arbitrarily precise. Since the log-likelihood is generally much easier to manipulate, one tends to maximize Λ :

$$\frac{\partial \Lambda}{\partial \theta_j} = 0, j = 1, 2, \dots, k \quad (4.21)$$

where θ_j indicates that there could be more than one parameter whose value is being estimated. For practical reasons, one generally chooses to maximize the log-likelihood by minimizing the negative log-likelihood.

I perform the minimization using MINUIT, a physics analysis tool originally written in FORTRAN by Fred James [69]. The FORTRAN code has since been translated into C++ and is incorporated into CERN's distribution of ROOT. The minimization itself is performed with a variable-metric method with an inexact line search, a stable metric updating scheme, and the ability to check positive definiteness (since the covariance matrix of a physical function must be positive-definite at the minimum).

Standard errors from MINUIT account for correlations between parame-

ters, but they do not account for non-linearities. MINUIT contains a processor called MINOS that can correct for non-linearities, and its error intervals are generally asymmetric. All of the errors I quote with my fits were calculated using MINOS.

Figure 4.17 shows the negative log-likelihood space for the MINUIT minimization of the simulated data in which the neutrino mass was assumed to be 0.4 eV. The error is determined by the steepness of the log-likelihood parabola. The 68% confidence interval is defined by the point at which the parabola has risen to $\frac{1}{2}$ its maximum value. The smooth parabolic negative log-likelihood space lends confidence to the fit's ability to avoid false-minima and calculate errors accurately. Figure 4.18 shows a similar negative log-likelihood space for a significantly larger 5 eV neutrino mass.

Negative Log Likelihood

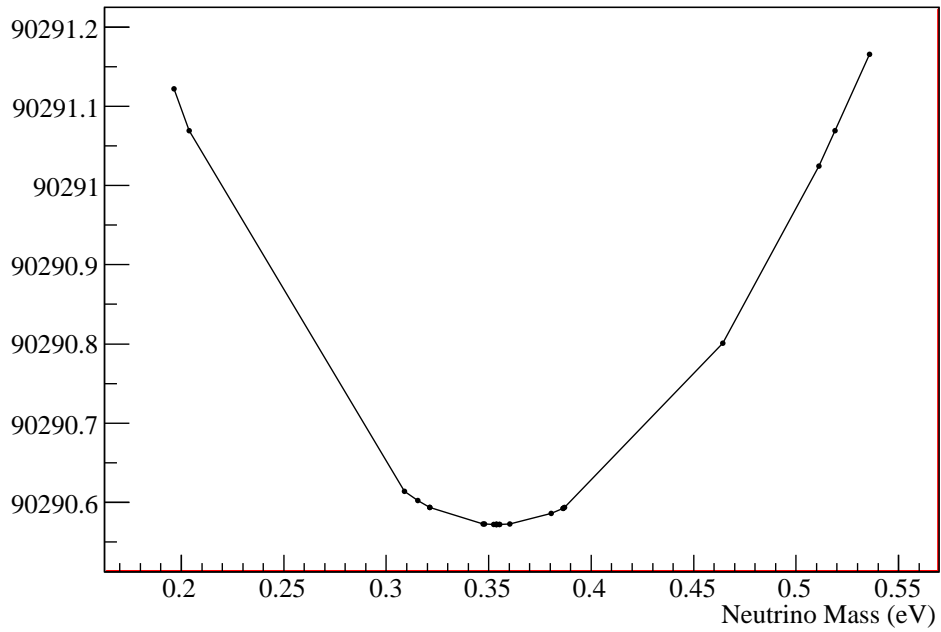


Figure 4.17: Negative log-likelihood space for the MINUIT fit of the data in which the neutrino mass was assumed to be 0.4 eV.

Negative Log Likelihood

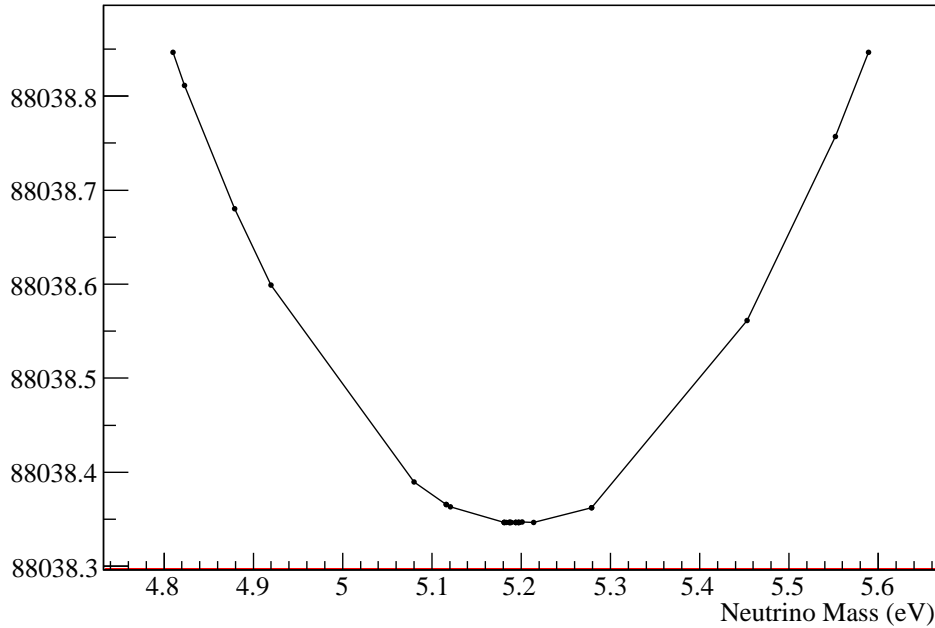


Figure 4.18: Negative log-likelihood space for the MINUIT fit of the data in which the neutrino mass was assumed to be 5.0 eV.

4.7.4 Fit Results and Number of Decays

In order to reach an m_ν limit comparable to KATRIN's, on the order of 10^{12} tritium decays would have to occur, which corresponds to trapping $\sim 2 \times 10^{13}$ tritium atoms as a source if the experimental live runtime is one year. That many atoms cannot be contained in a single $100 \mu\text{m}$ diameter trap, which cannot have a density exceeding 10^{15} atoms/cm³ without contributing significant scattering in the source. Any feasible experiment, therefore, will require an array of tritium traps spaced far enough apart to allow the fit reconstruction to accurately determine the decay origin. A third optical lattice

filled with Rydberg atoms could also be used to detect a track from the beta as it leaves the source, aiding in the reconstruction of where the decay occurred in the extended source. Tritium sources can be stacked by repeated launching and trapping. The primary limitation to the number that can be stacked is the trap lifetime. This trap lifetime can be on the order of 5-10 minutes using appropriate cryogenic cold fingers and careful bake-out of the chamber. We estimate that the necessary 10^{13} tritium atoms can be accumulated in this fashion.

Table 4.2 shows the results of the fit assuming 10^{12} tritium decays for six different assumed neutrino masses. The fit does quite a good job of finding the correct value of the neutrino mass that was assumed in the simulated data. Of course the same pdfs were used to find all of the results shown in Table 4.2, and the parameters for the fit were set uniformly for all of those datasets. In Section 4.7.5 I will discuss the stability of the fit results when those parameters are varied. The fit's ability to utilize both the reconstructed neutrino mass squared peak and the β spectrum information to accurately determine the neutrino mass is encouraging for this type of experiment.

One of the most helpful tests for determining whether or not a fit contains hidden bias is to examine the pull distribution. In this case the pull distribution is easily calculated since there is only one parameter being fit and we know what the correct value of the parameter ought to be for each simulated data set. We calculate the pull for each simulated data set as:

$$\text{Pull}(m_i) = \frac{m_i - m_{\text{true}}}{\sigma_{m_i}} \quad (4.22)$$

where m_i is the fit value returned for the neutrino mass, m_{true} is the assumed

value of the neutrino mass in the simulation, and σ_{m_i} is the average error returned by MINOS for the fit results. (I calculated the pull with the average error since the MINOS errors were approximately symmetric). The distribution of the pulls for many fits should tend toward a normal distribution with a mean of zero and a width of one. A normally distributed pull indicates that if the experiment were repeated many times, the error bars on the fit correctly predict the variation that would be observed. If the log-likelihood space is not sufficiently parabolic, then the pull distribution can be greater than one, indicating that the error estimation on the fit results is not accurate. If the fit includes multiple parameters with constraints placed on highly correlated parameters, one can also obtain pull distributions with a width less than one. Figure 4.19 shows the pull distribution of the fit results shown in Table 4.2, and its shape is consistent with a normal Gaussian. Figure 4.20 indicates how the size of the fit uncertainties increases as the number of tritium decays decreases.

Assumed m_ν	Fit m_ν	(+)error	(-)error
0.2	0.239	0.174	0.153
0.4	0.354	0.166	0.150
0.6	0.690	0.270	0.203
0.8	0.794	0.247	0.215
1.0	0.813	0.246	0.207
5.0	5.188	0.402	0.378

Table 4.2: MINUIT fit results and MINOS errors for simulated data runs which had different assumed neutrino masses.

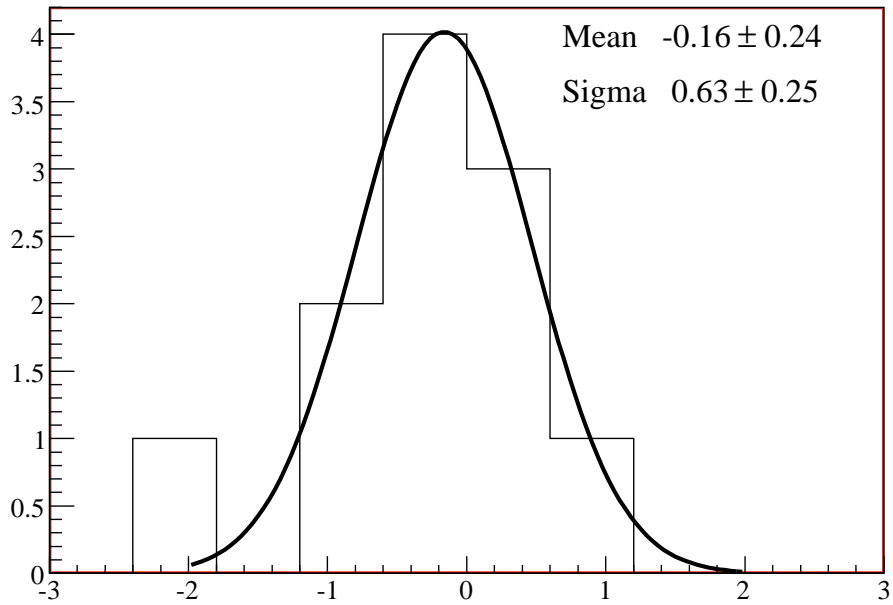


Figure 4.19: Pull distribution comparing the fit results shown in Table 4.2 to the neutrino mass that was assumed in the various simulation trials.

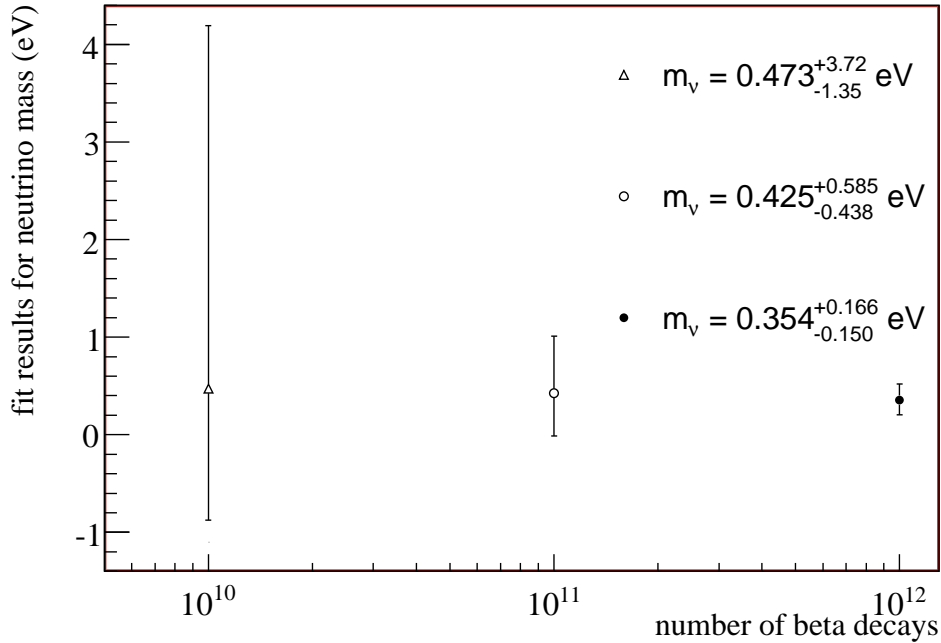


Figure 4.20: MINUIT fit results and MINOS errors from simulated data runs in which the neutrino mass was 0.4 eV.

Figures 4.21 and 4.22 show an example of the two dimensional fit results. These are projections of the fit compared with the simulated data when the neutrino mass was assumed to be 0.2 eV and the best fit value was $0.239^{+0.174}_{-0.153}$ eV. The one-dimensional projections, however, do not clearly convey the potential accuracy of the fit since much of the fit's power comes from the simultaneous two-dimensional utilization of information.

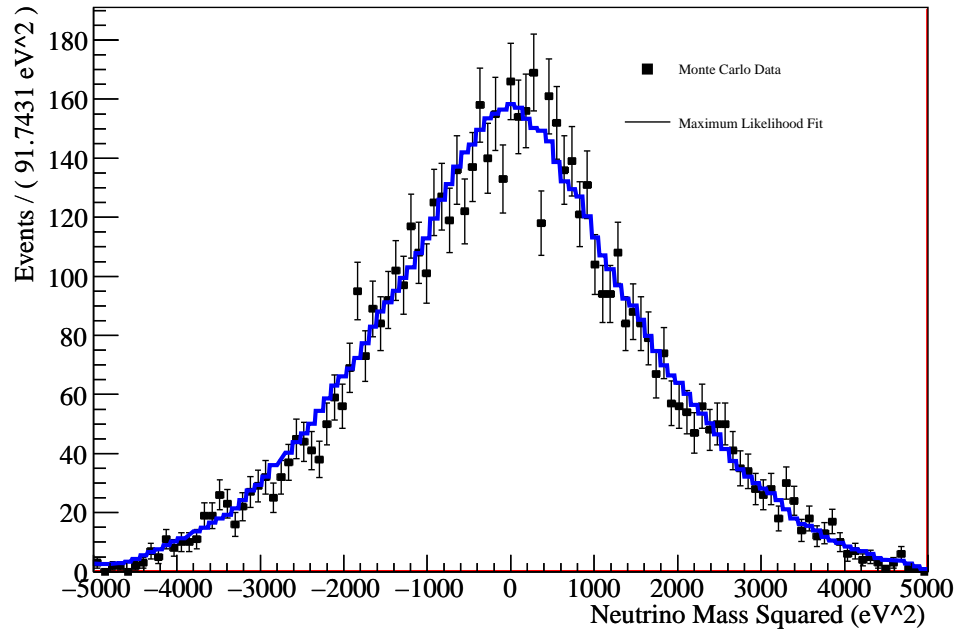


Figure 4.21: Maximum likelihood fit to the simulated $m_\nu=0.2$ eV data projected in m_ν^2

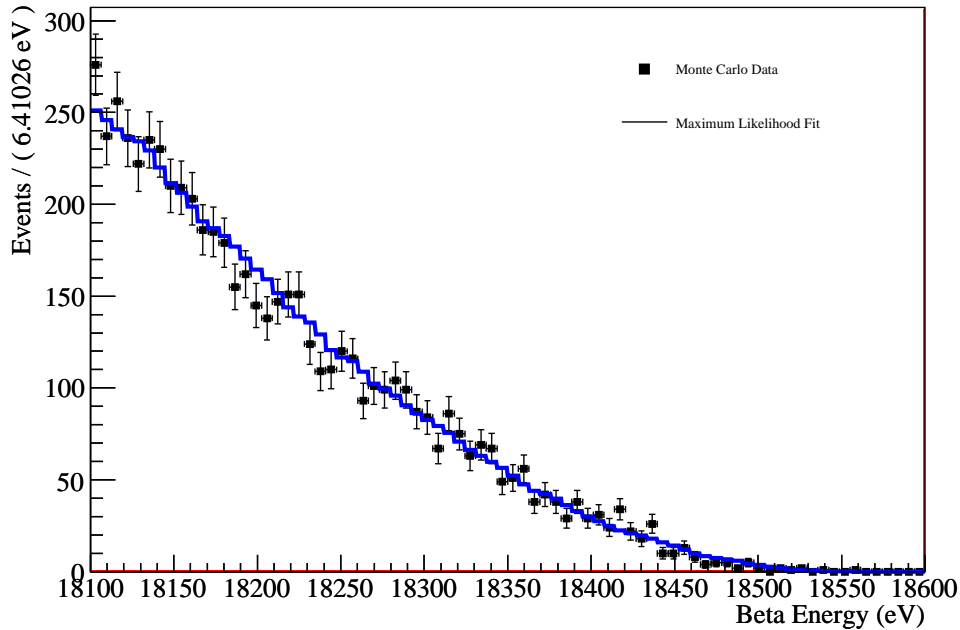


Figure 4.22: Maximum likelihood fit to the simulated $m_\nu=0.2$ eV data projected in β energy

4.7.5 Tests of the 2D Fit

One of the checks that I performed to test the two-dimensional fit was to perform the fit in energy slices. I only allowed the fit to see a 150 keV portion of the full β spectrum, and Table 4.3 summarizes those results. I chose 150 keV in order to allow the fit to have enough statistics in each slice to produce stable results. The fit performs well in each energy slice, finding the correct neutrino mass within the quoted minos errors. The error bars are not drastically larger for this limited energy slice fit than for the full fit, summarized in Table 4.2. This highlights the fact that our fit is not determined by the highest energy

events near the endpoint; we are obtaining meaningful information even out to 18.1 keV. The cutoff of 18.1 keV could be further investigated in order to determine if one could gain interesting information from events whose β energy is even lower.

Assumed m_ν	Energy slice (keV)	Fit m_ν	(+)error	(-)error
0.2	18.1-18.25	0.180	0.239	0.170
0.2	18.25-18.4	0.359	0.314	0.252
0.2	18.4-18.55	7.7E-6	0.227	0.227
1.0	18.1-18.25	0.482	0.302	0.256
1.0	18.25-18.4	1.131	0.326	0.298
1.0	18.4-18.55	0.433	0.656	0.0

Table 4.3: MINUIT fit results and MINOS errors for simulated data runs. Each fit was limited to a 150 keV slice of the β spectrum.

Similarly we can perform the two-dimensional fit on neutrino mass squared slices, where only a limited portion of the neutrino mass squared peak can be utilized. The results are shown in Table 4.4. The fit behaves as expected for the negative values of the neutrino mass squared, but for the slices in which the neutrino mass squared is positive, the fit does not perform well and tends to return the upper limit of the neutrino mass. Almost all of the information, therefore, is contained in the negative neutrino mass squared events. We have examined many kinematic considerations, and we conclude that the events that reconstruct with negative neutrino mass are not more likely to have had a large opening angle, a low temperature, or any other kinematic advantage. The advantage is most likely related to the asymmetry that

appears in the probability density functions as the neutrino mass increases.

Assumed m_ν	m_ν^2 slice (eV ²)	Fit m_ν	(+)error	(-)error
0.2	-5000 - 0.0	0.163	0.177	0.147
0.2	-5000 - (-1000)	0.480	0.262	0.214
0.2	-5000 - (-3000)	9.3E-7	0.286	0.0
0.2	-3000 - 0.0	0.241	0.200	0.184
0.4	-5000 - 0.0	0.510	0.213	0.197

Table 4.4: MINUIT fit results and MINOS errors for simulated data runs. Each fit was limited to a particular slice of the neutrino mass squared peak.

I also tested the stability of the fit by varying parameters like the starting value that I gave MINUIT for the neutrino mass. Table 4.5 shows how stable the fit remained for a wide variety of starting values, which lends confidence that the fit is finding a true minimum in the log-likelihood space as opposed to merely a local minimum. The fit even performed well when the starting value was negative.

Starting value (eV)	Fit value	(+)error	(-)error
0.0	0.23943	0.174	0.153
0.25	0.23902	0.174	0.153
0.5	0.23930	0.174	0.153
0.75	0.23946	0.174	0.153
1.0	0.23926	0.174	0.153
-1.0	0.23941	0.174	0.153

Table 4.5: MINUIT fit results and MINOS errors for the simulated data run $m_\nu=0.2$ eV. Each fit was done with a different assumed starting value, and the fit results did not depend on the initial starting value.

The fit result also did not depend on the range over which I allowed the neutrino mass parameter to vary. Table 4.6 shows the results of several fits over which the neutrino mass parameter was constrained differently, and the results are essentially independent of the allowed range.

Allowed fit range (eV)	Fit value	(+)error	(-)error
-5.0 to 5.0	0.23930	0.174	0.153
-10 to 10	0.23982	0.173	0.153
-20 to 20	0.23984	0.173	0.153
0.0 to 5.0	0.23992	0.173	0.153

Table 4.6: MINUIT fit results and MINOS errors for the simulated data run $m_\nu=0.2$ eV. Each fit was done with a different allowed range for m_ν , and the fit results did not depend on the allowed range.

In considering the stability of the fit, I also varied how the data was binned. Table 4.7 illustrates how changing the binning does not significantly affect the central value returned by the fit, but it does alter the MINOS error calculation somewhat, which is to be expected. Table 4.7 shows four different binning combinations for both the 0.2 eV and 1.0 eV cases.

m_ν (eV)	Size of m_ν^2 bins (eV^2)	Size of E_β bins (eV)	Fit results	(+)error	(-)error
0.2	100	2	0.313	0.131	0.122
0.2	100	4	0.221	0.167	0.163
0.2	200	2	0.243	0.173	0.156
0.2	200	4	0.076	0.269	0.195
1.0	100	2	0.820	0.180	0.172
1.0	100	4	0.786	0.264	0.209
1.0	200	2	0.816	0.277	0.209
1.0	200	4	1.072	0.506	0.340

Table 4.7: MINUIT fit results and MINOS errors for simulated data runs. Each fit was done with a different binning of the data, and the fit performed well for a wide variety of binnings

4.8 Future Prospects

These simulation results illustrate what would actually be required in order to kinematically reconstruct the neutrino mass, and admittedly the experiment would be difficult to construct. My work defines the detector requirements that would be necessary in order to pursue such an effort. From an R&D perspective, the most important intermediate development project would be

building prototypes of the Rydberg atom optical lattices, which could be valuable even apart from this particular experiment. Other significant R&D efforts would include designing a specialized hemispherical analyzer, as well as improving MCP timing and resolution, which is already being actively pursued since many experiments would benefit from better MCPs.

The most discouraging aspect of such an experiment is the large number of atomic sources that currently appear to be required. I believe the most promising direction for improving the outlook for a neutrino mass reconstruction experiment like this one is in lowering the source temperature. Since the source temperature is by far the most dominant smearing, if techniques like single-photon atomic cooling progress to the point of being able to create a BEC of tritium, an experiment like this could become significantly easier. I would recommend that future investigations of neutrino mass reconstruction should explore the neutrino mass limits that would be possible with significantly colder sources.

Ultimately the kinematic reconstruction of the neutrino mass could have the potential to establish an interesting limit. While KATRIN represents the largest possible tritium endpoint experiment of its kind, this approach is scalable and offers a measurement free of model dependencies. Although several engineering challenges remain, a kinematic reconstruction experiment could provide an independent and complementary method of measuring the neutrino mass.

Chapter 5

Separating Isotopes to Measure Neutrino Mass

While neutrinoless double β decay experiments are primarily focused on determining whether neutrinos are Majorana or Dirac particles, they also provide an avenue through which to investigate the absolute mass scale of neutrinos. This chapter begins by describing SNO+, a double β decay experiment that could benefit from acquiring tens of kilograms of highly enriched ^{150}Nd . I summarize the strengths and weaknesses of current methods of isotope separation before introducing the basic principles of a new method of isotope separation that we developed known as single-photon atomic sorting. This chapter outlines the development of this method, beginning with several implementations in Section 5.4 that are feasible but unnecessarily expensive to construct. In Section 5.5 I describe an improved design for single-photon atomic sorting that is inexpensive, scalable, and generally applicable to almost the entire periodic table. I conclude by discussing a demonstration experiment currently under

construction for ${}^6\text{Li}$ as well as exploring how this technique could be applied specifically to ${}^{150}\text{Nd}$.

5.1 Neutrinoless Double Beta Decay

Measurement of the lifetime of neutrinoless double β decay would determine the Dirac or Majorana nature of neutrinos and could also provide insight into the absolute mass scale of neutrinos, as discussed in detail in Chapter 2. Only a handful of elements have isotopes that undergo double β decay. While some experiments can search for neutrinoless double β decay using only the natural abundance of the isotope of interest, many experiments would gain a distinct advantage from working with isotopically enriched samples. Current techniques for isotope separation have significant limitations discussed in detail in Section 5.3, meaning that a new inexpensive and scalable method of isotope separation could have a meaningful impact in neutrino physics, as well as in other fields such as medicine, energy, basic research, and defense.

Table 5.1 summarizes data for the nuclei that have relatively high energies for double β decay. Since neutrinoless double β decay has never been observed, the 0ν lifetimes are all calculated and should be considered uncertain by approximately a factor of 2 because of uncertainties in calculating the nuclear matrix elements. Table 5.1 also shows the ratio of 2ν to 0ν rates because the tail of the 2ν double β decay process is a background for the 0ν process. Several nuclei stand out as being promising: ${}^{48}\text{Ca}$ has the highest energy, ${}^{150}\text{Nd}$ has the highest 0ν decay rate, and ${}^{130}\text{Te}$ has a very favorable natural abundance [70]. Although the ${}^{130}\text{Te}$ and ${}^{136}\text{Xe}$ 2ν rates look very favorable, these are the two cases for which recent, clear 2ν measurements are

missing.

Isotope	Energy (MeV)	2ν $T_{1/2}$ (yr)	$0\nu T_{1/2} \cdot m_\nu^2$ (yr eV ²)	$2\nu/0\nu$ Rates Ratio	Abundance (%)
⁴⁸ Ca	4.27	4×10^{19}	3×10^{24}	7.5×10^4	0.19
¹⁵⁰ Nd	3.37	7×10^{18}	3×10^{22}	4×10^3	5.6
⁹⁶ Zr	3.35	2×10^{19}	5×10^{23}	2.5×10^4	2.8
¹⁰⁰ Mo	3.03	8×10^{18}	1×10^{24}	1.3×10^5	9.6
⁸² Se	3.00	9×10^{19}	6×10^{23}	7×10^3	9.2
¹¹⁶ Cd	2.80	3×10^{19}	5×10^{23}	1.7×10^4	7.5
¹³⁰ Te	2.53	3×10^{21} G	5×10^{23}	1.7×10^2	34.5
¹³⁶ Xe	2.48	5×10^{21} C	2×10^{24}	4×10^2	8.9
⁷⁶ Ge	2.04	1×10^{21}	2×10^{24}	2×10^3	7.8

Table 5.1: High energy double β decay emitters [70]. G indicates a value determined by geochemical measurement, and C indicates a value calculated rather than measured.

In considering which double β decay emitters would be ideal to focus on separating isotopically, one must consider not only the basic information given in Table 5.1 but also how one would eliminate other potential background signals. Internal radioactivity inside the detector is problematic since the detector functions much like a calorimeter, recording the total energy of $\beta - \gamma$ decays. The thorium chain activity (particularly the daughter ²⁰⁸Tl) has an endpoint ~ 5 MeV, which implies that this background will have to be carefully controlled.

External radioactivity can create problematic backgrounds from gam-

mas whose energies are similar to the energy of the signal. Of particular concern is the 2.6 MeV gamma from ^{208}Tl , which is in the thorium chain. As shown in Table 5.1, ^{136}Xe and ^{130}Te both have energies such that this 2.6 MeV gamma would be a problem. ^{150}Nd has a high Q-value of 3.37 MeV, meaning that the 2.6 MeV external gamma is not a concern, and its phase space is relatively large. The calculation of the neutrino mass from the half-life of neutrinoless double β decay depends on the phase space involved and the nuclear matrix element:

$$[T_{1/2}^{0\nu}]^{-1} = G^{0\nu} |M^{0\nu}|^2 |\langle m_\nu \rangle|^2 \quad (5.1)$$

where $G^{0\nu}$ is the calculable phase space integral, $|M^{0\nu}|^2$ is the nuclear matrix element, and $\langle m_\nu \rangle$ is a linear combination of the neutrino masses, as discussed in Chapter 2. ^{150}Nd is a large atom, strongly deformed compared to the ideal spherical nuclei for which nuclear matrix element calculations are typically performed. Uncertainties in how to include the deformation effects are more significant for larger atoms, which is a drawback for ^{150}Nd . Nonetheless its high energy endpoint and 5.6% natural abundance make it a very strong candidate for a neutrinoless double β decay search.

5.2 SNO+

The Sudbury Neutrino Observatory (SNO) has finished taking data, but a large amount of the experimental equipment is being re-used for a follow-up experiment called SNO+. One of the primary physics goals of SNO+ is to utilize a large amount of ^{150}Nd for a double β decay experiment. The acrylic vessel used in SNO is capable of holding ~ 1000 tonnes of liquid, and it is

placed in a very low-background environment at a depth of ~ 6000 m water equivalent in the Inco., Ltd. Creighton mine near Sudbury, Ontario, Canada. The vessel is observed by photo-multiplier tubes (PMTs), and their effective volume coverage is approximately 60%. More details concerning the SNO detector are discussed in Section 6.1.2.

For the SNO+ experiment the acrylic vessel will be filled with liquid scintillator, an organic material similar to mineral oil that emits light when charged particles interact with it. Liquid scintillator emits ~ 50 times more light than the heavy water utilized by SNO, meaning that SNO+ will be able to detect lower energy events than SNO could and will have an energy threshold of 200-500 keV. Figure 5.1 shows the predicted solar neutrino flux as a function of energy, which includes several solar reactions that can be studied well with SNO+'s low energy threshold. The liquid scintillator will involve interactions with protons rather than deuterons, which will enable the detection of electron antineutrinos from the earth (geo-neutrinos), as well as electron antineutrinos from distant nuclear power reactors. SNO+ will be able to detect supernovae explosions utilizing both charged current (CC) and neutral current (NC) reactions on protons and carbon. Most significantly, ^{150}Nd could be added to the liquid scintillator, allowing SNO+ to make a measurement of the half-life of neutrinoless double β decay.

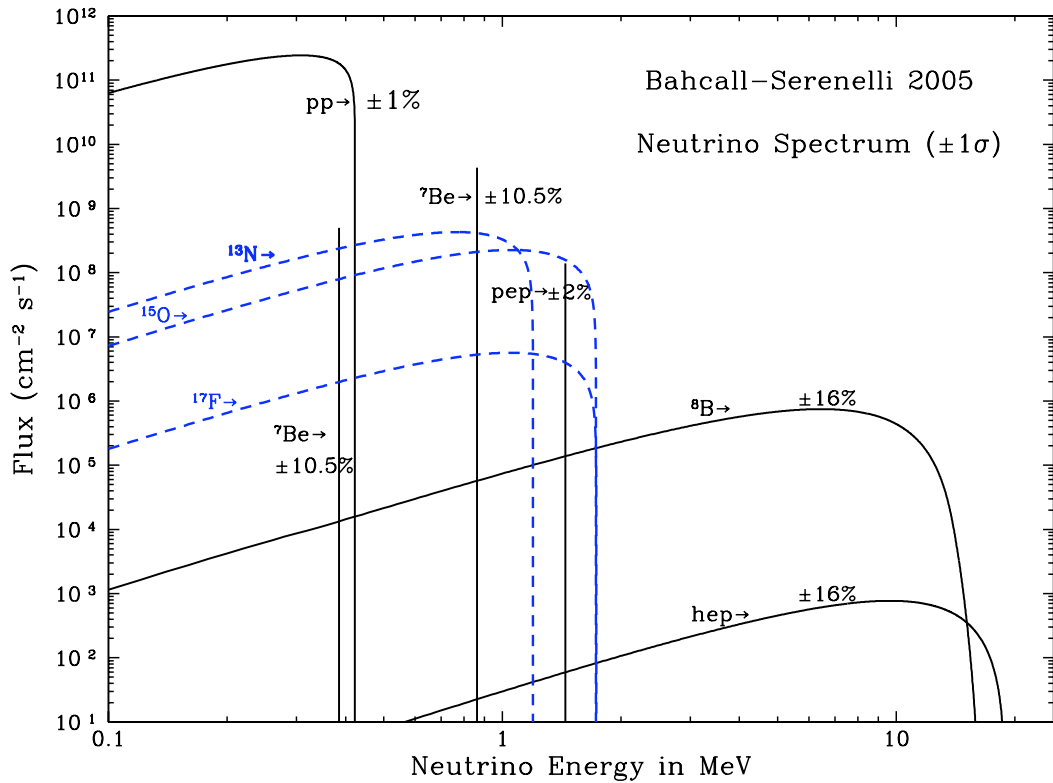


Figure 5.1: Predicted solar neutrino flux vs. energy. SNO's energy threshold gave it sensitivity to neutrinos produced in both the *hep* and ^8B chains, while SNO+ will have a much lower threshold of 200-500 keV that will allow it to observe many solar neutrinos that SNO could not have seen. Figure taken from [71].

5.2.1 Neodymium-Loaded Liquid Scintillator

Neodymium can be dissolved in an organic solvent by reacting with a carboxylic acid [72]. In the range of 370-415 nm the light attenuation length within SNO+ would be several meters, enabling scintillation light to propagate through the Nd-loaded liquid and be detected by PMTs. SNO+ intends to utilize linear alkylbenzene as its scintillating solvent because of its optical properties, purity, and low cost. A 1% Nd-loading would correspond to 560 kg of neodymium, and such a scintillator has been successfully produced in the laboratory. Figure 5.2 shows simulation results of what SNO+ would expect to measure after one year of data-taking assuming 1% natural Nd-loading and assuming a Majorana neutrino mass of 0.15 eV.

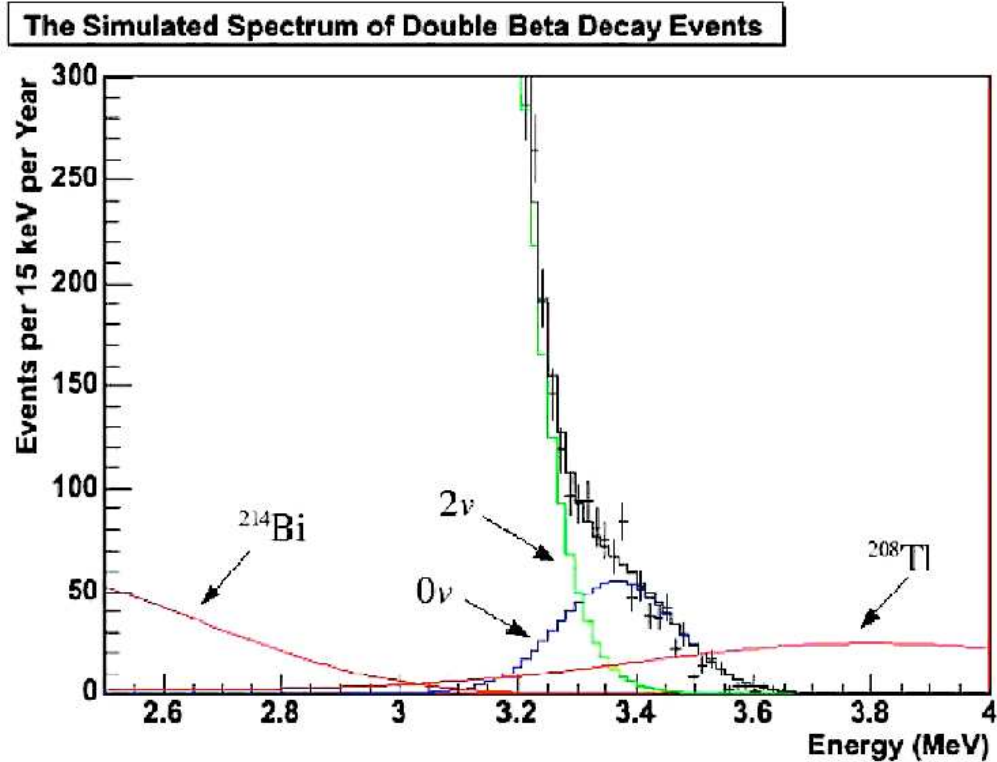


Figure 5.2: Simulation of one year of data taking with 1% Nd-loading, assuming a Majorana neutrino mass of 0.15 eV. Due to the energy resolution the signal appears as a kink at the end of the spectrum rather than a peak. The tail of the $2\nu\beta\beta$ -decay spectrum of ^{150}Nd is shown, as well as two potential background components from natural decay chains. Figure taken from [72]

5.2.2 Expected Sensitivity

The simulated light absorption for the 1% natural Nd-loaded scintillator discussed above is 47 ± 6 photoelectrons/MeV [72], which leads to rather poor energy resolution. For 0.1% Nd-loaded scintillator, simulations predict 400 ± 21

photoelectrons/MeV, which the SNO+ collaboration has determined is good enough to motivate an experiment. Even an experiment with 0.1% natural Nd in 1000 tons of scintillator would provide 56 kg of ^{150}Nd , which would be enough to detect a Majorana neutrino mass at the 0.15 eV level [34], though a much more sensitive experiment would be enabled by enrichment of ^{150}Nd .

Figure 5.3 shows the light output as a function of the Nd-concentration of the scintillator, and the benefits of Nd enrichment are readily apparent. As the Nd-concentration increases, the light output and therefore the energy resolution of the experiment worsens significantly. Enriching tens of kilograms of Nd is quite challenging given current isotope separation techniques. A new method of large-scale isotope separation that would apply to almost any element on the periodic table would enable SNO+ to acquire the 50-100 kg of ^{150}Nd that they need to optimize their experiment.

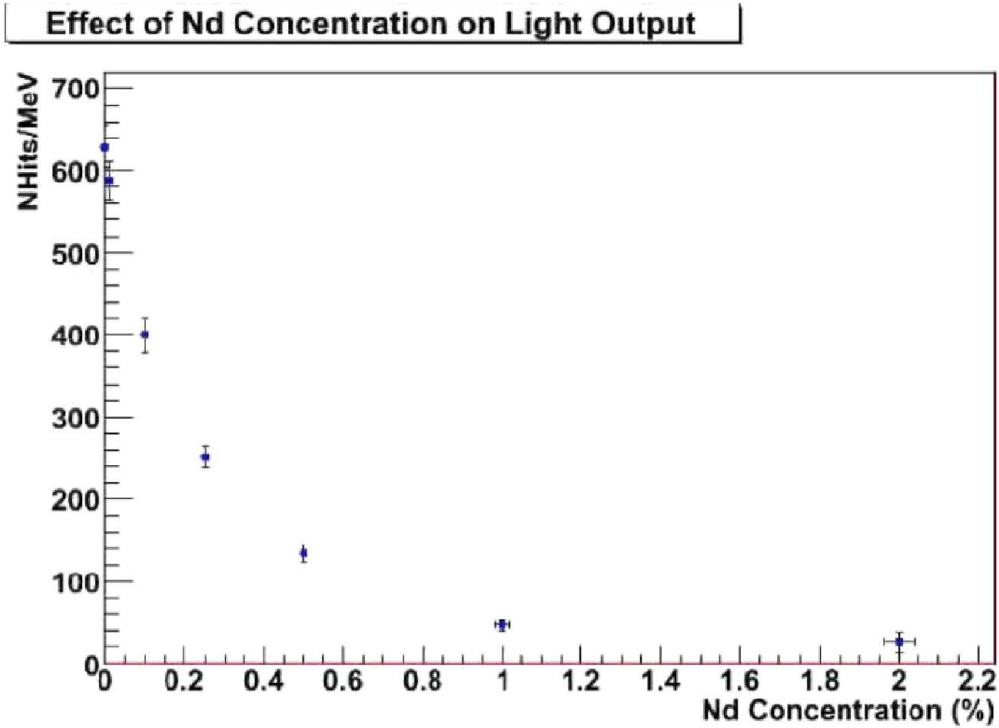


Figure 5.3: Simulated light output, given in the number of hit PMTs (NHIT) per MeV as a function of Nd-loading. Going to smaller Nd-loadings results in large improvements in light output, and therefore in energy resolution. Figure taken from [72]

5.3 Established Methods of Isotope Separation

The long standing efforts to separate isotopes date back to the 1930's and fall into several categories. Two standard methods of separation are gaseous

diffusion and the ultra-centrifuge [73, 74, 75]. These methods require many stages of enrichment and are very inefficient. Furthermore, these methods are only suitable for a few elements that can be kept in gas phase, which is a common limitation of isotope separation schemes [76].

Gaseous centrifuges utilize centripetal acceleration to separate molecules according to their mass. A cylinder containing the isotopically mixed gaseous compound is rotated, and the heavier molecules move toward the outer wall, while the lighter ones remain close to the center. One popular centrifuge design applies a thermal gradient in the perpendicular direction, which creates a convection current that carries the lighter molecules to the top of the centrifuge. Centrifuges typically operate in a continuous cascade, allowing the sample to become more and more isotopically pure with each successive stage. Centrifuges are a very economic way of separating isotopes, and they are used primarily for separating ^{235}U from ^{238}U using the quite dangerous compound uranium hexafluoride UF_6 . UF_6 is solid at room temperature, but it is easily vaporized. While it is a stable compound, it is corrosive to most metals and readily reacts with water to form hydrofluoric acid. Despite the difficulties inherent in working with UF_6 , it is the only compound of uranium sufficiently volatile to use in a centrifuge, and since fluorine consists of only one isotope, the difference in molecular weights comes only from the different uranium isotopes. Unfortunately many elements, such as neodymium, do not have a gaseous compound suitable for separation in a centrifuge.

Gaseous diffusion predates the centrifuge, and it also utilizes a stable gaseous compound for isotope separation. The process relies on the fact that particles in a closed box will have on average the same energy. Lighter particles, therefore, will be moving on average at a slightly faster velocity. If the

box contains a semi-permeable membrane, then more of the lighter molecules will escape than the heavier molecules. Like the centrifuge, gaseous diffusion must operate in cascades, often with thousands of stages, in order to achieve meaningful enrichment. The gas must be compressed at each stage because of pressure loss across the diffuser, and the compression leads to heating, meaning the gas must then be cooled before entering the next stage of diffusion. The energy requirements for the cooling and pumping make gaseous diffusion plants very expensive.

Both centrifuges and gaseous diffusion share a common drawback, which is that they require a stable gaseous compound with an element such as fluorine that has only one isotope. One device that overcomes this drawback and is capable of separating almost any element on the periodic table is the calutron, which relies on mass spectrometry [77, 78]. In a calutron high energy electrons bombard a vaporized sample, creating positively charged ions which are then accelerated and deflected by magnetic fields. The magnetic fields bend the heavier ions less, allowing for collection of the desired isotope. This method has high isotopic selectivity due to the use of a quadrupole mass filter, but it is very inefficient due to the low probability of electron-bombardment ionization, and it is limited by space-charge. Although only extremely limited quantities can be collected in a calutron, Figure 5.4 shows the number of elements whose isotopes are still produced today for commercial sale using calutrons. The limitations of centrifuges are evident in Figure 5.4 in that more isotopes for commercial sale are produced in calutrons than by all other methods combined, even though the calutron is extremely inefficient in its energy use and can produce only very small quantities. The majority of calutron plants operating in the world today are located in Russia, and given the increasing applications

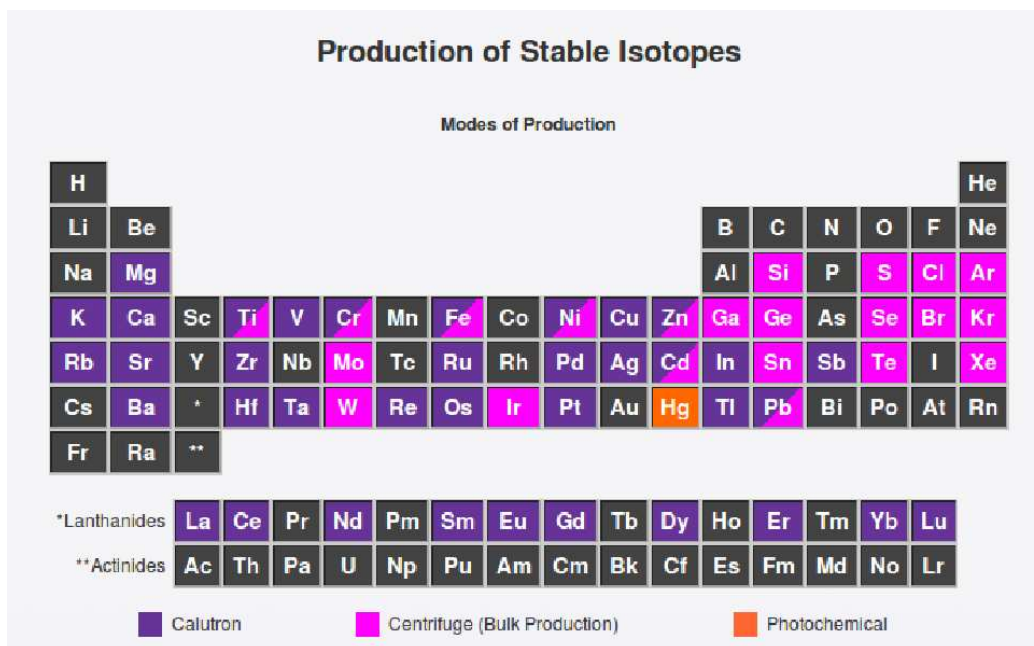


Figure 5.4: Although centrifuges are very efficient, most isotopes cannot be separated in centrifuges. The majority of isotopes available for commercial sale are produced using calutrons. Figure taken from Trace Sciences International, www.tracesciences.com

of isotopes in medical research and diagnosis, the United States may have a vested political interest in developing isotope separation methods that are implemented by American companies [79].

In recent years, the method of isotope separation by laser ionization has been developed [80]. This approach is highly selective but requires multiple (typically three) high-powered lasers for efficient ionization. One implementation of laser isotope separation is known as AVLIS (atomic vapor laser isotope separation). Utilizing the different laser excitation energies for various isotopes, AVLIS selectively ionizes only the isotopes of interest, and then utilizes electromagnetic fields to deflect those desired isotopes for collection. In ad-

dition to requiring multiple lasers for ionization, the production rate is also limited by resonant charge exchange. Although AVLIS could theoretically be applied to enrich neodymium, no AVLIS facilities will be available to the SNO+ collaboration. Another related method is called MLIS (molecular laser isotope separation). While AVLIS works with vaporized uranium, MLIS utilizes UF_6 , which it irradiates with an infrared laser, followed by a second laser that is either infrared or ultraviolet, which preferentially excites the $^{235}\text{UF}_6$. The second laser breaks the hexafluoride into fluorine and a pentafluoride, which forms a solid and is filtered out of the UF_6 gas. MLIS must be operated in a cascade mode to achieve sufficient enrichment. AVLIS and MLIS are focused primarily on enriching uranium, and they are difficult to apply in general to the entire periodic table.

The cost of producing isotopically pure samples is currently extremely high. For example, high-purity ^{43}Ca , which is used in medical research, costs a staggering \$400,000 per gram. Even those isotopes that are less exotic tend to possess only-slightly-less-shocking price tags of \sim \$20,000 per gram. As isotope use continues to increase, especially in medical research, the need for a less expensive method of production also increases, and if the price of isotopically pure samples were more reasonable, their applications would almost certainly multiply.

5.4 Introduction to Single Photon Atomic Sorting

Given that a new general technique for isotope separation could be beneficial not only to neutrino experiments but also in many diverse areas of physics and medicine, we have developed a new method for separating isotopes called single photon atomic sorting. This section describes the basic principles of single photon atomic sorting, using simulations of simplistic magnetic gradients that would require potentially complex superconducting magnets to construct. Section 5.5 introduces simulations of magnetic gradients that could be more easily and inexpensively constructed in a laboratory or industrial setting. Although all of the implementations of single photon atomic sorting discussed could be realistically constructed, we believe the implementation discussed in Section 5.5 is the most economically efficient.

We start with a generic prototype for isotope separation: a collimated atomic beam of a single element, composed of multiple isotopes. The key question is how to pick out the desired isotope from the beam. To be more specific, we consider a three-level atom with an initial ground state $|i\rangle$, an electronic excited state $|e\rangle$, and a final (metastable) state $|f\rangle$, as illustrated in Figure 5.5.

We further assume that the magnetic moment of state $|i\rangle$, m_i , is different than the magnetic moment of state $|f\rangle$, m_f . Now suppose that an atom crosses a laser beam which induces an irreversible transition from state $|i\rangle$ to state $|f\rangle$ by absorption followed by spontaneous emission. The atom then passes through a magnetic gradient $\nabla B(x)$, as shown in Figure 5.6, and experiences a deflection that is proportional to the ratio of mass-to-magnetic

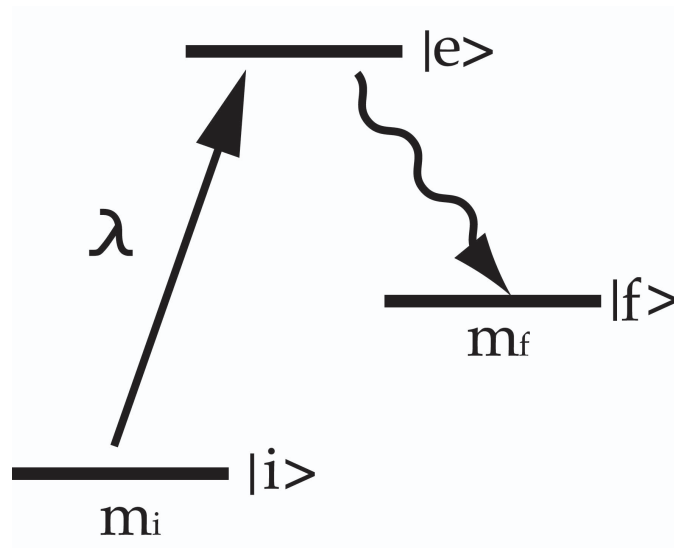


Figure 5.5: A three level atom with ground state $|i\rangle$. The atom absorbs a photon at wavelength λ , making a transition to an excited state, $|e\rangle$, and decays via spontaneous emission to final state $|f\rangle$. The magnetic moment in the final state is different than the initial state of the atom.

moment. Thus an atom in state $|i\rangle$ will be deflected differently than an atom in state $|f\rangle$.

Now assume that a beam of atoms consists of two species. These could be two different isotopes of the same element. The laser is tuned to one isotope, changing its magnetic moment, while not affecting the other. We call this process single-photon atomic sorting because each atom is sorted by scattering exactly one photon. It is closely related to a one-way barrier for atoms that was used as a general method for cooling the translational motion of atoms [81]. In the present case, the goal is to lower the entropy of the atomic beam by separating the isotopes. This process can be viewed as a realization of Maxwell's Demon in the sense proposed by Leo Szilard in 1929. In this case

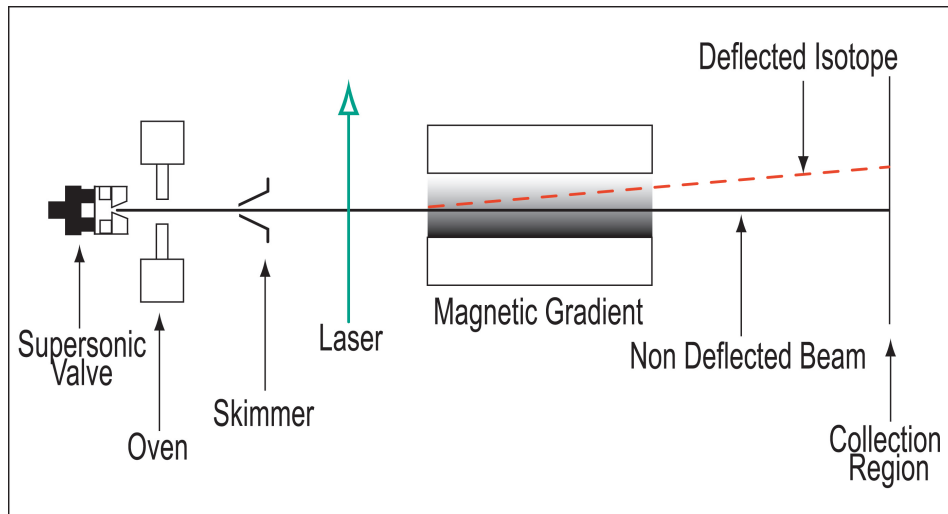


Figure 5.6: Schematic of the set-up for isotope separation. Atoms from two ovens are entrained into the flow of a carrier gas from a supersonic nozzle. The beam is collimated with a skimmer. A laser beam excites a certain isotope into a metastable which has a nonzero magnetic moment. The resulting metastables are deflected using a magnetic field gradient.

the Demon acts as a sorter, sending each isotope in a different direction. The entropy of the beam cannot be lowered with any time-dependent Hamiltonian such as an RF drive [82], and an irreversible step is required. The atom scatters one spontaneous photon from the laser beam, increasing the photon entropy. This increase compensates for the decrease in the entropy of the beam.

The starting point for this approach must be an atomic beam that has the lowest possible entropy of translational motion. Collimation of an effusive beam is not a viable approach since the resulting flux is too small [83]. The best candidate is a supersonic beam which is generated with a high pressure carrier gas expanding through a small aperture [84]. The properties of such beams are remarkable, with an angular divergence of only a few degrees and a velocity spread that is 1% of the mean velocity [85]. These beams are typically

pulsed, but for the purpose of isotope separation they should be run quasi-continuously to maximize throughput. The desired element can be entrained into the flow near the output of the nozzle, acquiring the characteristics of the carrier gas. Efficient entrainment can be accomplished using two ovens mounted opposite to each other and perpendicular to the supersonic flow of atoms, illustrated in Figure 5.6. A temperature gradient in each oven can produce a collimated effusive beam. The ovens are aligned so that atoms which are not entrained into the supersonic flow are deposited into the opposite oven. This “atomic ping-pong” between ovens reduces the need of recycling through vacuum pumps, reduces the background pressure, and greatly reduces the initial amount needed for separation. Once entrained, the beam is collimated with a skimmer and propagates into the laser region. The desired isotope will then undergo an irreversible change in magnetic moment, different from the other isotopes which are unaffected by the laser beam. The force due to the inhomogeneous magnetic field is:

$$F = \mu_B g_J m_J \nabla B \quad (5.2)$$

where μ_B is the bohr magneton, g_J is the Landé-g factor, m_J is the projection of the total angular momentum on the quantization axis, and ∇B is the gradient of the magnetic field. The Landé-g factor in atomic physics refers to a multiplicative factor in the expression for the energy levels of an atom in a weak magnetic field, which breaks the degeneracy that ordinarily exists in atomic energy levels. A first-order perturbation calculation of an atom’s

energy levels in a weak magnetic field yields the factor:

$$g_J = g_L \frac{J(J+1) - S(S+1) + L(L+1)}{2J(J+1)} + g_S \frac{J(J+1) + S(S+1) - L(L+1)}{2J(J+1)} \quad (5.3)$$

Under the common assumption that $g_L = 1$ and $g_S = 2$, the equation becomes the familiar expression for the Landé-g factor:

$$g_J = 1 + \frac{J(J+1) - L(L+1) + S(S+1)}{2J(J+1)} \quad (5.4)$$

The maximum magnetic field of the gradient would be strong enough to cause a few elements, such as lithium, to enter the Paschen-Back regime, in which the Landé-g factor must be calculated differently. Most of the periodic table, however, would remain in the weak field limit because of the strong LS coupling present in heavier atoms. All of the elements discussed in the following examples are in the weak field regime.

5.4.1 Single Gradient Simulation Results

In order to determine the viability of single-photon atomic sorting, I developed a simulation of the experimental setup shown in Figure 5.6. I utilized the same ROOT software described in Chapter 4, and in the magnetic gradient region I modeled the atoms' motion in a step-by-step way with a sufficiently small stepsize. In this section I describe several different implementations of single-photon atomic sorting that illustrate how the method developed, and in Section 5.5 I discuss the most promising experimental implementation of the technique.

Rather than begin the simulation at the nozzle, I begin the simulation

after the atoms have passed through the skimmer. The simulation assumes a beam with a mean velocity of 500 m/s and an initial Gaussian spread of 10 m/s in each component of the supersonic beam velocity. The skimmer shown in Figure 5.6 is simulated as a slit 5 mm high in the direction of the magnetic gradient. Since the deflection occurs in only one dimension, the skimmer slit is 4 cm wide, which allows 17% of the initial supersonic beam to pass the skimmer. The magnetic gradient is a constant 500 T/m acting over the distance of 1 m, which can be generated with superconducting magnets. Although the cost of superconducting magnets might inhibit large-scale industrial scalability, Section 5.5 discusses an alternative magnetic gradient implementation that is much less expensive. The simulation assumes that the isotopes are collected immediately after leaving the magnetic gradient, although if the collection occurred further downstream, the isotopes would continue to separate further during the time-of-flight.

Many elements have metastable states whose magnetic moments are distinct from the ground state. In particular, atoms with no magnetic moment in the ground state are particularly well suited for single photon atomic sorting. Figures 5.7 and 5.8 show simulation results of single photon atomic sorting applied to alkaline-earth metals.

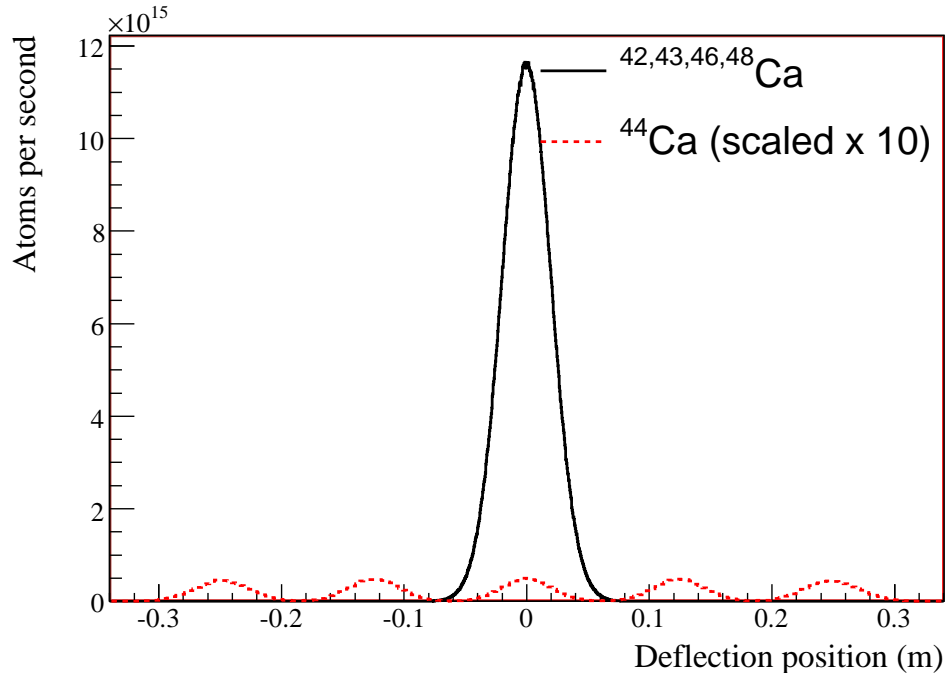


Figure 5.7: Simulation results of single-photon atomic sorting for ^{44}Ca using the method illustrated in Figure 5.6

Figure 5.7 demonstrates the separation of ^{44}Ca . By using a 272 nm laser, one can excite only a specific isotope of calcium to the $^1\text{P}_1^o$ state, which quickly decays to the metastable $^1\text{D}_2$ state. The deflection in the magnetic field gradient results in 80% of the ^{44}Ca being collected at 90% purity. As shown in Figure 5.8, a heavier isotope such as ^{137}Ba can also be separated using single photon atomic sorting. In order to achieve 90% purity, only 48% of the available isotope can be collected. One could easily collect less of the ^{137}Ba but at a higher purity; at 99% purity, 32% of the ^{137}Ba could be collected.

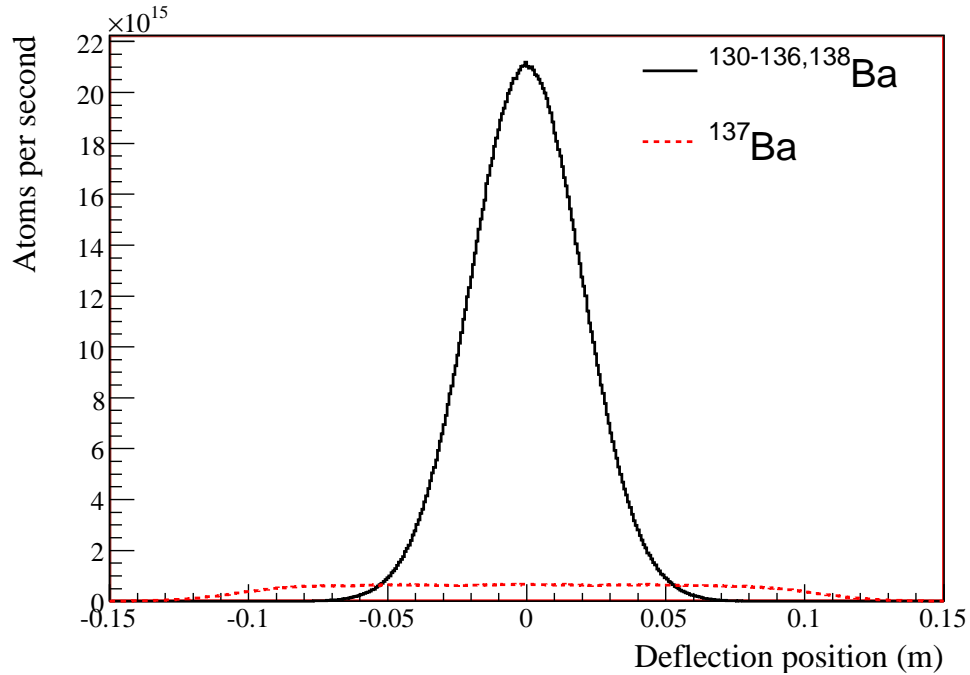


Figure 5.8: Simulation results of single-photon atomic sorting for ^{137}Ba using the method illustrated in Figure 5.6.

Single photon atomic sorting does not depend on the atoms having zero magnetic moment in their ground state. Figure 5.9 shows results for the separation of ^{71}Ga , which has a ground state of $^2\text{P}_{1/2}^o$. In this example, 67% of ^{71}Ga can be collected at 90% purity using the setup outlined in Figure 5.6. We summarize our results for a variety of elements in Table 5.2. These are just taken as representative examples. Other elements, such as Hg, can be separated with the use of two lasers to promote atoms into a suitable metastable state.

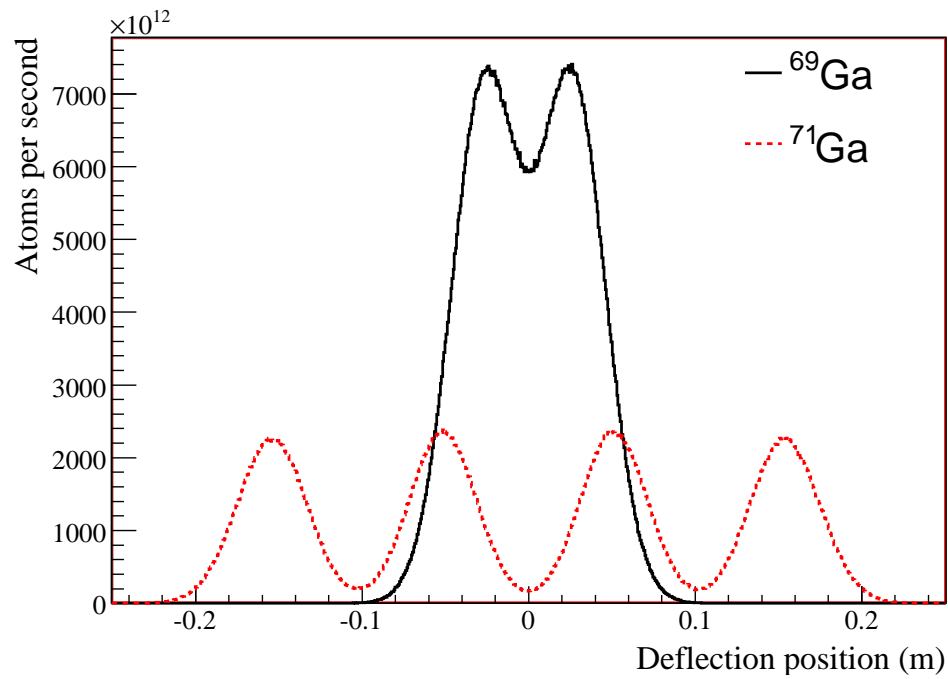


Figure 5.9: Simulation results of single-photon atomic sorting for ^{71}Ga using the method illustrated in Figure 5.6.

Table 5.2: Examples of isotopic separation from single-photon atomic sorting as illustrated in Figure 5.6. The reported collection percentages assume that collection occurs on either side of the isotopically mixed peak.

Target Isotope	Natural Abundance	Laser λ (nm)	Ground State	Metastable State	Landé-g Initial	Landé-g Final	Enrichment	Collected Isotope %
^{44}Ca	2.1%	272.2	$^1\text{S}_0$	$^1\text{D}_2$	1	5	90%	80.0%
^{71}Ga	39.9%	403.3	$^2\text{P}_{1/2}^o$	$^2\text{P}_{3/2}^o$	2/3	4/3	90%	67.5%
^{137}Ba	11.2%	553.6	$^1\text{S}_0$	$^3\text{D}_1, ^3\text{D}_2, ^1\text{D}_2$	1	1/2, 7/6, 1	90%	47.8%
^{186}W	28.4%	354.5	$^5\text{D}_0$	$^5\text{D}_1, ^5\text{D}_2$	1	3/2	90%	32.1%

Some elements do not have a suitable metastable state that allows for isotope separation by this method. Furthermore, even if the metastable state has a distinct magnetic moment from the ground state, that does not guarantee efficient separation. This limitation is illustrated in Figure 5.10 which shows the separation of ^{50}Ti , which has been excited from the $^3\text{F}_2$ ground state to the $a^5\text{F}_1$ metastable state; but the difference in the magnetic moment is insufficient to allow for collection of the specific isotope using the experimental setup from Figure 5.6.

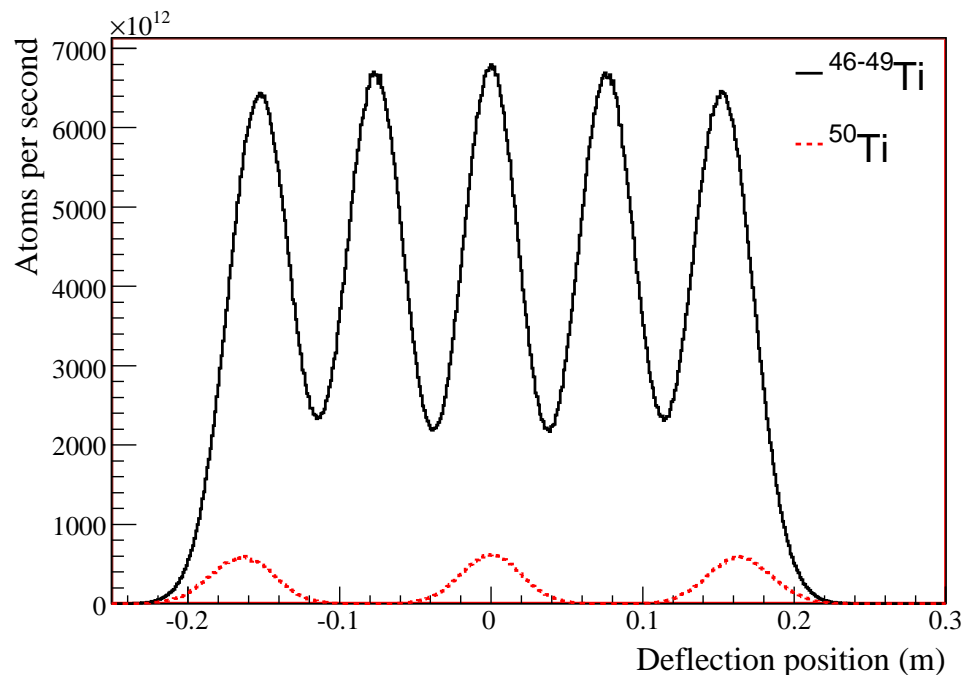


Figure 5.10: Simulation results of single-photon atomic sorting for ^{50}Ti using the method illustrated in Figure 5.6. This method does not effectively separate titanium isotopes.

5.4.2 Double Gradient Simulation Results

While the implementation discussed above works only for atoms with an appropriate metastable state, I now discuss an alternate implementation of single photon atomic sorting that is more general. This method will work on any element that has a nonzero magnetic moment in the ground state, which includes most of the periodic table.

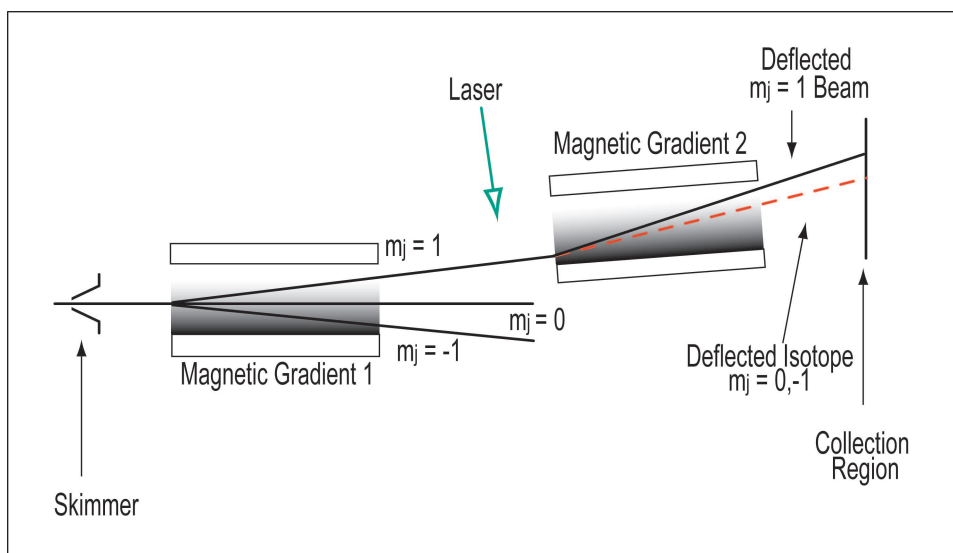


Figure 5.11: Schematic for isotope separation in the more general case of an atom with a magnetic moment in the ground state. The first magnetic field gradient is a Stern-Gerlach setup, separating the internal states of the beam. The $m_j = 1$ state is extracted. A laser with σ^- polarization drives a particular isotope to a lower magnetic moment ground state. The desired isotope is the one that is least deflected.

The second method for separation, illustrated in Figure 5.11, is similar to the first except that a second deflection gradient is added between the skimmer and the laser. This gradient acts like a Stern-Gerlach apparatus, splitting the atomic beam into different magnetic sublevels. Figure 5.11 shows

an example in which the initial ground state is $J = 1$. In the weak-field limit, the atomic beam is in a statistical mixture of its three sublevel states $m_j = -1, 0, 1$. Each of the three sublevels has a distinct magnetic moment and will be deflected differently through a magnetic field gradient. After the beam traverses the first magnetic gradient, the three resulting branches are state-separated, but they are not yet isotopically separated. Before the stretch state $m_j = 1$ atoms enter the second magnetic gradient, a laser applies an isotopically selective irreversible step. A σ^- polarized laser beam optically pumps the $m_j = 1$ of our desired isotope into the $m_j = 0, -1$ states. Having become an isotopically distinguished ensemble, the beam then goes through the second magnetic gradient, in which the desired isotope is deflected less than the other isotopes, which were unaffected by the laser. A small biased magnetic field is maintained between the two magnetic gradients to preserve the quantization axis and prevent spin-flips. This method does not rely on a long-lived metastable state and is general to all atoms that have a ground state magnetic moment.

Figure 5.12 shows this general method applied to ^{50}Ti , which could not be separated effectively by relying upon a metastable state.

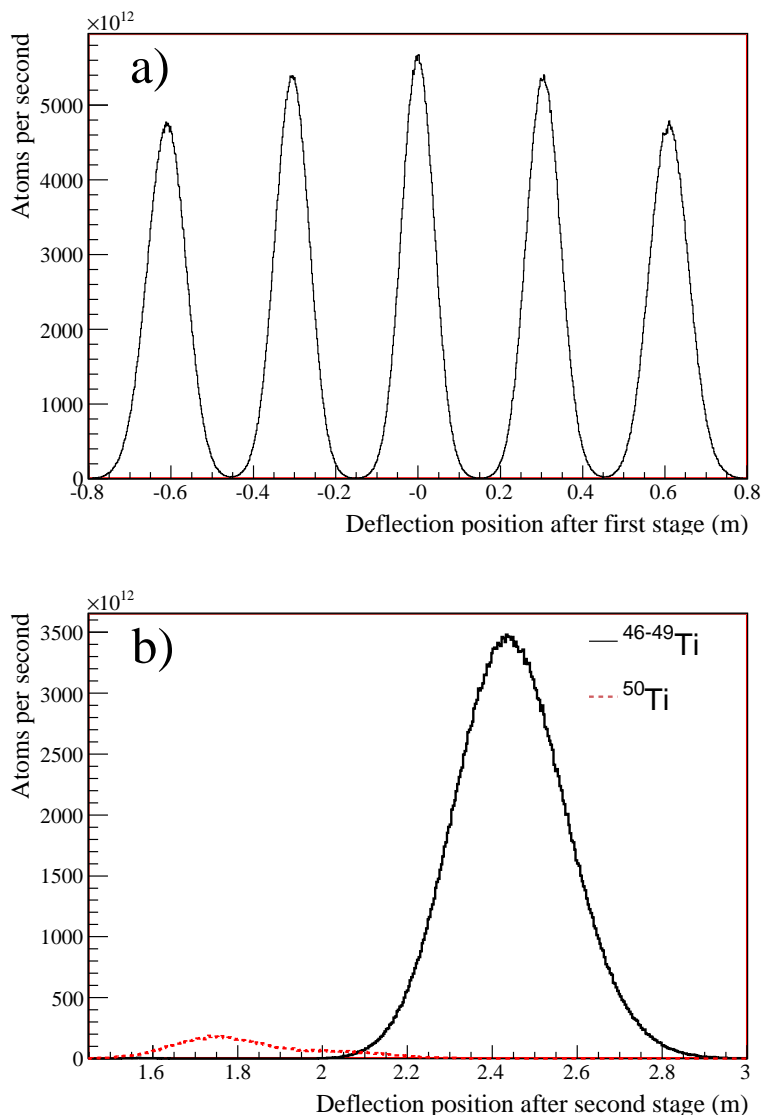


Figure 5.12: Simulation results of single-photon atomic sorting for ^{50}Ti using the method illustrated in Figure 5.11. To effectively separate ^{50}Ti , the simulation assumed magnetic gradients 2 m in length. a) The first stage of magnetic gradient produces Stern Gerlach splittings. b) The second stage of magnetic gradient separates the desired isotope.

Titanium's ground state is a $J = 2$ state, so after the first stage of magnetic gradient the atoms are separated into five branches. The $m_j = 2$ branch interacts with a laser as shown in Figure 5.11 that drives an isotopically selective transition to a $J' = 2$ excited state; for titanium, the 294 nm transition is one of several that would be appropriate. If the excited ^{50}Ti isotope decays back to the $m_j = 2$ state, it has another chance to be excited by the laser. The simulation assumes that the laser effectively depopulates the $m_j = 2$ state, meaning that every ^{50}Ti atom has an m_j that is different from the other titanium isotopes before entering the second stage of magnetic gradient. If one collects ^{50}Ti at 90% purity after the second magnetic gradient, one can collect 98.7% of the ^{50}Ti that enters the second gradient. Since only 20% of the initial isotope is in the $m_j = 2$ stretch state, this method allows for the collection of 19.7% of the overall ^{50}Ti that survives the skimmer.

Figure 5.13 shows isotope separation results for a heavier isotope, ^{150}Nd .

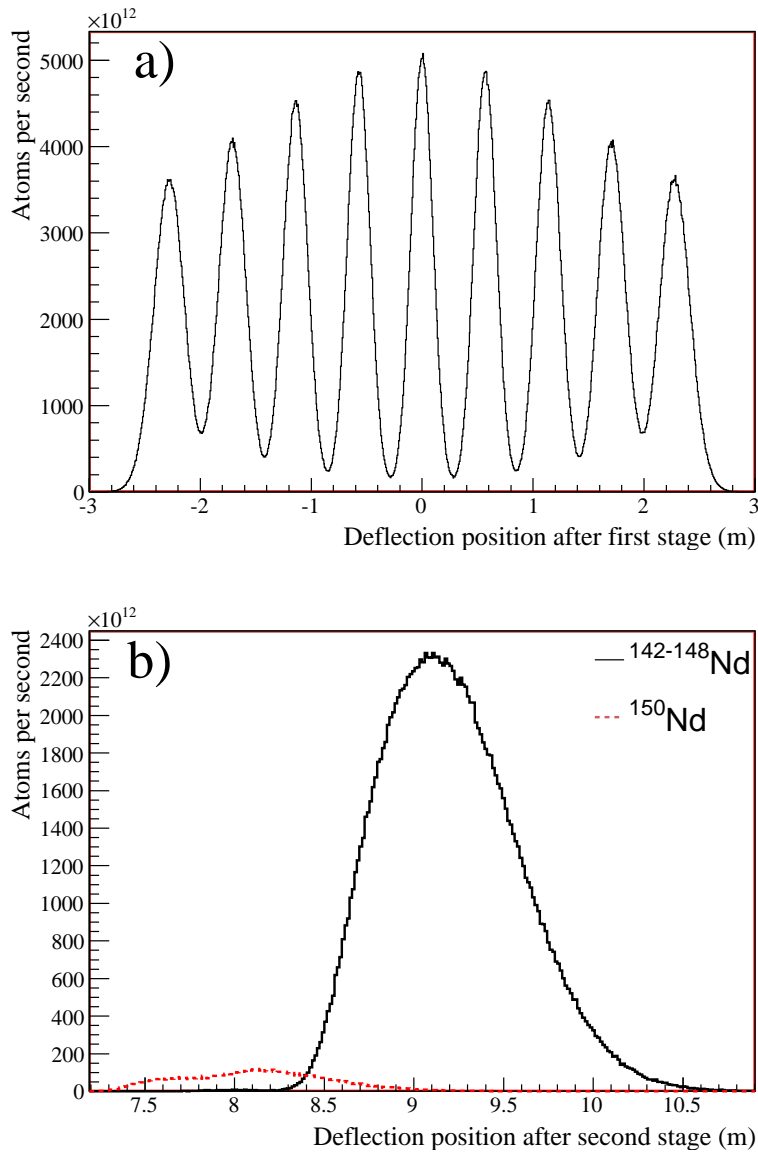


Figure 5.13: Simulation results of single-photon atomic sorting for ^{150}Nd using the method illustrated in Figure 5.11. To effectively separation ^{150}Nd , the simulation assumed magnetic gradients 5 m in length. a) The first stage of magnetic gradient produces Stern Gerlach splittings. b) The second stage of magnetic gradient separates the desired isotope.

Its ground state is 5I_4 , meaning that we see nine branches after the first stage of magnetic gradient. Using a laser that promotes the ground state to a $J' = 4$ excited state, such as a 471.9 nm laser [86], one could collect 75.7% of the ^{150}Nd from the stretch state at 90% purity, which corresponds to 8.4% of the total ^{150}Nd that survives the skimmer. This isotope is of particular interest because it is the double-beta emitter intended for use in the upcoming SNO+ experiment, as discussed in Section 5.2.

5.4.3 Optical Pumping

Looking at Figure 5.11, one obvious problem is that a lot of potential isotope collection is wasted because only the stretch state enters the second magnetic gradient. In order to avoid this problem, one could implement optical pumping. By introducing additional laser frequencies, one could pump the undesired isotopes into the plus stretch state, while pumping the desired isotope into the stretch minus state. Typically isotopic energy level shifts are on the order of a few GHz, so a single laser whose power is divided and whose frequency is then shifted should suffice.

Optical pumping works by taking advantage of selection rules. When an atom absorbs a photon and goes into an excited state, its m value can only change by 1. Whether m changes by +1, 0, or -1 depends on the polarization of the photon. If the applied magnetic field is parallel to the direction of propagation of the photon, then a right-circularly polarized photon will always induce transitions that have a $\Delta m = +1$. Similarly a left-circularly polarized photon will produce transitions having a $\Delta m = -1$. When the atom emits a photon and falls back to its original state, it is equally likely to emit a

left or right circularly polarized photon, meaning that we cannot control the change in m due to emission. If the atom absorbs several photons, its Δm due to emission will on average be zero. Since we can control the Δm of the absorption process, then repeated absorption and emission of photons will “walk” the electrons into a stretch state in m .

The advantage of this approach is that it maximizes the mass-to-magnetic-moment ratio that is being used as a handle for isotope separation. The magnetic gradients, therefore, do not have to be as long in such a setup. Simulations indicate that separation of ^{150}Nd would become feasible with a magnetic gradient that was less than 1 m in length.

5.5 Single Photon Atomic Sorting With Magnetic Guiding

5.5.1 Experimental Setup

The schematic designs discussed so far have the basic limitation that the atomic beam is spreading as it traverses the magnetic gradient region. The longer that region needs to be to effectively separate the isotopes, the more the beam diverges, leading to a larger and more complicated experimental apparatus. A more efficient and scalable design would employ magnetic guiding.

Figure 5.14 shows a schematic of the experiment currently under construction in the Raizen laboratory using lithium. Lithium serves as a simple example because it has two stable isotopes, ^6Li and ^7Li , with natural abundances of 7.5% and 92.5% respectively. In this experiment lithium is entrained into the supersonic beam, and a 670.96 nm laser tuned the ^7Li D₂-line

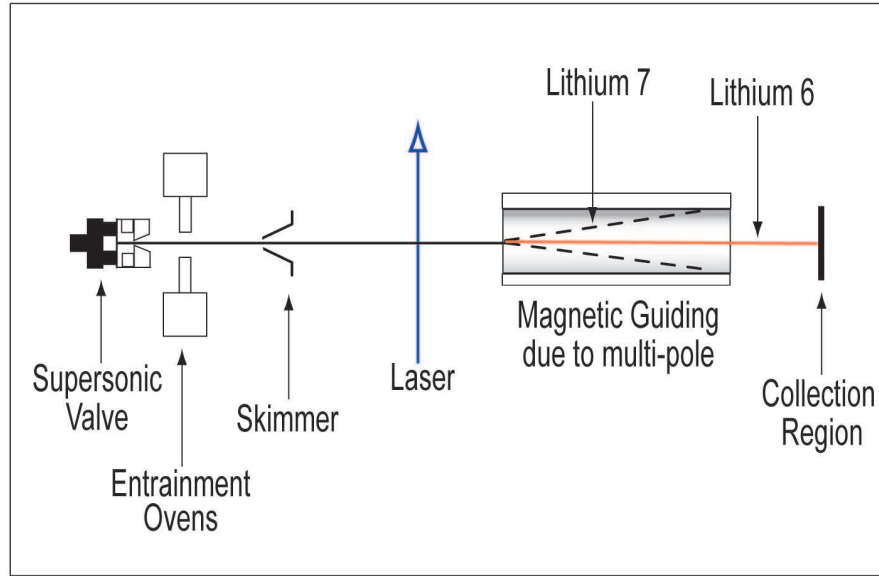


Figure 5.14: Schematic for single-photon atomic sorting using magnetic guiding.

($2^2S_{1/2}(F=2) \rightarrow 2^2P_{3/2}(F=1 \text{ or } F=2)$) optically pumps the ^7Li into a high-field seeking state. The laser depletes the $2^2S_{1/2} F=2$ manifold and optically pumps all of the atoms into the $2^2S_{1/2} F=1$ manifold. The atoms then propagate into the magnetic guiding region, which is a tube surrounded by guiding magnets [87]. For separation of lithium the inner diameter of the tube we intend to use is 1.5 cm, and it is placed 10 cm from the skimmer, which allows 99.7% of the atoms from the skimmer to enter the tube. Once inside, the ^7Li is antiguided and quickly pushed into the walls of the tube, where it sticks. The ^6Li is not affected by the laser, so half of the ^6Li atoms are naturally in the $m_j = -\frac{1}{2}$ guided state. Since we do not excite ^6Li , we take a statistical loss of one half of the ^6Li due to the magnetic sub-level projections. For magnetic

fields greater than about 50 G, the entire $F=1$ manifold becomes high-field seeking. This process allows us to efficiently pump all of the unwanted ${}^7\text{Li}$ atoms into an anti-guiding mode using a single laser wavelength. In an industrial scale experiment, the tube used for the magnetic guiding would have to be periodically changed after a sufficient amount of buildup occurred on the walls, but the tube can be made out of inexpensive stainless steel.

Figures 5.15 and 5.16 show a closer view of the hexapole and quadrupole magnet configurations that we utilized in our simulations. Those figures were produced using a finite element analysis program called COMSOL. Since we are only interested in collecting the atoms that successfully traverse the entire tube, no magnetic focusing is required. The magnets used are quite inexpensive, making scalability very feasible. We purchased our magnets from K&J Magnetics, Inc., and when bought in bulk the magnets cost only \$3.75 a piece.

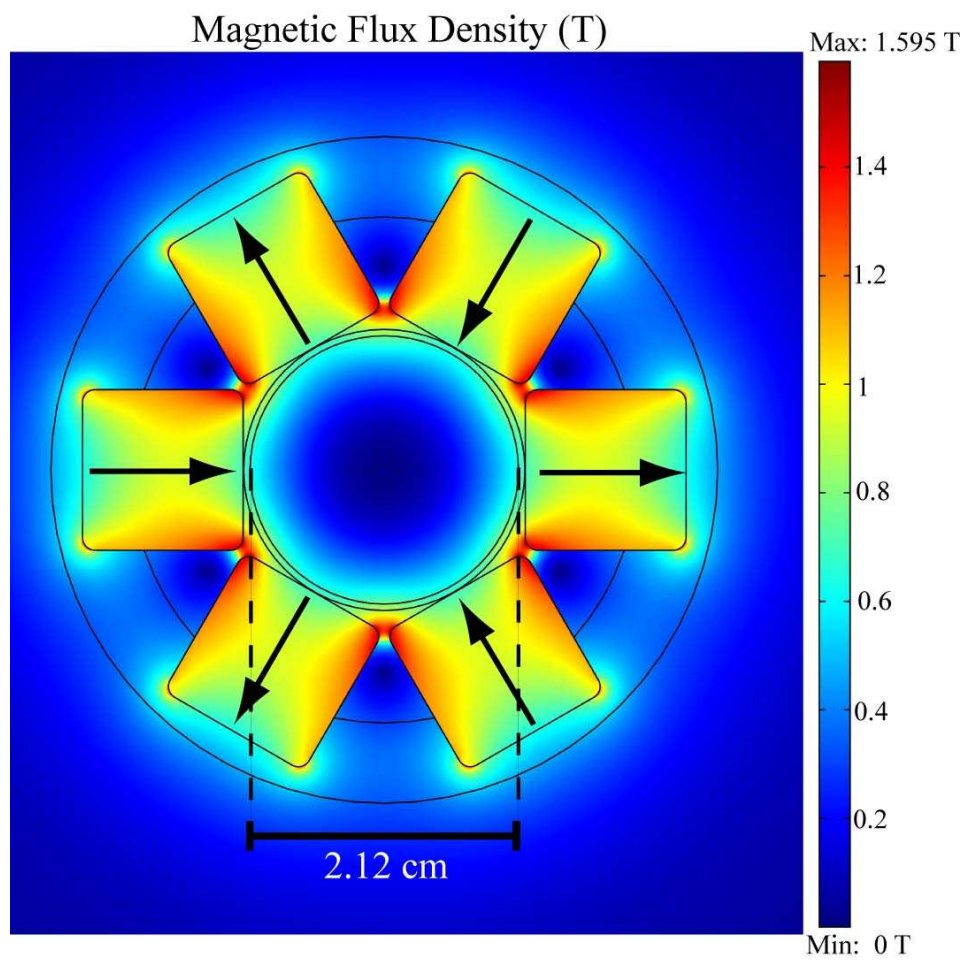


Figure 5.15: COMSOL finite analysis simulation of hexapole magnet for magnetic guiding.

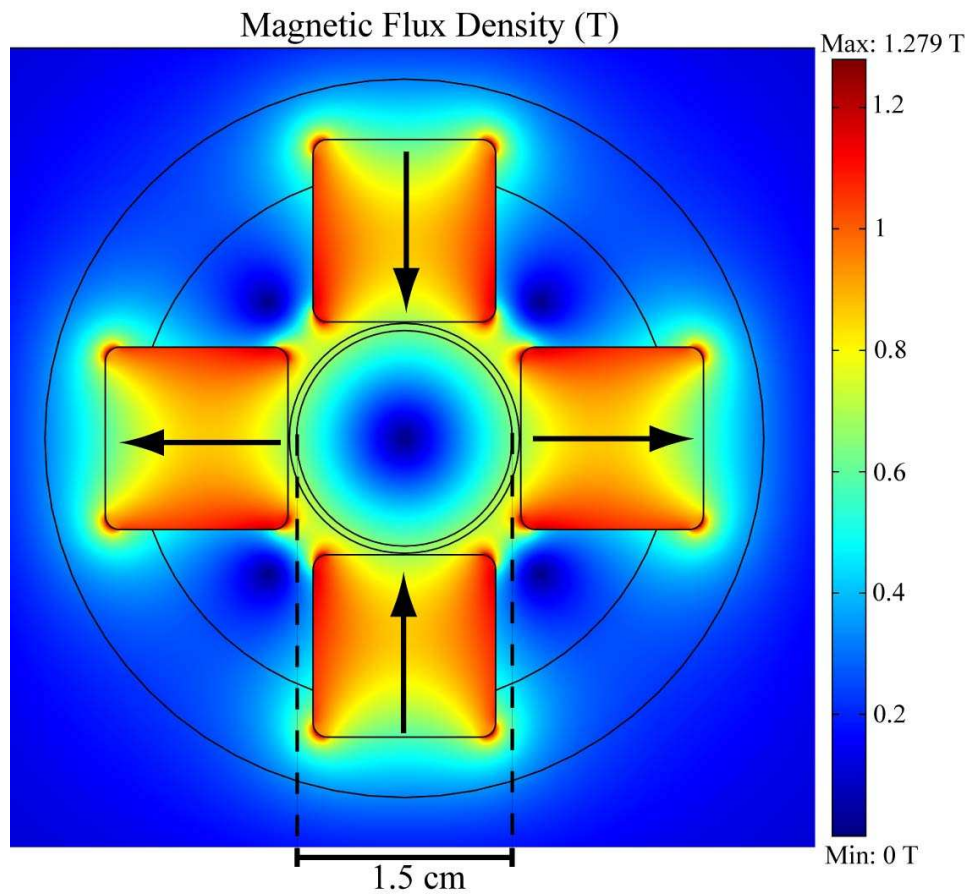


Figure 5.16: COMSOL finite analysis simulation of quadrupole magnet for magnetic guiding.

5.5.2 Theoretical Field Equations

The basic characteristics of a hexapole field can be described by a simple equation [88]:

$$|B(r)| = B_r \left(\frac{r}{r_o} \right)^2 \quad (5.5)$$

where B_r is the remnant field, r is the distance from the center of the hexapole, and r_o is the radius of the tube. This equation describes an ideal hexapole, and some simple corrections can be added to make it more realistic [89, 90]. The more realistic equation modeling a hexapole magnetic field is:

$$|B(r, \theta)| = B_r \left(\frac{r}{r_o}\right)^2 \left(1 - A_o \left(\frac{r}{r_o}\right)^6 \cos(6\theta)\right) \quad (5.6)$$

where A_o is the amplitude of the oscillation term.

Figure 5.17 shows a comparison between the analytical expression and the more realistic COMSOL simulation for a hexapole configuration. The comparison shows when the ${}^6\text{Li}$ collides with the wall in the simulation. While the general agreement is confirmation that the COMSOL simulation is working properly, even when the angular correction terms are included, the analytical expression is not as accurate as the COMSOL finite element analysis. Figure 5.18 shows a similar comparison for ${}^7\text{Li}$. In the simulation for both of these comparisons, the collection tube was 1 m long with an inner radius of 1.0 cm and an outer radius of 1.05 cm. While this tube was not the one we ultimately chose to use in our final designs, it serves to demonstrate the general agreement between the COMSOL simulation and our analytical expectations.

The equation for an ideal quadrupole is quite simple:

$$|B(r)| = B_r \left(\frac{r}{r_o}\right) \quad (5.7)$$

Comparisons of this equation with the COMSOL results show a little more deviation, however, because I did not apply any correction terms to the ideal quadrupole equation.

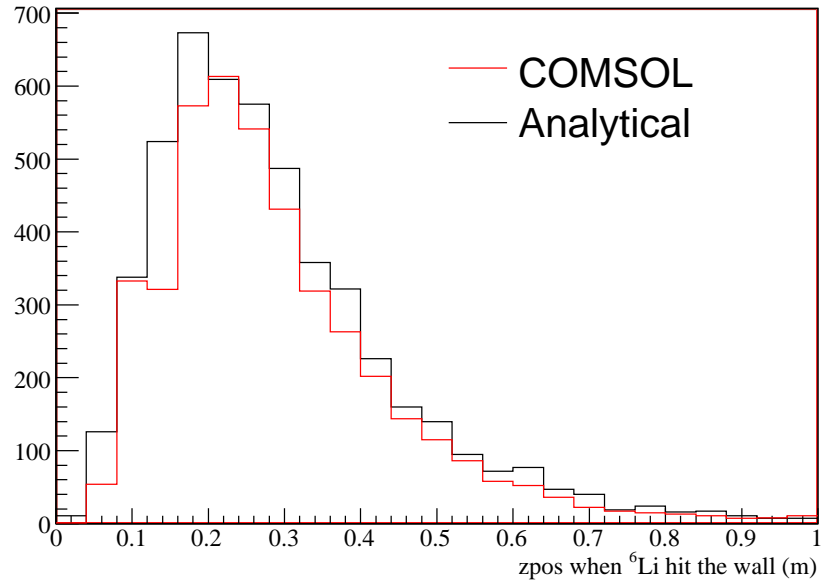


Figure 5.17: Comparison of when ${}^6\text{Li}$ hit the wall in a simulation based on COMSOL and a simulation based on the analytical expression for a hexapole. In both cases the tube had an inner radius of 1.00 cm and an outer radius of 1.05 cm. The hexapole was created using 6 magnets with $B_r = 0.75$ and $A_o = 0.068$.

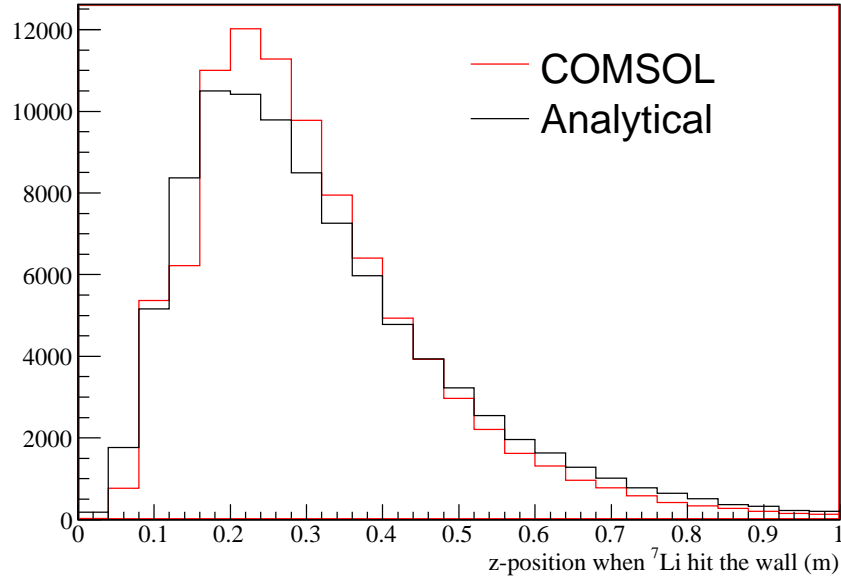


Figure 5.18: Comparison of when ${}^7\text{Li}$ hit the wall in a simulation based on COMSOL and a simulation based on the analytical expression for a hexapole. In both cases the tube had an inner radius of 1.00 cm and an outer radius of 1.05 cm. The hexapole was created using 6 magnets with $B_r = 0.75$ and $A_o = 0.068$.

5.5.3 Simulation Results for Lithium

These theoretical expressions were helpful in the initial stages of the experimental design, but the final simulation results relied on COMSOL modeling of the magnetic field. In COMSOL the hexapole and quadrupole magnets illustrated in Figures 5.15 and 5.16 were constructed out of individual magnets whose properties were defined as realistically as possible. The resulting magnetic field was output to a data file that then served as input to the simulation

controlling the magnetic guiding.

Figure 5.19 shows the radial distributions of the two lithium isotopes as they enter the magnetic guiding region, as well as their distributions as they leave the magnetic guiding region. The isotope-selective guiding and anti-guiding are clearly evident, and the enrichment can be made arbitrarily high by optimizing the geometry of the tube. The y-axis of Figure 5.19 has been scaled to represent atoms/s, even though only 10^7 atoms were actually simulated.

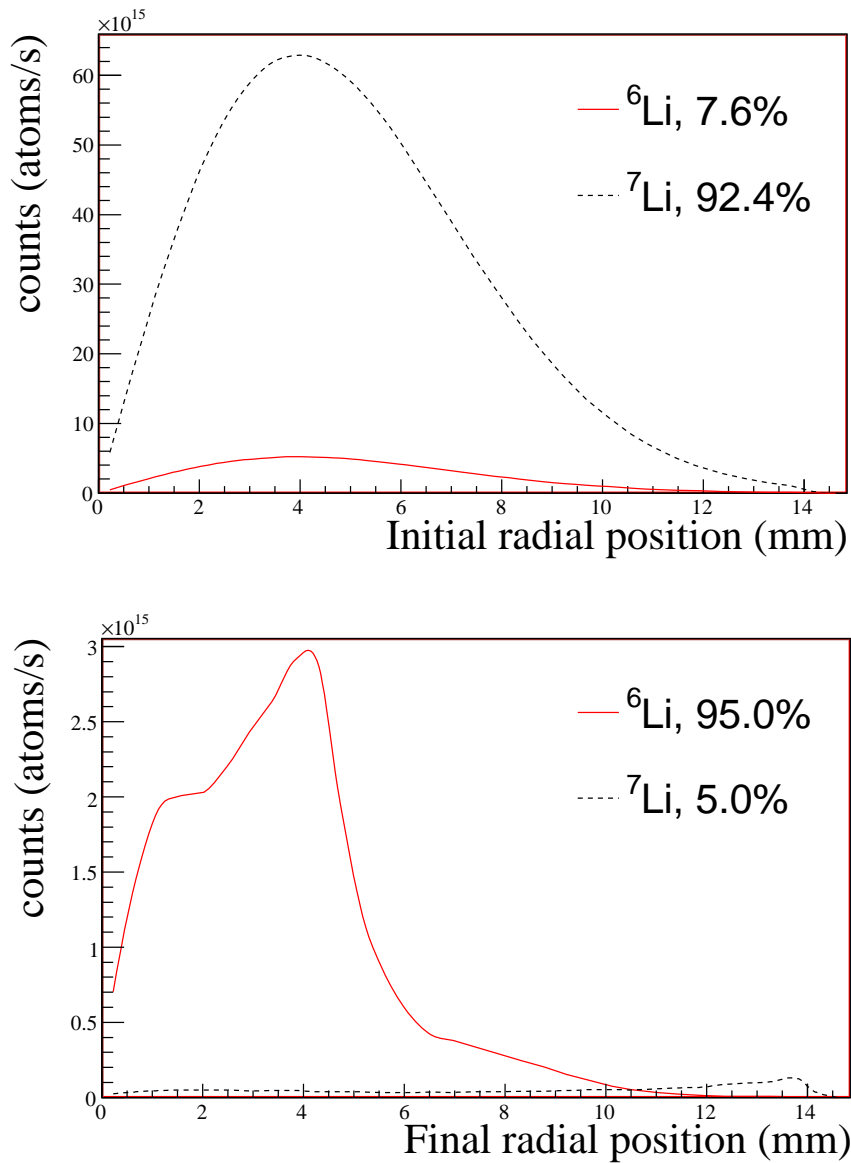


Figure 5.19: Simulation results of the radial positions of the two lithium isotopes as they enter the magnetic gradient that separates them isotopically, followed by their radial positions upon exiting the magnetic gradient. The magnetic guiding region was a 0.5 m long series of quadrupole magnets whose gradients were simulated using finite element analysis as shown in Figure 5.16.

The results shown in Figure 5.19 were simulated assuming a 0.5 m long region of quadrupole guiding magnets whose specifications are discussed below. That geometry yields 95% enrichment of ${}^6\text{Li}$, and 36.8% of the ${}^6\text{Li}$ that enters the guiding region survives to be collected. The simulation used for these results assumes a beam with a mean velocity of 800 m/s and an initial Gaussian spread of 15 m/s in each component of the supersonic beam velocity. This velocity corresponds to entraining the lithium into a beam of neon. The skimmer shown in Figure 5.14 is 5 mm in diameter, and approximately 2% of the beam survives it. Figure 5.20 illustrates how far the ${}^7\text{Li}$ atoms, which are being anti-guided, travel down the tube before colliding with the walls, where the simulation assumes that they stick. Figure 5.22 shows the probability of a ${}^6\text{Li}$ atom traveling all the way to the end of the tube to be collected vs. the atom's initial starting position when it enters the tube. The probability is calculated assuming that the ${}^6\text{Li}$ atoms all have the correct magnetic moment to be guided (which in our experiment would only be true for half of the ${}^6\text{Li}$ atoms). Figure 5.21 illustrates that same probability of survival for ${}^7\text{Li}$, which is pumped into an anti-guiding state and has a very small chance of actually traversing the tube. Figure 5.21 shows that the contamination comes primarily from ${}^7\text{Li}$ atoms that begin at the center of the tube with a low transverse velocity and from ${}^7\text{Li}$ atoms that begin near the edge of the tube but with a transverse velocity directing them towards the edge of the tube farthest away.

We simulated a quadrupole magnetic field produced by four permanent magnets for the separation of lithium. The magnets are $\frac{1}{2}'' \times \frac{1}{2}'' \times 1''$ and have a residual flux density of $B_r=1.48$ T. The magnets surround a 1.5 cm inner diameter (1.6 cm outer diameter) stainless steel tube. The resulting magnetic

flux density, illustrated in Figure 5.16, was simulated using finite element analysis. We chose this geometry to avoid putting the magnets in vacuum and to maximize the magnetic field gradients. While a smaller diameter tube will allow for higher field gradients, it will also reduce the total number of collected atoms of the desired isotope. Although our simulations assume the magnets are held in place with an aluminum holder, slightly higher gradients can be achieved by using a carbon steel holder. The simulation assumes that the isotopes are collected immediately after leaving the magnetic gradient.

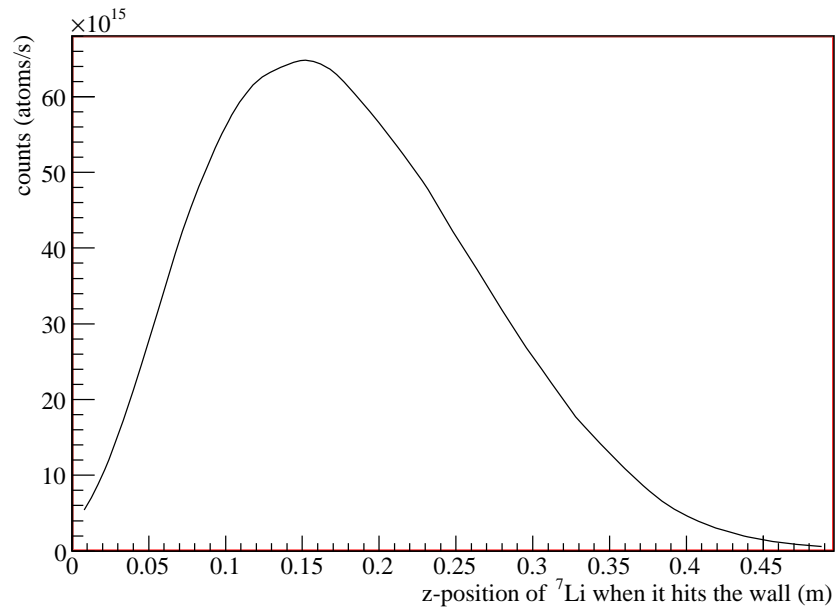


Figure 5.20: Simulation results of the z-position of ${}^7\text{Li}$ atoms when they hit the wall

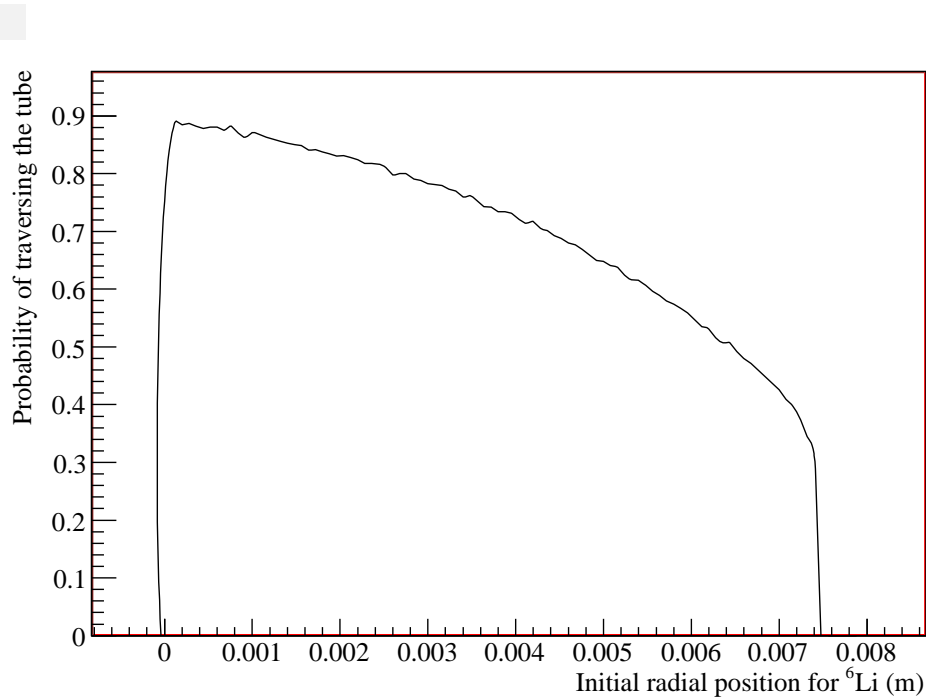


Figure 5.21: Simulation results of the probability of ${}^6\text{Li}$ traversing the magnetic guiding tube vs. initial radial position at the beginning of the tube. The probability was calculated assuming that all of the ${}^6\text{Li}$ atoms had the correct magnetic moment to be guided when they entered the tube.

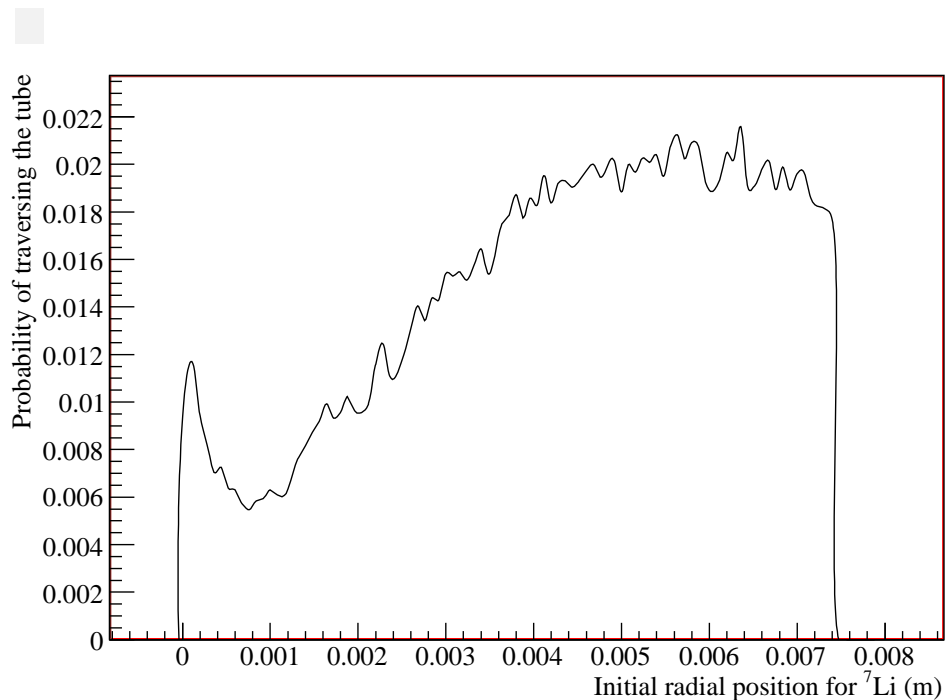


Figure 5.22: Simulation results of the probability of ${}^7\text{Li}$ traversing the magnetic guiding tube vs. initial radial position at the beginning of the tube. Atoms have the greatest chance of survival if they enter the center of the tube with low translational velocity or enter near the edge of the tube with a translational velocity directing them toward the far side of the tube. The jagged nature of the curve is statistical because so few of the ${}^7\text{Li}$ atoms survive the tube.

5.5.4 Additional Simulation Details

The simulation includes a variety of different effects describing how atoms behave in a magnetic gradient, and a good general discussion of these effects can be found in [91]. As long as an atom's Larmor frequency is much greater than the rate of the change of direction of the magnetic field, then the orientation

of the atom's magnetic moment will adiabatically follow the direction of the magnetic field [92]. In the simulation, therefore, as long as the atom's Larmor frequency is at least an order of magnitude greater than the rate of change of the magnetic field direction, then its magnetic moment is assumed to be aligned with the field. This condition is usually fulfilled except when the magnetic field becomes extremely small near the center of the tube. When the condition is not met, then the atom's magnetic moment precesses around the magnetic field until the condition is again fulfilled. The Larmor frequency of the atom is determined by:

$$\Omega_L = g_L \mu_B B / \hbar \quad (5.8)$$

where g_L is the Landé factor, μ_B is the Bohr magneton, and B is the magnitude of the magnetic field. The magnetic gradient applies a torque to the atom's magnetic moment that tends to cause the magnetic moment to be either aligned or anti-aligned to the field. In the simulation, I assume that the magnetic moment follows the field unless the atom's Larmor frequency falls within a factor of ten of the rate of change of the direction of the magnetic field. In that case, I assume that the magnetic moment precesses around the magnetic field with the Larmor frequency. This precession effect is very small; when I turn it off completely in the simulation, I see only a slight increase in the percent of the available isotope that is collected.

Atoms in a magnetic field gradient can behave differently depending on the strength of the gradient. The so-called Paschen-Back regime occurs when the magnetic field is so strong that it disrupts the coupling between the orbital and spin angular momenta, and the LS-coupling is broken. In that case L and

S remain “good” quantum numbers, and the Landé-g factor becomes simply (L+2S). The Paschen-Back regime applies when $\mu_B B_z \gg \Delta E_{\text{spin-orbital}}$, which for lithium is when the magnetic field reaches:

$$B_z \gg \Delta E_{\text{spin-orbital}} hc / \mu_B = 0.3 \text{cm}^{-1} hc / \mu_B = 0.64 \text{T} \quad (5.9)$$

For most elements, this regime does not have to be considered. The spin-orbit interaction increases as the mass of the atom increases, as one can see by comparing energy levels published by NIST [93] for the same states but with different J values. Even for an atom as light as calcium, the Paschen-Back regime would not begin to apply until the magnetic field was at least 10 T (for the 3P state). For lithium, however, this Paschen-Back regime does need to be included in the simulations since our magnetic field strength exceeds 0.6 T near the very edge of the tube. In the case of lithium, the deflection force caused by the magnetic gradient actually decreases in the Paschen-Back regime, so for lithium we actually would not benefit from stronger magnets because the atoms would spend even more time in the Paschen-Back regime. In the simulations, I do not include an intermediate transition region. As soon as the magnetic field reaches 0.6 T, I assume that the spin-orbit coupling is broken and the atom’s Landé-g factor has been lowered. Although that kind of on-off switch implementation is not strictly realistic, it presents a kind of worst-case scenario because as soon as the atom would begin entering the intermediate regime, I assume it is already governed by Paschen-Back dynamics. Since the atoms are rarely in fields above 0.6 T, the effect itself is small, and the effect of the automatic switch transition is even smaller. If I turn off the Paschen-Back effect altogether, the purity of the lithium collected increases by about 1%,

and the percent of the available lithium collected also increases by about 1%.

Another effect that is included in the simulation is hyperfine splitting. As opposed to the Paschen-Back regime, which occurs when the magnetic field is very strong, hyperfine splitting must be taken into account when the magnetic field is very small, approximately 0.005 T for lithium. In this regime the total angular momentum, F , must be calculated including nuclear spin, I . The Landé-g factor then becomes:

$$g_F \approx g_J \frac{(F(F + 1) - I(I + 1) + J(J + 1))}{2F(F + 1)} \quad (5.10)$$

where g_J is the Landé-g factor that applies in the weak-field limit where J is a good quantum number. In the simulation the hyperfine splitting is implemented like a switch so that once the field drops below 0.005 T, the Landé-g factor changes to account for the contributions from nuclear spin. The overall effect of the hyperfine splitting is to lower the purity of the collected sample by a few percent.

One of the distinct advantages of single-photon atomic sorting is that the technique can be applied to almost every atom in the periodic table. Lithium is particularly easy because it has only two isotopes, and its ground state is $^2S_{1/2}$. The details of the experimental implementation may vary for different elements. We now discuss two examples that represent qualitatively different categories of elements.

5.5.5 Simulation Results for Other Elements

The first example illustrates single-photon atomic sorting for elements with zero magnetic moment in the ground state and a metastable state that has

a nonzero magnetic moment. Figure 5.23 illustrates the slight adjustments required to apply single-photon atomic sorting to such an isotope, ^{44}Ca .

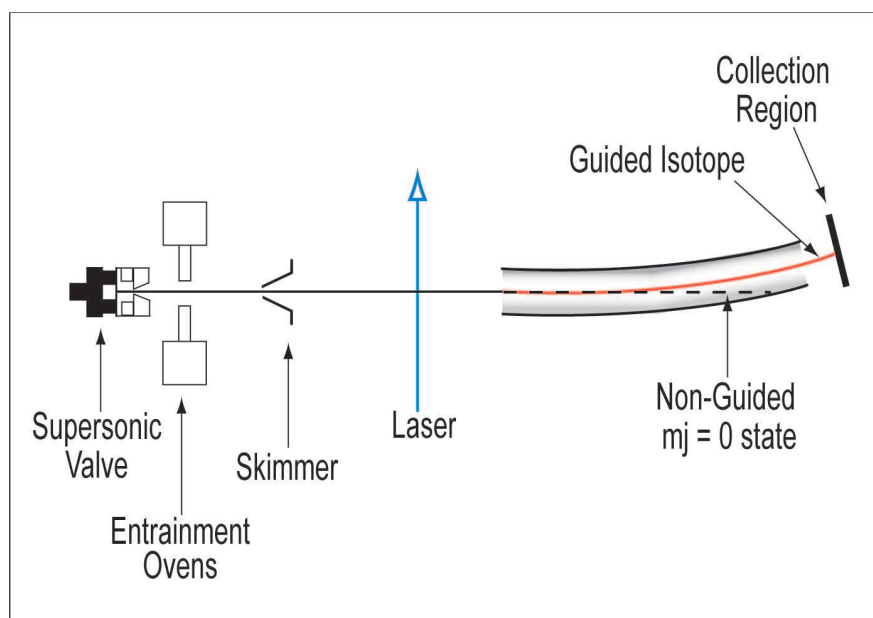


Figure 5.23: Schematic of the set-up for isotope separation for elements with zero magnetic moment in the ground state but a nonzero magnetic moment metastable state that can be excited with a laser. The bend in the magnetic multipole region allows for separation even though the laser only interacts with the desired isotope.

By using a 272 nm laser, one can excite only a specific isotope of calcium to the $^1P_1^o$ state, which quickly decays to the metastable 1D_2 state. Although there are six different isotopes of calcium, those that are unaffected by the laser will be unaffected by the magnetic gradients since they have zero mag-

netic moment in the ground state. The low-field seeking state of the ^{44}Ca will be guided by the magnetic gradients, meaning that a slight bend in the magnetic guiding tube [94] will allow the desired isotope to be collected at high enrichment. Figure 5.24 shows simulation results of the enrichment of ^{44}Ca . That simulation utilized a 2 m long hexapole magnetic field [90] created by six of the same magnets described above only arranged around a larger 2.1 cm inner diameter (2.2 cm outer diameter) stainless steel tube. The tube had a slight bend of 6.0 cm over its 2 m length that served to eliminate the unwanted calcium isotopes. Since calcium is heavier than lithium, it can be entrained into a heavier gas such as argon, which corresponds to a beam with a mean velocity of 500 m/s and a Gaussian spread of 15 m/s in each component of the supersonic beam velocity. As shown in Table 5.3, our simulated setup collected 9.0% of the available ^{44}Ca at 99.9% purity. Figure 5.24 shows the radial positions of the calcium isotopes as they enter and exit the magnetic guiding tube, and the percentage of ^{44}Ca goes from 2.1% to 99.9%. Figure 5.25 shows where the unwanted calcium isotopes hit the wall in the 2 m long tube. The shape of the curve is qualitatively different from the lithium example shown in Figure 5.20 because the calcium simulation assume a hexapole, and the desired purity of 99.9% required a longer tube extending well past the point at which most of the calcium isotopes collided with the wall.

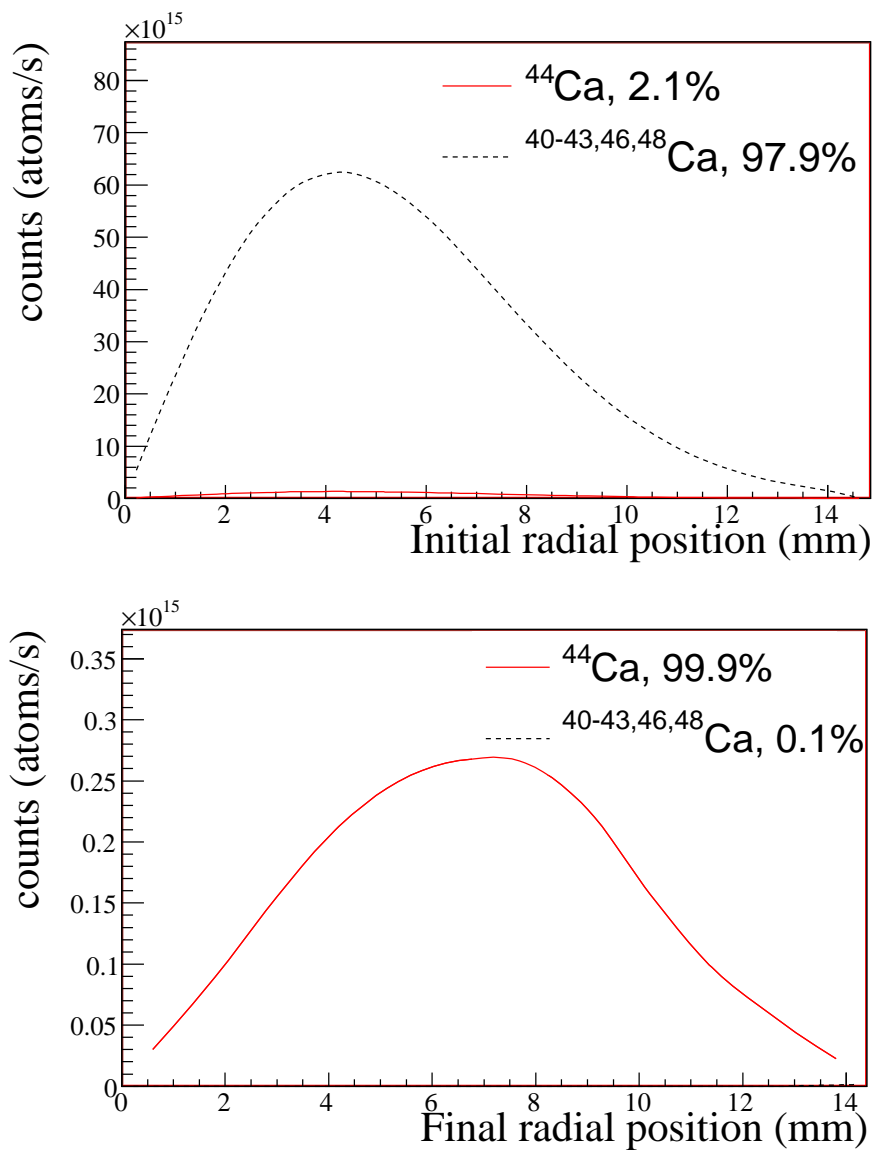


Figure 5.24: Simulation results of the radial positions of the calcium isotopes as they enter the magnetic gradient that separates them isotopically, followed by their radial positions upon exiting the magnetic gradient. The magnetic guiding region was a 2.0 m long series of hexapole magnets, and the guiding tube contained a 6.0 cm bend such as the one in Figure 5.23.

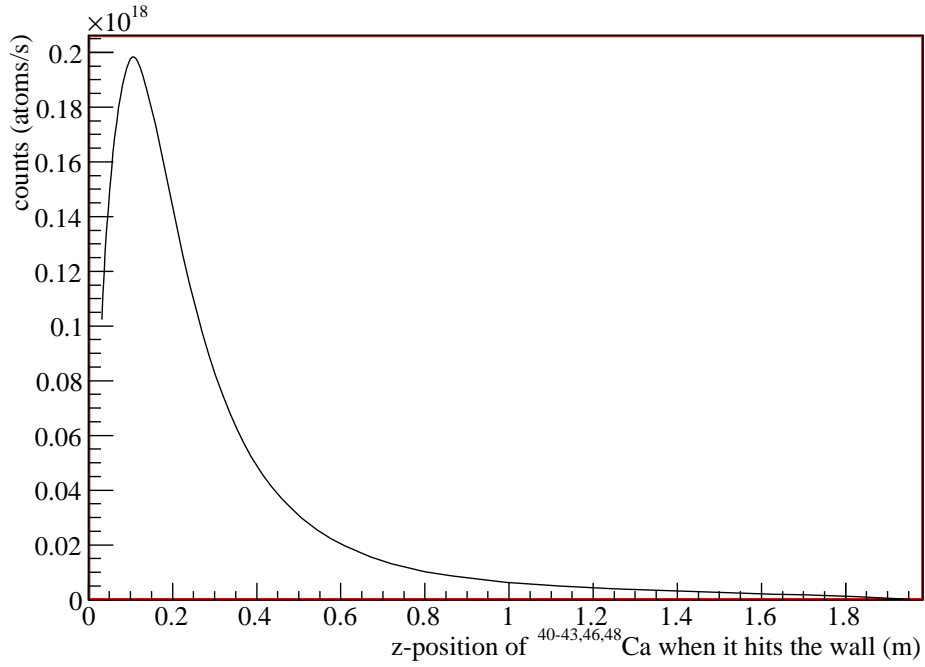


Figure 5.25: Simulation results of the z-position of Ca atoms other than ^{44}Ca when they hit the wall

Target Isotope	Natural Abundance	Laser λ (nm)	Ground State	Guiding Length (m)	Enrichment	Collected Isotope %
^6Li	7.6%	670.96	$^2\text{S}_{1/2}$	Quad. 0.5	95.0%	36.8%
^{44}Ca	2.1%	272.2	$^1\text{S}_0$	Hex. 2.0	99.9%	9.0%
^{150}Nd	5.6%	471.9	$^5\text{J}_4$	Hex. 2.0	97.9%	23.0%

Table 5.3: Examples of isotope separation from single-photon atomic sorting as illustrated in Figure 5.14 (^6Li and ^{150}Nd) and Figure 5.23 (^{44}Ca).

Many elements, however, do not have a suitable metastable state that

allows for isotope separation by this method. We discuss one final method of single photon atomic sorting that is the most general. This method will work on any element that has a nonzero magnetic moment in the ground state, which includes most of the periodic table. As the atoms approach the magnetic multipole guiding, a σ^- polarized laser beam optically pumps our desired isotopes into the stretch low-field seeking state. Simultaneously a σ^+ polarized laser beam optically pumps the other isotopes into the stretch anti-guided state. The laser beams can be multi-passed through the supersonic beam until almost all of the atoms have been pumped. While relying on optical pumping does mean that more than a single photon has to be scattered on average, the isotope separation is accomplished by the scattering of only a small number of photons, which still makes extremely efficient use of the available laser power. This method does not rely on a long-lived metastable state and is general to all atoms that have a ground state magnetic moment, although it does typically require multiple laser frequencies shifted by a few GHz to optically pump all of the isotopes.

Figures 5.27 and 5.26 show isotope separation results for a heavier isotope, ^{150}Nd , which has a ground state of $^5\text{I}_4$. Using a laser that promotes the ground state to a $J' = 4$ excited state, such as a 471.9 nm laser [86], one could collect 23% of the ^{150}Nd that survives the skimmer at 98% purity. These simulation results assume a beam with a mean velocity of 500 m/s and a Gaussian spread of 15 m/s in each component of the supersonic beam velocity. The hexapole magnetic field was a 2 m long tube like the one described for ^{44}Ca but without the bend. Similar separation results can be achieved using a 1.8 m long tube with a slight 1 cm bend to aid in eliminating unwanted isotopes. The precise shape of this bend could be further tuned to achieve the optimal

separation geometry for any given element.

Figure 5.28 shows the probability of a ^{150}Nd atom traveling all the way to the end of the tube to be collected vs. the atom's initial starting position when it enters the tube. The probability is calculated assuming that the ^{150}Nd atoms all have been optically pumped and have the correct magnetic moment to be guided. Figure 5.29 illustrates that same probability of survival for an undesired neodymium isotope, which is pumped into an anti-guiding state and has a very small chance of actually traversing the tube. Figure 5.29 shows that the contamination comes primarily from non- ^{150}Nd atoms that begin at the center of the tube with a low transverse velocity.

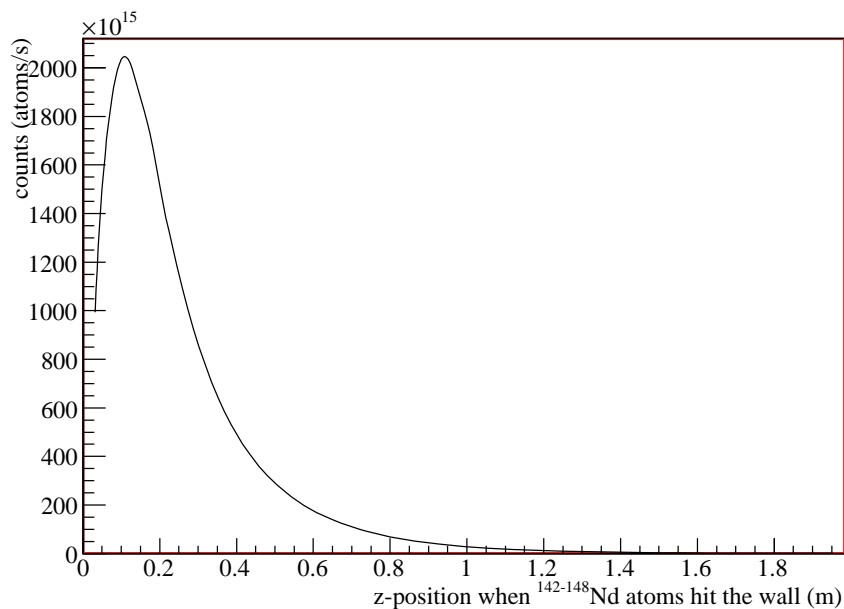


Figure 5.26: Simulation results of the z-position of Nd atoms when they hit the wall

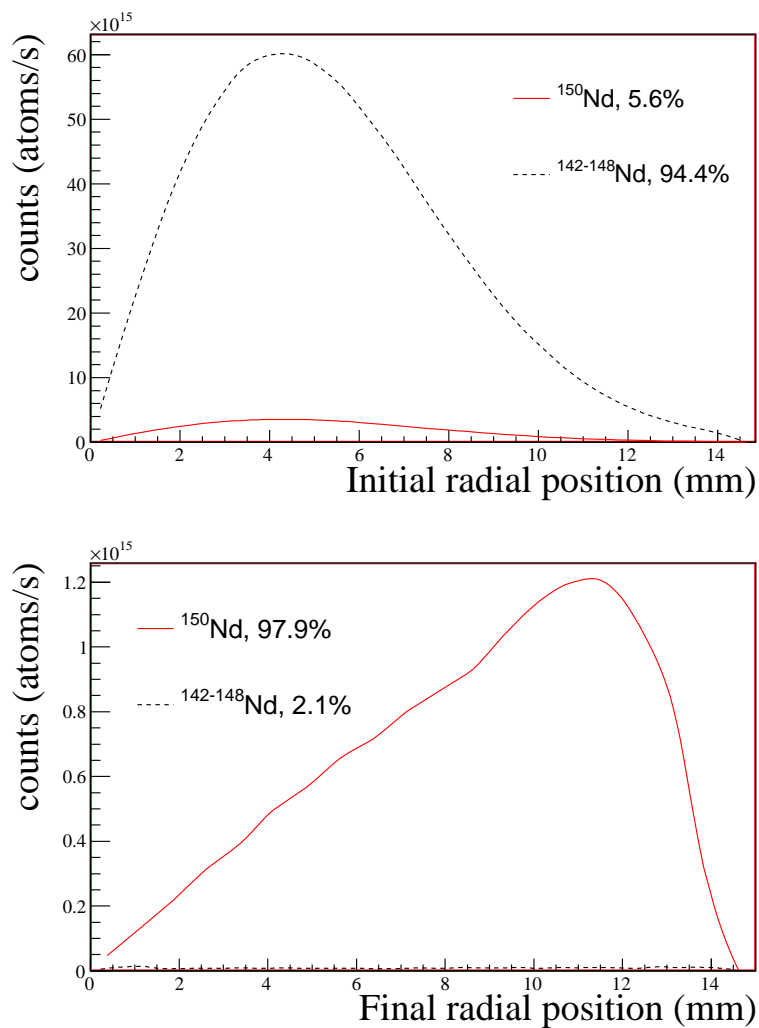


Figure 5.27: Simulation results of the radial positions of the neodymium isotopes as they enter the magnetic gradient that separates them isotopically, followed by their radial positions upon exiting the magnetic gradient. The magnetic guiding region was a 2.0 m long series of hexapole magnets whose gradients were simulated in COMSOL. Before entering the magnetic gradient, the neodymium atoms were optically pumped into guiding and anti-guiding states.

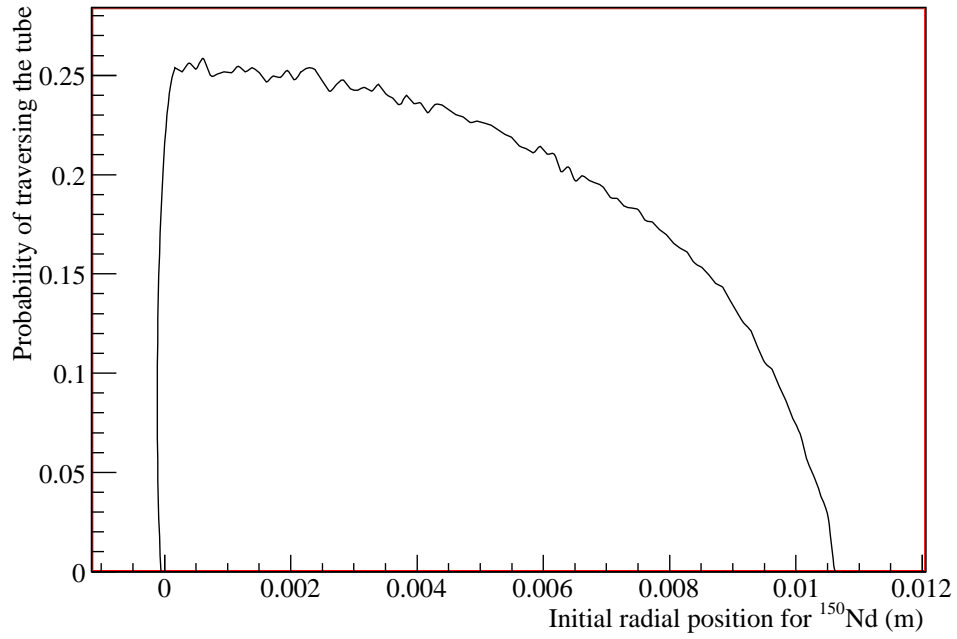


Figure 5.28: Simulation results of the probability of ^{150}Nd traversing the magnetic guiding tube vs. initial radial position at the beginning of the tube. The probability was calculated assuming that all of the ^{150}Nd atoms had the correct magnetic moment to be guided when they entered the tube.

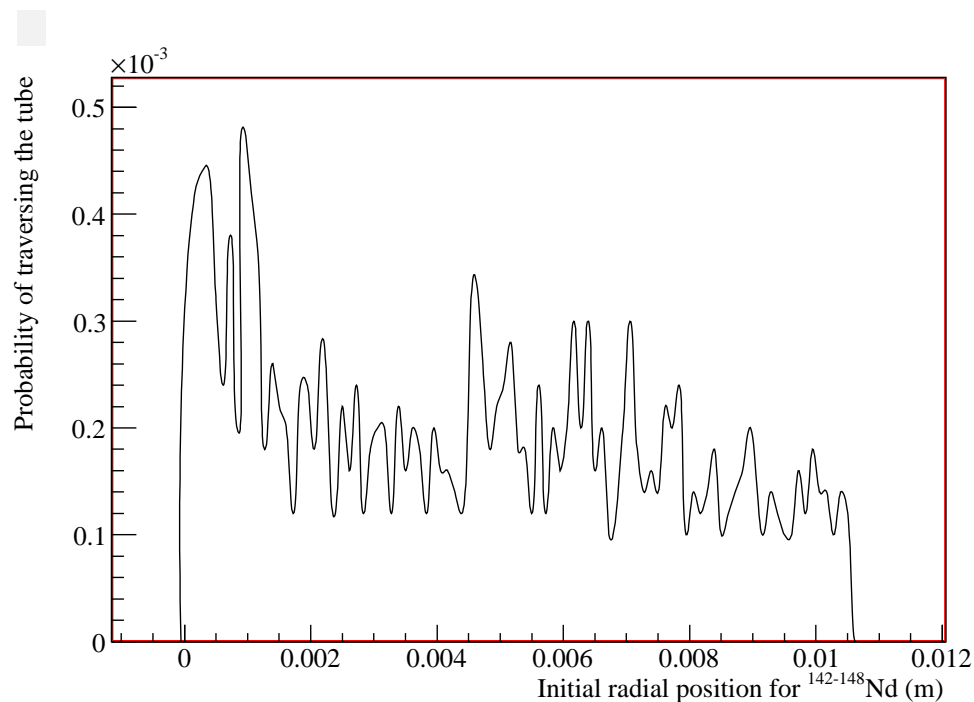


Figure 5.29: Simulation results of the probability of $^{142-148}\text{Nd}$ traversing the magnetic guiding tube vs. initial radial position at the beginning of the tube. Atoms have the greatest chance of survival if they enter the center of the tube with low translational velocity. The jagged nature of the curve is statistical because so few of the unwanted atoms survive the tube.

5.6 Neodymium Estimate and Entrainment Capabilities

Single-photon atomic sorting is a very general approach to isotope separation. One of the advantages of scaling the technique is that the laser can be recycled in a multi-pass configuration until it is depleted. For example, a laser with

1 Watt power can deliver approximately 10^{19} photons per second, which means that even such a modest laser could be used to separate the output from multiple supersonic nozzles in a mass-production setting. A supersonic beam can be operated in a continuous or quasi-continuous mode, and the flux is limited only by available vacuum pump speed. Large scale separation seems feasible using either diffusion pumps or cryopumps.

Because of neodymium's potential uses in determining the neutrino mass, I will estimate the amount of ^{150}Nd that could be collected over the course of one year using this technique, even though it is not the optimal case for separation because of its large mass. Using the above results that we could collect 23% of the ^{150}Nd at 98% purity, the significant remaining question is how much neodymium could be entrained into the supersonic beam. To address that question, our collaboration performed some preliminary entrainment simulations.

Simulating supersonic beam flows cannot be done using the Navier-Stokes equation because the transport terms are not valid in that regime. The Direct Simulation Monte Carlo (DSMC) method [95], proposed by Professor Graeme Bird of the University of Sydney, is a numerical method often utilized to simulate rarefied gas flows such as supersonic beams in which the mean free path of the atom or molecule is not negligible. In such a beam the molecular movement and collision phases can be decoupled over time periods that are smaller than the mean collision time. The DSMC method models fluid flows using a large number of atoms in a probabilistic simulation to solve the Boltzmann equation. Intermolecular collisions and molecule-surface collisions are calculated using phenomenological models. We performed our DSMC calculation using the freeware program DS2, which is coded in standard FOR-

TRAN 95.

These DSMC simulations were done assuming a supersonic beam of neon, with an annular oven placed 1 cm from the nozzle. The oven was assumed to be at a temperature of 900 K, and the lithium was under a pressure of 1 Pa. Figure 5.14 shows two opposing ovens to illustrate the concept of efficient entrainment, but the logical extension of that idea is an annular oven that allows atoms to be entrained into the beam from all directions, not just two. This kind of annular oven would surround the valve. The inner cylinder that contains the lithium is made from stainless steel (or Molybdenum if very high temperatures are required), and a heater element is wound around it. It sits on a stainless steel base, though its thermal contact with the base is minimized. Inner and outer heat shields made of stainless steel are attached to the base, and the based is continuously cooled.

Figures 5.30 and 5.31 show simulation results of lithium being entrained into a supersonic beam of neon. The entrainment we can achieve is as high as 5 – 10% of the initial beam flux because it occurs in an intermediate region in which the supersonic beam is no longer opaque, but there is still a large number of collisions, allowing the atoms to come into thermal equilibrium with the supersonic beam and continue cooling as the beam expands. Figure 5.32 illustrates this intermediate region by showing the mean free path of lithium atoms as they are entrained. The simulation assumes an Even-Lavie valve, which has a beam flux of 4×10^{23} atoms/s/sr. That valve can be operated in a pulsed mode at 1 kHz, and given available pumping speeds, the average continuous flux would be $\sim 5 \times 10^{22}$ atoms/s/sr. Although this beam flux could probably be improved with a nozzle designed specifically for maximum throughput, the following estimates will not assume any special modifications

or optimizations. Figure 5.33 shows simulation results of the number density of atoms as they emerge from the oven. We intend to place a 5 mm diameter skimmer 15 cm from the nozzle, which implies that $\sim 3 \times 10^{18}$ atoms/s will survive the skimmer. The 10% entrainment shown in Figure 5.30 means that we expect $\sim 3 \times 10^{17}$ entrained atoms/s through the skimmer. This beam flux is orders of magnitude higher than any atomic beam produced directly from an oven [83]. The intense brightness afforded by utilizing a supersonic beam will allow this method of isotope separation to be applied in a large-scale industrial setting, which was previously unrealistic using traditional sources collimated from an oven. Figures 5.34-5.36 show simulation results of the speed, temperature, and pressure profiles for the atoms as they are entrained.

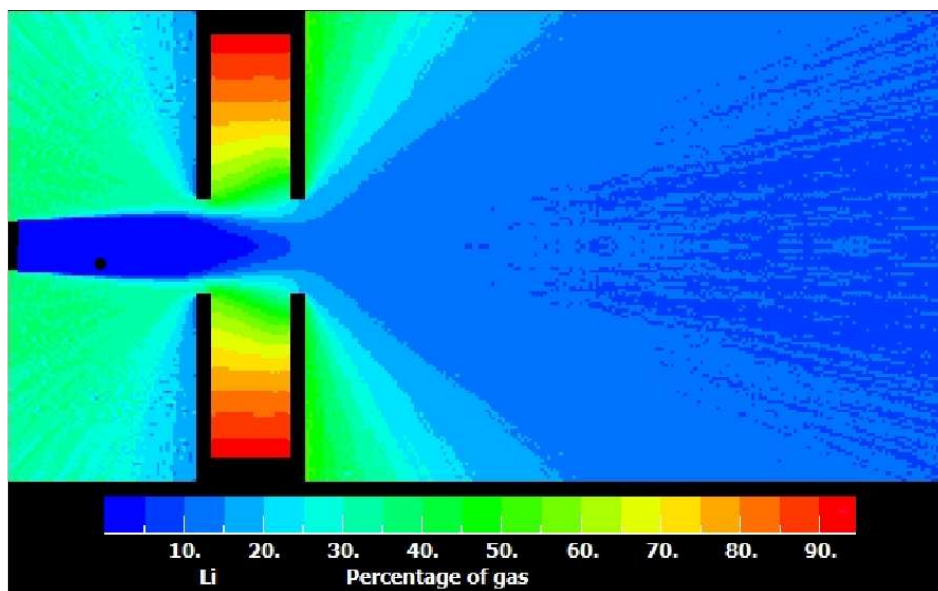


Figure 5.30: Simulation results of lithium entrainment in a supersonic beam of neon showing the percentage of the beam that is lithium atoms. Figure from private communications with Professor Uzi Even at the Sackler School of Chemistry, Tel-Aviv University.

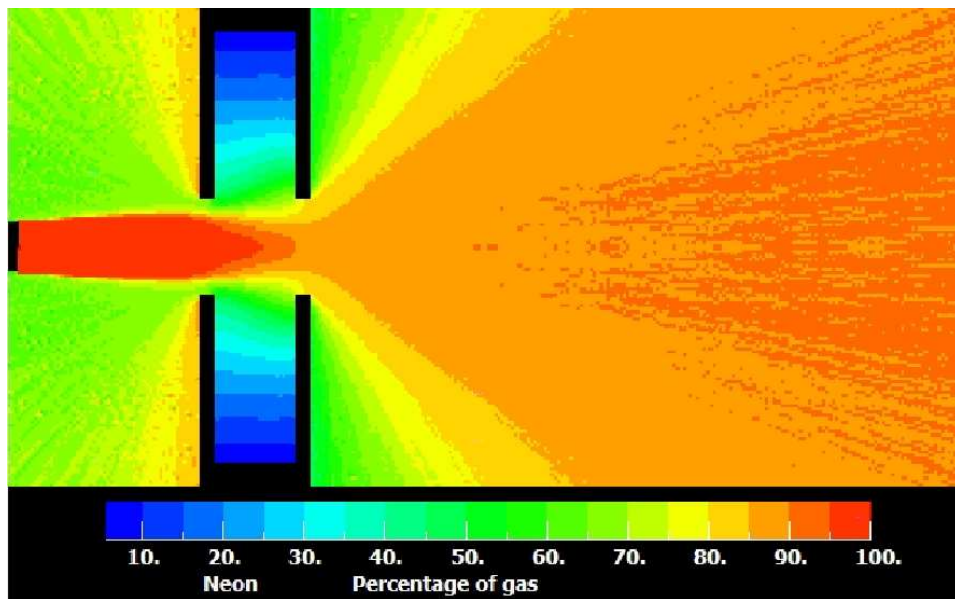


Figure 5.31: Simulation results of lithium entrainment in a supersonic beam of neon showing the percentage of the beam that is neon atoms. Figure from private communications with Professor Uzi Even at the Sackler School of Chemistry, Tel-Aviv University.

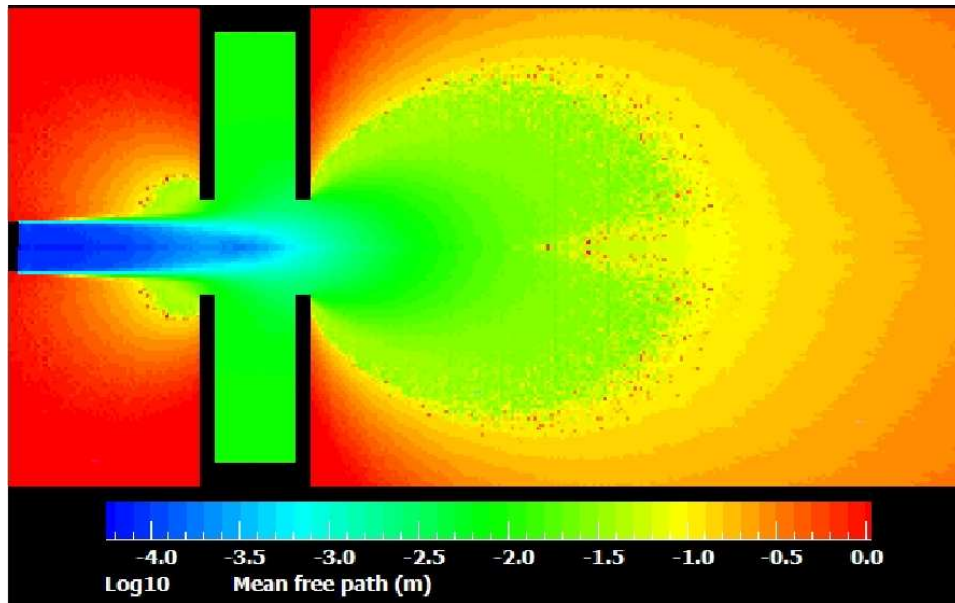


Figure 5.32: Simulation results of mean free path of lithium during entrainment. Figure from private communications with Professor Uzi Even at the Sackler School of Chemistry, Tel-Aviv University.

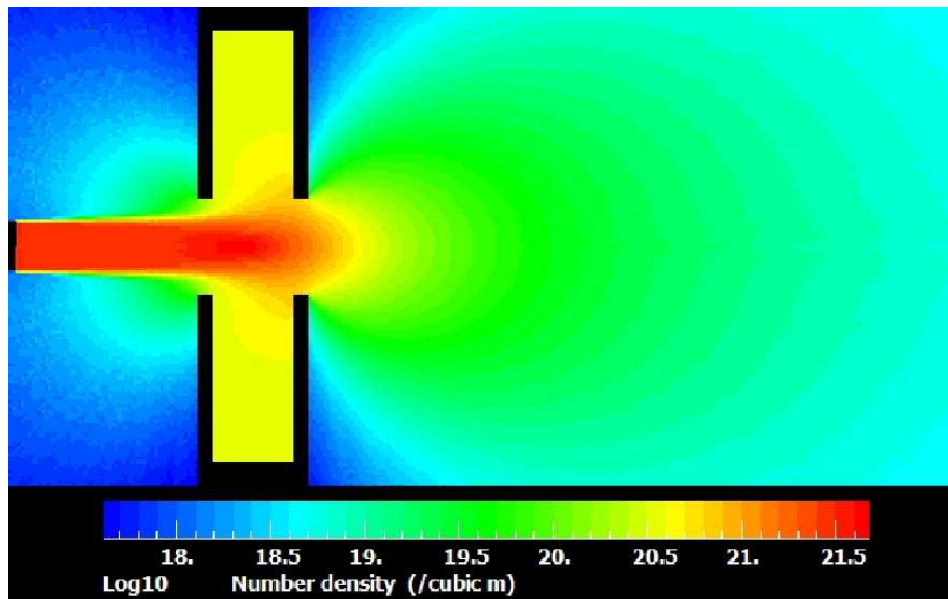


Figure 5.33: Simulation results of the number density of atoms during entrainment. Figure from private communications with Professor Uzi Even at the Sackler School of Chemistry, Tel-Aviv University.

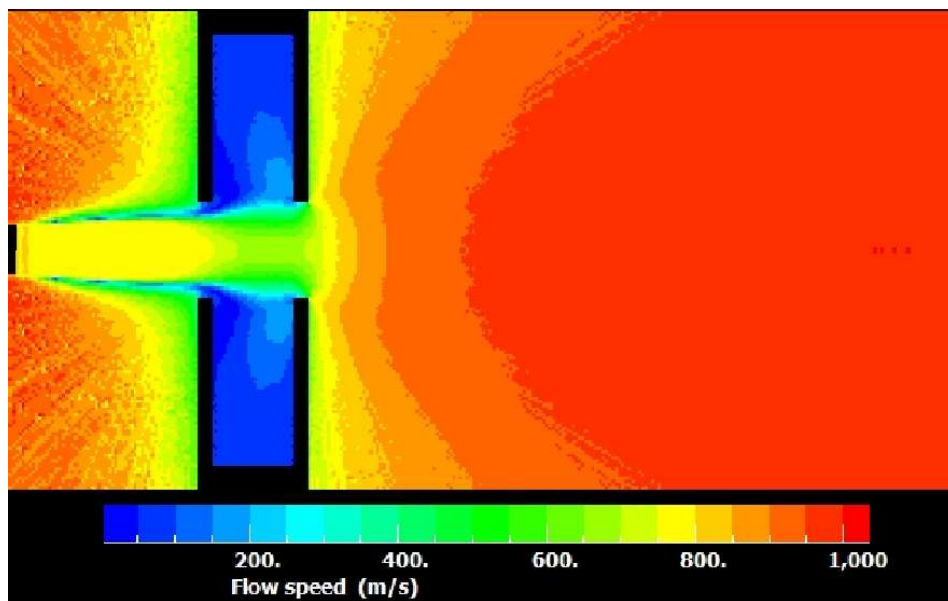


Figure 5.34: Simulation results of the speed of the lithium atoms following entrainment. Figure from private communications with Professor Uzi Even at the Sackler School of Chemistry, Tel-Aviv University.

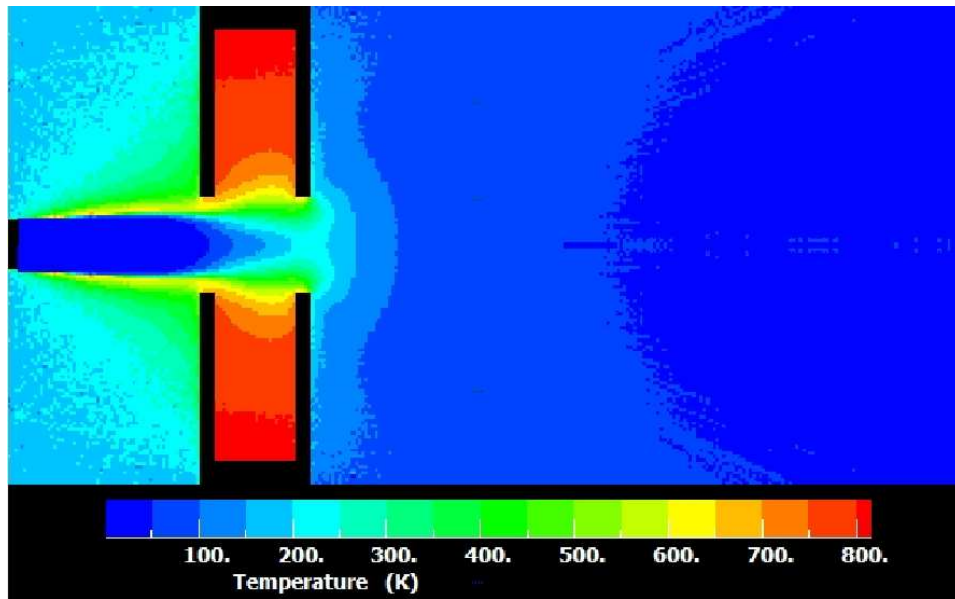


Figure 5.35: Simulation results of the temperature of the lithium atoms following entrainment. As the beam continues to undergo supersonic expansion, it will continue to cool. The beam is heated up by collisions with the lithium, but as the supersonic expansion continues, the beam cools further downstream. Figure from private communications with Professor Uzi Even at the Sackler School of Chemistry, Tel-Aviv University.

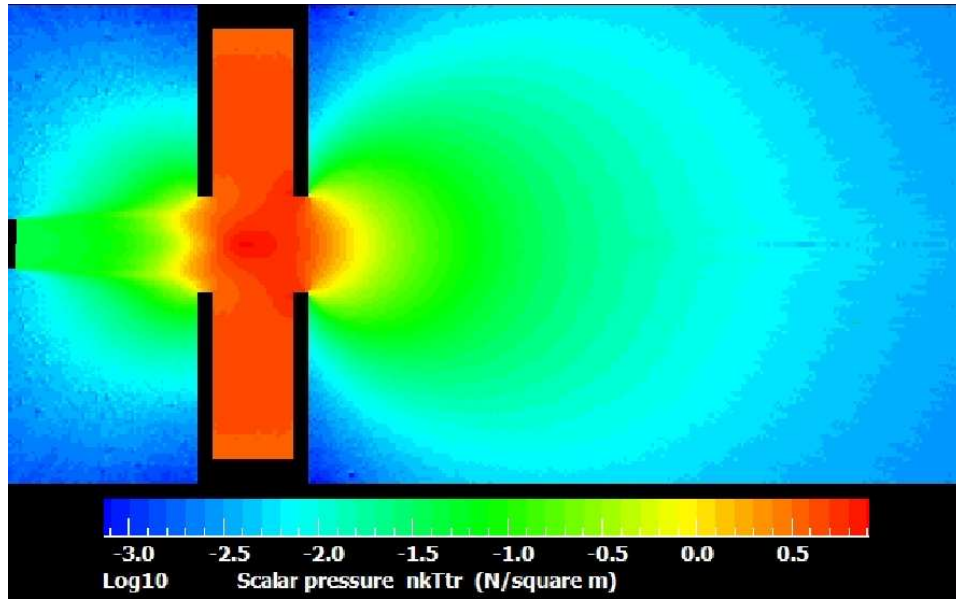


Figure 5.36: Simulation results of the pressure of the lithium atoms following the entrainment. Figure from private communications with Professor Uzi Even at the Sackler School of Chemistry, Tel-Aviv University.

SNO+ needs approximately 50 kg of enriched ^{150}Nd . The following calculation indicates how this method of isotope separation could ultimately benefit their experiment. Assuming that one could optimize a nozzle to run with a continuous flux equal to the Even-Lavie nozzle's pulsed flux of 4×10^{23} atoms/s/sr in conjunction with a skimmer that is 5 mm in diameter and 15 cm from the nozzle, then the solid angle that contributes to the percentage of the beam that survives the skimmer is:

$$\Omega = \pi r^2 / 4\pi d^2 = (0.0025)^2 / 4(0.10)^2 = 6.94 \times 10^{-5} \quad (5.11)$$

where d is the distance from the nozzle to the skimmer and r is the ra-

diameter of the skimmer. The flux of atoms through the skimmer is, therefore, 2.77×10^{19} atoms/s, and with 10% Nd-entrainment, 2.77×10^{18} atoms/s are neodymium, and since the natural abundance of ^{150}Nd is 5.6%, then 1.56×10^{17} of those are ^{150}Nd . If we collect 23% of the available ^{150}Nd , then in the course of a year we can collect:

$$(1.56 \times 10^{17})(60)(60)(24)(365)(0.150)(0.23)/(6.02 \times 10^{23}) = 0.29 \text{ kg/year} \quad (5.12)$$

of ^{150}Nd at 98% purity using a single separation setup with a magnetic guiding region that is only 2 m long. While this would require approximately 170 individual setups to achieve 50 kg, one could reduce the required scaling by optimizing the placement of the skimmer, using a single laser for multiple setups, and using multiple nozzles within a single setup. For example, simply placing the skimmer 10 cm instead of 15 cm from the nozzle would reduce the number of required setups by half, assuming that the beam flow was not disrupted too significantly by the closer placement. One could also consider entraining neodymium into a heavier gas than neon, which would cause the beam velocity to be slower than 500 m/s, meaning that more of the ^{150}Nd could be collected in each setup. Currently we assume a skimmer with a 5 mm diameter, which is conservative; beam testing would be required to determine how much larger the skimmer could be without disrupting the beam flow.

While the ability to change the magnetic state of a particular isotope and deflect it using a magnetic field is certainly not a new discovery, that capability alone cannot impact the industry of isotope separation. Previous experiments conducted decades ago have demonstrated isotopically selective magnetic deflection [83, 96], but the beam fluxes emerging from their sources

were typically on the order of 10^9 atoms/s, not including factors of isotopic abundance. In the experimental setup discussed here, we estimate achieving a flux of $10^{17} - 10^{18}$ atoms/s, and rather than being limited to working with atoms in stable gaseous compounds, we can apply our separation technique to almost every element in the periodic table. Hopefully this new approach to isotope separation can aid in the separation of ^{150}Nd , as well as other isotopes of interest to physics, medicine, and industry.

Chapter 6

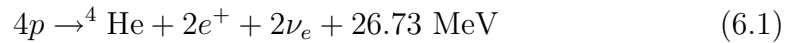
Searching for Supernova Neutrino Bursts in SNO

For more than two decades physicists have been exploring the possibility of using neutrinos to investigate astronomical phenomena like supernovae. Neutrino astronomy is a relatively new field, and as techniques develop to better explore it, it promises to deliver significant new insights into both neutrino physics and astrophysics. This chapter discusses one specific example of those techniques in detail, summarizing work I did with the SNO collaboration in searching their dataset for a supernova neutrino signal. The chapter begins with an overview of the SNO detector, followed by an introduction to supernova physics and the process of core collapse. The bulk of the chapter then details the analysis I developed to search for a supernova neutrino signal in SNO's data and differentiate it from any potential background signal. I conclude by discussing the results of the search and its overall sensitivity to potential supernovae.

6.1 Sudbury Neutrino Observatory

6.1.1 Introduction

The energy powering our sun comes from nuclear fusion, in which protons are converted into α particles, positrons, neutrinos, and surplus energy:



This reaction can proceed through different channels, producing neutrinos of very different energies. The primary source of neutrinos in the sun is $p - p$ reactions, which produce neutrinos of very low energies ($E_\nu < 0.42 \text{ MeV}$):



The largest flux of high energy solar neutrinos comes from the ${}^8\text{B}$ reaction, which results in neutrinos of energies as high as 15 MeV:



As discussed in Chapter 2, the first solar neutrino observations indicated a large deficit of neutrinos coming from the sun compared with what was predicted by the standard solar model (SSM). Since those experiments were sensitive almost entirely to electron neutrinos, theorists postulated that neutrino flavor oscillations could explain the deficit, but the reliability of the SSM predictions was uncertain. The Sudbury Neutrino Observatory (SNO), which took data from May 1999 to November 2006, was unique in its ability to determine not only the flux of electron neutrinos but also the total flux of

all flavors of neutrinos.

SNO ultimately confirmed that the SSM correctly predicted the solar neutrino flux, but by the time the neutrinos reached earth, they were no longer all electron flavored. Neutrino oscillation models explained SNO's results extremely well, and those results played a significant role in establishing that neutrinos were oscillating and therefore had nonzero mass.

6.1.2 The Detector

The SNO detector [97] is an imaging water Cherenkov detector located at a depth of 6800 ft (5890 m of water equivalent) in the Vale Inco., Ltd. Creighton mine near Sudbury, Ontario, Canada. SNO detected neutrinos using an ultra-pure (99.917%) heavy water target contained in a transparent acrylic spherical shell 12 m in diameter, shown in Figure 6.1. The acrylic vessel held 1000 tonnes of heavy water and was suspended by nylon ropes. An acrylic chimney provided access to the main shell volume for circulation piping to purify the heavy water and for deployment of calibration sources. Outside the acrylic vessel was a stainless steel geodesic sphere to which 9546 photomultiplier tubes (PMTs) were mounted. Between the acrylic vessel and the PMT support structure (PSUP) was 1700 tonnes of light water to shield the D_2O target from contamination by external radioactivity from the PMTs and the support structure.

The PMTs were R1408 Hamamatsu tubes with a 20 cm diameter that were operated at approximately 2000 V. The PMTs attached to this support structure were 8.4 m from the center of the main D_2O volume, and including reflective concentrators that were designed to increase the effective photo-

cathode coverage, the total photocathode coverage in SNO was $\sim 55\%$. For energies typical of ^8B neutrino interactions, the PMTs were likely to only generate one photoelectron at most, meaning that the time of the PMT hit is a more useful parameter in reconstruction than the charge. Generally SNO detected 8-9 photoelectrons per MeV of kinetic energy for an electron in the D_2O volume. Stray magnetic fields affected the trajectories of photoelectrons within the PMTs, so SNO utilized large “compensation coils” to offset the vertical component of the earth’s magnetic field, increasing the efficiency of the PMTs by approximately 10%.

Outside the PMT support structure were 5000 tonnes of light water that was monitored by 91 outward-looking (OWL) PMTs, which identified cosmic-ray muons that could create backgrounds that leak into the main detector volume. The acrylic vessel and the support structure hung from the deck at the top of the cavity, and that deck provided a space for the data acquisition electronics.

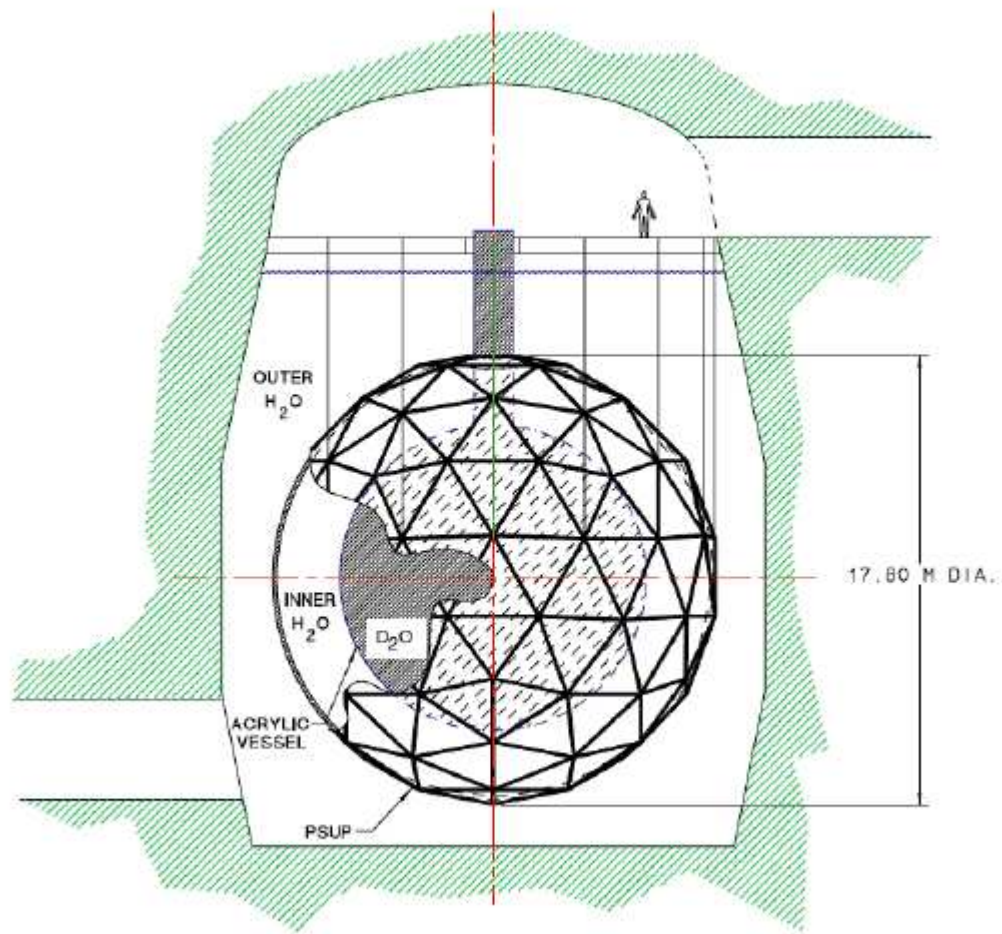


Figure 6.1: Diagram of the SNO detector, originally published in [97]

6.1.3 Data Acquisition Electronics

The SNO data acquisition (DAQ) and triggering electronics were organized into a hierarchy of crates, interface cards, and individual channels. When a photon was incident on one of the 9500 PMTs in the detector, it had a roughly

20% change of releasing a photoelectron from the PMT's photocathode, which started a cascade down the dynode chain. The resultant pulse was approximately 12 ns wide and a few mV in amplitude, and it traveled through a ~ 30 m long 75Ω RG59 coaxial cable from the PSUP to the deck. The cable was attached to a PMT Interface Card (PMTIC), which provided high voltage to the PMT as well as provided a connection to the Front End Cards (FECs, or motherboards) where the signal was processed, digitized, and temporarily stored. Cables from all of the PMTs were approximately the same length to ensure that pulses from simultaneously hit PMTs arrive at the FECs at approximately the same time.

For every group of 32 cables, there was one PMTIC. Each PMTIC had four high voltage relays that allowed the high voltage to be enabled or disabled for eight PMTs at a time. For every PMTIC there was an FEC, and for every FEC there were four daughterboards, each of which received eight PMT signals from the PMTIC. Each PMT signal was routed through a separate channel in the electronics, and the channels were organized in groups of 32 with 8 channels per daughterboard and four daughterboards per motherboard; these groups of 32 channels were referred to as "cards." The cards were arranged in one of 19 "crates," where a crate contained 16 cards, meaning a crate contained 512 channels.

Each crate had a Crate Trigger Card (CTC) that communicated with a detector-wide trigger system, which is described in detail in [98]. The design of the SNO trigger system had to account for the fact that the rate of PMT hits due to low-energy backgrounds alone was enough to swamp the electronics readout setup. Filtering the data in real time was essential, and SNO's trigger system acted as the first step in background removal by requiring that a certain

number of PMTs were hit within a given time. For example, in the D₂O phase the requirement was that at least 16 PMTs were hit within ~ 100 ns (NHIT 100 trigger). Although several different triggers were constructed and utilized, the NHIT 100 trigger was the primary one used in this low-level background removal stage.

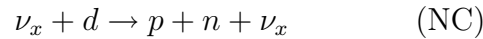
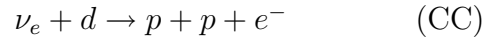
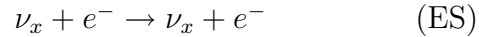
If a channel's signal had an amplitude larger than that channel's discriminator threshold, which was normally $1/4$ of a photoelectron, then the discriminator was fired, and the PMT pulse was integrated. The charge and various channel-specific triggers were then sent to the CTC in the form of analog sums. Each crate's CTC would feed that crate's cards' summed trigger information to a Master Trigger Card, Analog (MTC/A). The MTC/A performed the sum of trigger signals from all 19 crates and compared it to the pre-determined trigger threshold for each type of trigger. If the signal was above threshold, it was sent to the Master Trigger Card, Digital (MTC/D). If that trigger was enabled, then the MTC/D issued a global trigger signal to all crates synchronous with the next tick of an internal 50 MHz clock. It assigned a universal time to the event using a 10 MHz GPS-synchronized clock, along with a backup time stamp from the local 50 MHz clock.

If the MTC/D issued a detector-wide trigger, then each pulse read in through the FECs was processed; otherwise, the event was ignored. A PMT pulse that passed the discriminator threshold would be integrated in a variety of ways and stored until a detector-wide trigger arrived. A Time-to-Amplitude Converter (TAC) recorded the time at which the signal crossed the discriminator threshold. The data was digitized and put into memory to be read out by an Event Builder, which combined each event's PMT data with relevant run header information, which was then stored as part of a run. Even during

long periods of continuous running, SNO broke its data taking time into runs, which varied in length but were on average about 7 hours.

6.1.4 Neutrino Reactions

The D₂O target allowed SNO to detect events via three different reactions:



The elastic scattering (ES) reaction involves bound electrons in the water molecule, so it occurs similarly in both light and heavy water. The charged current (CC) reaction is mediated by the charged W gauge boson, while the neutral current (NC) reaction is mediated by the neutral Z .

When a charged particle passes through water, the surrounding atoms polarize (and subsequently depolarize), and a weak electromagnetic wave spreads out from the instantaneous position of the particle. For a particle traveling more slowly than the phase velocity of light in water ($\sim 0.75c$), the wave-fronts originating at different times can never meet; no interference occurs. For a particle traveling faster than light, the wave-fronts do overlap and cause a cascade of photons which are in phase with each other and can constructively interfere. The photons propagate away from where the interaction occurred in the shape of a cone, and the half-angle of the cone is related to the velocity of the charged particle:

$$\cos\theta_c = \frac{1}{\beta n(\omega)} \quad (6.4)$$

where $n(\omega)$ is the index of refraction in the medium as a function of angular frequency and $\beta = v/c$. This radiation is known as Cherenkov radiation. By detecting this radiation, SNO can reconstruct important information about the original interactions.

The Frank-Tamm formula expresses the amount of Cherenkov radiation emitted as a charged particle moves through a medium at a velocity faster than the phase speed of light in the medium. The energy emitted per unit distance along the path of the particle is [99]:

$$\left(\frac{dE}{dx}\right)_{\text{rad}} = \frac{(ze)^2}{c^2} \int_{\epsilon(\omega) > (1/\beta^2)} \omega \left(1 - \frac{1}{\beta^2 \epsilon(\omega)}\right) d\omega \quad (6.5)$$

where $\epsilon(\omega)$ is the dielectric constant of the medium. Higher energy particles have longer pathlengths in the detector and therefore produce more photons. When the index of refraction can be considered approximately constant, the intensity of the radiation is approximately:

$$\frac{dI}{d\omega} = \frac{\omega e^2 L \sin^2 \theta_c}{c^2} \quad (6.6)$$

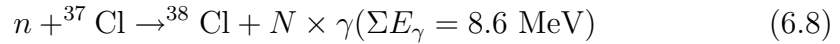
Using this formula to express the number of photons per unit wavelength implies that $dN/d\lambda = 1/\lambda^2$. Unlike fluorescence or emission spectra, Cherenkov radiation does not have characteristic spectral peaks. Higher frequencies are more intense in Cherenkov radiation, and in fact much of the Cherenkov spectrum emitted within SNO is in the ultraviolet. The acrylic vessel is 5.5 cm thick, meaning that the Cherenkov photons must pass through at least 5.5 cm of acrylic in order to be detected by the PMTs. Ordinary acrylic tends to be UV-absorbing, so SNO had to acquire a special type of UV-transmitting

acrylic that has an attenuation length of 5.5 cm for 320 nm light.

In the CC and ES reactions the outgoing electron produces Cherenkov light that SNO can directly detect. The NC current is traditionally more difficult to detect because it does not produce a relativistic charged particle, but it does produce a free neutron that SNO can detect in several different ways. In Phase I, also called the “D₂O phase,” the target volume was filled simply with heavy water, and free neutrons were detected through the following interaction:



In Phase II, also called the “SALT phase,” NaCl was added to the heavy water (0.2% by mass), which allowed free neutron detection via:



SNO also ran with a third phase known as the “NCD phase,” in which the collaboration used proportional counters filled with ³He to detect neutrons through the extremely high neutron capture cross section on ³He, but my analysis will focus just on Phase I and Phase II.

The NC reaction allowed SNO to detect all neutrino flavors while the CC reaction was exclusive to ν_e s because the ⁸B neutrinos from the sun are not energetic enough to produce a muon in the center-of-mass frame of the interaction. The ES reaction is primarily sensitive to ν_e s, but to other flavors as well, with a cross section approximately six times smaller. Additionally, SNO can see $\bar{\nu}_e$ s through the inverse β decay on deuterium and hydrogen, as well as through elastic scattering:

$$\bar{\nu}_e + d \rightarrow n + n + e^+$$

$$\bar{\nu}_e + p \rightarrow n + e^+$$

$$\bar{\nu}_e + e^- \rightarrow \bar{\nu}_e + e^-$$

The first reaction can provide a triple coincidence between the two neutrons and the positron, but it has a relatively small cross section. The second reaction has a much higher cross section but occurs only in SNO's 1700 tonne light water shield, which sits outside the acrylic vessel. For this analysis we have focused only on the D₂O region. Additional reactions on oxygen isotopes are also possible, but the rarity of ¹⁷O and ¹⁸O in either the H₂O or D₂O volumes makes the event rate from these processes very low.

6.1.5 Standard SNO Backgrounds

SNO's primary goal was to detect ⁸B solar neutrinos via Cherenkov radiation, and the experiment had to carefully remove a number of backgrounds in order to confidently identify their signal. The most basic background SNO had to eliminate was spurious neutrons, which could easily mimic the neutrons produced in NC neutrino reactions. Strategically locating SNO under ~ 6000 meter-water-equivalent (mwe) of rock provided enough shielding that only about 65 muons per day entered the detector. Figure 6.2 shows how SNO's muon rate compares to other underground laboratories. Such muons were tagged based on their Cherenkov signal in the light water, and a 20 s deadtime cut was applied after one entered the detector in order to remove spallation neutrons and short-lived isotopes that could be produced by a muon. The outer light water provided additional shielding from neutrons that could come from the cavity's rock wall.

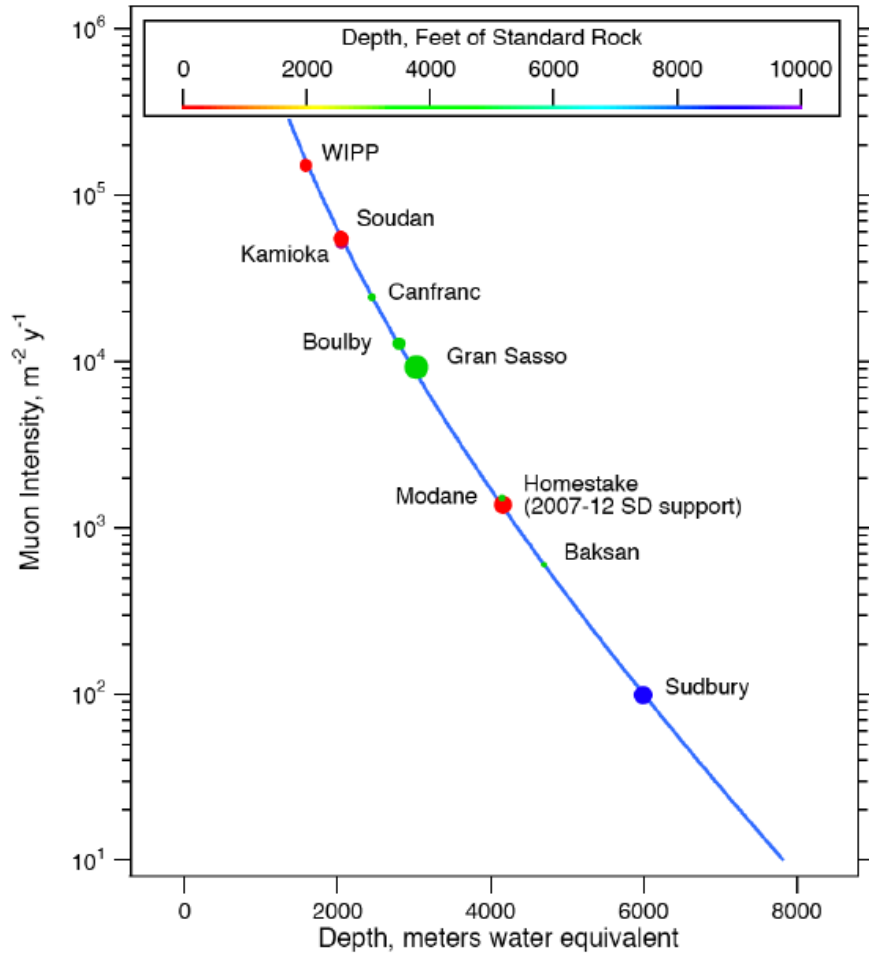


Figure 6.2: Integrated muon flux for multiple laboratories as a function of depth. The relative size of the laboratory is indicated by the size of its circle. Figure taken from [100]

Obviously SNO also had to worry about radioactive background contamination. Many steps were taken to ensure that the radioactive contamination levels were low, but some decay products from ^{238}U and ^{232}Th still re-

mained. Two decay products that caused SNO particular problems were ^{214}Bi and ^{208}Tl , which each product γ rays above the deuteron photodisintegration energy threshold of 2.2 MeV, interfering with SNO's NC signal. These low background levels were carefully measured by assaying the water to determine the amount of uranium and thorium that were present.

6.1.6 Calibrations

Frequent calibration of the SNO detector enabled a proper understanding of how the signals read out by the electronics relate to actual physical quantities. Two types of electronic calibration runs were performed in order to minimize the effect of drift in the response of the charge integrators and the analog-to-digital converters (ADCs). In a pedestal run the discriminator was fired with no incoming pulse. The input signal was then integrated according to standard data-taking methods, thereby providing a definition of zero charge on each channel. In a TAC-slope run the pedestals were fired at various separate time intervals relative to the global trigger, generating a slope of the time-to-amplitude converter that allowed a recorded ADC value from a TAC to be converted to a time in nanoseconds for the channel hit.

A variety of radioactive sources were used to calibrate the detector's response to different types of signals [101, 102, 103]. The “neck” of the acrylic vessel, a 1.46 m wide opening, allowed calibration sources to be placed inside the target volume. The sources could be placed at multiple points, varying not only in the up-and-down z-direction but also along the x and y horizontal plane. Some sources could also be deployed in the light water. A few of the most important calibration sources are summarized below:

- ^{16}N : This source was primarily used to calibrate the detector's light collection efficiency, as well as systematic uncertainties in the energy reconstruction as a function of position and time. Gaseous ^{16}N was pumped down an umbilical line to a stainless steel decay chamber, where it underwent β decay to an excited state of ^{16}O , which proceeded to emit a 6.13 MeV gamma ray. The initial beta is observed by a scintillator and PMT in the source, providing a tag to separate ^{16}N events from random backgrounds.
- Laserball: While ^{16}N was used to set the global PMT efficiency, the laserball was primarily used to calibrate the relative PMT efficiencies and timings. The laserball is constructed from a dye laser of adjustable wavelength that is used to send monochromatic light down a fiber to a diffuser ball. The laserball therefore creates a short isotropic light pulse from a fixed, well-defined location. By moving the source off-center, one can extract the attenuation lengths in the optical media as well as the PMT angular response.
- ^8Li : This source undergoes β decay with an endpoint of 14 MeV, and it is used to study energy reconstruction and uncertainties. The ^8Li is transported in a helium carrier gas through an umbilical line to a decay chamber that can be lowered into the detector, and the chamber walls are thin enough to allow most of the β s to escape.
- ^{252}Cf : This source was used to determine neutron capture efficiencies. ^{252}Cf undergoes spontaneous fission, producing gamma rays and one or more neutrons. On average ^{252}Cf decays produce ~ 4 neutrons and ~ 20 low energy gamma rays.

- **Radon Spike:** This source was used for the low energy background calibration. Radon-enriched D₂O was injected into the detector and mixed, providing a distributed source of uranium chain decays without any container that might absorb Cherenkov photons. The radon was later removed through the normal purification process. Radon spikes were deliberately introduced in both the heavy and light water regions.

6.1.7 Detector Simulation

The SNO detector was modeled in a simulation program called the SNO Monte Carlo and Analysis (SNOMAN). SNOMAN is a FORTRAN application used to simulate the response of the detector. The Monte Carlo code is a full photon-tracking simulation that begins with seed particles (e , γ , n , μ , ect.) and propagates them through the detector. The calibration measurements discussed above were helpful in providing SNOMAN with realistic physical parameters like optical constants and energy scales. The physics governing electrons and gammas was modeled using code from EGS4 [104], which computes energy loss from ionization, Compton scattering, pair production, and multiple scattering. The production of Cherenkov light was added to the simulation by seeding photon vertices along each segment of the electron track. Neutron propagation and capture are calculated with MCNP [105]. Higher energy particles like muons and electrons above 2 GeV are simulated with LEPTO [106], and hadrons are simulated using FLUKA [107] and GCALOR [108], all of which are maintained by the CERNLIB software library.

SNOMAN code reads in dimensions, materials, and optical properties of each element in the SNO detector, enabling particle tracking. The par-

ticle tracking code also handles photon propagation, along with reflection, refraction, Rayleigh scattering, and absorption. Once photons enter the PMT region, one can either enable a full 3D photon tracking model that includes detailed reconstructions of the PMTs, or one can opt to use a less-detailed approximation that allows for much faster running. If the photon produces a photoelectron in the PMT, a simulation of the DAQ integrates the pulse and models the trigger system. The code generates a structure for the event that is very similar to that produced by the real detector, and a user-supplied command file can initiate analysis tasks such as position reconstruction, energy estimation, application of cuts, and generation of output files in either HBOOK or ROOT formats.

6.1.8 Event Reconstruction

In order for SNO to extract a meaningful signal, we utilized variables such as the effective kinetic energy (T_{eff}), which is the estimated energy assuming the event consisted of a single electron, as well as the cubed of the reconstructed radial position of the event. We examined the direction of the event relative to the direction of a neutrino arriving from the sun. We also developed an “isotropy” parameter called β_{14} , which quantifies the spatial distribution of the PMT hits in a given event.

SNO utilized PMT hit times and locations in order to reconstruct an event’s position, time, and direction simultaneously using a log-likelihood function. After reconstructing an event’s position, its energy was estimated using an algorithm called FTK that utilized all of the detected PMT hits, including scattered and reflected light. The best value of the effective kinetic energy

was found by maximizing the likelihood given the observed number of hit PMTs and the expected optical effects. Much more detail concerning these reconstruction techniques can be found in reference [18].

6.2 Supernova Neutrino Bursts

6.2.1 Introduction

Although the SNO detector was not designed specifically to search for supernova bursts, its sensitivity to neutrino interactions provided an opportunity to potentially observe a relatively nearby supernova through the neutrinos emitted by a core collapse. A supernova is a highly energetic outburst resulting in the complete disruption of a star. Gravitational collapse, discussed in detail in Section 6.2.2, results when a massive star has exhausted its nuclear fuel. Although not all supernovae undergo core collapse, for most of this thesis I use the term “supernova” to refer to a supernova initiated by gravitational core collapse, a process which is predicted to release very large numbers of neutrinos.

Supernova neutrinos offer unique insights into both the fundamental nature of neutrinos and the complex process of core collapse. Although theoretical calculations predict that a typical supernova releases approximately 3×10^{53} ergs of gravitational binding energy, 99% of which is carried away by neutrinos, the only supernova neutrinos ever detected came from a single supernova, SN 1987A. SN 1987A resulted from the death of a star in the Large Magellanic Cloud approximately 52 kpc from earth. Three independent neutrino detectors observed a signal from SN 1987A, though the five events from

the Baksan group are not normally included in the official SN 1987A dataset because they occurred somewhat later in time [14]. The nineteen events that are considered part of the standard dataset came from Kamiokande-II and Irvine-Michigan-Brookhaven (IMB) [12, 13]. Many open questions in supernova core-collapse models could be resolved with additional supernova neutrino data, motivating large neutrino detectors to search their datasets for multiple events clustered closely in time, which could be considered candidate supernova neutrino events.

6.2.2 Gravitational Core Collapse

Supernova explosions are categorized into two major types, and the categories were defined based on observed emission spectra before enough was known to base them on the underlying physics mechanisms of the supernovae. Type I supernovae do not have hydrogen in their spectra, while type II supernovae spectra do contain hydrogen. Type I supernovae are further categorized as Ia, Ib, and Ic. Type Ia supernovae are thought to be the thermonuclear explosions of accreting white dwarf stars, and the temperatures they reach are not thought to be high enough to support the processes that would lead to a high neutrino output. Type Ib and Ic are more similar to type II because all of them result from the iron core of a massive star collapsing into a neutron star or black hole. The spectra of Ib and Ic do not contain hydrogen because they have lost some of their outer layers to a stellar wind before the collapse. The following description of gravitational core collapse applies to types II, Ib, and Ic supernovae, which occur more frequently than type Ia.

Gravitational collapse of an astronomical body occurs when all other

forces fail to supply a sufficiently high pressure to counterbalance gravity and keep the massive body in hydrostatic equilibrium. In the core of a star the fusion of hydrogen into helium releases thermal energy that creates an outward pressure, preventing gravitational collapse. When the core's supply of hydrogen is exhausted, the core begins to collapse due to the gravitational pressure from the attraction of mass in the outer shell. As the core begins to collapse the pressure and temperature increase, enabling the helium to begin fusing into carbon, which releases enough thermal energy to again balance the gravitational pressure. As this process progresses, successively producing oxygen, magnesium, and other heavier elements, the core becomes layered with a hydrogen-fusion outer layer, followed by other layers formed by the fusion of other elements. Each time the core collapses, the collapse is halted by the initiation of the fusion of even heavier elements at even higher temperatures and pressures. Each layer burns not only hotter but also faster than the previous layer, culminating in the fusion of silicon to form nickel, which maintains hydrostatic equilibrium for just a few days at most [109]. Nickel is the final fusion product, though it produces ^{56}Fe through radioactive decay, leaving a nickel-iron core that cannot produce the outward pressure necessary to support the star against gravitational collapse. The core collapse is delayed by the degeneracy pressure of the electrons due to Pauli's exclusion principle, but once the core's mass exceeds the Chandrasekhar limit (~ 1.3 solar masses), even the degeneracy pressure fails to prevent the collapse of the star. The Chandrasekhar limit is defined as:

$$M_{\text{Ch}} = 5.8Y_e^2 M_{\odot} \quad (6.9)$$

where $Y_e^2 = Z/A$, the fraction of electrons per nucleon, and M_\odot is the solar mass. Table 6.1 summarizes the evolution of a 15-solar mass star as it expends its nuclear fuel.

As the core increases in temperature and density, photodisintegration gamma rays decompose iron into helium nuclei and free neutrons. This process is endothermic and therefore reduces the average kinetic energy of the particles in the core, which results in decreased pressure to balance the collapse. Electrons and protons undergo inverse β decay ($e^- + p \rightarrow n + \nu_e$), producing a huge release of neutrinos known as the “neutronization burst.” Of the more than 10^{53} erg (or 10^{46} J) of energy radiated away by neutrinos in a supernova, approximately 10^{51} erg of that occurs in the form of ν_e s during the neutronization burst. Neutronization decreases the number of particles in the core, which also decreases the pressure and accelerates collapse.

Core collapse continues and electron neutrinos diffuse out of the core until its density approaches $\sim 10^{12}$ g/cm³, at which point the mean free path for NC ν_e scattering becomes less than the size of the core for time scales on the order of milliseconds. Neutrinos within this very dense core are thus considered to be trapped. Collapse continues until the inner core finally reaches a density comparable to that of an atomic nucleus. The degeneracy pressure of the neutrons then halts the collapse, and the infalling matter rebounds, producing a shock wave that propagates outward. The shock wave is a discontinuity in pressure, density, and temperature moving at about 70 km/ms, and its effect is to compress and heat the matter as it passes through it.

Approximately 1 ms after the bounce, the shock wave hits the point at which the core is no longer opaque to neutrinos, and the high temperatures behind the shock wave enable creation of all flavors of neutrinos through a

variety of processes, including pair annihilation ($\gamma + \gamma \rightleftharpoons e^+ + e^- \rightarrow \nu + \bar{\nu}$), plasmon decay (*plasmon excitation* $\rightarrow e^+ + e^- \rightarrow \nu + \bar{\nu}$), photoneutrino processes ($\gamma + e^- \rightarrow e^- + \nu + \bar{\nu}$), and Bremsstrahlung ($e^- + (A, Z) \rightarrow (A, Z) + e^- + \nu + \bar{\nu}$). Photoneutrino processes dominate at lower temperatures ($10^8 - 10^9$ K), while the main contributions at higher temperature ($10^9 - 10^{10}$ K) are due to pair production. Plasma processes dominate at high densities over the full range of temperatures [110].

This shock wave is not currently believed to be directly responsible for the supernova explosion. Models indicate that once the shock wave is a few hundred kilometers from the center of the star, both the shock wave and the explosion stall. The actual supernova explosion is not well understood, and neutrino reheating may play a role in allowing the outer layers of the core to reabsorb enough energy to produce the visible explosion. After the explosion, the remaining neutron star continues to emit $\nu\bar{\nu}$ pairs as it cools over a timescale of tens of seconds.

Table 6.1: Evolution of a 15-solar mass star [111].

Stage	Time Scale	Temperature (10^9K)	Density (g/cm^3)	Luminosity (solar units)	ν loss (solar units)
Hydrogen	11 My	0.035	5.8	28,000	1800
Helium	2.0 My	0.18	1390	44,000	1900
Carbon	2000 y	0.81	2.8×10^5	72,000	3.7×10^5
Neon	0.7 y	1.6	1.2×10^7	75,000	1.4×10^8
Oxygen	2.6 y	1.9	8.8×10^6	75,000	9.1×10^8
Silicon	18 d	3.3	4.8×10^7	75,000	1.3×10^{11}
Iron core collapse	~ 1 s	> 7.1	$> 7.3 \times 10^9$	75,000	$> 3.6 \times 10^{15}$

6.2.3 Neutrino Energy and Time Distributions

Almost all of the star's binding energy, approximately $1.5 - 4.5 \times 10^{53}$ erg, is eventually radiated away by neutrinos, and the neutronization burst accounts for $\sim 2 \times 10^{51}$ erg of that [112]. While only ν_e 's are emitted during the neutronization burst, afterward all neutrino flavors are emitted with approximately the same luminosity. The average energies are different for different flavors, and though the exact predictions vary slightly among supernova models, typical values are [112]:

$$\langle E_{\nu_e} \rangle = 13 \text{ MeV} \quad (6.10)$$

$$\langle E_{\bar{\nu}_e} \rangle = 16 \text{ MeV} \quad (6.11)$$

$$\langle E_{\nu_x} \rangle = 23 \text{ MeV} \quad (6.12)$$

where ν_x indicates ν_μ , ν_τ , and their antineutrinos. Since the ν_μ and ν_τ flavors can only interact in matter through the NC interaction, the supernova is more transparent to them. Their observed energy is higher since they are produced deeper in the core where the temperature is higher. The neutrino decoupling occurs in neutron rich matter, which is less transparent to ν_e than to $\bar{\nu}_e$, meaning that the $\bar{\nu}_e$ decouple at a higher temperature, leading to the generally predicted energy hierarchy: $E_{\nu_x} > E_{\bar{\nu}_e} > E_{\nu_e}$. Figure 6.3 shows the expected energy distributions for supernova neutrinos in a simulation modeled closely on SN 1987A where the progenitor is a main-sequence star of about $20 M_\odot$. Figure 6.4 shows the neutrino luminosity as a function of time for the same simulation, and Figure 6.5 shows both energy and luminosity on a log-scale.

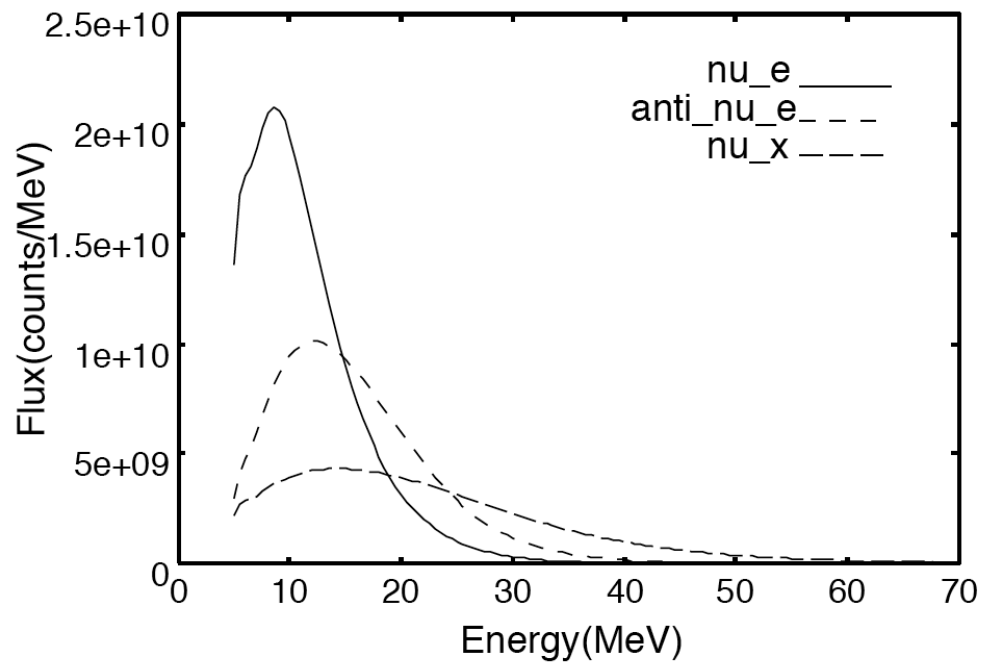


Figure 6.3: Expected distribution of original energies for supernova neutrinos. Oscillation effects have not been included [113].

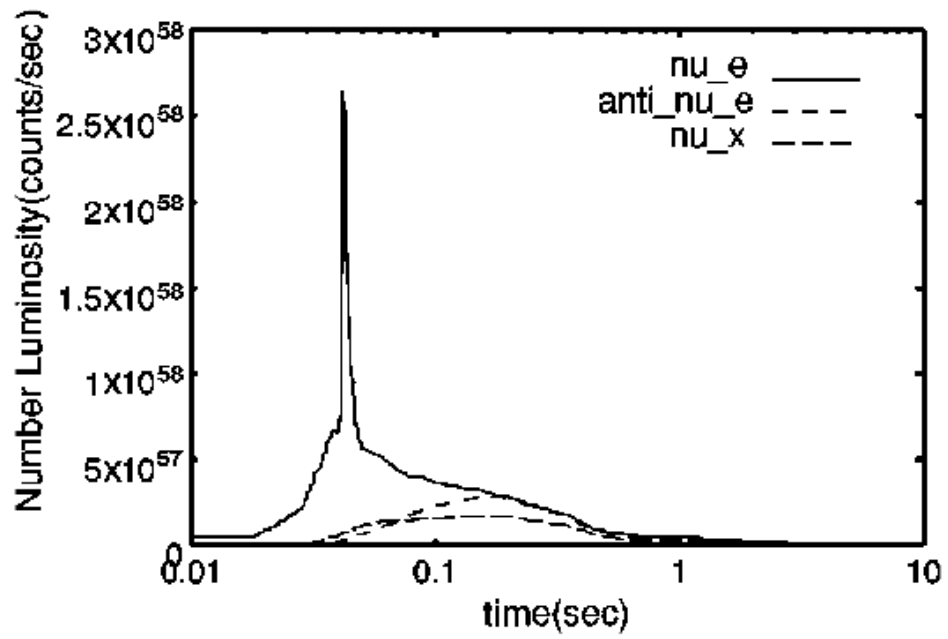


Figure 6.4: Neutrino luminosity as a function of time relative to core collapse without corrections for neutrino oscillations. [113].

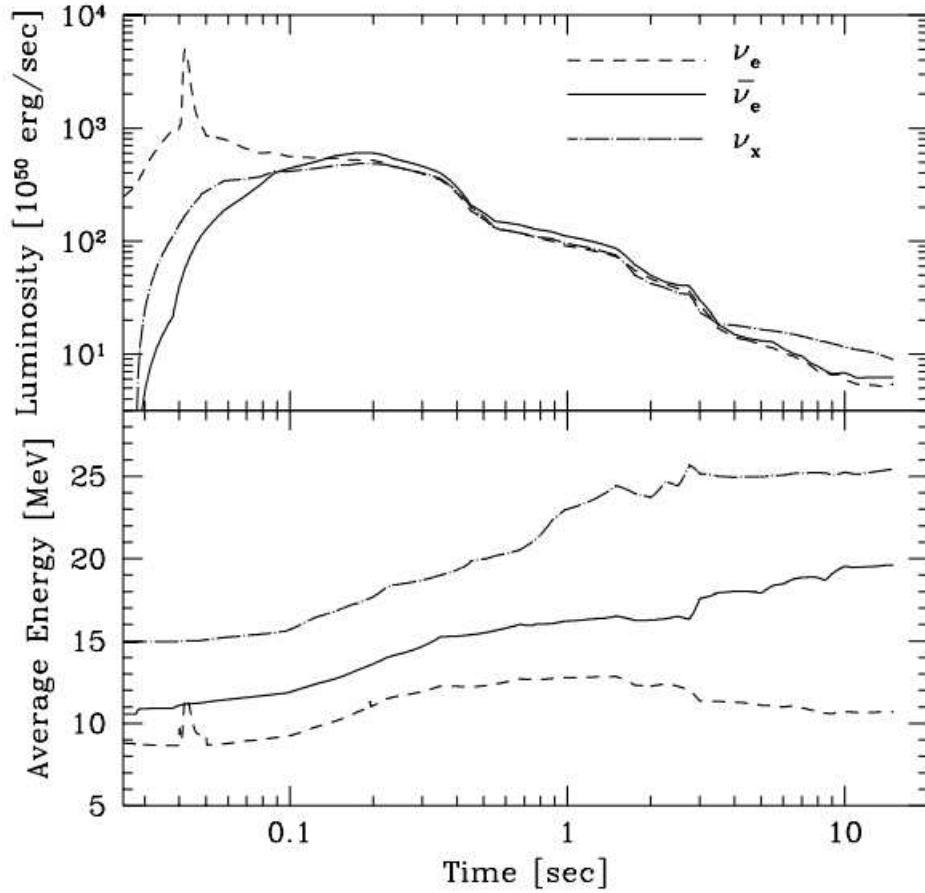


Figure 6.5: Neutrino energy and luminosity vs time on a log scale without corrections for neutrino oscillations [112].

6.2.4 Supernova Models

Many models exist to simulate gravitational core-collapse, and they often vary in the exact energy and time spectra of the emitted neutrinos. The most comprehensive model, accounting for the evolution of the neutrino flux in both time and energy, is the so-called Burrows model [114, 115], upon which many super-

nova simulations are based. The Burrows model began as a one-dimensional, general-relativistic hydrodynamic code that incorporated the neutrino transport of three flavors of neutrinos and their antiparticles. It later evolved to include two dimensions to account for the fact that the supernova is not perfectly spherically symmetric. The dominant relativistic effects include the redshift correction and the spatial volume contraction, and the hydrodynamics utilized has been extended to include the neutrino couplings to matter.

Other models, such as Beacom and Vogel or Bruenn-Mezzacappa, focus on specific aspects of the supernova process like timing or relativistic effects, and consequently they place more emphasis on modeling one feature of the supernova's behavior than on modeling the entire system as a whole. For example, the Beacom and Vogel model was created specifically to study timing distributions, and consequently it does not even include the robustly predicted neutronization burst. For the remainder of this chapter, I use the Burrows model to discuss our expectations for a "standard" supernova, always remembering that additional supernova neutrino data could substantially alter our current conceptions of a "standard" supernova.

6.3 SNO's Supernova Detection Potential

Although no supernovae were optically detected during the livetime of SNO, neutrino bursts could still be found in the SNO dataset from supernovae in satellites of the Milky Way that are hidden by interstellar dust, from non-standard supernovae in our own galaxy with relatively low neutrino fluxes, or from completely unknown and unexpected sources of neutrinos.

Detection of a large number of supernova neutrinos could illuminate

many fundamental questions, possibly even resolving the neutrino hierarchy question as discussed in Section 2.3.4. Large uncertainties associated with neutrino fluxes produced inside supernovae make a straight-forward extraction of the neutrino mixing parameters extremely difficult, motivating one to focus on features of the detected neutrino spectrum that are independent of unknown parameters. One such possibility is a modulation in the neutrino spectrum caused by the MSW H-resonance in the star, which is predicted in the neutrino (antineutrino) channel for the normal (inverted) hierarchy [19]. The passage of supernova shock waves through this density region corresponding to resonant neutrino oscillations with the atmospheric neutrino mass difference imprints specific modulations on both the time and energy spectra of the neutrinos that other effects could not easily mimic [116]. The amplitude of these modulations does depend on the emitted neutrino fluxes, but the specific shape of the modulations is independent of the flux details. Detection of the neutronization peak could also help distinguish various models, particularly if θ_{13} is still unknown [117].

SNO's sensitivity to all neutrino flavors and the comparison of the rates of the different possible reactions provide exciting opportunities to distinguish various supernova models and investigate neutrino properties [118, 119, 120]. During SNO's runtime, it participated in the Supernova Early Warning System (SNEWS), which was designed to notify the astronomical community within minutes of the detection of a large neutrino burst [121]. Although SNO never saw a burst large enough to trigger the early detection system, this system was not designed to look for low-multiplicity bursts. The primary identification criteria for the SNO supernova trigger was a detection of more than 30 events in less than 2 s, and even standard supernova bursts from beyond the Large

Magellanic Cloud would not have met this search criteria.

Even though SNEWS did not detect any high-multiplicity bursts of neutrinos in SNO's data, low-multiplicity bursts would not have triggered the live monitoring system. Such bursts could still contain interesting information, particularly if other neutrino detectors could confirm bursts at similar times, increasing the statistical significance of the detection.

6.4 Super-Kamiokande Triggerless Burst Search

Super-Kamiokande performed a search for bursts within their data set with no optical trigger, and they reported finding no evidence for any bursts [122]. They analyzed data from May 1996 to July 2001, as well as from December 2002 to October 2005. In order to perform their search, they set the length of their search windows, slid those windows through their datasets, and recorded any bursts found within those windows. Once they found a burst, they examined it more closely in order to determine if the burst was likely caused by a background or not. This method is in no way a “blind” analysis, and a more rigorous technique would be to calculate the number of backgrounds expected within the window length, develop methods for removing those backgrounds, and only then perform the search with the understanding that any bursts seen would then be considered non-background bursts. SNO's low multiplicity burst search followed this more rigorous method.

Super-Kamiokande's search utilized a variety of different search windows, each with its own energy threshold. In their first window, which was 20 s long, they looked for bursts of multiplicity ≥ 2 , and it was optimized to detect a signal from a supernova hundreds of kpc from our galaxy. They set a

very high energy threshold of 17 MeV for this window in order to prevent solar neutrino events from swamping a potential supernova signal. In order to look for supernovae that might have occurred closer, Super-Kamiokande performed a search for ≥ 3 events in 0.5 s, ≥ 4 events in 2.0 s, and ≥ 8 events in 10 s. For these search windows, they applied a threshold of 6.5 MeV to the first phase of data (SK-I) and 7.0 MeV to the second phase (SK-II). Super-Kamiokande also optimized a search for neutrinos emitted during the neutronization burst. To focus on the neutronization burst they looked for ≥ 2 events within a window of 1, 10, or 100 ms, where for SK-I the energy threshold was 5.0 MeV and for SK-II it was 7.0 MeV.

When they performed their search, they did observe several bursts. Upon further study, however, they determined that those bursts were caused by mine blasting, mislabeled calibration runs, flasher PMTs, or other backgrounds. In 2381.3 days of livetime, Super-Kamiokande observed no signal that they considered to be a candidate supernova burst.

6.5 SNO Triggerless Burst Search

I searched the SNO dataset for low-multiplicity bursts, which I defined as bursts of two or more events. The search was triggerless; I estimated all of the backgrounds that could mimic a supernova burst signal, and I designed search windows and analysis cuts to ensure that I was 90% confident of not seeing a false burst. I did not examine the real data until I had set all of our search parameters, and I did not change any of those parameters after I performed the search.

6.5.1 Data Set

The data I analyzed include two phases of SNO's operation. Phase I ran from November 1999 to May 2001, and the sensitive volume of the detector was filled only with D₂O. Phase II ran from July 2001 to August 2003, and during this phase NaCl was added to the detector, increasing the sensitivity to the NC reaction through the consequent enhancement of neutron detection efficiency. Phase II began running shortly after Super-Kamiokande's first phase of data taking ended, meaning that the majority of SNO Phase II contains no overlap with the supernova search performed by Super-Kamiokande. Because of the enhanced NC detection efficiency, SNO Phase II provides a higher sensitivity to a potential supernova signal. The total livetime of Phase I was 241.4 days, while the total livetime of Phase II was 388.4 days. The time of each event was provided by a GPS system with a resolution of 100 ns and an accuracy of ~ 300 ns [123].

6.5.2 Confidence Interval

We determined our 90% confidence limit using the Poisson distribution, which says that if the expected number of occurrences in an interval is λ , then the probability of exactly n occurrences is equal to:

$$f(n; \lambda) = \frac{\lambda^n e^{-\lambda}}{n!} \quad (6.13)$$

We treat our total expected backgrounds as the mean of a Poisson distribution. By estimating the number of background bursts that we expect in a given search window, we can then determine the probability that we will observe

exactly 0 background bursts. Conversely, if we want to be 90% confident of seeing 0 background bursts, then the Poisson distribution tells us that we can expect no more than 0.11 background events. In the following sections I describe how we set our search windows, estimated our expected backgrounds, and then designed analysis cuts in order to reduce those expected backgrounds to no more than 0.11 events for each window.

6.5.3 Search Windows

In order to maximize our sensitivity to supernova events, we want to set a long time window and a low energy threshold for the analysis. These requirements, however, must be balanced with the desire to eliminate background coincidences.

Based on the physics of supernovae, we performed the multiplicity two search twice using two different time windows. One time window is a short window (0.05 s), intended to detect neutrinos from a supernova neutronization burst. In the case of a failed supernova, the neutronization burst provides the only potential signal because shortly after the neutronization phase, the supernova collapses into a black hole, abruptly terminating the neutrino signal [124, 125, 126]. These unusual supernovae are of special interest to astronomers, and their neutrino signatures could provide interesting model constraints. The second window is of moderate length (0.2 s for D₂O and 1 s for SALT) to maximize our sensitivity to a standard supernova event. For the D₂O phase, the 0.05 s window had an energy threshold of 5.0 MeV, and the 0.2 s window had a threshold of 6.0 MeV. For the SALT phase, the 0.05 s window had an energy threshold of 6.5 MeV and the 1.0 s window had an en-

ergy threshold of 8.5 MeV. These search windows are summarized in Table 6.2, along with each window’s expected accidental coincidence rate and the neutral current signal acceptance loss that corresponds to the chosen energy threshold.

Table 6.2: The length of the search window and its corresponding energy threshold must be chosen so that the sum of the expected backgrounds in the window do not add to more than 0.11 events. Accidentals are among the most dangerous backgrounds because of their random spatial distribution. As the energy threshold is raised to decrease the chance of backgrounds, some neutral current signal sensitivity is lost.

	Window Length (s)	Energy Threshold (MeV)	Accidentals	NC Signal Loss
D ₂ O, mult=2	0.2	6.0	0.042	73%
D ₂ O, mult=2	0.05	5.0	0.021	44%
D ₂ O, mult=3	10.0	4.5	0.006	34%
SALT, mult=2	1.0	8.5	0.055	96%
SALT, mult=2	0.05	6.5	0.025	65%
SALT, mult=3	10.0	4.5	0.027	26%

The D₂O phase entirely overlaps with the running of Super Kamiokande, while much of the SALT phase does not overlap. Consequently for the D₂O phase we want to maintain some neutral current sensitivity even in our longest search window because we are primarily searching for non-standard supernovae that Super-Kamiokande might not have observed. For the SALT phase we want to maximize overall supernova sensitivity, so one of our search windows is quite large. The 1 s SALT window requires us to raise the energy threshold

high enough that there is very little remaining neutral current signal, but it increases our overall sensitivity.

For the multiplicity three search, the window for each phase is 10 s, and the energy threshold is 4.5 MeV. Primarily because of the low energy threshold available for this search, it provides the best sensitivity to a standard supernova.

In performing the search, if a candidate event was found inside the time window, then the window slid to make that event the beginning of the window before determining the multiplicity seen inside that window, as illustrated in Figure 6.6. This procedure ensured that the window would not miss any candidate bursts by arbitrarily dividing the events into two separate search windows when they could have been in a single one.

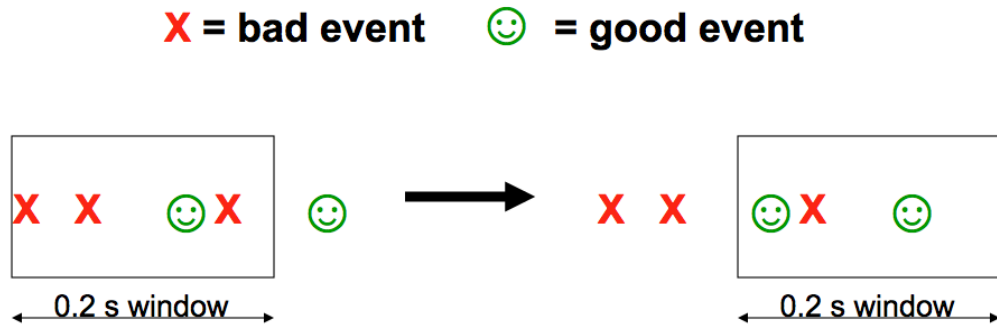


Figure 6.6: If a window observes a good event in the middle of its search, it slides to make that event the first event of the window before determining the burst multiplicity for that window, ensuring that a burst is not arbitrarily separated.

6.6 Backgrounds

6.6.1 Accidentals

In any given time window, the accidental coincidence rate is the average event rate multiplied by the Poissonian probability of one event having already occurred:

$$R_{coinc} = R_{det}^2 \tau e^{-R_{det}\tau} \quad (6.14)$$

where R_{det} is the rate of clean events in the detector (where “clean” events are those that pass the cuts described in Table 6.4), and τ is the length of the analysis window. The number of expected coincidences in the SNO dataset is

$$N_{coinc} = R_{coinc} T \quad (6.15)$$

where T is the length of the SNO detector livetime. For a burst of multiplicity three, the accidental coincidence rate is much lower:

$$R_{coinc}^{mult=3} = \frac{1}{2} R_{det}^3 \tau^2 e^{-R_{det}\tau} \quad (6.16)$$

The number of multiplicity three events due to accidental coincidences is then

$$N_{coinc}^{mult=3} = R_{coinc}^{mult=3} T \quad (6.17)$$

We treat each of these N_{coinc} values as the mean of a Poisson distribution. The accidental background will be one of many sources of backgrounds that we must add together to estimate our total expected backgrounds. Our backgrounds from accidentals, therefore, must be kept quite low, as shown in Ta-

ble 6.2. Figures 6.7 and 6.8 illustrate how much changing the energy threshold for a search window can impact the number of accidental coincidences.

Accidental Coincidences in D2O for different Energy thresholds

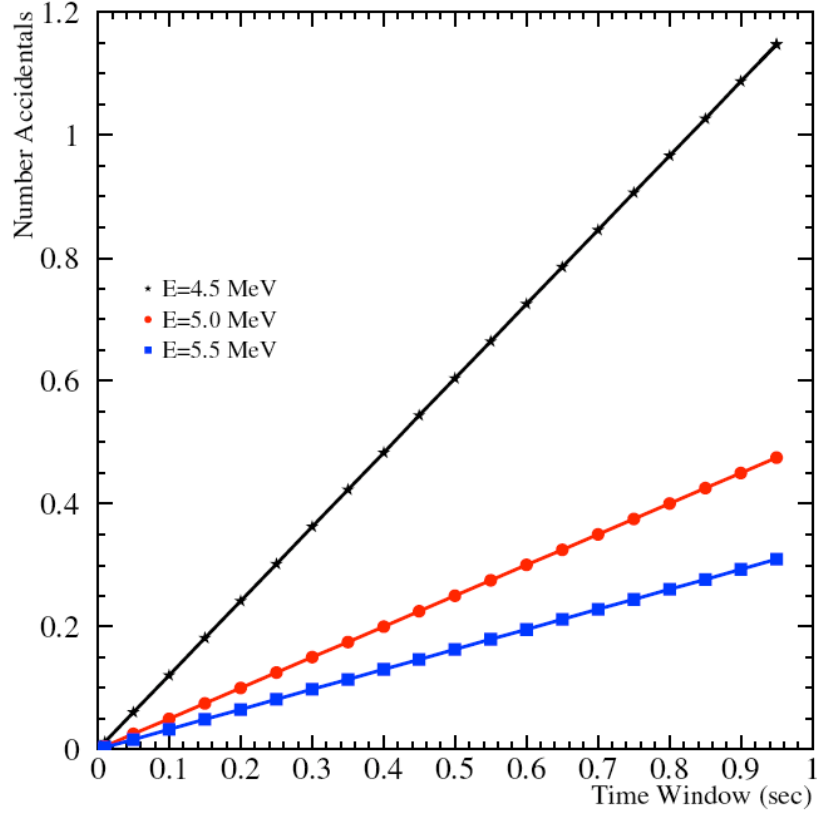


Figure 6.7: Expected values of accidental coincidences for the D₂O phase at three various energy thresholds

Accidental Coincidences in Salt for different Energy thresholds

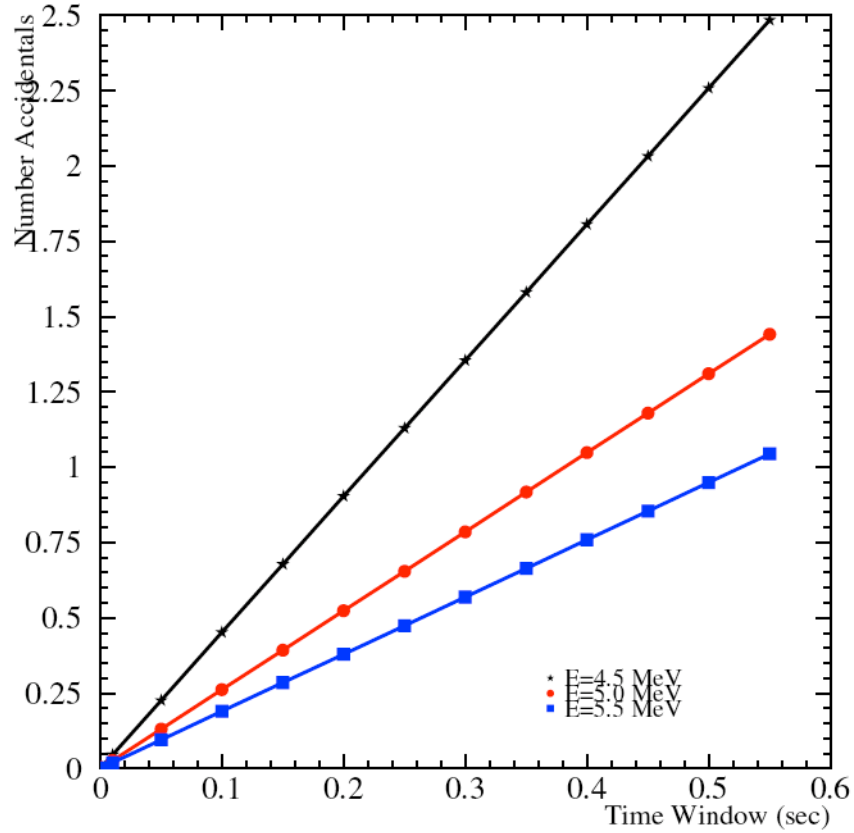


Figure 6.8: Expected values of accidental coincidences for the SALT phase at three various energy thresholds

6.6.2 Physics Backgrounds

The primary difficulty in performing a triggerless burst search is the elimination of background burst events. In addition to the accidental coincidences described above, a large number of physics backgrounds must be estimated

and eliminated. Any physics event that could produce multiple neutrons, thereby mimicking a supernova burst signal, must be estimated. The largest danger in making an estimate is underestimating a particular background, so we were more inclined to be conservative in our estimates whenever we were uncertain in order to reduce the likelihood of seeing a fake burst. Table 6.3 shows our background estimates for each of our search windows. Most of the small multiplicity three backgrounds are conservatively assumed to have upper limits corresponding to the multiplicity two estimates. We added the backgrounds using a simple Monte Carlo that sampled Gaussian and Poissonian distributions for a large number of events for each background. The limits were added assuming they were 90% confidence interval fluctuations of Poissonian processes. Once we estimated the expected backgrounds, we then designed additional analysis cuts to reduce them, as described in Section 6.7.

One of the most significant backgrounds is due to atmospheric neutrinos, which can produce neutrons without any accompanying energy deposit to tag the events. Atmospheric neutrinos result from interactions of cosmic ray protons in the atmosphere such as:

$$p \rightarrow X + \pi^- \rightarrow X + \mu^- + \bar{\nu}_\mu \rightarrow e^- + \bar{\nu}_e + \nu_\mu \quad (6.18)$$

$$p \rightarrow X + \pi^+ \rightarrow X + \mu^+ + \nu_\mu \rightarrow e^+ + \nu_e + \bar{\nu}_\mu \quad (6.19)$$

For both the D₂O and SALT phases, the atmospheric background was estimated with the neutrino-interaction generator NUANCE, whose output was further processed by a full SNO detector simulation. The simulation's atmospheric neutrino energies ranged from 100 MeV to 2 TeV, and flavor oscillation corrections were applied. The systematic error in the NUANCE simulation is

conservatively estimated to be $\pm 20\%$, and it is dominated by uncertainties in the neutrino cross sections. Table 6.3 shows how widely the atmospheric background estimations vary for different search windows and energy thresholds.

Most muons traveling through the SNO detector are vetoed by outward-looking PMTs, and neutrons following these muons are eliminated by a 20 s analysis cut. Some muons, however, do not have enough energy to trigger the outward-looking PMTs and will leak into the detector. Fortunately even these muons are not likely to produce multiple neutrons that could mimic a burst. In the 391-day livetime of the SALT phase, the effect of these leaked muons is estimated in Monte Carlo studies to cause less than 1.35 single-neutron events [127], which implies that less than 0.5 coincidence events is a safe upper limit for both the D₂O and SALT phases.

Although the SNO detector is remarkably clean, some radioactive backgrounds still exist, such as ^{238}U , and spontaneous fission from residual radioactivity can lead to false bursts due to multiple neutron capture. Many of the radioactive backgrounds discussed in previous SNO analyses are not significant in this search because they will not produce bursts of events, but fission neutrons from ^{238}U can create a background burst. The amount of ^{238}U in the detector was measured in September 2003 after the addition of NaCl to the heavy water. This measurement set an upper limit of 0.79 coincidences for Phase I due to spontaneous fission from ^{238}U [128]. In Phase II, the addition of NaCl prevented the use of SNO's reverse osmosis purification system, meaning that more ^{238}U could have been present. For this phase a very conservative upper limit of 10 fission bursts due to ^{238}U was estimated based upon the standard probability of the fission producing various neutron multiplicities [129]. This limit also assumed a 65% detection efficiency for neutrons above 4.5 MeV

and a 40% efficiency for detecting a gamma burst in coincidence with the fission. Figure 6.9 shows the preliminary estimate of the number of events in the SALT phase we can expect from ^{238}U fission.

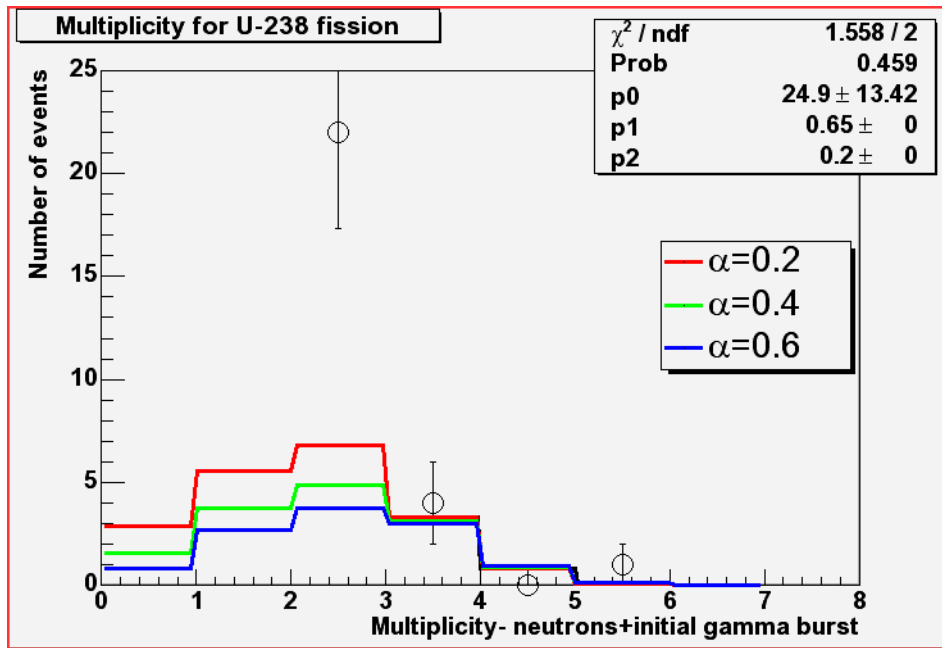


Figure 6.9: Background burst multiplicity expected from ^{238}U fission where α is the efficiency for detecting a gamma burst in coincidence with the fission. Figure taken from [130].

Neutrons in the SNO detector capture on deuterium, producing a γ -ray and tritium. That γ -ray then Compton scatters, producing a Compton electron that will be detected through Cherenkov radiation, and the γ -ray is re-emitted with a lower frequency. This process is the normal way in which neutrons are detected in SNO, but it can lead to a false burst signal if the re-emitted γ -ray is above 2.2 MeV and proceeds to photodisintegrate deuterium,

producing an additional neutron that can also be captured. This photodisintegration background has been estimated to cause 0.00084 coincidences in D₂O [128] and 0.43 ± 0.3 coincidences in SALT [131].

Antineutrinos can also lead to apparent bursts due to the primary positron created in the interaction and the following capture of one or two neutrons. Antineutrinos from radioactive nuclei in the earth surrounding the detector (primarily ²³⁸U and ²³²Th) have energies of 1-2 MeV, and they lead to a negligible background from this process for the D₂O phase [128] and 0.5 ± 0.1 bursts for the SALT phase [132]. Nuclear reactors also produce neutrinos that could eventually interact in the SNO detector, with an average energy of ~ 4 MeV and a cutoff energy around 8 MeV [133]. A study of all commercial reactors within 500 km of SNO determined that the coincidence background from these reactors would be small, 0.019 ± 0.002 coincidences for the D₂O phase [128] and 1.4 ± 0.3 for the SALT phase [132].

During the SNO detector construction, the acrylic was exposed to air containing radon. In the decay chain of radon is ²¹⁰Po, which can decay via α -emission. The α can interact with the carbon in the acrylic, leading to ¹³C(α, n)¹⁶O reactions in which the ¹⁶O will produce a e^+e^- pair or a γ -ray that can photodisintegrate deuterium. The estimates of (α, n) coincidences from Monte Carlo studies of this background are low [131]. Similarly, coincidences due to the diffuse supernova background and to instrumental background events are estimated to be quite low [128, 132], as shown in Table 6.3.

Table 6.3: A summary of the expected backgrounds that could mimic a super-nova burst signal in the SNO dataset. Since the search windows have different energy thresholds, we estimate the backgrounds for each search window for both the D₂O and SALT phases.

Backgrounds	Mult=2 Residuals D ₂ O 0.2s window	Mult=2 Residuals SALT 1s window	Mult=2 Residuals D ₂ O 0.05s window	Mult=2 Residuals SALT 0.05s window	Mult=3 Residuals D ₂ O 10s window	Mult=3 Residuals SALT 10s window
Atmospherics	1.90 ± 0.38	0.57 ± 0.11	4.53 ± 0.91	6.94 ± 1.39	2.47 ± 0.49	10.98 ± 2.20
Muon Spallation	< 0.5	< 0.5	< 0.5	< 0.5	< 0.5	< 0.5
Fission ²³⁸ U	< 0.79	< 10	< 0.79	< 10	< 0.79	< 3
Photoisintegration	< 8x10 ⁻⁴	0.43 ± 0.03	< 8x10 ⁻⁴	0.43 ± 0.03	< 8x10 ⁻⁴	< 0.43
geo- ν	0.0	0.5 ± 0.1	0.0	0.5 ± 0.1	0.0	< 0.5
reactor- ν	0.019 ± 0.002	1.4 ± 0.3	0.019 ± 0.002	1.4 ± 0.3	< 0.019	< 1.4
($\alpha, n e^+ e^-$)	0.02 ± 0.10	0.07 ± 0.07	0.02 ± 0.10	0.07 ± 0.07	< 0.02	< 0.07
($n, 2n$)	< 0.02	< 0.07	< 0.02	< 0.07	< 0.02	< 0.07
DSNB	< 0.005	< 0.005	< 0.005	< 0.005	< 0.005	< 0.005
Instrumentals	< 0.027	< 1	< 0.027	< 1	< 0.027	< 1
Total Backgrounds	2.86 ± 1.05	9.28 ± 2.96	5.48 ± 1.33	15.66 ± 3.27	1.73 ± 0.56	9.52 ± 2.07

6.7 Analysis Cuts

6.7.1 Standard Cuts

We developed a set of analysis cuts, beyond the standard cuts used by other SNO analyses [18, 123], to reduce the level of correlated backgrounds shown in Table 6.3. We utilized a fiducial volume radius of 550 cm, as well as a variety of instrumental cuts based on PMT charge and timing information. Our high level cuts incorporated information such as the isotropy of the detected light and the event's reconstruction quality, but we did not include any of the cuts SNO previously designed to remove bursts from the data set. Instead we designed new cuts that could discriminate between background bursts and potential supernova bursts.

Most of the standard SNO analysis cuts are applicable for this search, with the notable exceptions of two cuts that would remove any potential signal as well as backgrounds since they were designed to remove bursts. The Burst Cut eliminated events where three or more events occurred within 1 ms, while the Missed Muon Follower Cut removed events that occurred within 250 ms of an $\text{NHIT} > 60$ event; neither of those cuts can be utilized in a low-multiplicity burst search. For events whose reconstructed FTK energy was greater than 15.0 MeV, we applied the cuts shown in Table 6.4. For events whose reconstructed FTK energy was less than 15.0 MeV, the full Low Energy Threshold Analysis (LETA) cuts were also applied, and the LETA analysis is described in detail in reference [18].

Table 6.4: Summary of the standard SNO cuts applied to the data

- Reconstructed position < 550 cm
- ITR > 0.55 : The in-time ratio (ITR) compares the prompt hits to the total hits, and events reconstructed at a position far from their true origin tend to have a small ITR
- $0.89 < \theta_{ij} < 1.60$: Events whose true origin is outside the detector but that are misreconstructed inside tend to appear very anisotropic, as can be seen by looking at the charge-weighted mean angle between pairs of PMTs, θ_{ij}
- Retrigger: Tags events that are within $5 \mu\text{s}$ of a previous event.
- QVT: Removes events where the highest charge tube displays abnormal behavior
- Q/NHIT: Tags events whose Q/NHIT ratio is suspiciously low (< 0.25)
- Crate Isotropy: Tags events where more than 70% of the hits occur on one crate and more than 80% of those hits occur on two adjacent cards
- AMB: Cuts events if they lie more than 3.7 sigma away from the mean in either the integral/NHIT or peak/NHIT distributions
- FTS: Tags events where the median time difference of hit PMT pairs within 3 m of each other is too large
- OWL: Tags events in which three or more outward looking PMTs fired
- JUNK: Removes events containing the same PMT more than once, as well as other events involving abnormal electronics
- NECK: Cuts events containing neck tubes
- ESUM: Tags events whose analog sum PMT pulses exceed a certain threshold but which fail many of the other triggers
- QCluster: Tags events that have abnormal charges or are overly clustered (i.e. 6 hits in a paddle card or more than 200 hits in a crate)
- Muon: Tags events that trigger enough OWLs to be considered muons
- Muon follower short: Tags all events in a time window of 20 s following a muon
- In-Time Channel: Tags events having fewer than 60% of the tubes within 93 ns coincidence
- Flasher Geometry: Tags events in a cluster where the separation between the average position of the cluster and the rest of the tubes is great than 12 m
- OWL Trigger: Tags events where the the analog sum of PMT pulses in the OWLs exceeds a charge threshold
- Muon Follower Blindness: When this tag is off, certain muon follower events are allowed to leak through the cuts; it was a blind analysis tool for a previously conducted analysis

6.7.2 High NHIT Cut

To attempt to remove false bursts while leaving most of our supernova signal, we implemented a High NHIT cut. Based on our current understanding of supernovae, any event whose energy reconstructs to more than 80 MeV is far more likely to be an atmospheric event than a supernova event. The High NHIT cut is designed to tag high energy atmospheric events and remove any followers of those events. The High NHIT cut relies on the number of PMTs hit for a given event, which is a very basic parameter free from uncertainties associated with more complicated energy reconstruction algorithms.

By looking at Monte Carlo simulations of isotropic electron events in the SNO detector, I determined a relationship between the number of PMTs hit and the corresponding MeV energy for both the SALT and D₂O phases. I broke the simulations up into roughly 8 MeV regions and plotted the nhit/energy ratio for the events in each region. I fit a Gaussian to the nhit/energy ratio peak and plotted the mean value of the Gaussian vs. energy. Figures 6.10 and 6.11 show the analytic functions that I fit to the curves from those plots for both the D₂O and SALT phases, which allowed me to estimate the expected nhit/energy ratio for any given energy. As the energy of the event increases, multiple hits on a single tube also increase, leading to a slight overall decrease in the nhit/energy ratio. Any event whose NHIT count corresponded to an energy higher than 80 MeV was cut, along with any events following within 600 ms for the D₂O phase (200 ms for the SALT phase). Since the average neutron capture time is 47.58 ms for the D₂O phase and 5.041 ms for the SALT phase, these cuts are large enough to remove any neutrons that might result from the high NHIT event.

Energy-to-NHIT conversion for D2O phase

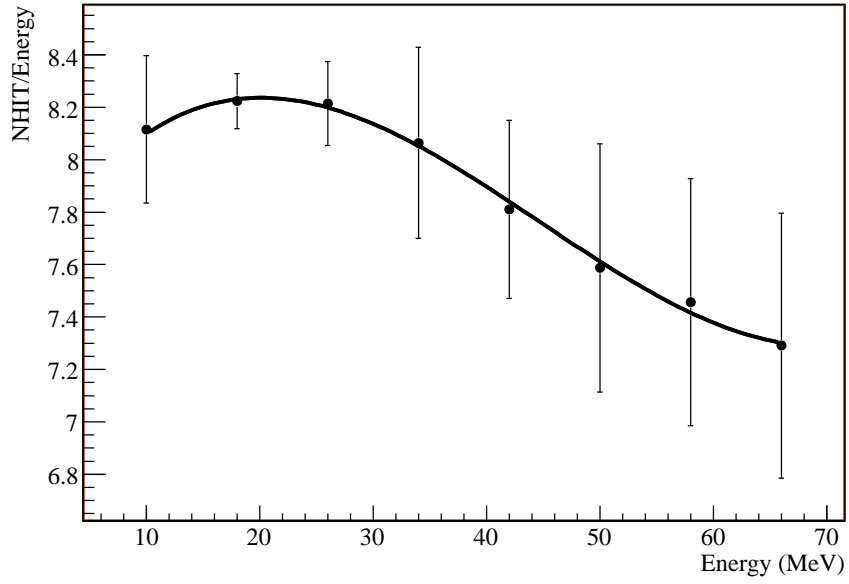


Figure 6.10: Number of PMTs hit vs. energy for a Monte Carlo simulation of isotropic electrons in the SNO detector for the D₂O phase.

Energy-to-NHIT conversion for salt phase

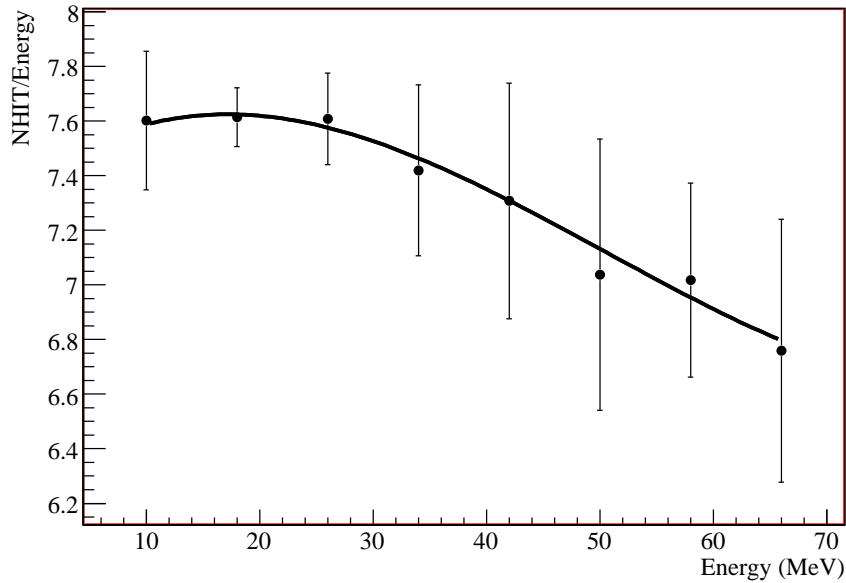


Figure 6.11: Number of PMTs hit vs. energy for a Monte Carlo simulation of isotropic electrons in the SNO detector for the SALT phase.

Figure 6.12 shows readout from the SNO event display illustrating two types of events that are eliminated by the High NHIT cut. Clearly those events should be eliminated, but a 200 ms (or 600 ms) window is applied after such an event that prevents any background related to that high NHIT event from being misidentified as signal. Figure 6.13 illustrates a sample burst that follows an event tagged by the High NHIT cut. That burst would be indistinguishable from legitimate signal burst, but the events fall within the elimination window and would therefore not be mistaken for a supernova.

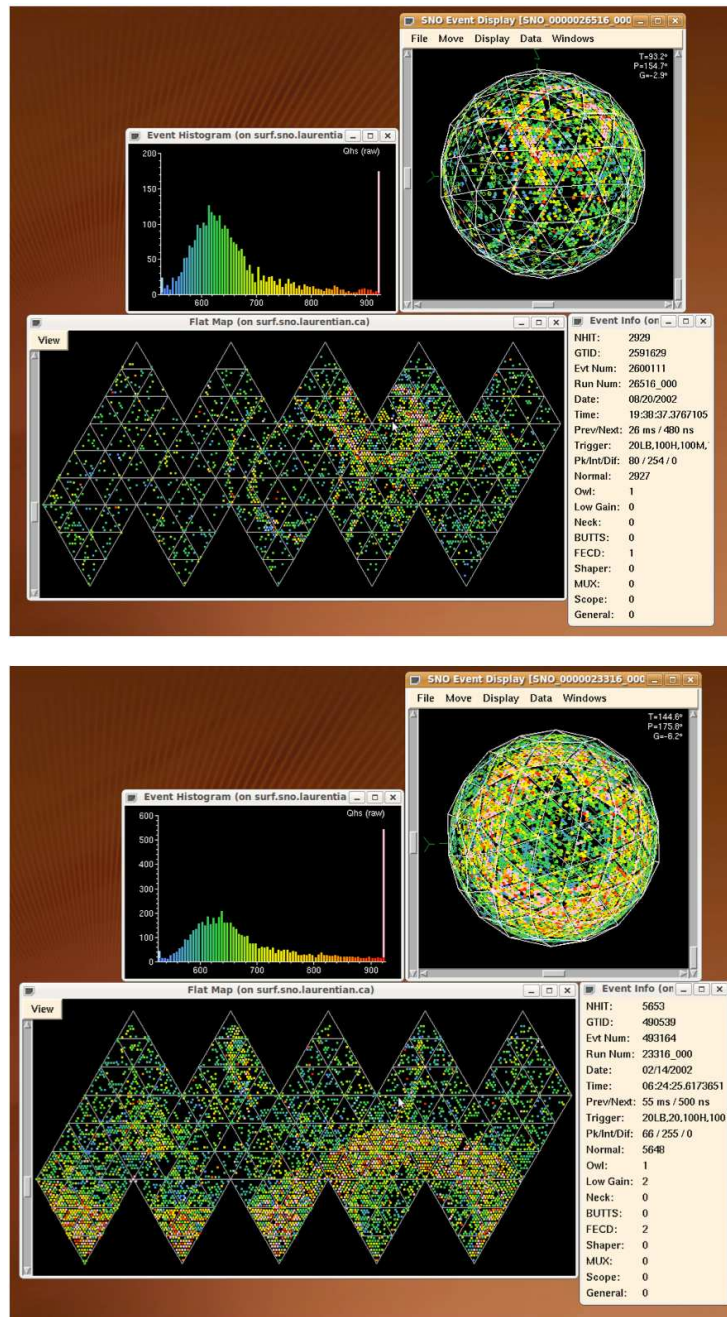


Figure 6.12: These two events are representative examples of the types of events tagged by the High NHIT cut. Whatever follows 200 ms or 600 ms after these events is ignored.

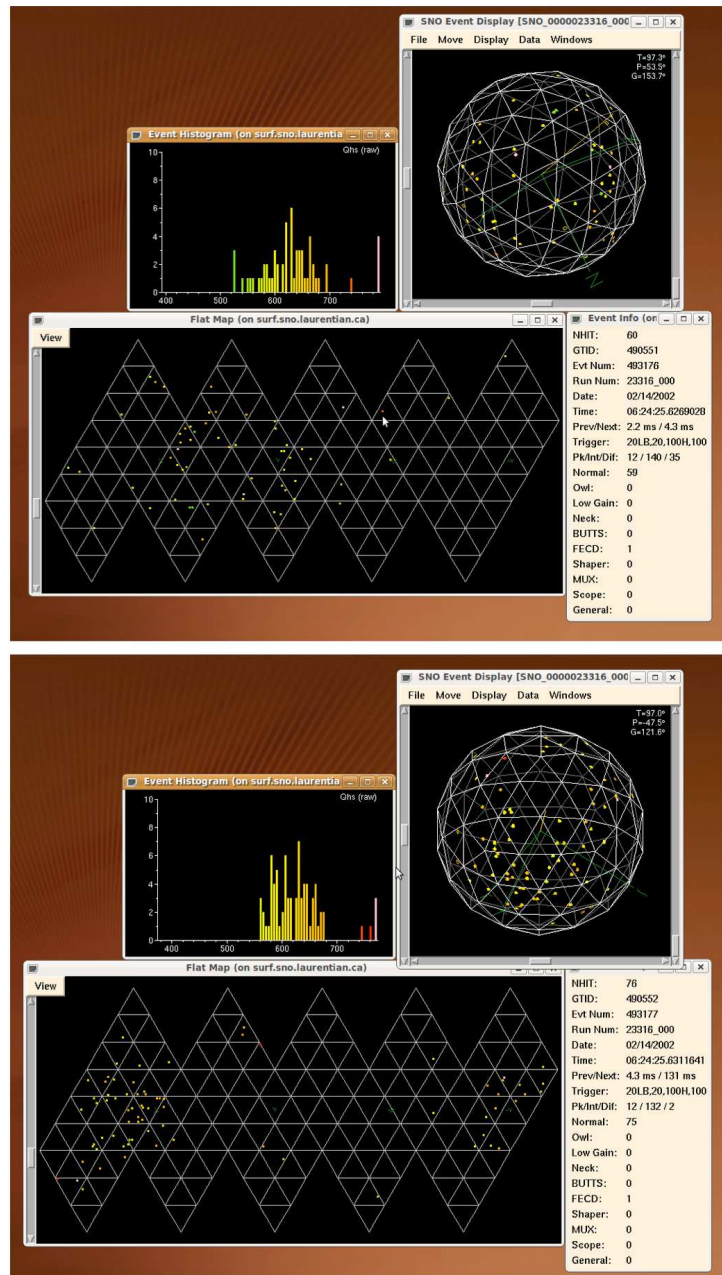


Figure 6.13: This burst appears normal and could easily be mistaken for a genuine supernova burst, but these events fall with the 200 ms elimination window that follows one of the High NHIT events shown in Figure 6.12

6.7.3 Non-Electron Follower Cut

In a further attempt to eliminate background bursts, we developed a Non-Electron Follower (NEF) cut. This cut tags events whose hit pattern is non-electron-like and removes any followers of those events. Supernova neutrinos can only produce single-electron events because of their energies, so events that are clearly not single-electron events should not be considered candidate bursts. SNO's low-energy threshold analysis [18] describes in detail the tests that define "electron-like" events. The two most useful cuts are called the β_{14} isotropy cut and the angular-fitter figure of merit cuts (FOMs). β_{14} is a linear combination of the average value of the first and fourth Legendre polynomials of the cosine of the angle between each pair of PMTs hit in an event. This variable characterizes the isotropy of the PMTs hit in any given event. The FOM cuts are Komogorov-Smirnov (K-S) tests on the angular distribution of Cherenkov light from the reconstructed events, utilizing the hypothesis that each event is a single 5 MeV Cherenkov electron.

This NEF cut is particularly helpful in eliminating events for which a high-energy event in the SNO detector has an unusually low number of hit PMTs because it is not an electron event but rather an event caused by a heavier charged particle. One example of such an event is shown with readout from the SNO event display in Figure 6.14 where a double-ring event was misreconstructed as a single low-energy event; the event was probably due to an atmospheric neutrino interaction that produced heavier particles like a proton and a charged pion. The NEF cut successfully eliminates this problematic event and others like it.

When we apply the NEF cut criteria to a supernova simulation for both

the D₂O and SALT phases, we see that only 1.2% of genuine supernova events are eliminated by these cuts. When we apply both the High NHIT and the NEF cuts to our atmospheric neutrino simulation, we eliminate 57% of the atmospheric events that pass the standard analysis cuts from the D₂O phase and 63% from the SALT phase.

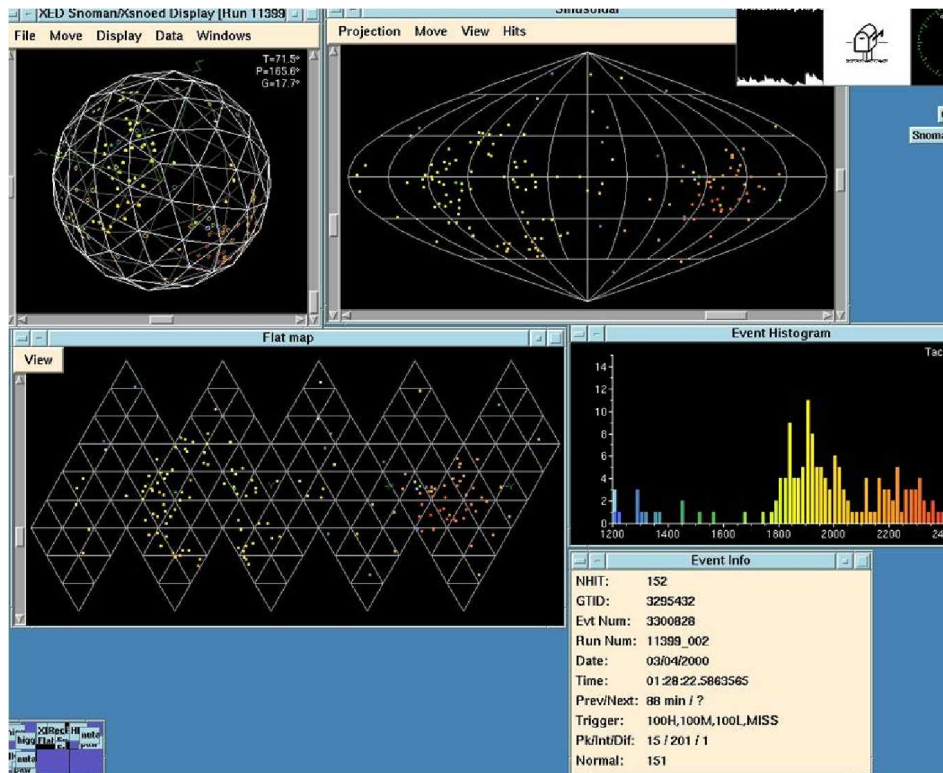


Figure 6.14: Example of a double-ring event in SNO that was misreconstructed as a single low-energy event because of the unusually low number of PMTs hit. The event was probably caused by Cherenkov light from heavier particles like a proton and a charged pion. The NEF cut successfully eliminates this event.

6.7.4 Δr Cut

Super-Kamiokande developed a cut designed to remove bursts whose events were localized in a small volume, based on the assumption that supernova events would be more likely to be dispersed throughout the volume of the detector [122], while background events would be more likely to be spatially correlated. We adopt a similar cut, and we define Δr as a weighted mean of the distances between events reconstructed positions for any candidate burst:

$$\Delta r = \frac{\sum_{i=1}^{M-1} \sum_{j=i+1}^M |\vec{r}_i - \vec{r}_j|}{{}_M C_2} \quad (6.20)$$

where $|\vec{r}_i - \vec{r}_j|$ is the distance between the reconstructed positions of events i and j within a burst, M is the multiplicity of the burst, and ${}_M C_2$ is the number of non-redundant combinations. Figures 6.15 and 6.16 show how distinct the background burst Δr distribution is from the simulated supernova Δr distribution.

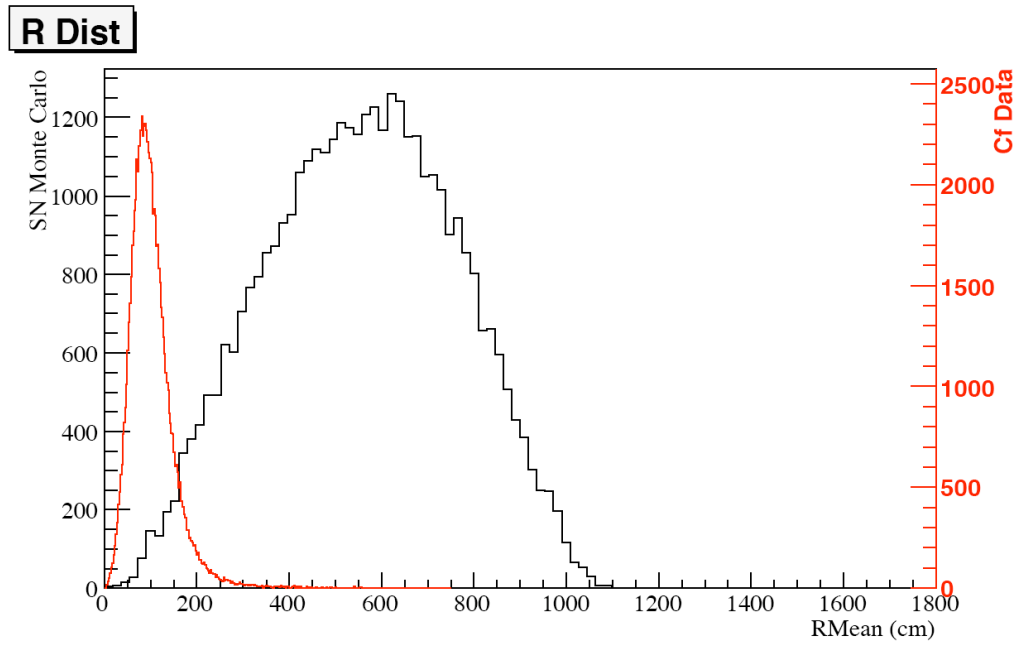


Figure 6.15: Sample MC Δr for supernova bursts plotted with sample Δr for calibration Cf bursts for the SALT phase.

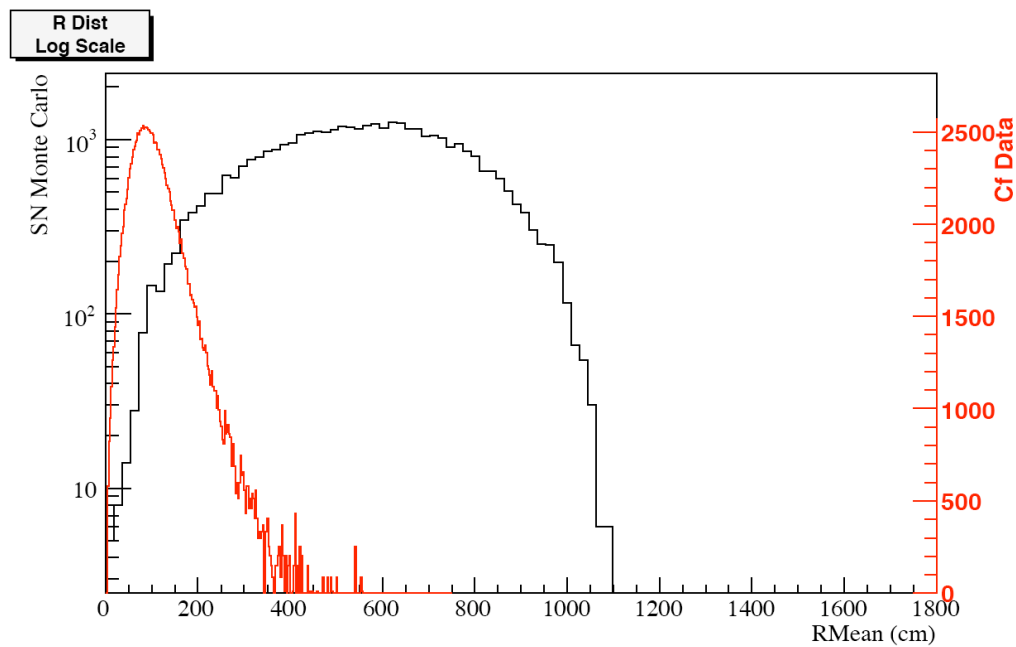


Figure 6.16: Sample MC Δr for supernova bursts plotted with sample Δr for calibration Cf bursts for the SALT phase, log scale.

Since most of our physics background events are atmospheric, the most logical approach to designing our Δr cut would be to use the atmospheric Monte Carlo simulation to generate Δr curves that we could then use to determine the percentage of background events eliminated by a particular Δr cut. Unfortunately the time investment required to simulate enough atmospheric background events was prohibitive; however, high statistics simulations already existed of neutrons produced by the Cf calibration source discussed in Section 6.1.6. Figures 6.17-6.20 show comparisons of the the Δr curves for the atmospheric simulation and the Cf calibration source simulation. The shapes of the curves agree very well, but the high statistics of the Cf calibration curves

greatly reduce the uncertainty in the fraction of events that pass any particular Δr cut.

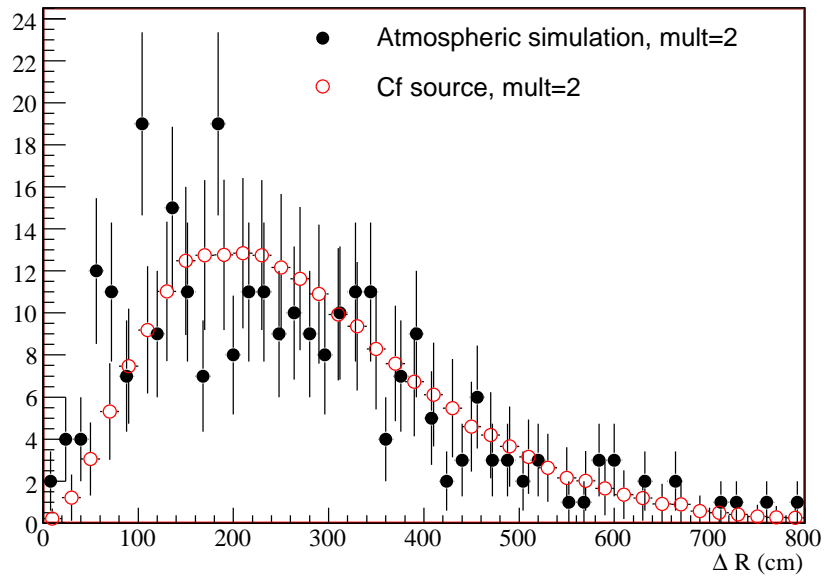


Figure 6.17: Comparison of Δr curves for the atmospheric simulation and the Cf calibration source simulation for the Phase I 200 ms window. The good agreement in the shapes allows us to use the higher statistics Cf calibration simulation to model the shape of the Δr curves for the background bursts caused (primarily) by atmospheric events.

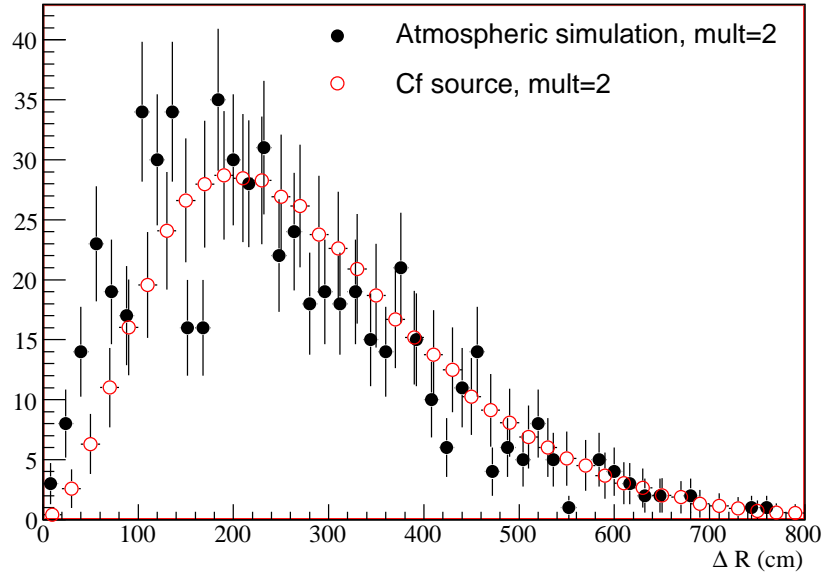


Figure 6.18: Comparison of Δr curves for the atmospheric simulation and the Cf calibration source simulation for the Phase I 50 ms window. The good agreement in the shapes allows us to use the higher statistics Cf calibration simulation to model the shape of the Δr curves for the background bursts caused (primarily) by atmospheric events.

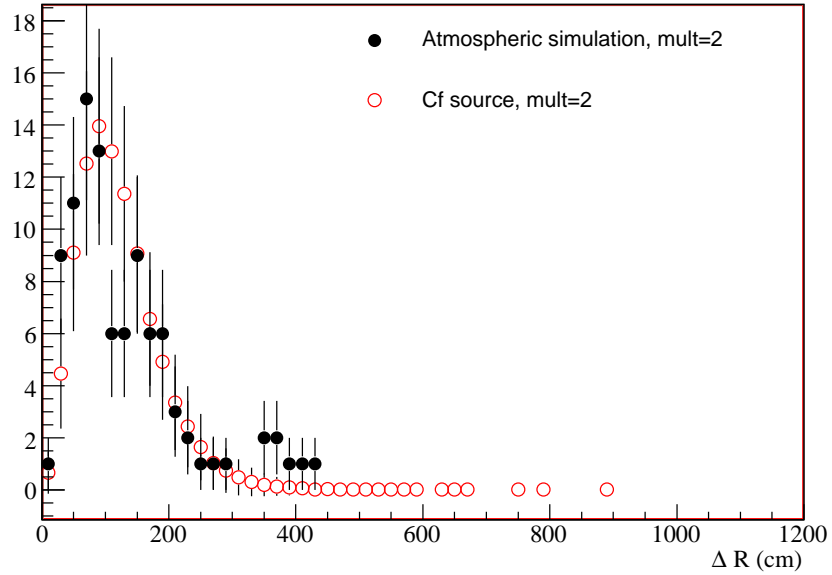


Figure 6.19: Comparison of Δr curves for the atmospheric simulation and the Cf calibration source simulation for the Phase II 1 s window. The good agreement in the shapes allows us to use the higher statistics Cf calibration simulation to model the shape of the Δr curves for the background bursts caused (primarily) by atmospheric events.

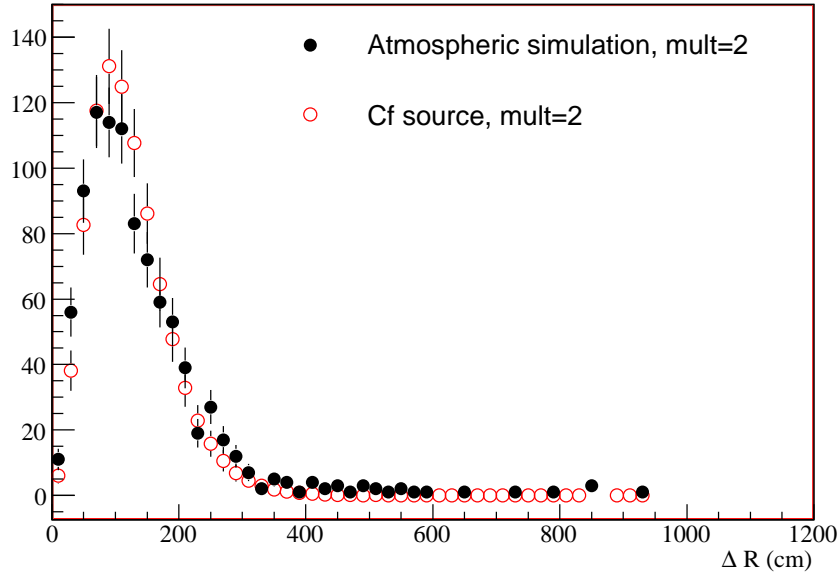


Figure 6.20: Comparison of Δr curves for the atmospheric simulation and the Cf calibration source simulation for the Phase II 50 ms window. The good agreement in the shapes allows us to use the higher statistics Cf calibration simulation to model the shape of the Δr curves for the background bursts caused (primarily) by atmospheric events.

6.7.5 $\Delta r \Delta t$ Cut

The Δr cut alone, however, does not optimize our sensitivity to a supernova signal. A better cut examines not just the spatial separation of burst events but also simultaneously their separation in time, Δt . Events that are spatially close but far apart in time are unlikely to be background events, so a simple Δr cut would be needlessly removing them. Figures 6.21-6.23 show $\Delta r \Delta t$ plots from the SALT phase, where the two-dimensional cut is clearly beneficial. Part

a) of Figure 6.21 illustrates that all of the backgrounds in that 1 s window fall within a small $\Delta r \Delta t$ region; by removing that small region from our search, we eliminate almost all of our backgrounds while maintaining a high sensitivity to a potential supernova signal, as shown in part b) of Figure 6.21. Figures 6.24 and 6.25 show plots from the D₂O phase, where we chose a simple Δr cut since the longer neutron capture time led to greater dispersion in Δt . For both phases we applied the two-dimensional cut to the multiplicity three search, as shown in Figures 6.23 and 6.26. For the multiplicity three search, the $\Delta r \Delta t$ cut leaves 99.9% of the expected supernova signal in the search region for the SALT phase and 94.4% for the D₂O phase. For the multiplicity two search in the SALT phase, the cut leaves 97.4% of the expected supernova signal for the 1.0 s window and 84.8% of the signal for the 0.05 s window. In the D₂O phase eliminating backgrounds is more difficult, and the Δr cut is harsher in order to ensure 90% confidence of seeing no false bursts. For the multiplicity two search in the D₂O phase, the cut leaves 30.5% of the expected supernova signal in the 0.2 s window and 36.8% in the 0.05 s window. Table 6.5 summarizes these results.

The shape of the $\Delta r \Delta t$ cut is rather box-like. While more complicated functional forms were tested, the background bursts themselves are clustered in a rather box-like fashion in the Δr - Δt space. In the 50 ms window where the background bursts were distributed differently, a more complicated functional form was chosen that resembled a box with a rounded corner, as shown in Figures 6.22 and 6.25. For every window the functional form of the cut was selected so as to reduce the total number of expected background events to 0.11 while sacrificing the smallest amount of standard supernova signal.

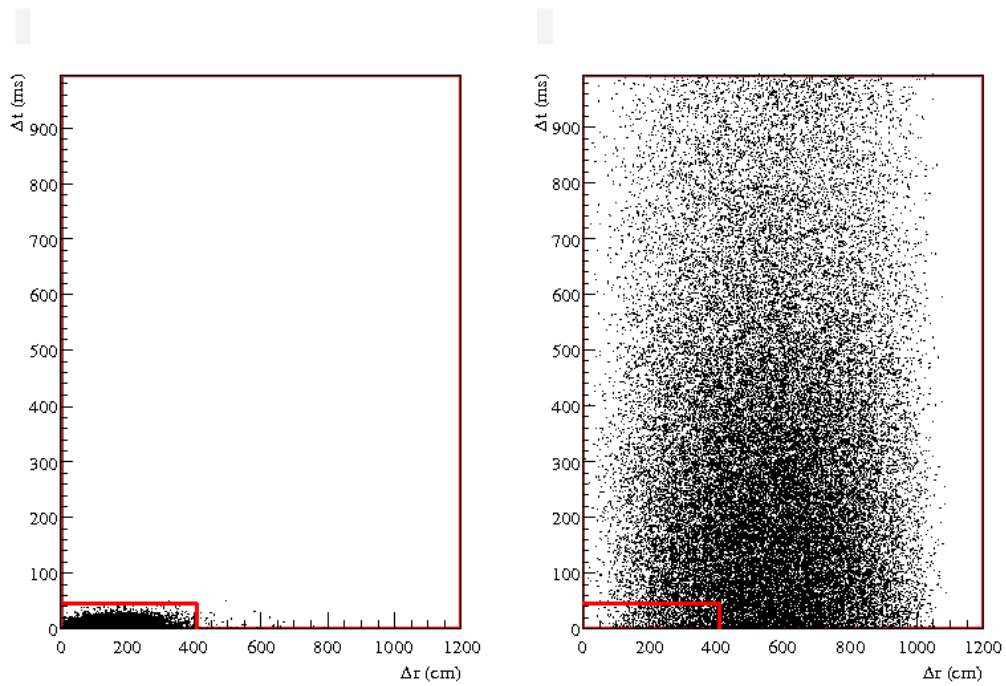


Figure 6.21: $\Delta r \Delta t$ cut for the background simulation and the standard supernova simulation for the SALT phase whose search window is 1 s long and whose energy threshold is 8.5 MeV. The region inside the box is removed from the search, eliminating almost all of the backgrounds without sacrificing much of the potential supernova signal.

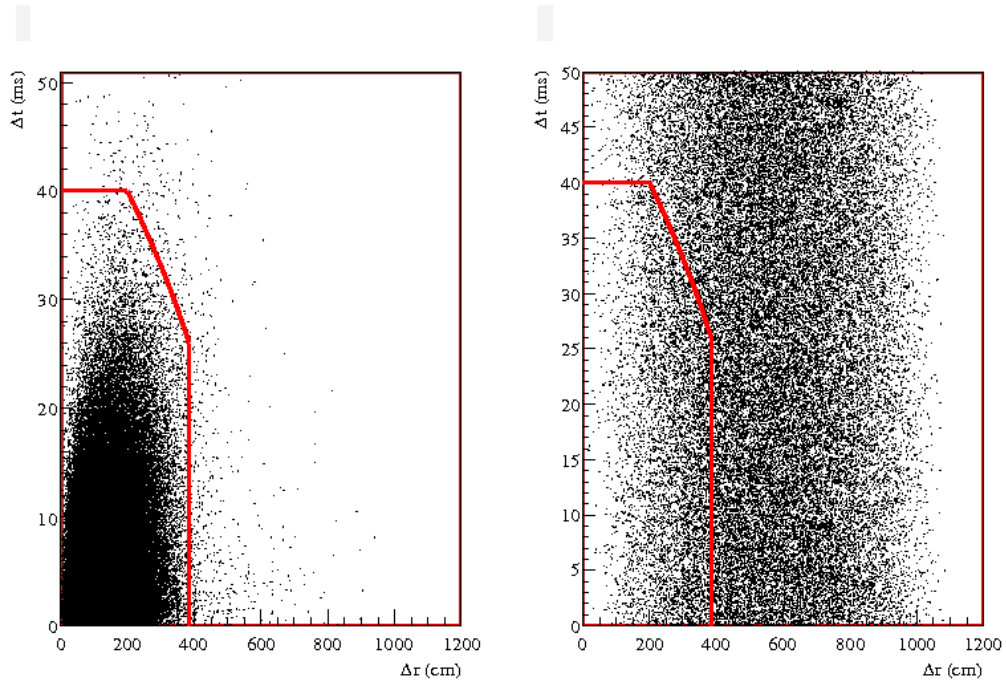


Figure 6.22: $\Delta r \Delta t$ cut for the background simulation and the standard supernova simulation for the SALT phase whose search window is 50 ms long and whose energy threshold is 6.5 MeV. The region inside the box is removed from the search, eliminating almost all of the backgrounds without sacrificing much of the potential supernova signal.

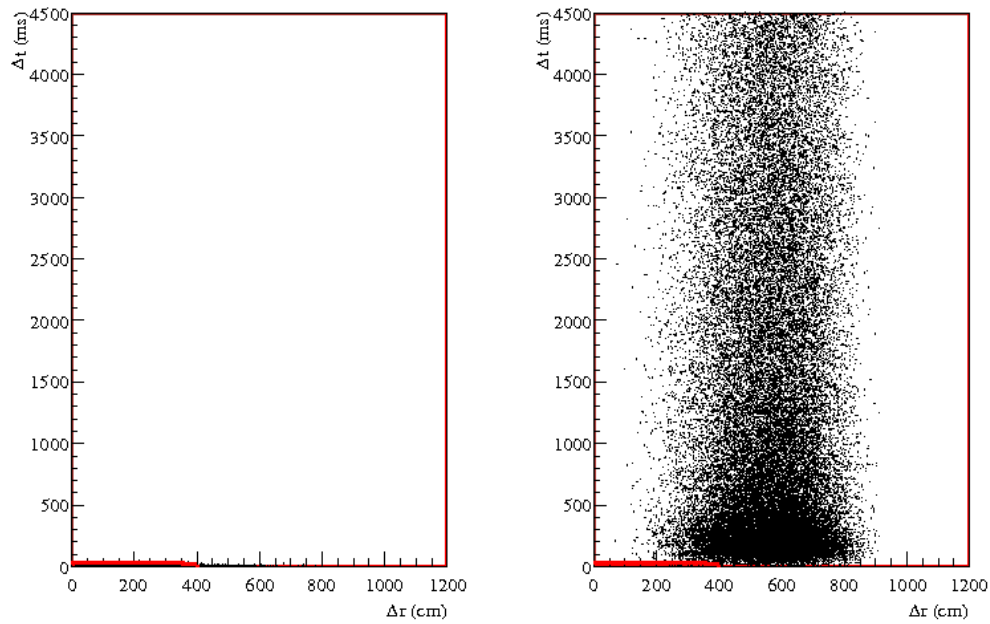


Figure 6.23: $\Delta r \Delta t$ cut for the background simulation and the standard supernova simulation for the SALT phase whose search window is 10 s long and whose energy threshold is 4.5 MeV. This search is for multiplicity=3 events. The region inside the box is removed from the search, eliminating almost all of the backgrounds without sacrificing much of the potential supernova signal.

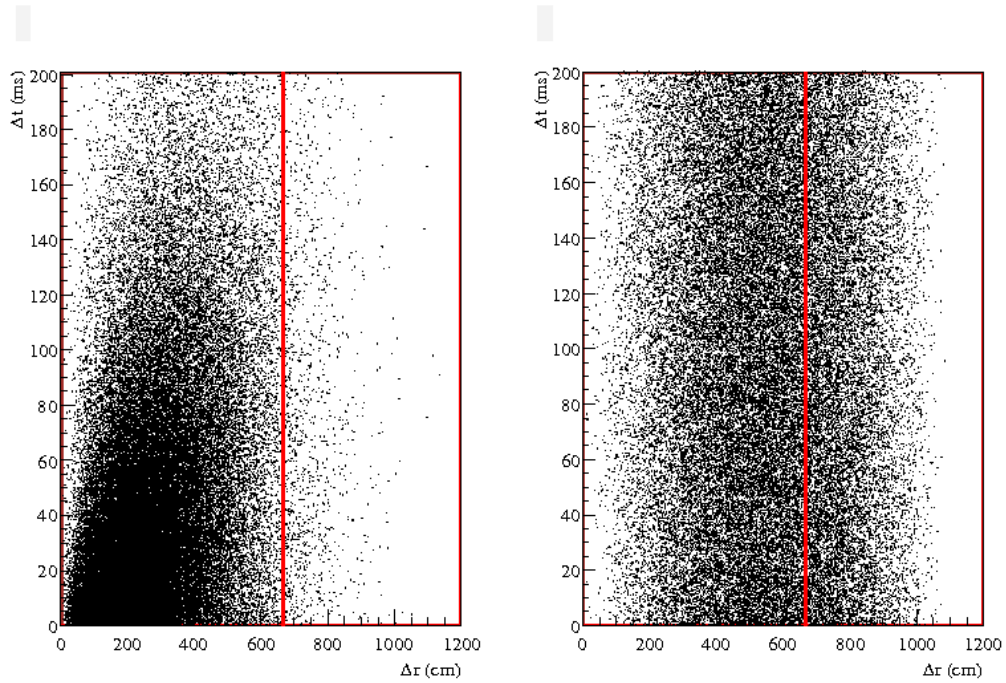


Figure 6.24: $\Delta r \Delta t$ cut for the background simulation and the standard supernova simulation for the D_2O phase whose search window is 200 ms long and whose energy threshold is 6.0 MeV. The region to the left of the line is removed from the search, which eliminates most of the backgrounds and unfortunately a lot of the potential supernova signal as well.

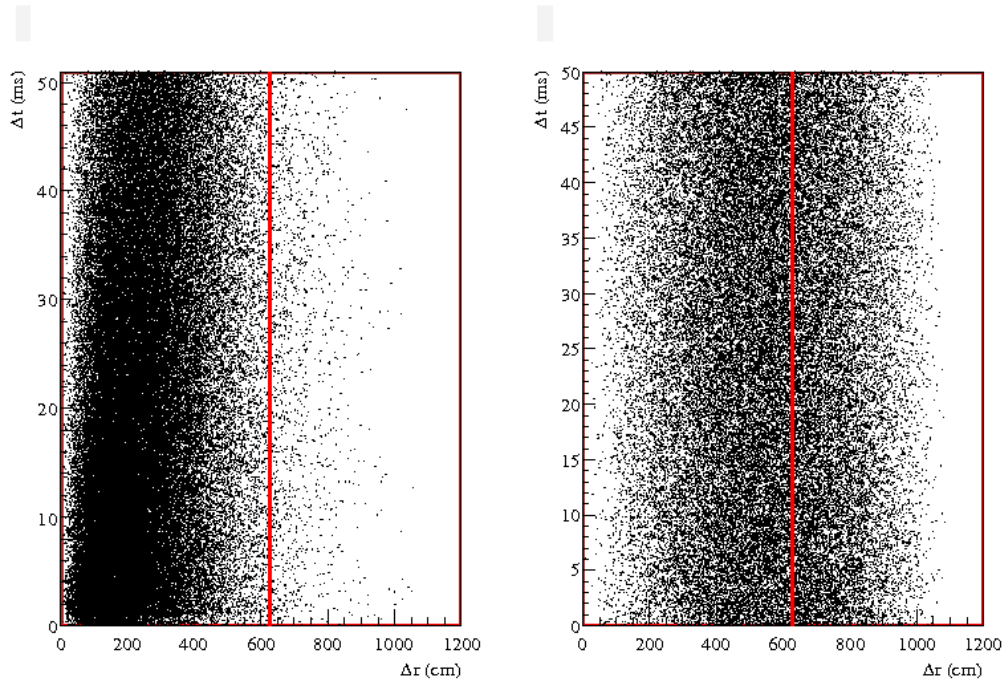


Figure 6.25: $\Delta r \Delta t$ cut for the background simulation and the standard supernova simulation for the D_2O phase whose search window is 50 ms long and whose energy threshold is 5.0 MeV. The region to the left of the line is removed from the search, which eliminates most of the backgrounds and unfortunately a lot of the potential supernova signal as well.

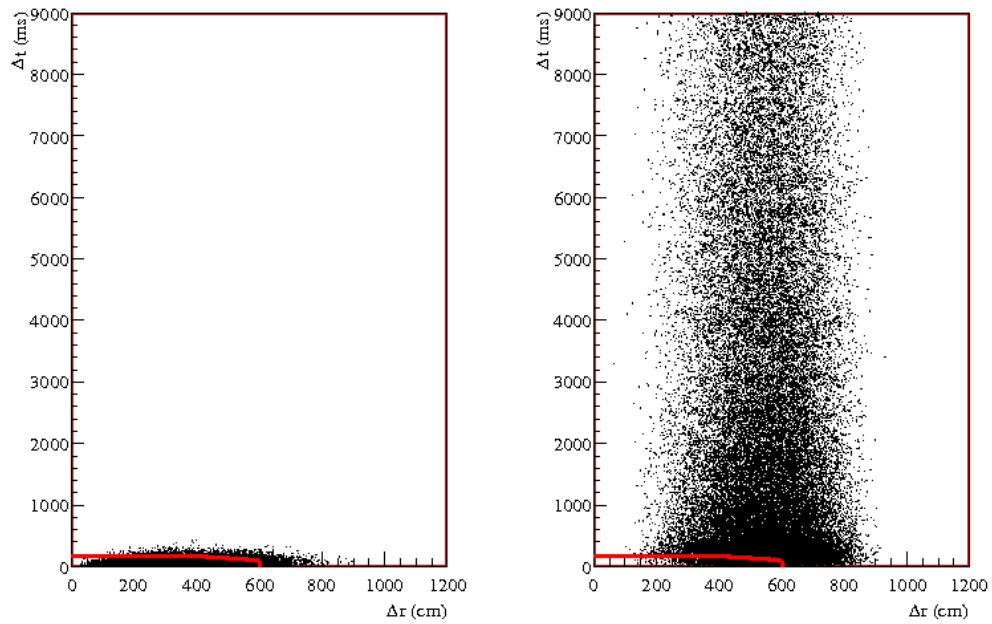


Figure 6.26: $\Delta r \Delta t$ cut for the background simulation and the standard supernova simulation for the D_2O phase whose search window is 10 s long and whose energy threshold is 4.5 MeV. This search is for multiplicity=3 events. The region inside the box is removed from the search, eliminating almost all of the backgrounds without sacrificing much of the potential supernova signal.

Table 6.5: The fraction of the standard supernova signal that survives the Δr or $\Delta r\Delta t$ cut for each of the search windows. Only the Δr cut was applied to Phase I, while we applied a $\Delta r\Delta t$ cut to Phase II. (The cuts listed here ignore the rounded corner used in a few of the search windows.) These cuts were set to eliminate the backgrounds in Table 6.3 to no more than 0.11 events.

	Δr Cut (cm)	Δt Cut (ms)	SN Signal
Phase I $N_{\text{event}}=2$ 0.2s window	668	–	0.303
Phase I $N_{\text{event}}=2$ 0.05s window	626	–	0.389
Phase I $N_{\text{event}}=3$ 10s window	600	180	0.867
Phase II $N_{\text{event}}=2$ 1.0s window	410	45	0.977
Phase II $N_{\text{event}}=2$ 0.05s window	385	40	0.811
Phase II $N_{\text{event}}=3$ 10s window	400	35	0.999

6.7.6 Bursts Found in the Antibox

Before I opened the box and looked at the real data, I performed the search on real data that was excluded from our final search by the $\Delta r \Delta t$ cut. By comparing what we found in the excluded real data with our expectations from our background estimates, we gained confidence that we correctly understood our sources of background bursts before we searched the valid $\Delta r \Delta t$ region in our real data. Table 6.6 shows the comparison between the number of bursts I found in the region below the $\Delta r \Delta t$ cutoff with the number I expected to find. Since atmospheric are the dominant source of background, I show the number of bursts predicted by the atmospheric simulation. The number of bursts I observed agrees well with the atmospheric simulation prediction in each case. This agreement confirms the estimates of the physics backgrounds discussed in Section 6.6 and validates this blind analysis search procedure.

Table 6.6: In the $\Delta r \Delta t$ regions that we excluded from our search due to heavy background contamination, we found burst levels that were consistent with our background estimates, which are dominated by atmospheric.

	Atm. MC Bursts	No. Bursts Found
Phase I, 0.2s window	1.90 ± 0.38	1
Phase I, 0.05s window	4.53 ± 0.91	2
Phase I, 10s window	1.51 ± 0.30	2
Phase II, 1s window	0.57 ± 0.11	1
Phase II, 0.05s window	6.94 ± 1.39	7
Phase II, 10s window	7.51 ± 1.50	9

In order to increase statistics, we can turn off the NEF and High NHIT

cuts in both the atmospheric simulation and the antibox. Table 6.7 shows the number of bursts predicted by the atmospheric simulation, along with the number of bursts found in the antibox, without applying the NEF and High NHIT cuts.

Table 6.7: When I turn off the NEF and High NHIT cuts in the $\Delta r \Delta t$ regions that I excluded from the search, I find burst levels that are consistent with my background estimates, which are dominated by atmospheric.

	Atm. MC Bursts	No. Bursts Found
Phase I, 0.2s window	11.81 ± 2.36	9
Phase I, 0.05s window	24.14 ± 4.83	19
Phase I, 10s window	13.22 ± 2.64	11
Phase II, 1s window	6.62 ± 1.32	7
Phase II, 0.05s window	47.53 ± 9.51	35
Phase II, 10s window	53.56 ± 10.71	47

We can also compare not just total bursts but the multiplicity categorization in the atmospheric simulation and the antibox. Tables 6.8 and 6.9 show the multiplicity categorization for the 0.05 s window for both the SALT and the D₂O phases with the NEF and High NHIT cuts turned off in order to increase the available statistics.

Table 6.8: Multiplicities of the atmospheric simulation compared to those seen in the antibox. These results are from the SALT phase, 0.05 s window, with the NEF and High NHIT cuts turned off to increase statistics.

Burst Multiplicity	Atm. MC Bursts	No. Bursts Found
2	24.0 ± 4.8	15
3	9.9 ± 2.0	7
4	4.7 ± 0.9	5
5	2.6 ± 0.5	0
2+	47.5 ± 9.54	35
3+	23.5 ± 4.7	20

Table 6.9: Multiplicities of the atmospheric simulation compared to those seen in the antibox. These results are from the D₂O phase, 0.05 s window, with the NEF and High NHIT cuts turned off to increase statistics.

Burst Multiplicity	Atm. MC Bursts	No. Bursts Found
2	13.5 ± 2.7	10
3	4.8 ± 1.0	7
4	2.3 ± 0.5	0
5	1.3 ± 0.3	2
2+	28.4 ± 5.7	19
3+	13.2 ± 2.6	9

We can also look at the shape of the Δr distribution for the antibox bursts and compare that to the shape we expect from the atmospheric simulation. Shown in Figure 6.27 is the comparison for the SALT phase multiplicity=2 data with the low energy threshold of 4.5 MeV. The good shape agreement lends confidence that we understand our background contamination bursts.

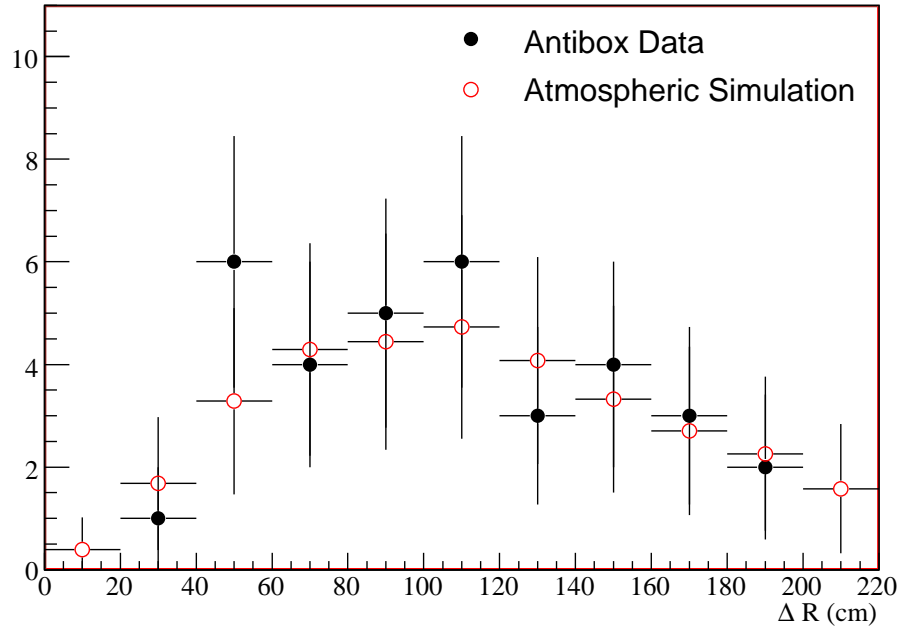


Figure 6.27: Δr in the region below the $\Delta r \Delta t$ cut for both the atmospheric simulation and the real data. The atmospheric simulation has been scaled. This data is from the SALT phase with an energy threshold of 4.5 MeV and a multiplicity of two, and the NEF and high NHIT cuts have been turned off to increase statistics. The good shape agreement lends confidence that we understand our background contamination.

As an additional check, we looked at bursts throughout the entire data set that failed the Muon Follower Short test, meaning that the events fell within 20 s of a tagged muon. For the 0.05 s window, we found 216 such bursts in the SALT phase and 63 in the D₂O phase. Figure 6.28 shows the Δr distribution for the SALT multiplicity=2 bursts, and clearly some of those

bursts would pass the Δr cut. None of those bursts, however, pass the NEF and High NHIT cuts, giving us confidence that any muon that sneaks past the muon cut will not produce a false supernova signal in our dataset.

DeltaR for SALT bursts failing Muon Follower Short

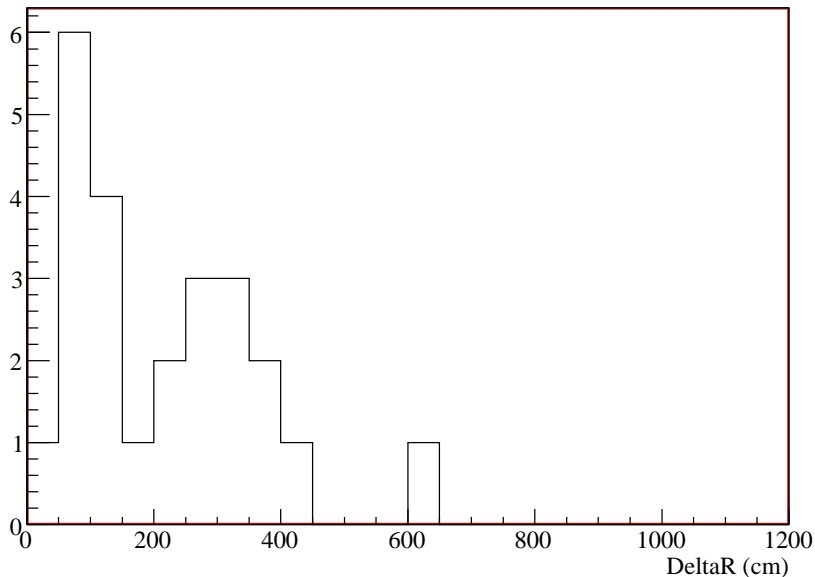


Figure 6.28: Δr for multiplicity=2 events in the SALT phase failing the Muon Follower Short cut. All of these bursts are eliminated by the NEF and High NHIT cuts.

I also compared my results to the candidate events found in SNO's electron antineutrino search [128]. Of the two candidate events discussed in that paper, I found one of them in both my 0.05 s window and 10 s window, and I found it in my antibox search since its Δr was quite small. I did not find it in my 0.2 s window because the energy threshold of 6.0 MeV excluded two of the three events. The second candidate event discussed in the paper

did not appear in my search because it came from a run later discovered to contain a radon spike, which means the run was eliminated from my runlist.

6.8 Results

6.8.1 Bursts Found in the Box

After all the cuts were developed and tested on simulations, we froze our analysis and performed our burst searches on both the Phase I and Phase II data. We observed no bursts in any of our search windows, as summarized in Table 6.10.

Table 6.10: No candidate bursts were observed in any of the search windows for either Phase I or Phase II.

Search Description	Bursts Expected	Bursts Found
Phase I, 0.2s window	< 0.11	0
Phase I, 0.05s window	< 0.11	0
Phase I, 10s window	< 0.11	0
Phase II, 1s window	< 0.11	0
Phase II, 0.05s window	< 0.11	0
Phase II, 10s window	< 0.05	0

Because our 10 s window search was optimized for an $N_{\text{event}} = 3$ burst, we did observe some $N_{\text{event}} = 2$ bursts in that window. Using the same energy threshold and analysis cuts designed for the Phase II 10 s $N_{\text{event}} = 3$ search, we observed 14 $N_{\text{event}} = 2$ bursts, which is in keeping with our expectations from accidental coincidences. While our search gives us no reason to suspect that

these are anything other than accidental bursts, we can examine them closer to assure ourselves that we have not overlooked any genuine supernova signal. Figures 6.29 and 6.30 show the distribution of Δr and Δt for these $N_{\text{event}} = 2$ bursts. The distribution in Δr is approximately uniform, which is consistent with the hypothesis that these are accidental bursts. The Δt distribution further supports this conclusion. The event with the lowest Δt separation also has a Δr too low to have survived any of the $\Delta r \Delta t$ cuts for the multiplicity two searches, meaning that it is more likely to have been a background burst than a genuine supernova burst. We also observed two $N_{\text{event}} = 2$ bursts in the $N_{\text{event}} = 3$ search for Phase I. These two bursts are separated by 3.2 s and 8.0 s respectively, which puts them well outside of the $N_{\text{event}} = 2$ search windows. These bursts are also consistent with our accidental coincidence expectations.

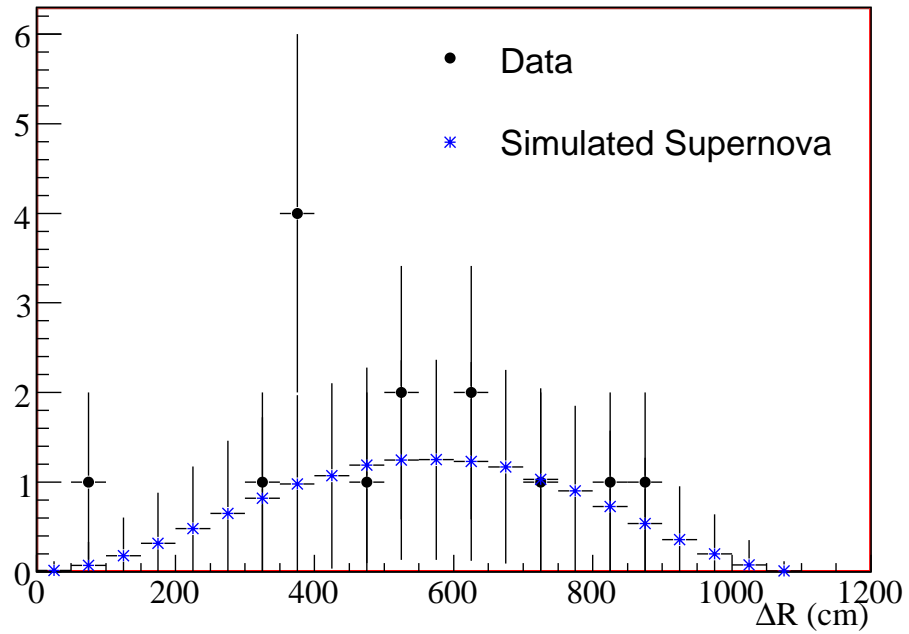


Figure 6.29: Δr distribution for multiplicity two bursts found in the multiplicity three search window for Phase II. The Δr distribution is consistent with what would be expected for accidental coincidences or for standard supernova events.

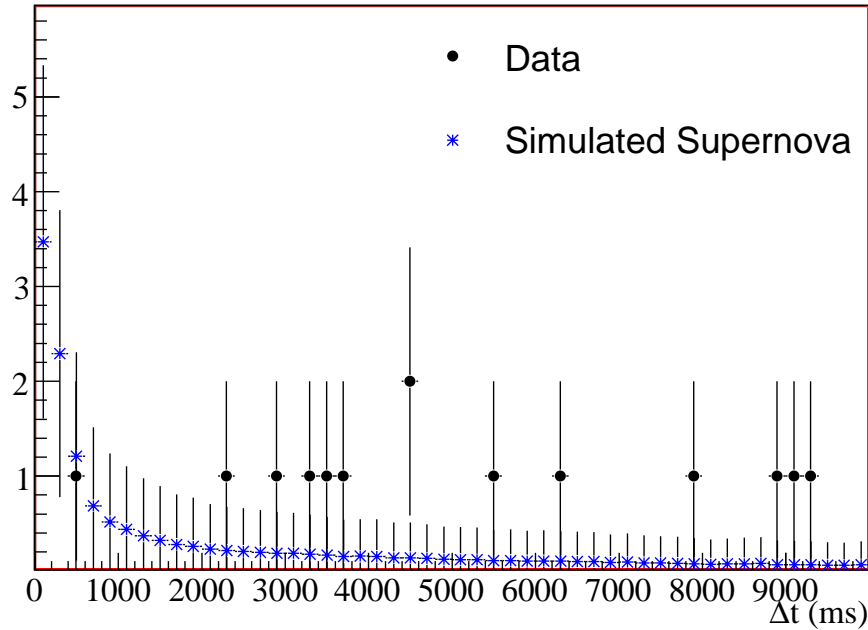


Figure 6.30: Δt distribution for multiplicity two bursts found in the multiplicity three search window for Phase II. The Δt distribution is consistent with what would be expected for accidental coincidences, not for standard supernova events.

6.9 Sensitivity Study

We performed a triggerless search for low-multiplicity bursts in data from Phase I (D_2O only) and Phase II (D_2O loaded with $NaCl$) of the Sudbury Neutrino Observatory, finding no candidate bursts. Our results are consistent with the null signal observed by Super-Kamiokande where the datasets overlapped. In order to determine the sensitivity we had to a potential supernova,

we utilized a supernova simulation code called SNGEN that was based on the Burrows model [115, 114] and developed specifically for SNO.

The SNGEN luminosities $\mathcal{L}(t)$ and energies $E_\nu(t)$ for each type of neutrino come from the Burrows model, and one can calculate the flux of neutrinos that would arrive at Earth:

$$\mathcal{F}(t) = \frac{k\mathcal{L}(t)}{4\pi R^2 E_\nu(t)} \quad (6.21)$$

where R is the distance to the supernova in kilo-parsecs (1 parsec=3.26 light-years), $k = 6.65545 \times 10^{17}$ is a conversion factor to account for astrophysical units, $\mathcal{L}(t)$ is the luminosity of the neutrinos at time t in units of 10^{51} erg/s², and $E_\nu(t)$ is the energy of a neutrino produced at time t in MeV. The observed differential neutrino flux at Earth is a convolution of the above equation and the neutrino spectrum as the neutrinos are emitted from the supernova:

$$\frac{d^2 N}{dE_\nu dt} = \mathcal{F}(t) f(\epsilon_\nu, t) \quad (6.22)$$

where the spectrum of the neutrinos is of the Fermi-Dirac form:

$$f(\epsilon_\nu, t) = \frac{\epsilon_\nu^2}{e^{\epsilon_\nu/T-\eta} + 1} \left(\int_0^\infty \frac{\epsilon_\nu^2}{e^{\epsilon_\nu/T-\eta} + 1} d\epsilon_\nu \right)^{-1} \quad (6.23)$$

where T is the temperature of the neutrino, ϵ_ν is the energy of the neutrino, and η is the degeneracy parameter. The degeneracy parameter accounts for the fact that the distribution is “pinched,” meaning that the lowest and highest energy neutrinos are suppressed relative to a Maxwell-Boltzmann distribution. The lowest energy neutrinos are suppressed because there are fewer of them produced in the core of the star, and the highest energy neutrinos are sup-

pressed because they have a higher probability of interacting before leaving the star.

The detected flux for any detector depends on the number of target particles N_T and the cross section $\sigma(\epsilon_\nu)$ of the specific interaction:

$$\frac{d^2 N_{det}}{dE_\nu dt} = N_T \sigma(\epsilon_\nu) \frac{d^2 N}{dE_\nu dt} \quad (6.24)$$

That equation assumes a massless neutrino.

SNGEN takes the distance of the supernova as a parameter and outputs the parameters needed for SNOMAN, such as energy, position, time, ect. The neutrino energies are converted into the energies of the resulting particles (electrons, positrons, neutrons, ect.) The code assumes that the neutrons produced are thermalized, meaning that their total number and their time of creation are the important outputs. The electrons and positrons from the NC and CC reactions have energies defined by $E_e = \epsilon_\nu - Q$, where Q is the threshold energy. The energy for an electron from the ES interaction can be calculated from relativistic kinematics:

$$E_e = \frac{2\epsilon_\nu^2}{(1 + 2\epsilon_\nu)} \quad (6.25)$$

The specific creation position in the detector is assumed to be isotropic. The propagation direction of the electron is highly forward peaked, i.e. the electron will be scattered along the direction of the incoming neutrino. SNGEN accounts for the angular distribution of the electrons, positrons, and any resulting photons, and it converts them to direction cosines with respect to the center of the detector, which is required for SNOMAN input. The final

SNGEN output is a file that can be analyzed by SNOMAN to produce the standard output ROOT or HBOOK file.

In order to calculate the probability that SNO would have detected supernovae that occurred at various distances, we could have produced many SNGEN supernova simulations at each distance, but that would have been unnecessarily computationally intensive. Instead I produced several supernova simulations all at 1 kpc. In order to scale them to the appropriate distance, I randomly rejected all but $1/R^2$ of the events where R is the distance in kpc from the earth to where the simulated supernova should have been. I then searched through the simulated data as if it were real SNO data and recorded the number of bursts detected in each of the search windows. Because most of the simulated data is being rejected in this pass by the $1/R^2$ factor, I make multiple passes through the dataset (anywhere from 10 to 100 passes, depending on the distance R) and treat each pass as if it were statistically independent. For each distance R I collect a total of at least 100 passes, each of which is equivalent to one supernova simulated at that distance, and I record the bursts found in each search window. For each burst, I assume that the events were equally likely to occur at any position in the detector, and I reject the appropriate fraction of those bursts that would have failed the Δr cut. Then I calculate the probability of detecting a supernova at that distance by dividing the number of supernova that were detected in a particular window by the total number of simulated supernova that could have been detected. I take the standard deviation to be the uncertainty associated with that probability. In finding the probability of detection, I did not consider whether a supernova was detected by the observation of one burst or multiple bursts; the supernova either was or was not seen in a particular search window.

Figures 6.31-6.32 show the sensitivity of our various search windows to a standard supernova for both phases as a function of supernova distance. For Phase I, which was completely overlapped by the run time of Super-Kamiokande, our search was primarily looking for non-standard supernova signals in which ν_e emission would be suppressed, allowing SNO to detect a neutral current signal that Super Kamiokande could not have seen.

At a typical distance in our galaxy, 10 kpc, we retain a 100% detection probability for a standard core-collapse supernova. In Phase I we maintain a 50% detection probability for a standard supernova out to 60 kpc. In Phase II we retain a 100% detection probability out to 30 kpc and a greater than 50% detection probability out to 70 kpc.

Given the estimated rate of supernova explosions in our galaxy, our null result is not terribly surprising. Although estimating the expected rate of supernovae is difficult and involves large uncertainties, the rate is thought to be in the range of 1.6 – 3.2 supernova per century (or 1 supernova every 31-63 years), of which approximately 85% would emit a substantial neutrino signal [134]. Combining the Milky Way galaxy together with the Large and Small Magellanic Clouds, theorists have estimated that neutrino detectors like SNO and Super-Kamiokande would be sensitive to ~ 2 Type II or Ib supernovae per century [134]. Despite the low probability of catching a nearby supernova during an experiment's livetime, the potential significance of an observation continues to motivate physicists to search. As SNO+ and other underground neutrino experiments are developed, supernova neutrino detection remains a priority for both the neutrino and astrophysics communities.

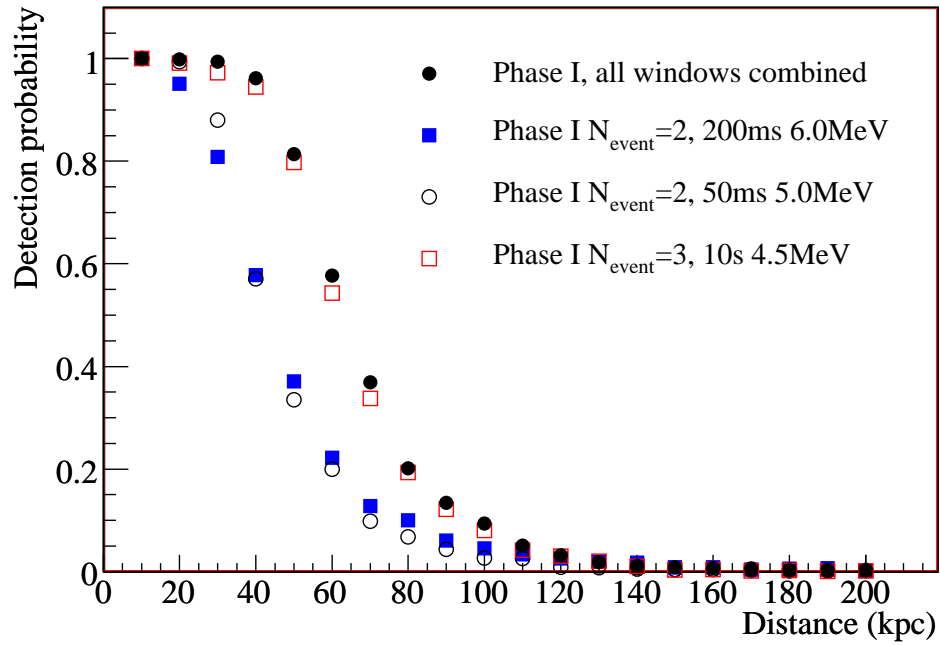


Figure 6.31: Probability of detecting a standard supernova in each of the search windows for Phase I, as well as the combined detection probability of all of the windows.

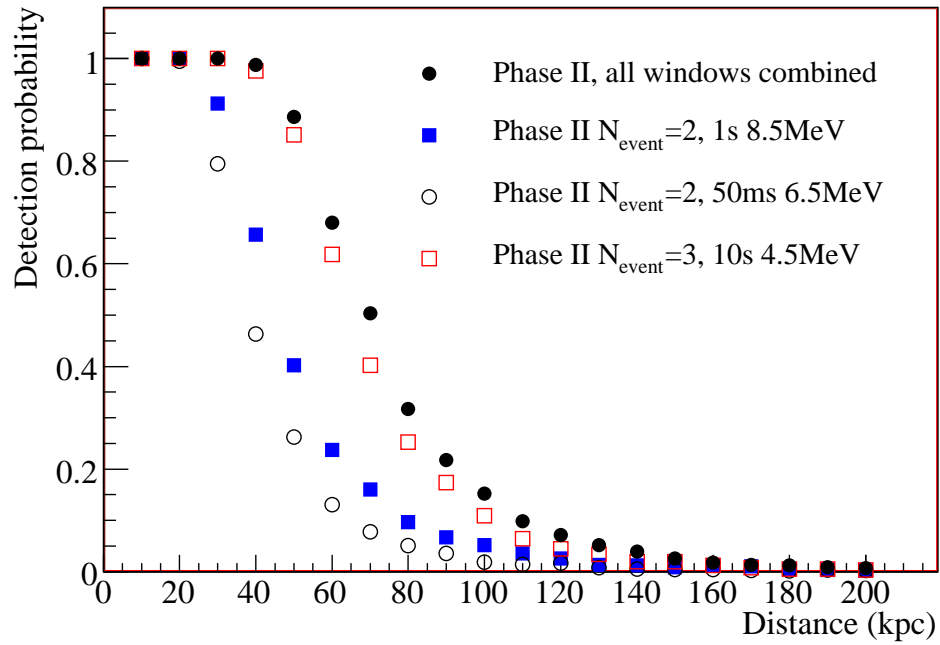


Figure 6.32: Probability of detecting a standard supernova in each of the search windows for Phase II, as well as the combined detection probability of all of the windows.

Chapter 7

Conclusions

Since Pauli first suggested their existence in 1930, neutrinos have continued to provide insight into fundamental questions of physics. Their weak interaction strength makes them interesting probes, though it also increases the challenge of detecting them and extracting useful information. Neutrinos have provided numerous surprises for physicists, including the fact that they come in three flavors, interact through both charged and neutral currents, and display flavor oscillations due to differences in their masses, which are themselves surprisingly small. Many important fundamental questions surrounding these particles persist, such as their absolute mass scale, their Dirac or Majorana nature, their normal or inverted hierarchy, and the size of their smallest mixing angle θ_{13} . With all of these open questions to pursue, neutrino physics promises to be a fruitful field of study for many years to come.

As this field matures, the questions surrounding neutrinos become more difficult answer. Increasingly physicists are seeking new tools through which to study neutrinos, as well as new ways in which neutrinos themselves can become tools to study other phenomena. My work has focused on exploring non-

traditional avenues through which to investigate neutrinos, primarily drawing inspiration from sub-fields of physics outside of high energy particle physics.

Because of the recent advances in atomic physics described in Chapter 3, opportunities exist to work with a new type of tritium β decay source to explore the absolute mass scale of the neutrino. I created simulations and data analysis techniques to explore the feasibility of a tritium β decay experiment in which the neutrino mass could be directly reconstructed, as well as inferred from the β spectrum distortions. While this type of experiment would certainly be challenging, it possesses an appealing scalability and model-independence. Future developments in both atomic physics techniques and current neutrino mass investigations will determine what the next step will be for this type of approach, but the work summarized in Chapter 4 represents the most realistic proposal to date for kinematically reconstructing the neutrino mass.

The same techniques for manipulating atoms that enable the creation of an atomic tritium source also enable a new method of isotope separation. My investigation of single-photon atomic sorting began because I joined both the SNO Collaboration (working on neutrino physics) and the Raizen Laboratory (working on atomic physics). I learned about the difficulty SNO+ faces in acquiring a large amount of ^{150}Nd , and I became involved in conversations within the Raizen Laboratory about how supersonic beams might be helpful in large-scale isotope separation. The development of single-photon atomic sorting outlined in Chapter 5 is a perfect example of the benefits of robust dialog between sub-fields of physics. Currently a demonstration experiment for this technique is being constructed, and the possibility of industrial-scale development of the idea appears promising.

In working with SNO I became involved in an emerging sub-field of

physics known as neutrino astronomy. While solar neutrinos and SN 1987A neutrinos remain the only data collected in this field so far, the impact of those observations serves to illustrate the potential of this area of research. Many astrophysical phenomena that are opaque to traditional probes can be investigated via neutrinos. Studies like the one described in Chapter 6 serve to develop and refine the tools that will be needed in future searches for astrophysical signals in neutrino data. Although SNO did not observe a candidate supernova burst in its livetime, future underground experiments hope to observe a supernova neutrino signal that would provide insight into the nature of both neutrinos and core-collapse.

My work has focused on exploring neutrino physics using new approaches, utilizing tools as small as atoms and as large as supernovae. As physics becomes increasingly specialized, opportunities for collaboration between sub-fields become easier to miss. Having spent the last few years working in regions of overlap between particle physics, atomic physics, and astronomy, I have found that cross-discipline investigations raise new questions and (sometimes) suggest surprising answers. In the space that separates specialized fields there are opportunities to see connections, and as the field of neutrino physics continues to develop, its collaboration with diverse branches of physics promises to yield exciting results.

Appendix A

Beta Spectrum Derivation

In ordinary β decay experiments like the ones discussed in Chapter 2, the only experimental observable is the energy of the electron from the decay. The neutrino mass appears directly in the equation for the shape of the β spectrum curve, and the following section outlines the derivation of the β spectrum curve shown in Figure A.1.

A.0.1 Fermi's Golden Rule

Fermi developed a theory of β decay that correctly predicted the shape of the β energy spectrum, and it was eventually modified to include the W and Z bosons in a renormalizable way. Figure A.2 shows the Feynman diagram that represents our current understanding of β decay. Fermi modeled his theory on the already existing theory of γ radiation from an atomic electron cloud, which used perturbation theory to formulate a transition probability per unit time for an initial state i , consisting of an atom in an excited state, to change to a final state f , consisting of an emitted photon and an atom in a less

excited state. The photon was represented as an electromagnetic radiation field, and the transition from the initial to the final state occurred through a field interaction process expressed by an operator.

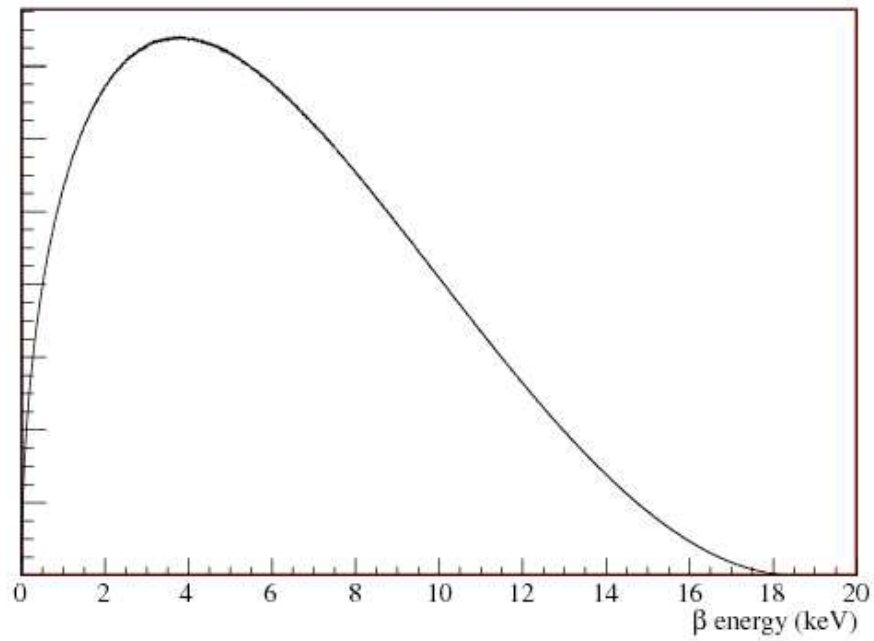


Figure A.1: Beta energy spectrum from tritium beta decay.

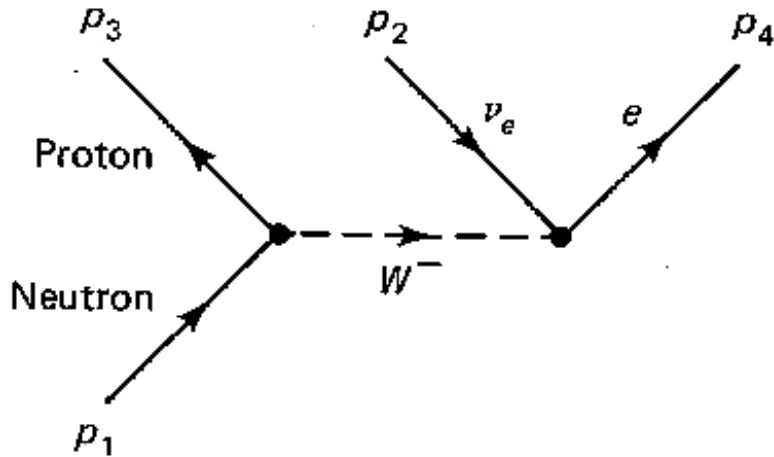


Figure A.2: Feynman diagram with external lines labeled for the reaction $n \rightarrow p + e^- + \bar{\nu}_e$. Figure taken from reference [135]

Similarly Fermi described β decay through a Hamiltonian operator transforming a nuclear system from an initial state i into one of several possible final state f through lepton creation by means of a weak interaction. The strength of this weak interaction was expressed by a matrix element H_{fi} , which could be written as a volume integral:

$$H_{fi} = \int \Psi_f^* H' \Psi_i d\Omega \quad (\text{A.1})$$

Utilizing perturbation theory, Fermi wrote the transition probability per unit time in a form now known as Fermi's Golden Rule:

$$W = \frac{2\pi}{\hbar} |H_{fi}|^2 \rho(E_f) = \frac{2\pi}{\hbar} |H_{fi}|^2 \frac{dN}{dE} \quad (\text{A.2})$$

where $\rho(E_f)$ is the density of states, i.e. the number of states per unit energy interval around E_f . If the linear momenta of the emitted electrons corresponding to the energy interval dE in the vicinity of E_f range from p to $p + dp$, then the above transition probability per unit time simply gives the mean number of β particles emitted in unit time with momenta within this range. Fermi's Golden Rule, therefore, also acts as a probability function that determines the shape of the β momentum (or energy) spectrum.

The density of states is a statistical factor describing the density of possible final states in the phase space of the electron-neutrino field. This phase space density can be derived using the Heisenberg uncertainty relation, which implies that an electron cannot be confined to an area in phase space smaller than $\Delta x \Delta p_x \approx h$. In the six dimensional phase space defined by (x, y, z, p_x, p_y, p_z) , the uncertainty relation implies that the state of an electron cannot be specified to a greater precision than:

$$\Delta x \Delta y \Delta z \Delta p_x \Delta p_y \Delta p_z \approx h^3 \quad (\text{A.3})$$

If we suppose the electron to be within a spatial volume V and a momentum volume expressed by a spherical shell of volume $4\pi p^2 dp$ in momentum phase space, then the net volume of the electron is $V(4\pi p^2 dp)$. Since a single state occupies a volume of h^3 , then we can write the number of electron states in phase space as:

$$dn_e = V \frac{4\pi p^2 dp}{h^3} \quad (\text{A.4})$$

Similarly the probability of encountering a neutrino within a spatial volume

$dx dy dz$ with a linear momentum between p and $p + dp$ can be written:

$$dn_\nu = V \frac{4\pi p_\nu^2 dp_\nu}{h^3} \quad (\text{A.5})$$

The total probability of encountering both of these leptons is the product, $dN = (dn_e)(dn_\nu)$, where dN indicates the number of accessible states in the phase space of the electron-neutrino field. The state density within a small interval dE about the final energy E_f can be written:

$$\frac{dN}{dE} = \frac{16\pi^2 V^2}{h^6} p^2 p_\nu^2 \frac{dp_\nu}{dE} dp \quad (\text{A.6})$$

From the relativistic energy-momentum relation, the neutrino momentum can be written as:

$$p_\nu = \frac{1}{c} \sqrt{E_\nu(E_\nu + 2m_\nu c^2)} \quad (\text{A.7})$$

where E_ν refers to the kinetic energy of the neutrino. Using that expression, one can write:

$$p_\nu^2 \frac{dp_\nu}{dE} = \frac{1}{c^3} (E_\nu + m_\nu c^2) \sqrt{E_\nu(E_\nu + 2m_\nu c^2)} \quad (\text{A.8})$$

Neglecting the extremely small recoil energy of the massive daughter nucleus, the energy of the neutrino can be written as $E_\nu = E_o - E - m_\nu c^2$, which implies:

$$p_\nu^2 \frac{dp_\nu}{dE} = \frac{1}{c^3} (E_o - E) \sqrt{(E_o - E)^2 + (m_\nu c^2)^2} \quad (\text{A.9})$$

Inserting that expression into the equation for the density of states (Equa-

tion A.6) leads to:

$$\frac{dN}{dE} = \frac{16\pi^2 V^2}{c^6 h^6} p^2 (E_o - E) \sqrt{(E_o - E)^2 + (m_\nu c^2)^2} dp \quad (\text{A.10})$$

Using the relativistic energy-momentum relation, one can also express the density of states as:

$$\frac{dN}{dE} = \frac{16\pi^2 V^2}{c^6 h^6} p E_{\text{tot}} (E_o - E) \sqrt{(E_o - E)^2 + (m_\nu c^2)^2} dE \quad (\text{A.11})$$

where E_{tot} is the total energy of the β . This equation can be plugged into Fermi's Golden Rule to describe the density of states for β decay.

In order to obtain a final expression for the β spectrum we must return to the matrix element in Fermi's Golden Rule,

$$H'_{fi} \equiv \int \Psi_f^* H' \Psi_i d\Omega \quad (\text{A.12})$$

where Ψ_i and Ψ_f are initial and final state normalized energy eigenfunctions that can be decomposed. We can write the wave function of the nucleons in the parent (daughter) nucleus as ψ_i (ψ_f), and we can write the electron-neutrino field as a product of wave functions $\phi_e(\mathbf{r})\phi_\nu(\mathbf{r})$. Using that notation, $\Psi_i = \psi_i$, $\Psi_f = \psi_f \phi_e(\mathbf{r})\phi_\nu(\mathbf{r})$, and the interaction matrix element can be written:

$$H'_{fi} = g_F \int (\psi_f^* \phi_e^*(\mathbf{r}) \phi_\nu^*(\mathbf{r})) M \psi_i d\Omega \quad (\text{A.13})$$

where g_F is an empirical constant and M is a dimensionless Hamiltonian operator. The Fermi coupling constant $g_F = 0.9 \times 10^{-4} \text{ MeV fm}^3$ expresses the strength of the β interaction.

We can further simplify this expression by assuming that the interaction between the nucleus and the leptons is weak, meaning that the lepton waves comprising the field are undistorted by the nuclear potential and may be taken as plane waves. In reality the electron will be distorted by its interaction with the nuclear charge, but this effect will be taken into account in the next section. For now we ignore this effect and simply write:

$$\phi_e(\mathbf{r}) = N_e e^{i(\mathbf{k}_e \cdot \mathbf{r})}, \phi_\nu(\mathbf{r}) = N_\nu e^{i(\mathbf{k}_\nu \cdot \mathbf{r})}, \quad (\text{A.14})$$

where \mathbf{k}_e and \mathbf{k}_ν are lepton wave vectors. We can normalize these wave functions within a volume V , which is equal to the spatial volume element $V = dx dy dz$ discussed previously:

$$\int_V \phi_e^* \phi_e d\Omega = 1, \int_V \phi_\nu^* \phi_\nu d\Omega = 1 \quad (\text{A.15})$$

This normalization implies that $N_e = N_\nu = V^{-1/2}$. The nuclear wavefunctions ψ_i and ψ_f are obviously nonzero only within the dimensions of the nuclei being considered, meaning that the integral in the expression for the interaction matrix element extends only over V . The nuclei are small, however, when compared with the volume over which the leptons can be localized, meaning that we can expand the lepton wave functions as power series about the origin $\mathbf{r} = \mathbf{0}$:

$$\phi_e(\mathbf{r}) = \mathbf{V}^{-1/2} [\mathbf{1} + i(\mathbf{k}_e \cdot \mathbf{r}) + \dots] \phi_\nu(\mathbf{r}) = \mathbf{V}^{-1/2} [\mathbf{1} + i(\mathbf{k}_\nu \cdot \mathbf{r}) + \dots] \quad (\text{A.16})$$

Generally we can consider only the first term in the expansion since the second

term is so much smaller, meaning that:

$$\phi_e(0) = \phi_\nu(0) = V^{-1/2} \quad (\text{A.17})$$

We can now write the expression for the interaction matrix element as:

$$H'_{fi} = g\phi_e^*(0)\phi_\nu^*(0) \int \psi_f^* M \psi_i d\Omega = g\psi_e^*(0)\psi_\nu^*(0)M_{fi} \quad (\text{A.18})$$

where the matrix element M_{fi} is defined as:

$$M_{fi} = \int \psi_f^* M \psi_i d\Omega \quad (\text{A.19})$$

The matrix element in Fermi's Golden Rule can then be expressed as

$$H'_{fi} = \frac{g}{V} M_{fi} \quad (\text{A.20})$$

where the matrix element M_{fi} can be envisioned as the overlap integral of the initial and final state wave functions in the presence of a perturbing potential.

For allowed transitions the matrix element M_{fi} is independent of the electron energy, and for forbidden transitions it tends to zero. Generally its value can be calculated when the structures of the parent and daughter nuclei are known. In the case of tritium β decay, the transition is a superallowed transition, meaning that the parent and daughter nuclei belong to an isospin multiplet, which also implies they have the same shell model state. Superallowed transitions have matrix elements that can be evaluated without reference to the details of the nuclear wavefunctions, and for tritium $|M|^2 \approx 5.55$ [136]. Since it can be calculated more accurately than standard allowed transition

matrix elements, the matrix element for tritium β decay does not introduce a dominant uncertainty into neutrino mass investigations.

Inserting the expression for the interaction matrix element and the density of states into Fermi's Golden Rule yields the final expression for the equation of the shape of the β decay momentum spectrum:

$$N(p)dp = \frac{g^2}{2\pi^3 c^3 \hbar^7} |M_{fi}| p^2 (E_o - E) \sqrt{(E_o - E)^2 + (m_\nu c^2)^2} dp \quad (\text{A.21})$$

A.0.2 Final State Effects

The expression for the β energy spectrum must be modified to account for the distortion of the electron wave due to the Coulomb force. When the β is emitted, it experiences a Coulomb force due to the nucleus, which slightly retards the energy of the β and results in more electrons at low energy than the above equation would predict. This effect is normally accounted for by the inclusion of the Fermi function [137]:

$$F(Z_D, E_e) \sim \frac{2\pi\eta}{1 - e^{-2\pi\eta}} \quad (\text{A.22})$$

where $\eta = Z_D\alpha/\beta_e$, Z_D is the atomic number of the nucleus, and α is the fine structure constant.

The distortions of the β spectrum due to the surrounding atomic electrons are generally called the final-state effects, but this term includes two distinct effects. The charges modify the potential near the nucleus where the decay occurs, and this effect is what the Fermi function $F(Z, E)$ takes into consideration. Final-state effects, however, also include the fact that the sudden change in the nuclear charge Z causes a change ΔV in the atomic potential,

which accordingly shifts the energies of the surrounding electrons. To further complicate the situation, the final ion is typically not in an energy eigenstate but rather in a superposition of eigenstates [56]. In order to extract the neutrino mass from the experimental spectrum, the branching ratios and energies of all final states populated in the decay must be calculated.

To illustrate the influence of these final state effects, we consider the conservation of energy in the following way:

$$M_i^{(n)} + E_i = M_f^{(n)} + E_f + E_e + E_\nu \quad (\text{A.23})$$

where $M^{(n)}$ is the nuclear mass, E_i is the initial atomic binding energy, and E_f is the final atomic binding energy. The β is moving so much faster than the atomic electrons that the sudden approximation is appropriate [56]. The average endpoint energy of the electron and the neutrino is:

$$\langle E_e + E_\nu \rangle = M_i^{(n)} - M_j^{(n)} - \langle i|\Delta V|i \rangle \quad (\text{A.24})$$

where the last term corresponds to the average endpoint shift. For a free tritium atom $\Delta V = -e^2/r$, and the shift is 27.2 eV. The spread of the endpoints can be written:

$$\langle (E_e + E_\nu)^2 \rangle = \langle i|(\Delta V)^2|i \rangle - \langle i|\Delta V|i \rangle^2 \quad (\text{A.25})$$

which is $(27.2)^2 \text{ eV}^2$ for free tritium. This spread of the endpoints results in a decrease of the slope in the Kurie plot, which unfortunately masks the effect of the finite neutrino mass. Of course the β spectrum actually consists of many branches because the final state is typically a superposition of energy

eigenstates, which implies that the actual endpoints should be written as:

$$E_o^k = M_i^{(n)} - M_f^{(n)} + E_i - E_f^k \quad (\text{A.26})$$

where the index k labels the various possible final states. The population of each state is the square of the corresponding overlap integral $\langle i|f^k \rangle^2$. This calculation can be done exactly for free tritium atoms [138], where the ^3He ion goes into the 1s ground state 70% of the time, the 2s state at 40.8 eV 25% of the time, the 3s state at 48.4 eV 1.4% of the time, ect. For more complicated systems such as molecular tritium, numerical calculations are required, and the results are significantly more complicated than in the atomic case [139].

Figure A.3 illustrates how significant the final state corrections to the β spectrum curve can be. It shows a hypothetical case in which the atom has an equal chance of decaying into the ground state, the first excited state at 20 eV, the second excited state at 40 eV, or the third excited state at 60 eV.

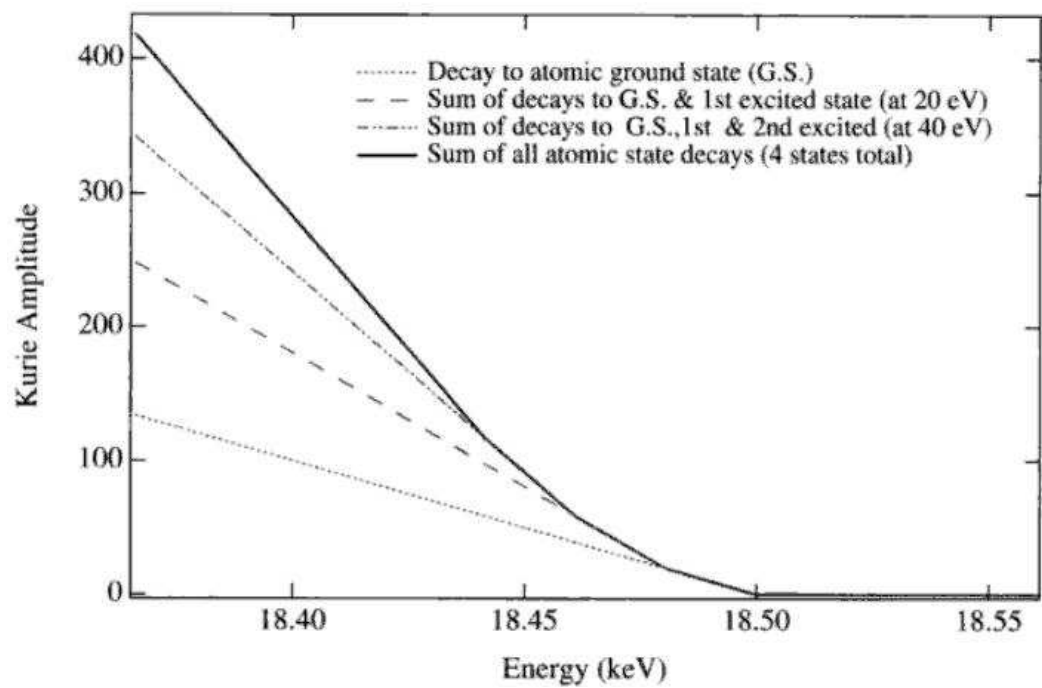


Figure A.3: Effect of final state corrections on Kurie plot for the hypothetical case in which the atom has an equal probability of decaying into any of the excited states at 20 eV, 40 eV, or 60 eV. Figure taken from reference [136]

Appendix B

Boundstate Tritium Beta Decay

Tritium undergoes not only ordinary β decay but also bound-state β decay in which the electron is created in a bound state of the daughter atom. The simple-two body decay kinematics allow for a possible determination of the neutrino mass by measuring the recoil velocity of the daughter atom. This appendix outlines one experimental proposal and discusses simulation results of its potential neutrino mass sensitivity. While the observation of tritium boundstate β decay would certainly be an interesting and novel approach to investigating neutrinos, it does not seem like a promising avenue through which to set a competitive limit on the neutrino mass.

B.1 Boundstate Decay

Boundstate β decay has been studied theoretically for more than fifty years [140, 141, 142, 143, 144, 145], and for most atoms it is extremely improbable because the inner electron states that would make the most favorable final states for the β are already filled in the daughter atom. Tritium β decay is, therefore,

unique in its ability to undergo boundstate β decay with non-negligible probability. Although tritium boundstate β -decay has not yet been experimentally observed, its kinematics are simple. Such a decay emits a monoenergetic neutrino whose energy is equal to the initial tritium atom's energy minus the final ^3He atom's energy. If the neutrino were massless, the nuclear recoil velocity would be $v_R = \frac{Q}{Mc}$, where Q is the $^3\text{H}-^3\text{He}$ mass difference, and M is the ^3He mass. Accounting for the neutrino's mass, the recoil velocity is

$$v'_R = \frac{[Q^2 - (m_\nu c^2)^2]^{1/2}}{Mc} \quad (\text{B.1})$$

Q is very precisely known [146], meaning that a measurement of the recoil velocity would provide an experimental measurement of the neutrino mass [144].

Calculations indicate that a remarkable 0.69% of all tritium decays are bound state decays [145], making this decay a statistically appealing avenue through which to explore the neutrino mass.

B.2 Experimental Design

When tritium undergoes boundstate decay, 80% of the decays go into the ground state of ^3He , which cannot be easily detected [144], but 3% go into an excited 3^32_1 state. This excited state quickly decays by emitting a photon of energy 706.52 nm, which can be detected using a lens and a PMT. The atom then decays to a metastable state, emitting a photon of 1083 nm that we would not detect. Figure B.1 shows the grotrian diagram for ^3He , highlighting the transitions that are significant for this experiment.

Figure B.2 shows our proposed experimental setup to make the first

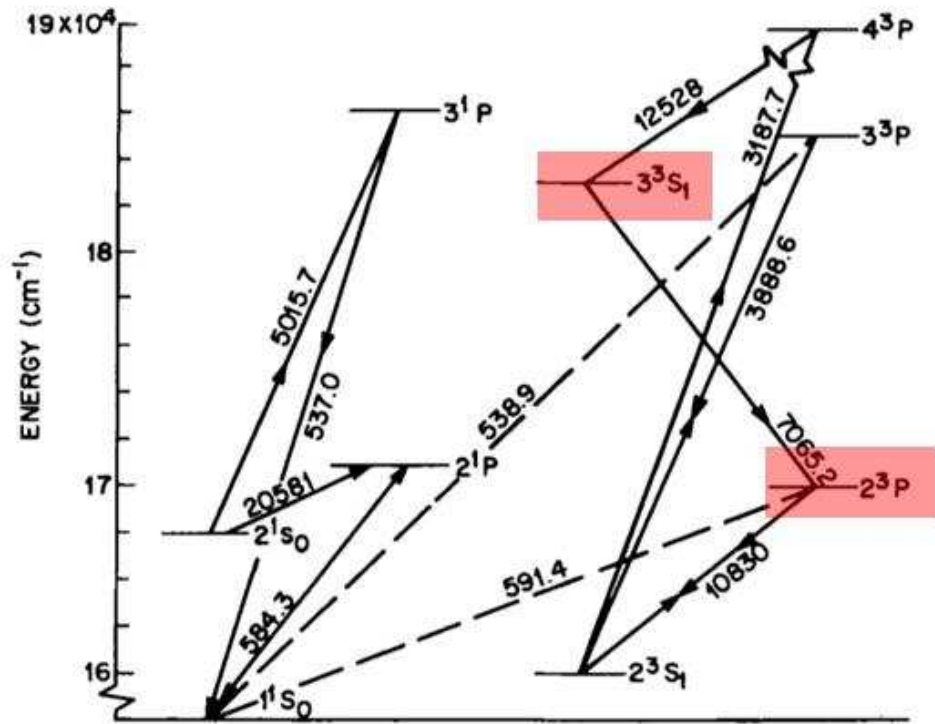


Figure B.1: Grotrian diagram for ${}^3\text{He}$, taken from [144]. The highlighted transitions are the ones that could be most easily detected in an experimental like the one shown in Figure B.2

observation of the two-body boundstate decay of tritium. The atomic tritium source is similar to the one discussed in Chapter 4, and we place a $50 \times 50 \text{ cm}^2$ microchannel plate (MCP) 0.5 m from the source. We detect the photon emitted by the excited helium atom using a single-photon imaging technique, which can provide the z-position of the photon emission with an optical resolution of $20 \mu\text{m}$. The metastable helium atom is detected by the MCP, and the coincidence with the photon detection can be used to discriminate against background signals. The atom's time-of-flight to the MCP, along with the

measured z-position of photon emission and the MCP x and y hit positions allow for a reconstruction of the atom's recoil velocity. Unfortunately little is known about the direction of the photon emission, so the atom's velocity is altered in an unpredictable way by that emission. The lenses used to detect the photon are 1.5 inches in diameter, and they are placed 2 cm from the tritium source. The lenses are positioned such that an equal number of photons hit the front and back halves of each lens, and approximately 15% of photons that hit the lens also hit the PMT.

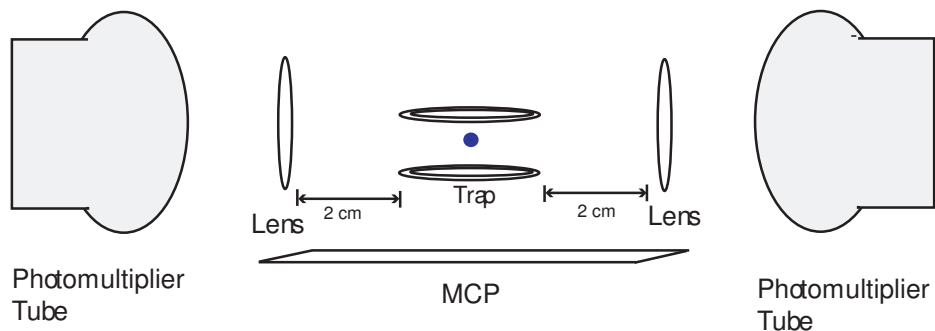


Figure B.2: Experimental setup for observation of tritium boundstate β -decay

B.3 Simulation Results

The simulation I created to model this experiment is similar to the ROOT simulation described in Chapter 4. The source is 100 μm in diameter, and its temperature is 10 μK . Figure B.3 shows sample simulation data in which an unrealistically large neutrino mass of 20 eV has been assumed. The peak is the reconstructed neutrino mass squared, and the Gaussian fit to the peak indicates a neutrino mass of $19.6 \text{ eV} \pm 6.9 \text{ eV}$, with a 90% confidence level for

discovery of 8.8 eV.

Figure B.4 shows the 90% confidence level on a neutrino mass measurement that is possible in this experimental setup, which obviously depends on the number of tritium decays that occur during the experimental runtime. Clearly reaching sub-eV precision on the neutrino mass would require an unrealistic number of decays.

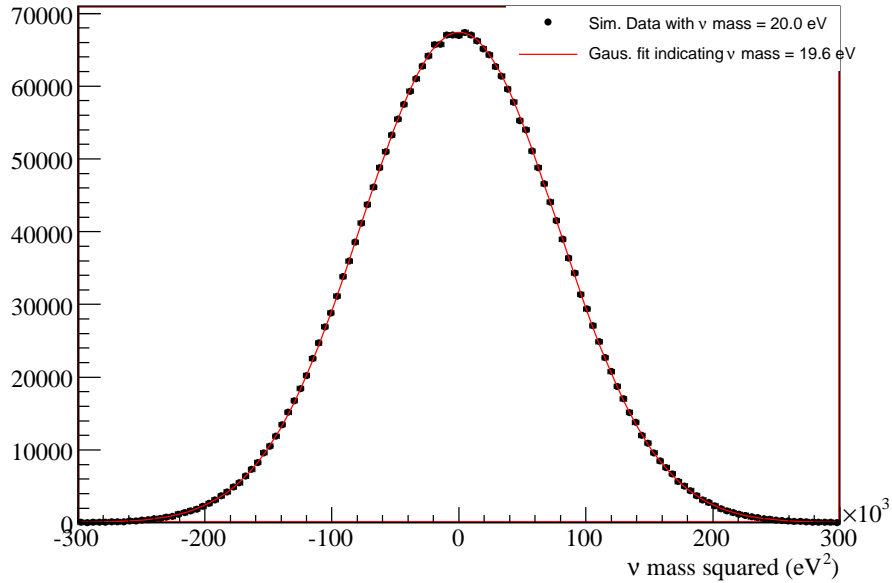


Figure B.3: The data is from a simulation that assumed an (unrealistic) 20 eV neutrino mass. The Gaussian fit yields a neutrino mass of 19.6 eV, with a 90% confidence interval of 8.8 eV.

The difficulty in making a competitive measurement with this technique can be illustrated by noting that the velocity precision required to detect a neutrino mass of 0.2 eV is approximately $\Delta v'_R/v'_R = 6 \times 10^{-11}$ [144]. That level of precision is difficult given the incomplete information concerning the direction of photon emission for both the 706.52 nm photon and the subsequently

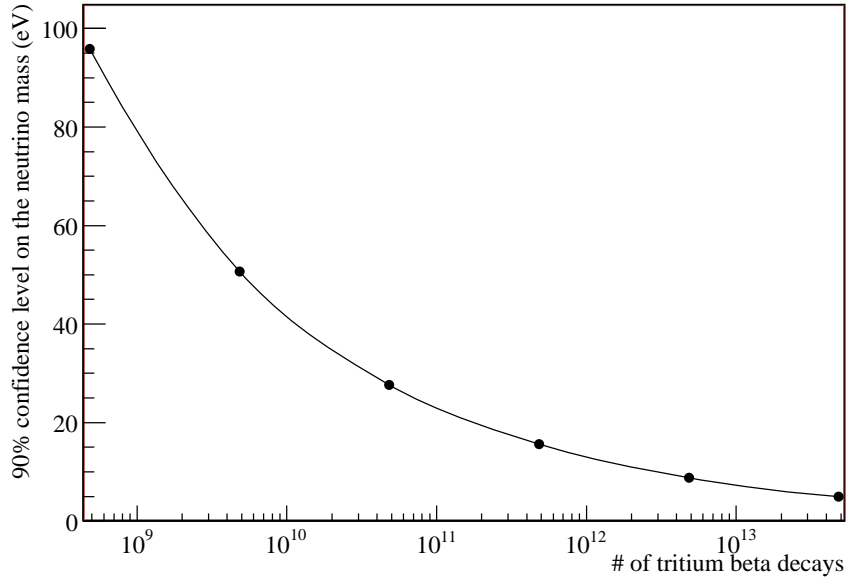


Figure B.4: 90% confidence intervals achievable from simulations of data sets involving different numbers of tritium β decays from the source.

emitted 1083 nm photon. Increasing statistics certainly improves the precision of the neutrino mass fit, but simulations indicate that a sub-eV limit on the neutrino mass is not promising given currently achievable trapping densities. Even assuming as many as 5×10^{13} tritium β -decays, the best 90% confidence level on the upper limit of the neutrino mass that we can obtain is 8.8 eV. Detecting sub-eV neutrino mass probably requires moving beyond the simple kinematics of two-body boundstate β decay, although the observation of boundstate β decay in tritium could be significant for other experiments, such as a neutrino Mössbauer experiment [147] like the one discussed in Appendix C.

Appendix C

Mössbauer Neutrinos

Neutrino cross sections are so small that the possibility of increasing them many orders of magnitude through an effect like Mössbauer resonance is very appealing. This chapter begins by introducing the ordinary Mössbauer effect for atoms before proceeding to discuss how that effect could be applied to neutrino investigations. I discuss the basic principles involved in previous proposals for Mössbauer neutrino detection and highlight some of the most significant difficulties in those approaches. I then discuss a new experimental design for Mössbauer neutrino detection made possible through the atomic slowing techniques introduced in Chapter 3. I conclude by presenting simulation results of this experiment as well as discussing a significant theoretical uncertainty that could undermine the ultimate success of such an experiment.

C.1 Ordinary Mössbauer Effect

C.1.1 Ordinary Resonance Fluorescence

The Mössbauer effect involves the recoilless emission of a photon by an atom bound in a solid, followed by the recoilless resonant absorption of that same photon. Ordinarily when an atom decays from some excited state by emission of a photon of energy E_γ , momentum conservation requires that the atom receive recoil momentum P equal and opposite to the momentum p of the photon. The recoiling atom, therefore, receives an energy equal to:

$$E_{recoil} = \frac{P^2}{2M} = \frac{p^2}{2M} = \frac{E_\gamma^2}{2Mc^2} \quad (\text{C.1})$$

This treatment obviously assumes that the recoiling atom is nonrelativistic, which is a very good assumption since the gamma rays studied in atomic and nuclear resonance fluorescence have energies that are small compared to the rest masses of the atoms. One can estimate the recoil energy by noting that conservation of energy requires that $E_\gamma + E_{recoil} = E_{level}$ where E_{level} is the energy separation of the two levels in the atom that constitute the initial and final states. Since E_{recoil} is much less than E_γ , one can assume that $E_{recoil} \cong E_{level}^2/2Mc^2$. Of course the excited state of the atom also possesses a width. If the lifetime of the excited state is τ , then the Heisenberg uncertainty principle dictates that the energy of the excited state cannot be measured exactly and has a width corresponding to:

$$\Gamma = \frac{\hbar}{\tau} \quad (\text{C.2})$$

Figure C.1 shows that for ordinary resonance fluorescence, the energy of the emitted photons is reduced by the recoil energy, the energy required to excite the target atoms is increased by the recoil energy, and the probability of observing resonance absorption depends on the overlap of the two curves shown in part d) of the figure. While optical transitions for atoms can fulfill the condition $2E_{recoil} < \Gamma$, nuclear transitions do not fulfill it. One must also take into account, however, that both the source and target atoms are in motion, which introduces additional broadening into the emission and absorption lines known as Doppler broadening. The natural linewidth Γ is not always the dominant broadening in resonance fluorescence. For optical radiation, the recoil energy is typically small compared to the Doppler broadening; the emission and absorption lines overlap, and resonance conditions can be obtained. For nuclear gamma rays, however, the recoil energy is often comparable to the Doppler broadening, and the calculation of when to expect to observe resonance fluorescence becomes more complicated.

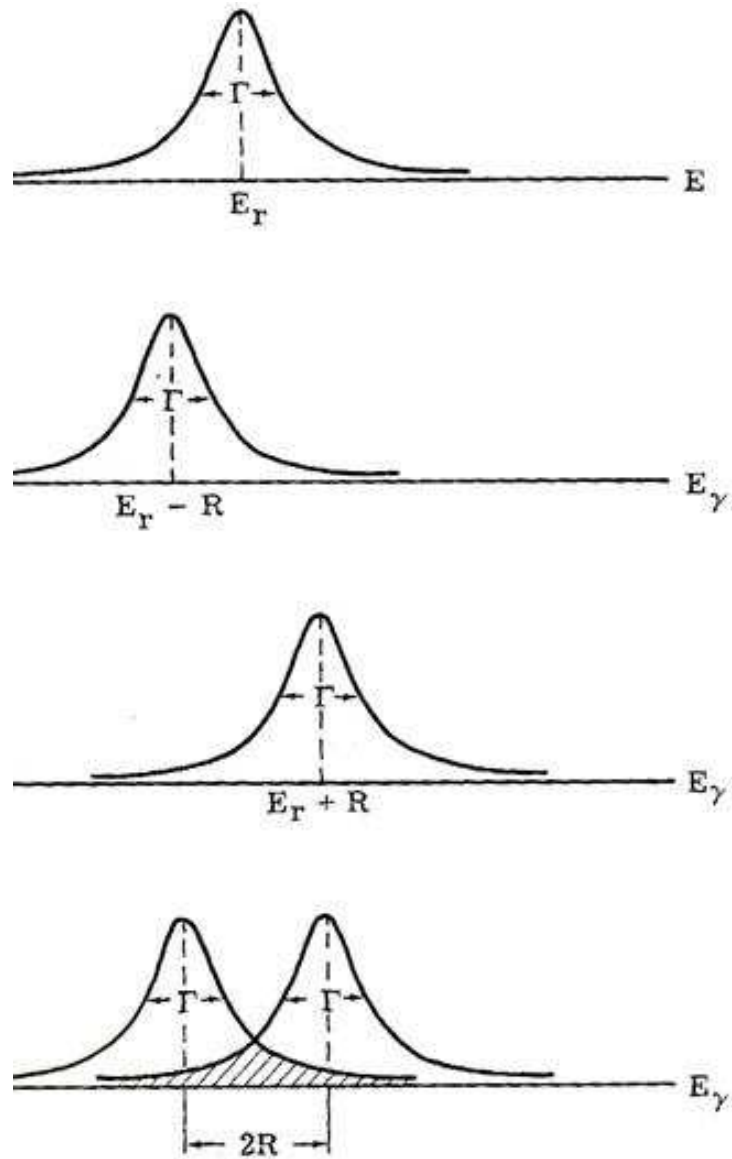


Figure C.1: Illustration of ordinary resonance fluorescence. E_R shown in a) is equivalent to E_{level} , the energy of the atom's excited state. $E_r - R$ in b) shows the slightly shifted energy distribution of the photons emitted by the source. $E_r + R$ in c) shows the energy distribution required to excite atoms in the target. The curves in d) show the overlap region that enables ordinary resonance fluorescence. Figure taken from [148].

C.1.2 Mössbauer's Discovery

In the late 1950s Rudolph Mössbauer was studying nuclear resonance scattering of the 129 keV gamma ray from Ir^{191} in solid Ir. For this transition the recoil energy is 0.05 eV, and the Doppler broadening at room temperature is approximately 0.1 eV, meaning that at room temperature the emission and absorption peaks should overlap sufficiently to allow for observation of resonance. Mössbauer decided to cool both the source and the absorber to reduce the Doppler broadening, expecting that the observed resonance effect would decrease. Much to his surprise, he actually observed an increase in the resonance scattering. After studying preliminary work done by Lamb [149], Mössbauer proposed that for atoms in a solid, some fraction of the emissions could be recoilless since the lattice itself could absorb the recoil [150]. This explanation fit with his observation that some fraction of the gamma rays did not display any Doppler broadening and had a width corresponding to the natural line width.

Initially Mössbauer's results were questioned and in some cases flatly disbelieved. The early experiments on Ir^{191} were complicated because the effect was small, and the low-temperature requirements were difficult. Shortly afterwards, however, the Mössbauer effect was observed in Fe^{57} , and unlike in Ir^{191} , the effect in iron is large, and it persists up to temperatures as high as 1000°C.

Qualitatively the Mössbauer effect can be understood through basic considerations of momentum and energy. When an atom bound in a solid emits a photon, the recoil momentum cannot go into translational motion of the atom because the energy required to leave the lattice site is on the order

of 10 eV, while the energy from the recoil will not exceed more than a few tenths of an eV. Lattice vibrations in the form of phonons, however, cannot take up momentum. Each phonon excited with its momentum pointing in one direction will have a corresponding phonon with its momentum pointing in the opposite direction, so the expectation value of the momentum for lattice vibrations vanishes. The momentum must, therefore, go into the translational motion of the entire solid.

Energy conservation is more complicated to understand in this process. The transition energy could theoretically be shared among the emitted photon, the atom, lattice vibrations, and the entire solid. As discussed above, the atom does not acquire translational motion, so it also does not acquire translational energy. The energy of motion that goes into the entire solid is extremely small and can be neglected. A Mössbauer transition occurs, therefore, if the state of the lattice remains unchanged, meaning that the emitted photon receives the entire transition energy. The probability of the photon receiving the full transition energy can be calculated quantum mechanically, but it can also be approximated through simple considerations. In 1907 Einstein postulated that a solid consisted of a large number of independent oscillators each vibrating with a frequency ω_E . Although this is a somewhat naive picture, the smallest energy that can be give to an Einstein solid is $E_E = \hbar\omega_E = k\Theta_E$, where Θ_E is a temperature. If the recoil energy of a free nucleus is small compared to this excitation energy, the probability of emission of a phonon will be small, and the photon will likely be emitted with the full transition energy. The full calculation for an Einstein solid shows that this probability is [148]:

$$f = e^{-E_{recoil}/k\Theta_E} \tag{C.3}$$

A more realistic picture of a solid is given by the Debye model, which assumes that a continuum of oscillator frequencies exists ranging from zero to a maximum frequency ω_D where the spectrum of lattice vibrations depends on ω^2 . In this model the lattice vibration with the maximum energy produces a phonon of energy:

$$E_D = \hbar\omega_D = 2\pi\hbar u/\lambda \approx 2\pi\hbar u/2d \quad (\text{C.4})$$

where d is the lattice constant and u is the velocity of sound in the solid. If this lattice wave were the only one that could be excited, then the probability for a recoilless emission would be similar to Equation C.3 except with the Debye temperature replacing the Einstein temperature. In the Debye solid, however, the possibility exists to excite photons with longer wavelengths. These low energy phonons are not easily excited, however, due to the fact that the most efficient mode of exciting lower energy phonons involves two adjacent atoms moving in phase. The full calculation for the probability of a transition occurring without changing the lattice states shows that [148]:

$$f = e^{-3E_{recoil}/2k\Theta_D} \quad (\text{C.5})$$

where Θ_D is the Debye temperature of the lattice and k is the Boltzmann constant. Even at very low temperatures the vibrations of the atoms cannot be completely eliminated, meaning that the recoilless fraction is always less than one.

C.2 Mössbauer Effect for Neutrinos

C.2.1 Boundstate Decay

After the observation of the Mössbauer effect for γ -transitions in nuclei, several authors suggested the possibility of observing recoilless emission and absorption of antineutrinos [151, 147]. The Mössbauer resonance would greatly enhance the antineutrino absorption cross section, making certain neutrino interactions easier to observe. Tritium β decay offers a unique opportunity to observe the Mössbauer effect for neutrinos because such a large fraction of tritium β decays are boundstate decays, 0.69%. The basic idea, shown in Figure C.2, is that in a tritium lattice, some fraction of the boundstate decays will emit an 18.6 keV antineutrino without recoil, and that antineutrino would be on resonance to be absorbed (again without recoil) by an atom in a ${}^3\text{He}$ lattice through the reverse boundstate process.

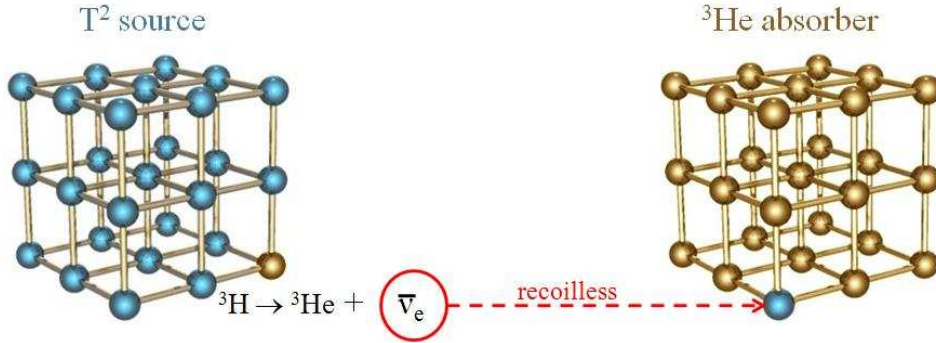


Figure C.2: Conceptual illustration of the Mössbauer effect in which an antineutrino from a tritium β decay is on resonance to undergo reverse β decay when it encounters a ${}^3\text{He}$ lattice. (The illustration of the two lattices is conceptual and does not actually convey information about the realistic lattice structure.)

C.2.2 Physics Potential

Mössbauer neutrino detection could enable several interesting future experiments. Because of their sharp energy distribution, oscillations of Mössbauer neutrinos are interesting to theorists who want to explore the quantum mechanical evolution of the neutrino state [152].

More importantly the low 18.6 keV endpoint energy of the $\bar{\nu}_e$ would enable very short baseline experiments to determine oscillation parameters. For example, by optimizing the probability for oscillation discussed in Chapter 2, which depends on $\sin^2(\frac{\Delta m^2 L}{4E})$ (where L is in km, Δm^2 is in eV^2 , and E is in GeV), one finds that for 18.6 keV electrons, a baseline of only 10 m is necessary. If precision measurements could be made of both Δm_{31}^2 and θ_{13} , then a determination of the neutrino mass hierarchy is also possible [153, 154].

One could consider a disappearance experiment to search for $\bar{\nu}_e \rightarrow \nu_{sterile}$. If $\Delta m^2 \approx 1$ eV, then the oscillation length would be ~ 5 cm. The short baselines possible for Mössbauer neutrinos would enable such a search.

One could also perform gravitational redshift measurements using $\bar{\nu}_e$'s instead of photons in a kind of recreation of the Pound-Rebka experiment [155]. In that experiment they varied the Doppler shift of the emitted Mössbauer photons and observed the subsequent change in the absorption rates, and they performed this experiment on both the roof and the basement of a building to study how the results changed in a gravitational field. Since antineutrinos have a small rest mass (and are antimatter), they could in principle behave differently from photons (or neutrinos) in a gravitational field.

C.2.3 Recoilless Fraction

The most important calculation in Mössbauer spectroscopy is the fraction of events that will be emitted without recoil. This fraction is given by [156]:

$$f = e^{-\frac{E}{\hbar c}^2 \cdot \langle x^2 \rangle} \quad (\text{C.6})$$

where E is the transition energy, which is 18.6 keV for the ${}^3\text{H}$ - ${}^3\text{He}$ system, and $\langle x^2 \rangle$ is the mean-square atomic displacement. The recoilless fraction is largest at low temperatures where few lattice excitations are present. Assuming very low temperatures and a Debye model for the solid [157],

$$f(T \rightarrow 0) = e^{-\frac{E^2}{2Mc^2} \cdot \frac{3}{2k\Theta_D}} \quad (\text{C.7})$$

C.2.4 Previous Proposals

Most of the previous suggestions for observing the Mössbauer effect with neutrinos have involved putting ^3H and ^3He in a metal matrix, such as niobium. The Debye temperature for such a matrix is estimated to be approximately 800 K [158], which leads to $f(0) \approx 0.27$ for the probability of a recoilless emission. Of course in order to observe recoilless emission and absorption, one has to apply that factor twice, but $f^2 \approx 0.07$ still leaves a high enough fraction of decays to be potentially observable.

The biggest challenge faced by methods intending to embed tritium and helium into niobium is detection. Once the ^3He atoms have undergone reverse β decay and become ^3H atoms, the tritium must then be detected. No convenient way exists to extract the tritium from the niobium and measure it, so one must simply wait for the ^3H to undergo ordinary β decay. Since the half life of tritium is 12.3 years, many ^3He atoms need to undergo reverse β decay in order to enable sufficient detection. Other problems specific to the niobium matrix, such as lattice expansion and contraction, will be discussed later in this chapter.

Creation of the target niobium lattice is also challenging. Generally proposals suggest using the so-called “tritium trick” [156, 158], in which tritium is put into a metallic matrix, and one waits until almost all of the tritium has decayed to ^3He . This method ensures that the ^3He and ^3H share the same tetrahedral interstitial sites in the matrix, but tritium that remains in the target will provide background to the final measurement of β decay coming from the target.

C.3 Calculations

C.3.1 cross section

The reaction $\bar{\nu}_e + e^- + A_Z \rightarrow A_{Z-1}$, in which an atom undergoes reverse boundstate β decay, is resonant in character and should occur at a definite $\bar{\nu}_e$ energy equation to:

$$E_{\bar{\nu}^{res}} = E_o + E_i \quad (\text{C.8})$$

where E_o is the endpoint energy of the β spectrum and E_i is the electron binding energy. In order to calculate the cross section involved one must find the width Γ of the process, and in terms of that width the cross section formula is [159]:

$$\sigma = 2S \left(\frac{\pi \hbar c}{E_{\bar{\nu}^{res}}} \right)^2 \rho(E_{\bar{\nu}^{res}}) \Gamma \quad (\text{C.9})$$

where $\rho(E_{\bar{\nu}^{res}})$ is the resonant spectral density, meaning the number of antineutrinos in an energy interval of 1 MeV around $E_{\bar{\nu}^{res}}$, and $S = (2I_K + 1)(2I_H + 1)$ is the spin statistical factor. For allowed transitions we can utilize the following expression for allowed K capture:

$$\Gamma_K = 2(GE_{\bar{\nu}^{res}})^2 |\psi(R_o)|^2 |M|^2 \frac{1}{\pi \hbar^3 c^3} \quad (\text{C.10})$$

where $G = 1.41 \times 10^{-49}$ erg-cm³, M is a dimensionless matrix element, and $|\psi(R_o)|^2$ is the value of the square of the wave function of the K electron on the surface of the nucleus.

Experimentally we can measure a quantity known as the comparative

half-life (or reduced half-life) that is helpful in rewriting the above expression:

$$ft_{1/2} = \frac{2\ln 2\pi^3\hbar^7}{G_F^2 m_e^5 c^4} \cdot \frac{1}{|M|^2} \quad (\text{C.11})$$

The comparative half-life is a direct measure of the matrix element, and one can use it to express the width as:

$$\Gamma = 4\pi^2 \left(\frac{E_{\bar{\nu}}^{res}}{mc^2}\right)^2 \frac{\hbar\ln 2}{ft_{1/2}} \left(\frac{\hbar}{mc}\right)^3 |\psi(R_o)|^2 \quad (\text{C.12})$$

Plugging that expression for the width into the expression for the cross section yields:

$$\sigma = S8\pi^4 \left(\frac{\hbar}{mc}\right)^2 \frac{\hbar\ln 2}{ft_{1/2}} \left(\frac{\hbar}{mc}\right)^3 |\psi(R_o)|^2 \rho(E_{\bar{\nu}}^{res}) \quad (\text{C.13})$$

This cross section is not explicitly dependent on the energy of the antineutrino and is determined by the spectral density of the flux in the resonant region. Using the convention that $g_o^2 = 4\pi \left(\frac{\hbar}{mc}\right)^3 |\psi(R_o)|^2$, we can write the cross section as:

$$\sigma = S2\pi^3 \left(\frac{\hbar}{mc}\right)^2 \frac{\hbar\ln 2}{ft_{1/2}} g_o^2 \rho(E_{\bar{\nu}}^{res}) \quad (\text{C.14})$$

Multiplying the constants, one finally obtains:

$$\sigma = 4.18 \times 10^{-41} g_o^2 \frac{\rho(E_{\bar{\nu}}^{res})}{ft_{1/2}} \text{ cm}^2 \quad (\text{C.15})$$

Numerically we can approximate g_o^2 for low-Z hydrogen-like wavefunctions as [159]:

$$g_o^2 \approx 4 \left(\frac{Z}{137}\right)^3 \quad (\text{C.16})$$

For a super-allowed transition like the one in the ${}^3\text{H}$ - ${}^3\text{He}$ system, the reduced

lifetime $\Gamma t_{1/2}$ is approximately 1000 s [157].

Without utilizing the Mössbauer effect, one could attempt to observe resonant absorption and emission with ^3H and ^3He in gas phase. At room temperature the Doppler broadening is approximately 0.16 eV, and the energy separation of the emission and absorption lines due to the recoil is approximately 0.12 eV, leading to a resonance cross section of $\sigma \approx 10^{-42} \text{ cm}^2$. The large source and target masses required in this case would make experimental observation practically impossible. By harnessing the Mössbauer effect to increase the cross section by several orders of magnitude [145, 158], an experiment could be feasible.

C.3.2 Linewidth and Broadening

Two types of broadening are significant for any experiment attempting to measure the Mössbauer effect for neutrinos. The first is homogeneous broadening, which is caused by electromagnetic relaxation. For example, spin-spin interactions between atomic and nuclear spins of ^3H and ^3He with the spins of the atoms and nuclei in the metallic lattice lead to fluctuating magnetic fields. One simple model of magnetic relaxation is a three-level system consisting of a ground state and two excited hyperfine states that have an energy separation $\hbar\Omega_o$. The relaxation consists of transitions that occur between the two hyperfine states with an average frequency of Ω . If $\Omega \gg \Omega_o$, then the system only remains for a short time in one of the levels and stochastically jumps into the other one. An averaging process over both energy levels results in one line at the center of the hyperfine splitting, and this line's width is close to the natural linewidth. Unfortunately the typical hyperfine splittings due to spin-spin

interactions in metallic lattices are $\Omega_o \approx 10^5 \text{ s}^{-1}$ [156], while the typical relaxation times are anywhere from ms to μs . Homogeneous broadening cannot, therefore, be overcome with motional narrowing, and one must accept that the broadened linewidth will be on the order of $10^{-13} - 10^{-12} \text{ eV}$ [156, 157].

The second type of line broadening is known as inhomogeneous broadening. It is caused by stationary effects such as crystal impurities, lattice defects, and variations in the lattice constant. In the best single crystals used for ordinary Mössbauer spectroscopy, inhomogeneous broadening is on the order of $10^{-13} \text{ eV} - 10^{-12} \text{ eV}$, and for Mössbauer antineutrinos, the effect could be larger, especially if one relies on a metallic matrix.

C.3.3 Second Order Doppler Shift

In addition to broadening effects that smear the natural linewidth, other effects cause a shift in the resonant energy. An atom vibrating around its equilibrium position in a lattice exhibits not only a mean-square displacement $\langle x^2 \rangle$ but also a mean-square velocity $\langle v^2 \rangle$. Special relativity indicates that a time-dilation effect results, which corresponds to a reduction of the atom's frequency: $\Delta\nu = \nu - \nu' = -v^2/(2c^2)$. The reduction is proportional to $(v/c)^2$ and is often called the second order doppler shift (SOD).

We must also consider that the source and the target may not be at exactly the same temperature. In the Debye model of a solid the energy shift between a source at temperature T_s and a target at temperature T_t is [157]:

$$(\Delta E/E) = \frac{9k}{16Mc^2}(\theta_s - \theta_t) + \frac{3k}{2Mc^2}[T_s \cdot f(T_s/\theta_s) - T_t \cdot f(T_t/\theta_t)] \quad (\text{C.17})$$

where $f(T/\theta) = 3(T/\theta)^3 \int_0^{\theta/T} \frac{x^3}{e^x - 1} dx$. At low temperatures the temperature-dependent term does not contribute if the source and target are at approximately the same temperature, which can be achieved with a helium bath [157]. The first term, however, comes from the zero-point energy and will not be zero since the Debye temperatures of the source and target will not be identical. Even if the Debye temperatures vary by only 1 K, the resulting energy shift would be $(\Delta E/E) \approx 2 \times 10^{-14}$, which would prohibit resonance absorption. Technically the Debye temperatures (i.e. the chemical bonds) of ^3H and ^3He do not have to be the same, but the chemical bond for ^3H has to be the same in the source and in the target, and the same applies to ^3He . This requirement is difficult to meet using a metallic matrix since the source and target contain vastly different amounts of ^3H and ^3He . The nearest higher-order neighbors of the atoms in the lattice sites need to be identical in the source and the target, but the source contains a lot of ^3H and very little ^3He , while the target contains a lot of ^3He and very little ^3H .

C.3.4 Isomer Shift

The binding energies of ^3H and ^3He certainly effect the energy of the antineutrino. Ideally the difference in the binding energies leads to a little bit of extra energy being given to the emitted antineutrino, and that energy exactly compensates for the extra energy needed in the reverse process. In the ordinary Mössbauer effect involving photons, different binding energies due to inhomogeneities in the source and target affect the photon energy via the change in the mean-square nuclear charge radius between the groundstate and the excited state of the nucleus. This effect is known as the isomer shift. For the

case of an antineutrino emission, the antineutrino energy is directly affected because the antineutrino is directly involved in the decay. The isomer shift is, therefore, likely to be larger in a Mössbauer neutrino experiment.

C.4 Experimental Design

Given all of the expected energy shifts in a neutrino Mössbauer experiment, one would like some degree of tunability in the experimental design. Without the ability to tune a significant experimental parameter, a null result would be extremely difficult to interpret. Given the complexities of working with a metallic matrix, one would also prefer to avoid that method. The slowing and trapping techniques described in Chapter 3 create the possibility of a new type of source and target that would have considerable advantages over the traditionally considered metallic systems.

Figure C.3 shows our proposed experimental setup. We suggest using two diamond anvil cells (DACs), one filled with molecular tritium and one filled with ^3He . The diamond anvil cells can create enormous pressures, and we propose using a pressure of approximately 10 GPa. The DACs enable the high pressures that lead to high Debye temperatures, which increase the recoilless fraction. While they do impose a volume constraint that prevents our sample size from being larger than $\sim 0.004 \text{ cm}^3$, the ability to tune the pressure more than compensates. The small volume size actually helps reduce backgrounds from neutrons, which have a high absorption cross section on ^3He .

As shown in Figure C.4, the Debye temperature of ^3He can be directly controlled by changing the pressure [160, 161]. This pressure dependence pro-

vides the tunability necessary to counteract the various energy shifts. Looking at Equation C.17 for the second order doppler shift, one sees that the energy shift from this effect can be positive or negative depending on whether the Debye temperature of the source is higher or lower than that of the target. By controlling the target's Debye temperature, we can use the second order doppler shift to cancel out any other energy shifts. While we still have to worry about homogeneous and inhomogeneous broadening, even those effects should be more favorable than they appeared in a metallic matrix because our source and target materials are pure substances. The primary inhomogeneous effects will come as β decays occur in the target, producing a ${}^3\text{He}$ atom in a site that previously contained ${}^3\text{H}$.

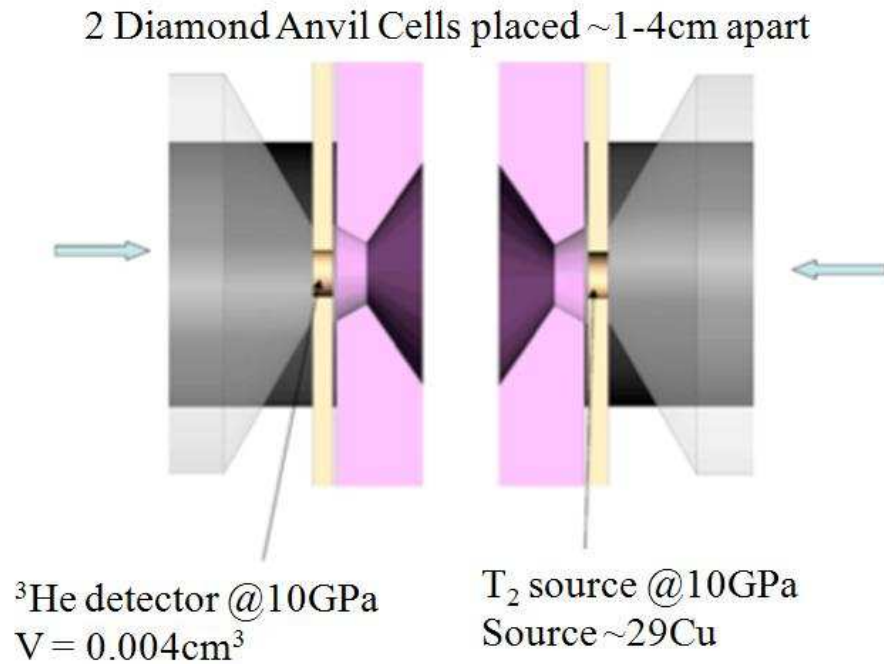


Figure C.3: Two diamond anvil cells keep a source of ${}^3\text{H}$ and a target of ${}^3\text{He}$ under high pressure to increase the Debye temperature and maximize the recoilless fraction.

In addition to the inherent advantage of tunability, this method also has advantages in detecting the tritium atoms produced by Mössbauer neutrinos. The atomic slowing techniques discussed in Chapter 3 enable a much more efficient detection than simply waiting to detect β 's from the tritium produced in the target. Using a cold finger that absorbs ${}^3\text{H}$ but not ${}^3\text{He}$, one could extract the tritium from the target and then mix it with neon. That gas mixture could be shot through a supersonic nozzle toward a magnetic slower like the one described in Chapter 3, and approximately 0.1% of the tritium

could ultimately be detected.

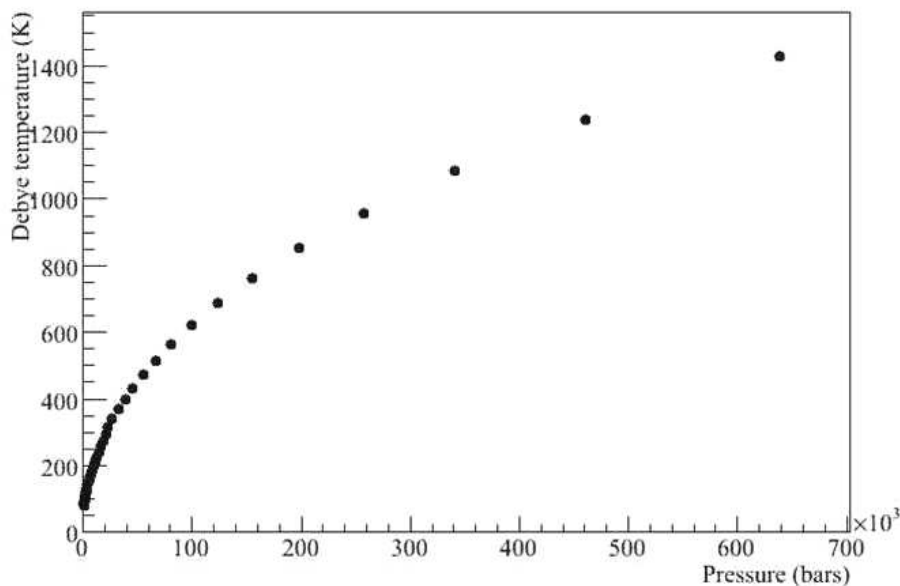


Figure C.4: The effective Debye temperature vs. pressure for solid ^3He . By tuning the pressure of the DACs, the Debye temperature can be adjusted, which allows the emission and absorption peaks to be aligned experimentally.

C.5 Simulation Results

I created a simple simulation of the experiment shown in Figure C.3 using the basic ROOT software discussed in Chapter 4. I constructed the DAC target volume a cylinder with length= 0.77103 mm and radius= 1.28505 mm. The initial position of each decay was chosen randomly, as was the direction of the outgoing neutrino. The source and target volumes were 1 cm apart, and $\sim 7.9\%$ of the neutrinos from the source actually hit the target at that distance. When a neutrino from the source hit the target, I computed the

distance that it would travel through the target in order to have an interaction length to put into the cross section calculation. Since the probability of interacting is still quite low, I scaled the probability up and subsequently scaled down the number of events I had to run in order to have simulated a certain number of boundstate decays. I calculated the fraction of decays that are recoillessly emitted and absorbed using Equation C.7, and I computed the interaction probability of those neutrinos using the cross section in C.15. The resonant spectral density from C.15 is the inverse of the line broadening, which I assume is dominated by inhomogeneous broadening at a level of 1×10^{-12} eV. I assume both the emission and absorption peaks are Breit-Wigner distributions with widths defined by the inhomogeneous broadening. The peaks are offset by a small amount representing the imperfection in the alignment of the Debye temperatures. The fraction of overlap of the peaks conveys the fraction of Mössbauer neutrinos that will be on resonance even when the Debye temperatures of the source and target are not exactly the same. Since we can tune the Debye temperature in order to maximize the signal, I assume that the peaks are perfectly aligned for the results discussed below.

Molecular tritium will have a slightly different boundstate decay fraction than atomic tritium. The boundstate decay fraction for molecular tritium is estimated to be 0.002 [162], as opposed to 0.0069 for atomic tritium. I assume that the helium atom still goes into the groundstate for 80% of those decays. Tritium activity is 9650 Ci/g, which leads to a simple calculation of the boundstate neutrino flux that depends on the source geometry and pressure.

Figure C.5 shows simulation results of the number of expected Mössbauer neutrino events in the target for a variety of different pressures. Given that

approximately 0.1% of those events could be detected using a magnetic slower, I estimate that one could detect ~ 30 events per week for a reasonable Debye temperature of ~ 700 K. At that temperature the recoilless fraction is ~ 0.217 (Equation C.7) and the cross section is $\sim 4.5 \times 10^{-31}$ cm² (Equation C.15). At that pressure the absorber's density is ~ 0.76 g/cm³, and given our small target volume, that corresponds to only ~ 0.003 g of ³He.

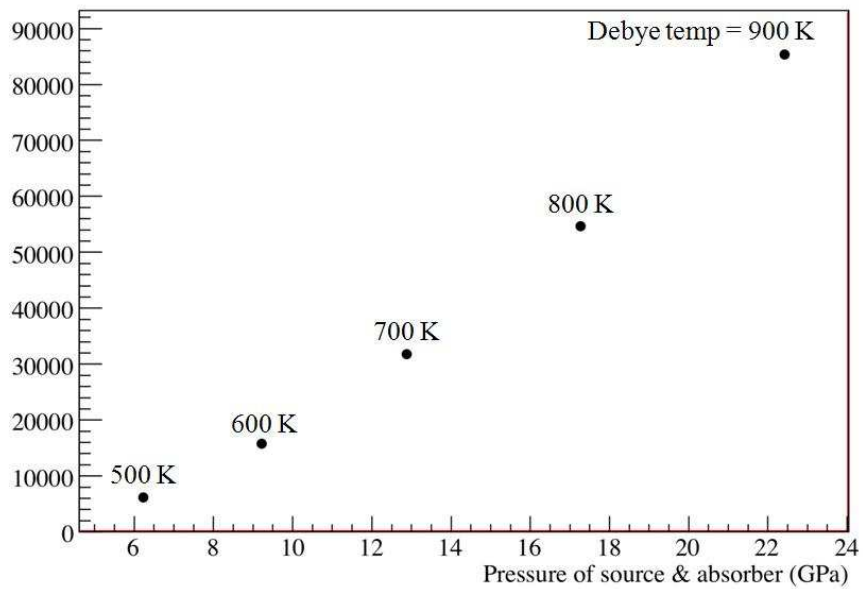


Figure C.5: Simulation results indicating the expected number of Mössbauer neutrino events per week assuming the geometry shown in Figure C.3 with the source and absorber placed 1 cm apart. About 0.1% of these events could be detected with the use of a magnetic slower.

C.6 Lattice Expansion and Contraction

While this experimental design looks more promising than previous proposals for observing the neutrino Mössbauer effect, one important theoretical calculation has to be added before anything definitive can be stated. In calculating the recoil fraction in Equation C.7, I used the same procedure one would use for Mössbauer photons, and I ignored one significant difference that is not directly analogous to the photon case. In the photon case a parent nucleus decays to a long-lived nuclear level of the daughter nucleus. The daughter then emits a photon, decaying to the ground state. Because the intermediate state is fairly long-lived, the rearrangement processes of the electron shell, which occur on a timescale of 10^{-12} s, have settled by the time the photon is emitted. The photon is, therefore, not directly involved in the nuclear decay, making it more likely to possess the energy required for resonant absorption in the target. Unfortunately the antineutrinos are directly involved in the nuclear decay. ${}^3\text{He}$ in a ${}^3\text{H}$ lattice is likely to bond at a different strength, and it will certainly take up a different amount of space. Consequently one must calculate the lattice deformation energies for ${}^3\text{He}$ in a ${}^3\text{H}$ lattice, as well as for ${}^3\text{H}$ in a ${}^3\text{He}$ lattice.

This deformation correction has been estimated for ${}^3\text{He}$ and ${}^3\text{H}$ in an Nb lattice, and the results are not encouraging. The probability that the lattice deformations will not cause lattice excitations can be estimated as [156]:

$$e^{-(E_L^{3\text{He}} - E_L^{3\text{H}})/(k\theta)} \tag{C.18}$$

where E_L is the lattice deformation energy, which for ${}^3\text{H}$ and ${}^3\text{He}$ in a Nb lattice

has been estimated as $E_L^{3\text{H}} = 0.099$ eV and $E_L^{3\text{He}} = 0.551$ eV [163]. Assuming a Debye temperature of 800 K, this factor comes to 1×10^{-3} , which applies to both the emission and absorption, reducing the overall recoilless fraction by a factor of 1×10^{-6} . This calculation is only a preliminary estimate for the Nb case, and a rigorous theoretical calculation that is specific for ^3He and ^3H lattices is necessary in order to determine if Mössbauer neutrinos could actually be experimentally observed through this method. While we have solicited the help of theorists in performing this calculation, we do not yet have a definitive number to report. While I believe this approach to Mössbauer neutrinos is more advantageous than the other existing proposals because of its tunability and direct tritium detection, its viability ultimately hinges on a more detailed calculation of the recoilless fraction that includes the lattice deformation energies.

Bibliography

- [1] C. L. Cowan, Jr., F. Reines, F. B. Harrison, H. W. Kruse, and A. D. McGuire, “Detection of the Free Neutrino: A Confirmation,” *Science*, vol. 124, 1956.
- [2] G. Danby, J.-M. Gaillard, K. Goullanos, L. M. Lederman, N. B. Mistry, M. Schwartz, and J. Steinberger, “Observation of high-energy neutrino reactions and the existence of two kinds of neutrinos,” *Phys. Rev. Lett.*, vol. 9, 1962.
- [3] K. K. *et al.*, “Observation of tau neutrino interactions,” *Physics Letters B*, vol. 504, 2001.
- [4] R. Davis, “Attempt to Detect the Antineutrinos from a Nuclear Reactor by the $\text{Cl}^{37}(\bar{\nu}, e^-)\text{A}^{37}$ Reaction,” *Phys. Rev.*, vol. 97, pp. 766–769, 1955.
- [5] J.N. Abdurashitov *et al.*, “Measurement of the solar neutrino capture rate with gallium metal,” *Phys. Rev. C*, vol. 60, p. 055801, 1999.
- [6] A. I. Abazov *et al.*, “First Results from the Soviet-American Gallium Experiment,” *Nucl. Phys. B. Proc. Suppl.*, vol. 19, p. 84, 1991.

- [7] W. Hampel *et al.*, “GALLEX solar neutrino observations: results for GALLEX IV,” *Phys. Lett. B*, vol. 447, p. 127, 1999.
- [8] P. Anselmann *et al.*, “GALLEX results from the first 30 solar neutrino runs,” *Phys. Lett. B*, vol. 327, p. 377, 1994.
- [9] D. L. Wark, “Neutrino Mass Measurements,” *Phi. Trans. R. Soc. Lond. A*, vol. 361, p. 2527, 2003.
- [10] J. N. Bahcall and C. Pena-Garay, “Global analyses as a road map to solar neutrino fluxes and oscillation parameters,” *JHEP*, vol. 11, 2003.
- [11] A. Y. Smirnov, “The MSW effect and solar neutrinos,” <http://arxiv.org/abs/hep-ph/0305106v1>, 2003.
- [12] K. Hirata *et al.*, “Observation of a neutrino burst from the supernova SN1987A,” *Phys. Rev. Lett.*, vol. 58, p. 1490, 1987.
- [13] R. M. Bionta *et al.*, “Observation of a neutrino burst in coincidence with supernova 1987A in the Large Magellanic Cloud,” *Phys. Rev. Lett.*, vol. 58, p. 1494, 1987.
- [14] E. N. Alekseev *et al.*, “Possible detection of a neutrino signal on 23 February 1987 at the Baksan underground scintillation telescope of the Institute of Nuclear Research,” *JETP Lett.*, vol. 45, p. 589, 1987.
- [15] J. F. Beacom, “The Diffuse Supernova Neutrino Background,” *Annual Rev. Nucl. Part. Sci.*, vol. 60, 2010.
- [16] T. Araki *et al.*, “Experimental investigation of geologically produced antineutrinos with KamLAND,” *Nature*, vol. 436, pp. 499–503, 2005.

- [17] C. A. *et al.*, “Particle Data Group,” *Phys. Lett. B*, vol. 667, 2008.
- [18] B. Aharmim *et al.*, “Low Energy Threshold Analysis of the Phase I and Phase II Data Sets of the Sudbury Neutrino Observatory,” *Phys. Rev. C*, vol. 81, 2010.
- [19] A. S. Dighe *et al.*, “Identifying Earth matter effects on supernova neutrinos at a single detector,” *JCAP*, vol. 0306, 2003.
- [20] S. W. B. *et al.*, “APS Neutrino Study: Report of the Neutrino Astrophysics and Cosmology Working Group,” <http://arxiv.org/abs/astro-ph/0412544>, 2004.
- [21] S. Boris *et al.*, “Neutrino Mass from the Beta Spectrum in the Decay of Tritium,” *Phys. Rev. Lett.*, vol. 58, p. 2019, 1987.
- [22] E. Holzschuh *et al.*, “Measurement of the electron-neutrino mass from tritium beta decay,” *Phys. Lett. B*, vol. 287, p. 381, 1992.
- [23] H. Kawakami *et al.*, “New upper bound on the electron anti-neutrino mass,” *Phys. Lett. B*, vol. 256, p. 105, 1991.
- [24] R. G. H. Robertson *et al.*, “Limit on $\bar{\nu}_e$ mass from observation of the β decay of molecular tritium,” *Phys. Rev. Lett.*, vol. 67, p. 957, 1991.
- [25] W. Stoeffl and D. J. Decman, “Anomalous Structure in the Beta Decay of Gaseous Molecular Tritium,” *Phys. Rev. Lett.*, vol. 75, p. 3237, 1995.
- [26] V. M. Lobashev *et al.*, “Study of the tritium beta-spectrum in experiment Troitsk ν -mass,” *Prog. Part. Nucl. Phys.*, vol. 48, p. 123, 2002.

- [27] J. Bonn *et al.*, “Results from the Mainz neutrino mass experiment,” *Prog. Part. Nucl. Phys.*, vol. 48, p. 133, 2002.
- [28] C. E. Aalseth *et al.*, “The Majorana Ge-76 double-beta decay project,” <http://arxiv.org/abs/hep-ex/0201021>, 2002.
- [29] I. Abt *et al.*, “A new Ge-76 double beta decay experiment at LNGS,” <http://arxiv.org/abs/hep-ex/0404039>, 2004.
- [30] R. Ardito *et al.*, “CUORE: A cryogenic underground observatory for rare events,” <http://arxiv.org/abs/hep-ex/0501010>, 2005.
- [31] M. Danilov *et al.*, “Detection of very small neutrino masses in double-beta decay using laser tagging,” *Phys. Lett. B*, vol. 480, p. 12, 2000.
- [32] F. Deppisch, C. Jackson, I. Nasteva, and S. Sldner-Rembold, “Probing the mechanism of neutrinoless double beta decay with SuperNEMO,” *Progress in Particle and Nuclear Physics*, vol. 64, p. 278, 2010.
- [33] SNO+, K. Zuber *et al.*, “Nd double beta decay search with SNO+,” *AIP Conf. Proc.*, vol. 942, p. 101, 2007.
- [34] H. V. K.-K. *et al.*, “Search for neutrinoless double beta decay with enriched ^{76}Ge in Gran Sasso 19902003,” *Phys. Rev. B*, vol. 586, 2004.
- [35] C. E. A. *et al.*, “Comment on Evidence for Neutrinoless Double Beta Decay,” *Modern Physics Letters A*, vol. 17, 2002.
- [36] S. Hannestad, “Neutrino mass bounds from cosmology,” *Nucl. Phys. B Proc. Suppl.*, vol. 145, 2005.

- [37] A. M. Malinovsky, A. A. Voevodkin, V. N. Lukash, E. V. Mikheeva, and A. A. Vikhlinin, “Cosmological constraints on the neutrino mass from CMB anisotropy and large-scale structure of the universe,” *Astronomy Letters*, vol. 34, 2008.
- [38] E. K. *et. al.*, “Seven-Year Wilkinson Microwave Anisotropy Probe (WMAP) Observations: Cosmological Interpretation,” <http://arxiv.org/abs/1001.4538>, 2010.
- [39] E. Komatsu *et. al.*, “Five-Year Wilkinson Microwave Anisotropy Probe (WMAP) Observations: Cosmological Interpretation,” *Astrophys. J. Suppl.*, vol. 180, 2009.
- [40] K. Ichikawa, “Neutrino mass constraint from CMB and its degeneracy with other cosmological parameters,” *J. of Physics: Conf. Ser.*, vol. 120, 2008.
- [41] G. Scoles, Ed., *Atomic and Molecular Beam Methods*. New York: Oxford University Press, 2000, vol. 1 and 2.
- [42] E. Narevicius, C. G. Parthey, A. Libson, J. Narevicius, I. Chavez, U. Even, and M. G. Raizen, “An atomic coilgun: using pulsed magnetic fields to slow a supersonic beam,” *New J. of Phys.*, vol. 9, p. 358, 2007.
- [43] E. Narevicius, A. Libson, C. G. Parthey, I. Chavez, J. Narevicius, U. Even, and M. G. Raizen, “Stopping Supersonic Beams with a Series of Pulsed Electromagnetic Coils: An Atomic Coilgun,” *Phys. Rev. Lett.*, vol. 100, p. 093003, 2008.

- [44] S. D. Hogan, A. W. Wiederkehr, H. Schmutz, and F. Merkt, “Magnetic Trapping of Hydrogen after Multistage Zeeman Deceleration,” *Phys. Rev. Lett.*, vol. 101, p. 143001, 2008.
- [45] M. G. Raizen, “Comprehensive Control of Atomic Motion,” *Science*, vol. 324, p. 1403, 2009.
- [46] H. J. Metcalf and P. van der Straten, *Laser Cooling and Trapping*. New York: Springer-Verlag, 1999.
- [47] M. G. Raizen, A. M. Dudarev, Q. Niu, and N. Fisch, “Compression of Atomic Phase Space Using an Asymmetric One-Way Barrier,” *Phys. Rev. Lett.*, vol. 94, 2005.
- [48] G. N. Price, S. T. Bannerman, K. Viering, E. Narevicius, and M. G. Raizen, “Single-Photon Atomic Sorting,” *Phys. Rev. Lett.*, vol. 100, p. 093004, 2008.
- [49] S. T. Bannerman, G. N. Price, K. Viering, and M. G. Raizen, “Single-photon cooling at the limit of trap dynamics: Maxwell’s demon near maximum efficiency,” *New J. Phys.*, vol. 11, p. 063044, 2009.
- [50] L. Szilard, *Z. Phys.*, vol. 53, p. 840, 1929.
- [51] C. E. Shannon, *Bell Syst. Tech.*, vol. 27, p. 379, 1948.
- [52] A. Ruschhaupt, J. G. Muga, M. G. Raizen, “One-photon atomic cooling with an optical Maxwell demon valve,” *J. Phys. B: At. Mol. Opt. Phys.*, vol. 39, p. 3833, 2006.

- [53] P. M. Binder, “Reflections on a Wall of Light,” *Science*, vol. 322, p. 1334, 2008.
- [54] A. Osipowicz *et. al.*, “KATRIN: A next generation tritium beta decay experiment with sub-eV sensitivity for the electron neutrino mass,” <http://arXiv.org/abs/hep-ex/0109033>, 2001.
- [55] S. Elliott and J. Engel, “Double-beta decay,” *J. Phys. G*, vol. 30, p. R183, 2004.
- [56] F. Boehm and P. Vogel, *Physics of massive neutrinos*. New York: Cambridge University Press, 1987.
- [57] F. James, “Montecarlo Phase Space,” *CERN*, vol. 56, 1968.
- [58] A. Lehmann, A. Britting, W. Eyrich, and F. Uhlig, “Studies of MCP Properties,” *JINST*, vol. 11, 2009.
- [59] O. H. W. Siegmund, J. Vallerger, and B. Wargelin, “Background events in microchannel plates,” *IEEE Transactions on Nuclear Science*, vol. 35, no. 1, p. 524, 1988.
- [60] S. K. Dutta, J. R. Guest, D. Feldbaum, A. Walz-Flannigan, and G. Raithel, “Ponderomotive Optical Lattice for Rydberg Atoms,” *Phys. Rev. Lett.*, vol. 85, p. 5551, 2000.
- [61] S. Haroche and D. Kleppner, “Cavity Quantum Electrodynamics,” *Physics Today*, vol. 42, no. 1, pp. 24–30, 1989.

- [62] R. Côté, A. Russell, E. E. Eyler, and P. L. Gould, “Quantum random walk with Rydberg atoms in an optical lattice,” *New J. of Phys.*, vol. 8, p. 156, 2006.
- [63] T. A. Johnson, E. Urban, T. Henage, L. Isenhower, D. D. Yavuz, T. G. Walker, and M. Saffman, “Rabi Oscillations between Ground and Rydberg States with Dipole-Dipole Atomic Interactions,” *Phys. Rev. Lett.*, vol. 100, p. 113003, 2008.
- [64] T. Cubel, B. K. Teo, V. S. Malinovsky, J. R. Guest, A. Reinhard, B. Knuffman, P. R. Berman, and G. Raithel, “Coherent population transfer of ground-state atoms into Rydberg states,” *Phys. Rev. A*, vol. 72, p. 023405, 2005.
- [65] D. R. Beaulieu *et. al.*, “Nano-engineered ultra-high-gain microchannel plates,” *Nucl. Instrum. Methods Phys. Res. A*, vol. 607, p. 81, 2009.
- [66] A. Vredenburg, W. G. Roeterdink, M. H. M. Janssen, “A photoelectron-photoion coincidence imaging apparatus for femtosecond time-resolved molecular dynamics with electron time-of-flight resolution of $\sigma = 18\text{ps}$ and energy resolution $\Delta E/E = 3.5$,” *Rev. Sci. Instru.*, vol. 79, p. 063108, 2008.
- [67] J. Genat, G. Varner, F. Tang, and H. Frisch, “Signal processing for picosecond resolution timing measurements,” *Nucl. Instrum. Methods Phys. Res. A*, vol. 607, 2009.

- [68] G. H. Fetcher *et al.*, “Bulk sensitive photo emission spectroscopy of C1_b compounds,” *J. Electron Spectrosc. Relat. Phenom.*, vol. 156-158, p. 97, 2007.
- [69] F. James and M. Roos, “MINUIT - a system for function minimization and analysis of the parameter errors and correlations,” *Computer Physics Communications*, vol. 10, 1975.
- [70] M. Boulay *et al.*, “A Letter Expressing Interest in Staging an Experiment at SNOLAB Involving Filling SNO with Liquid Scintillator Plus Double Beta Decay Candidate Isotopes,” <http://www.snoplus.phy.queensu.ca/LOI.pdf>, 2004.
- [71] J. N. Bahcall, A. M. Serenelli, and S. Basu, “New solar opacities, abundances, helioseismology, and neutrino fluxes,” *Astrophys. J.*, vol. 621, 2005.
- [72] K. Z. on behalf of the SNO+ collaboration, “Nd double beta decay search with SNO + ,” *AIP Conference Proceedings*, vol. 942, no. 1, pp. 101–104, 2007. [Online]. Available: <http://link.aip.org/link/?APC/942/101/1>
- [73] J. W. Beams, F. G. Haynes, “The Separation of Isotopes by Centrifuging,” *Phys. Rev.*, vol. 50, p. 491, 1936.
- [74] W. W. Watson, “Concentration of Heavy Carbon by Thermal Diffusion,” *Phys. Rev.*, vol. 56, p. 703, 1939.
- [75] W. H. Furry, R. Clark Jones, L. Onsager, “On the Theory of Isotope Separation by Thermal Diffusion,” *Phys. Rev.*, vol. 55, p. 1083, 1939.

- [76] R. J. Bartlett and J. R. Morrey, *US Patent 4,105,921*, August 8 1978.
- [77] A. O. Nier, "A Mass-Spectrographic Study of the Isotopes of Hg, Xe, Kr, Be, I, As, and Cs," *Phys. Rev.*, vol. 52, p. 933, 1937.
- [78] L. Love, "Electromagnetic Separation of Isotopes at Oak Ridge," *Science*, vol. 182, p. 343, 1973.
- [79] E. S. Lyman, "Making domestically produced medical isotopes a national priority," <http://www.thebulletin.org/web-edition/oped/making-domestically-produced-medical-isotopes-national-priority>, December 2008.
- [80] P. A. Bokhan, V. V. Buchanov, N. V. Fateev, M. M. Kalugin, M. A. Kazaryan, A. M. Prokhorov, D. E. Zakrevshii, *Laser Isotope Separation in Atomic Vapor*. Weinheim: WILEY-VCH Verlag GmbH & Co. KGaA, 2006.
- [81] M. G. Raizen, "Comprehensive Control of Atomic Motion," *Science*, vol. 324, p. 1403, 2009.
- [82] A. Amirav, U. Even, "Isotope separation in supersonic molecular beams using rf spectroscopy," *J. Appl. Phys.*, vol. 51, p. 1, 1980.
- [83] W. A. van Wijngaarden, J. Li, "Laser isotope separation of barium using an inhomogeneous magnetic field," *Phys. Rev. A*, vol. 49, p. 1158, 1994.
- [84] G. Scoles, Ed., *Atomic and Molecular Beam Methods*. New York: Oxford University Press, 2000, vol. vol. 1 and 2.

- [85] U. Even, M. Hillenkamp, S. Keinan, “Condensation limited cooling in supersonic expansions,” *J. Chem. Phys.*, vol. 118, p. 8699, 2003.
- [86] V. N. Gorshkov, V. A. Komarovskii, A. L. Osherovich, N. P. Penkin, “Lifetimes of excited levels of Nd I and Nd II. Oscillator strengths of the spectral lines of Nd I,” *Astrophysics*, vol. 17, no. 4, p. 437, 1982.
- [87] W. G. Kaenders, F. Lison, I. Müller, A. Richter, R. Wynands, D. Meschede, “Refractive components for magnetic atom optics,” *Phys. Rev. A*, vol. 54, p. 5067, 1996.
- [88] K. Halbach, *Nucl. Instrum. Methods*, vol. 169, p. 1, 1980.
- [89] J. P. Beardmore, A. J. Palmer, K. C. Kuiper, R. T. Sang, “A hexapole magnetic guide for neutral atomic beams,” *Rev. Sci. Instrum.*, p. 073105, 2009.
- [90] K. C. Kuiper, “Magnetic bender for metastable neon lithography,” Master’s thesis, Eindhoven University of Technology, 2007.
- [91] D. Budker, D. F. Kimball, and D. P. DeMille, *Atomic Physics: an exploration through problems and solutions*. New York: Oxford University Press, 2004.
- [92] D. C. Lau, R. J. McLean, A. I. Sidorov, D. S. Gough, J. Koperski, W. J. Rowlands, B. A. Sexton, G. I. Opat, P. Hannaford, “Magnetic mirrors with micron-scale periodicities for slowly moving neutral atoms,” *Quantum Semiclass. Opt.*, vol. 1, p. 371, 1999.

- [93] Yu. Ralchenko, A. E. Kramida, J. Reader, and NIST ASD Team, “NIST Atomic Spectra Database (version 3.1.5),” [Online] Available: <http://physics.nist.gov/asd3>, Gaithersburs, MD, 2008.
- [94] J. P. Beardmore, A. J. Palmer, K. C. Kuiper, and R. T. Sang, “A hexapole magnetic guide for neutral atomic beams,” *Rev. Sci. Instrum.*, vol. 80, p. 073105, 2009.
- [95] G. A. Bird, *Molecular Gas Dynamics and the Direct Simulation of Gas Flows*. New York: Oxford University Press, 1994.
- [96] G. H. *et al.*, “High-Resolution Laser Spectroscopy of the D Lines of On-Line Produced $^{21,22,24,25}\text{Na}$ Using a New High-Sensitivity Method of Detection of Optical Resonances,” *Phys. Rev. Lett.*, vol. 34, 1975.
- [97] J. Boger *et al.*, “The Sudbury Neutrino Observatory,” *Nucl. Instrum. Methods in Phys. Research Sect.*, vol. A449, p. 172, 2000.
- [98] J. R. Klein, M. S. Neubauer, R. Van Berg, and M. Newcomer, “The SNO Trigger System,” SNO technical report SNO-STR-97-035, University of Pennsylvania 1997.
- [99] J. D. Jackson, *Classical Electrodynamics*. Hoboken, NJ: John Wiley and Sons, Inc., 1999.
- [100] C. Kyba, “Measurement of the atmospheric neutrino induced muon flux at the Sudbury Neutrino Observatory,” Ph.D. dissertation, University of Pennsylvania, 2006.
- [101] J. Cameron, “The Photomultiplier tube calibration of the Sudbury Neutrino Observatory,” Ph.D. dissertation, University of Oxford, 2001.

- [102] R. Ford, “Calibration of SNO for the detection of ^8B neutrinos,” Ph.D. dissertation, Queen’s University, 1998.
- [103] M. R. D. *et al.*, “The N-16 calibration source for the Sudbury Neutrino Observatory,” *Nucl. Instrum. Meth. A*, vol. 481, 2002.
- [104] W. R. Nelson, H. Hirayama, and D. W. O. Rogers, “The EGS4 code system,” SLAC-0265.
- [105] J. F. E. Briesmeister, “MCNP: A General Monte Carlo N-Particle Transport Code,” LA-12625-M.
- [106] J. R. A. E. G. Ingelman, “LEPTO version 6.3 - The Lund Monte Carlo for Deep Inelastic Lepton-Nucleon Scattering,” 1995.
- [107] P. A. Aarnio *et al.*, “FLUKA: Hadronic benchmarks and applications,” Prepared for International Conference on Monte Carlo Simulations in High-Energy and Nuclear Physics - MC 93, Tallahassee, FL, 22-26 Feb 1993.
- [108] C. Aeitnitz and T. A. Gabriel, “The GEANT-CALOR interface and benchmark calculations of ZEUS test calorimeters,” *Nuclear Instruments and Methods in Physics Research A*, vol. 349, Sept 1994.
- [109] T. J. S. Woosley, “The physics of core-collapse supernovae,” *Nature*, vol. 1, p. 147, 2005.
- [110] N. I. *et al.*, “Neutrino energy loss in stellar interiors. III. pair, photo-, plasma, and bremsstrahlung processes,” *Astrophys. J.*, vol. 339, p. 354, 1989.

- [111] T. J. S. Woosley, “The physics of core-collapse supernovae,” *Nature Physics*, vol. 1, 2005.
- [112] K. E. Takahashi, “Effects of neutrino oscillation on the supernova neutrino spectrum,” *Phys. Rev. D*, vol. 64, 2001.
- [113] T. Totani, K. Sato, H. E. Dalhed, J. R. Wilson, “Effects of neutrino oscillation on the supernova neutrino spectrum,” *Astrophys. J.*, vol. 496, p. 216, 1998.
- [114] E. Myra and A. Burrows, “Neutrinos from Type II supernovae: The first 100 milliseconds,” *Astrophys. J.*, vol. 364, 1990.
- [115] A. Burrows, D. Klein, and R. Gandhi, “The future of supernova neutrino detection,” *Phys. Rev. D*, vol. 45, p. 3361, 1992.
- [116] G. L. Fogli, E. Lisi, D. Montanino, A. Mirizzi, “Analysis of energy and time dependence of supernova shock effects on neutrino crossing probabilities,” *Phys. Rev. D*, vol. 68, p. 033005, 2003.
- [117] R. Tomás, “Identifying the neutrino mass hierarch with supernova neutrinos,” *J. Phys. Conf. Ser.*, vol. 39, p. 297, 2006.
- [118] K. Scholberg, “Supernova neutrino detection,” <http://arxiv.org/abs/astro-ph/0701081>, 2007.
- [119] W. C. Haxton, “Neutrino Astrophysics,” <http://arxiv.org/abs/0808.0735v1>, 2008.

- [120] R. C. Schirato and G. M. Fuller, “Connection between supernova shocks, flavor transformation, and the neutrino signal,” <http://arxiv.org/abs/astro-ph/0205390>, 2002.
- [121] P. Antonioli et al., “SNEWS: The SuperNova Early Warning System,” *New J. Phys.*, vol. 6, 2004.
- [122] M. Ikeda *et al.*, “Search for Supernova Neutrino Bursts at Super-Kamiokande,” *Astrophys. J.*, vol. 669, p. 519, 2007.
- [123] B. A. *et al.*, “Determination of the ν_e and Total ^8B Solar Neutrino Fluxes with the Sudbury Neutrino Observatory Phase I Data Set,” *Phys. Rev. C*, vol. 75, 2007.
- [124] K. Sumiyoshi, S. Yamada, H. Suzuki, and S. Chiba, “Neutrino signals from the formation of a black hole: A probe of the equation of state of dense matter,” *Phys. Rev. Lett.*, vol. 97, p. 091101, 2006.
- [125] J. F. Beacom, R. N. Boyd, and A. Mezzacappa, “Technique for Direct eV-Scale Measurements of the Mu and Tau Neutrino Masses Using Supernova Neutrinos,” *Phys. Rev. Lett.*, vol. 85, p. 3568, 2000.
- [126] G. C. McLaughlin and R. Surman, “Supernova neutrinos: The accretion disk scenario,” *Phys. Rev. D*, vol. 75, 2007.
- [127] A. Marino, “Evidence for Neutrino Oscillations in the Sudbury Neutrino Observatory,” Ph.D. dissertation, University of California Berkeley, 2004.
- [128] B. *et al.* Aharmim, “Electron antineutrino search at the sudbury neutrino observatory,” *Phys. Rev. D*, vol. 70, no. 9, p. 093014, Nov 2004.

- [129] J. Terrell, “Distributions of Fission Neutron Numbers,” *Phys. Rev.*, vol. 108, 1957.
- [130] A. Hallin, “Limits on Fission,” Technical Report, Sudbury Neutrino Observatory, 2003.
- [131] J. Orrell, “A Search for an Electron Antineutrino Signal in the Sudbury Neutrino Observatory,” Ph.D. dissertation, University of Washington, 2004.
- [132] S. B. Aharmim *et al.*, “Electron energy spectra, fluxes, and day-night asymmetries of 8B solar neutrinos from measurements with NaCl dissolved in the heavy-water detector at the Sudbury Neutrino Observatory,” *Phys. Rev. C*, vol. 72, p. 055502, 2005.
- [133] K. Inoue *et al.*, “Reactor neutrino oscillation studies with KamLAND,” *New J. Phys.*, vol. 6, 2004.
- [134] G. A. Tammann, W. Löffler, and A. Schröder, “The galactic supernova rate,” *Astrophys. J.*, vol. 92, 1994.
- [135] D. Griffiths, *Introduction to Elementary Particles*. New York: Harper and Row Publishers, 1987.
- [136] D. O. Caldwell, *Current Aspects of Neutrino Physics*. New York: Springer-Verlag Berlin Heidelberg, 2001.
- [137] P. Marmier and E. Sheldon, *Physics of Nuclei and Particles, v1*. New York: Academic Press, 1969.
- [138] K. E. Bergkvist, *Nucl. Phys. B*, vol. 39, 1972.

- [139] P. F. A. Saenz, “Effect of final-state interactions in allowed β decays. I. General formalism,” *Phys. Rev. C*, vol. 56, 1997.
- [140] R. Daudel and P. Benoist and R. Jacques and M. Jean, *Comptes Rend*, vol. 224, p. 1427, 1947.
- [141] R. Daudel and M. Jean and M. Lecoïn, *Comptes Rend*, vol. 225, p. 290, 1947.
- [142] R. Daudel, M. Jean, and M. Lecoïn, *J. de Phys.*, vol. 8, p. 238, 1947.
- [143] R. Sherk, “Bound Electron Creation in the Decay of Tritium,” *Phys. Rev.*, vol. 75, p. 789, 1949.
- [144] S. G. Cohen, D. E. Murnick, and R. S. Raghavan, “Boundstate-state beta decay and kinematics search for neutrino mass,” *Hyperfine Interactions*, vol. 33, pp. 1–8, 1987.
- [145] J. Bahcall, “Theory of Bound-State Beta Decay,” *Phys. Rev.*, vol. 124, p. 495, 1961.
- [146] R. S. Van Dyck, Jr., D. L. Farnham, and P. B. Schwinberg, “Tritium-helium-3 mass difference using the Penning trap mass spectroscopy,” *Phys. Rev. Lett.*, vol. 70, pp. 2888–2891, 1993.
- [147] W. P. Kells and J. P. Schiffer, “Possibility of observing recoilless resonant neutrino absorption,” *Phys. Rev. C*, vol. 28, p. 2162, 1983.
- [148] H. Frauenfelder, *The Mössbauer Effect*. New York: W. A. Benjamin, Inc., 1962.

- [149] J. W. E. Lamb, “Capture of Neutrons by Atoms in a Crystal,” *Phys. Rev.*, vol. 55, p. 190, 1939.
- [150] R. L. Mössbauer, “Gammastrahlung in Ir¹⁹¹ (in German),” *Zeitschrift für Physik A Hadrons and Nuclei*, vol. 151, p. 124, 1958.
- [151] W. M. Visscher, “Neutrino Detection by Resonance Absorption in Crystals at Low Temperatures,” *Phys. Rev.*, vol. 116, p. 1581, 1959.
- [152] S. M. Bilenky, F. von Feilitzsch, and W. Potzel, “Time-energy uncertainty relations for neutrino oscillation and Mössbauer neutrino experiment,” *J. Phys. G: Nucl. Part. Phys.*, vol. 35, 2008.
- [153] H. Nunokawa, S. Parke, and R. F. Zukanovich, “Another possible way to determine the neutrino mass hierarchy,” <http://arxiv.org/abs/hep-ph/0503283>, 2005.
- [154] H. Minakata and S. Uchinami, “Recoilless Resonant Absorption of Monochromatic Neutrino Beam for Measuring Δm_{31}^2 and θ_{13} ,” <http://arxiv.org/abs/hep-ph/0602046>, 2006.
- [155] R. V. Pound and G. A. Rebka Jr., “Gravitational Red-Shift in Nuclear Resonance,” *Phys. Rev. Lett.*, vol. 3, 1959.
- [156] W. Potzel, “Recoilless Resonant Emission and Detection of Electron Antineutrinos,” *J. Phys. Conf. Ser.*, vol. 136, p. 022010, 2008.
- [157] —, “Recoilless resonant capture of antineutrinos: basic questions and some ideas,” *Phys. Scr.*, vol. T127, p. 85, 2006.

- [158] R. S. Raghavan, “Hypersharp Resonant Capture of Neutrinos as a Laboratory Probe of the Planck Length,” *Phys. Rev. Lett.*, vol. 102, p. 091804, 2009.
- [159] L. A. Mikaélyan, B. G. Tsinoev, A. A. Borovoi, “Induced Capture of Orbital Electron,” *Sov. J. Nucl. Phys.*, vol. 6, 1968.
- [160] G. L. Morley, K. L. Kliewer, “Lattice Dynamics of hep He^3 and He^4 at High Pressure,” *Phys. Rev.*, vol. 180, p. 245, 1969.
- [161] J. Stewart, “Compression of Solid He^3 and He^4 to 20000 Bars,” *Phys. Rev.*, vol. 129, 1963.
- [162] B. Budick, “Atomic Effects on the Tritium ft Value,” *Phys. Rev. Lett.*, vol. 51, 1983.
- [163] M. J. Puska and R. M. Nieminen, “Theory of hydrogen and helium impurities in metals,” *Phys. Rev. B*, vol. 29, 1984.

Vita

Melissa Travis Jerkins attended David Lipscomb High School in Nashville, Tennessee. In 1999 she enrolled at Abilene Christian University in Abilene, Texas. She completed a Bachelor of Science degree in Physics in May, 2003. In August 2005 she began graduate studies in Physics at the University of Texas in Austin.

Permanent Address: 1701A Coronado Hills Drive
Austin, TX 78752

This dissertation was typeset with L^AT_εE_X² by the author.

¹L^AT_εE_X is an extension of L^AT_EX. L^AT_EX is a collection of macros for T_EX. T_EX is a trademark of the American Mathematical Society. The macros used in formatting this dissertation were written by Dinesh Das, Department of Computer Sciences, The University of Texas at Austin, and extended by Bert Kay, James A. Bednar, and Ayman El-Khashab.